

**ARTIFICIAL NEURAL NETWORKS BASED SUBGRID
CHEMISTRY MODEL FOR TURBULENT REACTIVE
FLOW SIMULATIONS**

A Thesis
Presented to
The Academic Faculty

by

Baris A. Sen

In Partial Fulfillment
of the Requirements for the Degree
Doctor of Philosophy in the
School of Aerospace Engineering

Georgia Institute of Technology
December 2009

**ARTIFICIAL NEURAL NETWORKS BASED SUBGRID
CHEMISTRY MODEL FOR TURBULENT REACTIVE
FLOW SIMULATIONS**

Approved by:

Dr Suresh Menon, Committee Chair
School of Aerospace Engineering
Georgia Institute of Technology

Dr Lakshmi Sankar
School of Aerospace Engineering
Georgia Institute of Technology

Dr Timothy Lieuwen
School of Aerospace Engineering
Georgia Institute of Technology

Dr Mitchell Walker
School of Aerospace Engineering
Georgia Institute of Technology

Dr Thorsten Stoesser
School of Civil and Environmental
Engineering
Georgia Institute of Technology

Dr Saadat Syed
Pratt and Whitney

Date Approved: August 12, 2009

To my family:

*those who had passed away, who are with me regardless of the distance and who have
not yet joined*

ACKNOWLEDGEMENTS

This thesis work has been done with the sole purpose of leaving an echo of my existence in this vast universe and I want to express my sincere gratitude to my advisor Dr. Suresh Menon, for making it possible. I am greatly indebted to him for his guidance, support, and for letting me work on this very interesting subject. Without any doubt, I learned a lot from his experience and from the endless discussions that we had.

I would like to thank the members of my thesis committee, Dr. Lakshmi Sankar, Dr. Timothy Lieuwen, Dr. Mitchell Walker, Dr. Thorsten Stoesser, and Dr. Saadat Syed for the critical examination of the dissertation and excellent suggestions, which increased the quality of this work. I also would like to thank Dr. Evatt R. Hawkes from University of New South Wales for providing the data obtained from direct numerical simulation of the non-premixed syngas flame.

I am grateful for the financial support from the NASA Glenn Research Center over the five years I have spent for my research.

I had the privilege to work under the guidance of three different advisors during my graduate studies. Among those, I would like to thank Dr. I. Bedii Ozdemir at Istanbul Technical University (ITU) for introducing me into this field and sparking the fire of research. My sincere thanks extend to Dr. Kadir Kirkkopru for teaching me critical thinking and being patient, which I lacked when I started working with him.

After spending three years as one of the few people working on the turbulent combustion modeling at ITU, the crowded and highly challenging environment in the computational combustion lab (CCL) was really amazing. I would like to start thanking my senior advisors Dr. Hossam El-Asrag and Dr. Ionut Porumbel for

helping me understand the models and the codes used in the CCL. I wish to thank my crazy Mexican friend Dr Martin Sanchez-Rocha, Tzatzhilha (Zazy) Torres and my French friends Matthieu Masquelet, Dr Franklin Genin, Diane de Zelicort, Leon Phan for showing that friendship does not have any boundaries, and people coming from different parts of the world can share the same interests.

My thanks extend to current and past members of the CCL with whom I had the chance to work with: Dr. Mehmet Kirtas, Dr. Satish Undapalli, Dr. Kenji Miki, Dr. Srikant Srinivasan, Dr. Jung Choi, Valerio Parisi, Leandro Gryngarten, Andy Smith, Jean-Pierre de la Croix, Kaushik Balakrishnan, Tim Gallagher, Chaitanya Ghodke, Anuradha Sanyal and Sudharshan Renganathan.

I am also proud to be a member of the CCL soccer team 'Time for Glory'. Although we were eliminated twice in the play-offs by the same team, I enjoyed being a member of this team, and hope that it will remain as a CCL tradition.

The inspirations given by Mozart, Vivaldi, and Tolkien at the moments of desperation when getting a Ph.D. seemed as impossible were also very important.

My special thanks go to the members of the Turkish gang, Faruk Cavusoglu, Can Cavusoglu, Engin Orcun Kozaka, and Dr. Ayse Gul Gungor who helped me in getting used to the life in Atlanta. Their friendship was invaluable, and I spent almost all my spare time outside the lab (when I had any) with them.

Finally, I would like to thank my parents, Nagihan Sen, Mehmet Sen and my sister Nur Banu Sen. Although we have been separated by an ocean, I can always feel their love and prayers. A great debt of gratitude I owe to my wife, Dr. Nurhak Erbas Sen, for patiently waiting my graduation over the years. Her encouragement and her continuous support propelled my will to finish my Ph.D. at the moments of dissapointment (Yo Nurhak we did it!).

TABLE OF CONTENTS

DEDICATION	iii
ACKNOWLEDGEMENTS	iv
LIST OF TABLES	x
LIST OF FIGURES	xii
NOMENCLATURE	xviii
SUMMARY	xxvi
I INTRODUCTION AND OBJECTIVES	1
1.1 Turbulent Combustion Modeling and Chemical Kinetics: An Overview	1
1.2 Chemical Kinetics	4
1.3 Turbulent Combustion Modeling	5
1.3.1 Turbulent Flow Modeling	6
1.3.2 Flame Turbulence Interaction Modeling	8
1.3.3 Chemical Kinetics Modeling	17
1.4 Neural Networks	21
1.4.1 Biological Neurons	23
1.4.2 Artificial Neurons	24
1.4.3 ANN for Chemical Kinetics Calculations	26
1.5 Fundamental Flame-Turbulence Interaction Studies	28
1.6 Objectives	31
II MATHEMATICAL FORMULATION	36
2.1 Gas Phase Governing Equations	36
2.1.1 Transport Properties	37
2.2 LES Modeling	41
2.2.1 Subgrid Momentum Modeling	43
2.2.2 Subgrid Combustion Modeling	46

2.3	Artificial Neural Networks	50
III	NUMERICAL IMPLEMENTATION	55
3.1	Discretization of the Governing Equations	55
3.1.1	The Finite Volume Formulation	55
3.1.2	Domain Discretization	58
3.1.3	Time Integration	59
3.2	Characteristic Boundary Conditions	61
3.3	Linear Eddy Mixing Model Implementation	66
3.3.1	The Reaction Diffusion Equation	66
3.3.2	The Splicing Algorithm	68
IV	ANN VALIDATION	71
4.1	<i>A-priori</i> Testing of the GDR and AGDR	71
4.2	Validating the ANN Training Code on Generic Functions	79
V	EVALUATION OF DIFFERENT TABULATION STRATEGIES FOR ANN TRAINING	83
5.1	ANN Trained on Laminar Flames	84
5.1.1	Laminar Premixed Flame Computation	84
5.1.2	Turbulent Premixed Flame Computations	87
5.1.3	Conclusions	99
5.2	ANN trained on Laminar Flame-Vortex Interactions	101
5.2.1	Training Table Generation	101
5.2.2	Test Cases	102
5.2.3	Results and Discussion	102
5.2.4	ANN Speed-Up and Memory Savings	109
5.2.5	Conclusions	110
5.3	ANN trained on Flame Turbulence Interaction	111
5.3.1	Training Table generation	111
5.3.2	Test Cases	112

5.3.3	Results and Discussion	115
5.3.4	ANN Speed-Up and Memory Savings	136
5.3.5	Conclusions	138
VI	LES OF EXTINCTION AND REIGNITION WITH ANN	141
6.1	Numerical setup and ANN training	141
6.2	LES with LANN	142
6.2.1	LANN Validation Against DI for Case M-1	142
6.2.2	Extinction and Reignition Predictions for Cases M-1 and M-2	145
6.2.3	Scalar Field Conditional Statistics	150
6.2.4	Syngas Flame Structure	154
6.2.5	Scalar Dissipation Rate Statistics	157
6.3	LES with TANN	161
6.3.1	TANN Model Description	161
6.3.2	Results	163
6.4	Time and Memory Savings	169
VII	LES OF SPRF COMBUSTOR WITH ANN	171
7.1	Numerical Setup and ANN Training	171
7.2	LES with LANN	174
7.2.1	Instantaneous Reaction Rate Comparison	174
7.2.2	Comparison of the Time Averaged Data	177
7.3	LES with TANN	181
7.4	Time and Memory Savings	186
VIII	CONCLUSIONS AND FUTURE WORK	188
8.1	Conclusions	188
8.2	Recommendations for Future Work	193
APPENDIX A	SHORT MANUAL FOR 1-D STAND-ALONE LINEAR EDDY MIXING MODEL SOLVER	197
APPENDIX B	REDUCED MECHANISMS USED IN THE STUDY	206

REFERENCES	209
VITA	216

LIST OF TABLES

1	Handling species equation with different flame-turbulence interaction models.	16
2	Sub-models used to handle chemistry, diffusion and turbulent stirring by different flame-turbulence interaction models.	17
3	Comparison of Biological and Artificial Neurons	26
4	Comparison of Biological and Artificial Neurons	26
5	Simulation parameters for flame turbulence interaction problem	92
6	Flame parameters used for flame turbulence interaction	92
7	Case table for the LES of flame-vortex-turbulence interaction	102
8	Flame Parameters	102
9	Effect of number of hidden layers and PEs on the training phase	104
10	Speed-up obtained by ANN compared to DVODE	108
11	Memory requirement for the look-up table approach and the ANN	109
12	Test Cases	112
13	LEMLES Test Cases	112
14	Flame Parameters for LEMLES Case A	112
15	List of ANN architectures and their properties used for Case C	120
16	Memory saving by ANN for Case A	137
17	Timing for Case B	137
18	Timing for Case C	137
19	Grid resolution used for Cases M-1 and M-2.	142
20	Speed-up obtained for 21 steps syngas mechanism	170
21	Boundary conditions used for the LES (88).	173
22	Speed-up obtained for 12 steps methane skeletal mechanism.	187
23	Memory savings obtained for 12 steps methane skeletal mechanism.	187
24	Explanations for the variables defined in input.data	201
25	The compilation options that can be defined in the Makefile.	202

26	Explanations for the Fortran files	203
27	A sample input file used for stand-alone LEM computations for the Case B in Section 5.3.	204

LIST OF FIGURES

1	Schematics of (a) biological (53) and (b) artificial neurons.	22
2	Scalar field evolution with LEM. (a) initial field, (b) after triplet map and (c) after solving the diffusion-reaction equation	48
3	Scalar field on the LEM level and LES cell fluxes for a hypothetical example	68
4	Species field before and after the splicing of the cell (i,j)	70
5	Testing GDR on a hypothetical example. (a) $\alpha = 0$, (b) $\alpha = 1$ and (c) $\alpha = 2$	73
6	Variation of the step size with the AGDR method for a case with (a) the same sign and (b) alternating sign of the error gradient for consecutive iterations.	74
7	Variation of the global error with respect to the ANN iterations.	74
8	Testing AGDR on a hypothetical example. (a) $\alpha_{init} = 1$, and (b) $\alpha_{init} = 2$	75
9	Number of iterations required for convergence based on the initial value of the momentum coefficient.	77
10	AGDR method.	78
11	Function prediction by the GDR and AGDR methods.	80
12	Validation of the ANN code on a simple test function	82
13	Actual test data and ANN predictions.	85
14	Application of ANN to a laminar, time dependent syngas-air flame.	86
15	Actual test data and ANN predictions (a) for all equivalence ratios and (b) for close up view of three equivalence ratios. ANN-MER approach applied to a methane-air flame	88
16	CH_4 mass fraction surface plot and temperature contours obtained with (a) DI, (b) ANN-SER and (c) ANN-MER	89
17	CH_4 mass fraction profile comparison at cross-sections (a) A-A and (b) B-B	90
18	Composition state-space accessed by SER, MER training approaches and DI computations	91

19	Actual test data and ANN predictions for an ANN-MER approach applied to a syngas-air flame. (a) general, (b) close-up view	93
20	Application of ANN to a turbulent premixed syngas-air flame:(a) Case 1, (b) Case 2.	94
21	Comparison of species profiles obtained by DI and ANN approaches for turbulent, premixed syngas-air flame, Case 1. (a) CO and H_2O , (b) O , and (c) OH mass fraction.	95
22	Comparison of species profiles obtained by DI and ANN approaches for turbulent, premixed syngas-air flame, Case 2. (a) CO and H_2O , (b) O , and (c) OH mass fraction.	96
23	$CO_2 - OH$ Hyperplane Accessed by (a) DI-LES, (b) ANN training on coarse data and ANN-LES, and (c) ANN training on fine data and ANN-LES.	97
24	Comparison of species profiles obtained by DI and ANN approaches for turbulent, premixed syngas-air flame, Case 2 with refined table . .	98
25	Training Phase.	103
26	FFT analysis of the flow across the flame front.	104
27	Convergence history.	105
28	Comparison of the instantaneous species profiles obtained by the DVODE (●), the 10/5 ANN (- - -) and, the 10/5/4 ANN (—) at $3t^*$ for Case 1.	106
29	Comparison of the instantaneous species profiles obtained by the DVODE (●), the 10/5 ANN (- - -) and, the 10/5/4 ANN (—) at $3t^*$ for Case 2.	107
30	Comparison of the instantaneous species profiles obtained by the DVODE (●), the 10/5 ANN (- - -), and the 10/5/4 ANN (—) at $3t^*$ for Case 3.	109
31	Schematics of the actual problem and the LEM sub-domain	112
32	Effect of diffusivity for different species.	116
33	(a) Thermo-chemical database accessed by the 1D-LEM solver. (b) Correlation obtained by the ANN testing	117
34	ANN speed-up with respect to the number of connections.	118
35	Comparison of the time-averaged species profiles obtained by the DI (●), the P-ANN (- - -), F-ANN (- . - .), and L-ANN (—) for Case A1.	122
36	Comparison of the instantaneous species profiles obtained by the DI (●), the P-ANN (- - -), F-ANN (- . - .), and L-ANN (—), at $t = 5t^*$ for Case A2.	123

37	Comparison of the instantaneous species profiles obtained by the DI (●), the P-ANN (- - -), F-ANN (- . - .), and L-ANN (—), at $t = 5t^*$ for Case A3.	124
38	Comparison of the instantaneous species profiles obtained by the DI (●), the P-ANN (- - -), F-ANN (- . - .), and L-ANN (—), at $t = 5t^*$ for Case A4.	125
39	Instantaneous scalar profiles obtained for $Re_t = 90$ and at $N_{iter} = 15N^*$: Case B.	128
40	Instantaneous scalar profiles obtained for $Re_t = 290$ and at $N_{iter} = 5N^*$: Case B.	129
41	Time evolution of the scalar profiles for $Re_t = 290$	130
42	Conditional means of OH mass fraction and χ_{st} with respect to the mixture fraction for Case C.	131
43	Instantaneous scalar profiles obtained for $Re_t = 20$ and at $t = 10t_j$: Case C.	132
44	Instantaneous scalar profiles obtained for $Re_t = 20$ and at $t = 25t_j$: Case C.	133
45	Time evolution of the scalar profiles for $Re_t = 80$	134
46	Time averaged scalar profiles obtained for $Re_t = 80$: Case C.	135
47	Instantaneous scalar profiles obtained for $Re_t = 70$ and at $t = 15t_j$ - Case C.	136
48	Comparison of the time-averaged data obtained for Case M-1 using DI-(●) and ANN-(—) LEMLES.	143
49	Comparison of the time-averaged scalar field obtained for Case M-1 using DI-(●) and ANN-(—) LEMLES.	144
50	Comparison of the OH statistics obtained by the coarse and fine LEMLES at $t_j =$ (a) 20, (b) 40. (●) DNS, (- - -) Case M-1, (—) Case M-2, (...) initial data, and (- . -) laminar flamelet value at extinction. . . .	145
51	Variation of the mean temperature at the stoichiometric mixture fraction obtained by the DNS (●), Case M-1 (- - -), and Case M-2 (—). . . .	146
52	FFT of the mean flow total kinetic energy obtained by the fine LEMLES at a point located (a) $1H$ and (b) $4H$ away from the centerline. . . .	147
53	Comparison of the instantaneous data obtained by the fine LEMLES using DI (●) and ANN (—) at $t_j=4.5$	148

54	Conditional means of CO and H_2 at extinction (a, c) and reignition (b, d) obtained by ANN-LEMLES and DNS. (●) DNS, (—) ANN-LEMLES, (...) initial data, and (- . -) laminar flamelet value at extinction.	149
55	Conditional means of the CO_2 and H at extinction (a, c, e) and reignition (b, d, f) obtained by ANN-LEMLES and DNS. (●) DNS, (—) ANN-LEMLES, (...) initial data, and (- . -) laminar flamelet value at extinction.	151
56	Conditional mean of the temperature at extinction (a) and reignition (b) obtained by ANN-LEMLES and DNS. (●) DNS, (—) ANN-LEMLES, (...) initial data, and (- . -) laminar flamelet value at extinction.	152
57	The time variation of the PDF of temperature at the stoichiometric surface obtained by the ANN-LEMLES.	153
58	Surface plot of CO ((a)-(b)) and H_2 ((c)-(d)) mass fraction at $t_j = 20$ ((a)-(c)) and $t_j = 40$ ((b)-(d)).	154
59	Surface plot of OH mass fraction at (a) $t_j = 20$ and (b) $t_j = 40$	155
60	Surface plot of HO_2 mass fraction at (a) $t_j = 20$ and (b) $t_j = 40$	156
61	Surface plot of $\log_{10}(\chi_{st}/\chi_q)$ at (a) $t_j = 20$ and (b) $t_j = 40$	157
62	PDF of normalized logarithm of scalar dissipation rate at the stoichiometric mixture fraction at $t_j = 30$. (—) DNS, (- - -) ANN-LEMLES, (-.-.-) log-normal distribution	158
63	PDFs of normalized logarithm of scalar dissipation rate at the stoichiometric mixture fraction at (a) $t_j = 20$ and (b) $t_j = 40$. (●) log-normal distribution, (—) χ , (- - -) χ_{CO} , (-.-.-) χ_{OH}	159
64	The time variation of the PDF of χ , χ_{CO} , χ_{OH} at the stoichiometric surface obtained by the ANN-LEMLES.	160
65	Y_{OH} profiles obtained by stand alone LEM computations (a)0.05 ms, (b) 0.1 ms	162
66	Conditional mean of OH mass fraction obtained by TANN-LES and DNS. (●) DNS, (—) TANN-LES at $t_j = 20$; (◆) DNS, (- - -) TANN-LES at $t_j = 40$; (- . -) laminar flamelet value at extinction.	164
67	Conditional means of (a) CO and (b) H_2 mass fraction obtained by TANN-LES and DNS. (●) DNS, (—) TANN-LES at $t_j = 20$; (◆) DNS, (- - -) TANN-LES at $t_j = 40$; (- . -) laminar flamelet value at extinction.	165

68	Conditional means of (a) CO_2 and (b) H mass fraction obtained by TANN-LES and DNS. (●) DNS, (—) TANN-LES at $t_j = 20$; (◆) DNS, (- - -) TANN-LES at $t_j = 40$; (- . -) laminar flamelet value at extinction. 166
69	Conditional mean of T obtained by TANN-LES and DNS. (●) DNS, (—) TANN-LES at $t_j = 20$; (◆) DNS, (- - -) TANN-LES at $t_j = 40$; (- . -) laminar flamelet value at extinction. 167
70	Variation of the mean temperature at the stoichiometric mixture fraction obtained by the DNS (●) and the TANN-LES (—). 168
71	Mean value of the PDF of Y_{OH} conditioned on mixture fraction calculated by LANN-LES, TANN-LES and EBU-LES at $t_j =$ (a) 20 and (b) 40. 168
72	Schematics of the SPRF combustor (88). 172
73	Side and cross-sectional views of the grid used for the LES. 173
74	CH_4 reaction rate surface plot obtained by (a) DI, (b) DSTE and (c) LANN (in 1/s). 175
75	CO_2 reaction rate surface plot obtained by (a) DI, (b) DSTE and (c) LANN (in 1/s). 176
76	CO reaction rate surface plot obtained by (a) DI, (b) DSTE and (c) LANN (in 1/s). 177
77	Comparison of the time-averaged (a) axial velocity and (b) temperature along the centerline. Experiment, LEMLES, TF-LES, and EBU-LES from (88). 178
78	Comparison of the time-averaged (a) CH_4 and (b) CO_2 mole fraction along the centerline. Experiment, LEMLES, TF-LES and EBU-LES, from (88). 179
79	Comparison of the time-averaged axial velocity radial profiles at four sections. (●) Experiment, (—) LEMLES with DTSE and (- - -) LANN-LEMLES. Experiments and LEMLES from (88). 180
80	(a) Instantaneous and (b) time-averaged temperature surface plot. . . 182
81	(a) Instantaneous and (b) time-averaged CH_4 mass fraction surface plot. 183
82	Comparison of the time-averaged (a) axial velocity and (b) temperature along the centerline. 183
83	Comparison of the time-averaged (a) CH_4 and (b) CO_2 mole fraction along the centerline. Experiment, LEMLES, TF-LES and EBU-LES, from (88). 184

84	Comparison of the time-averaged axial velocity radial profiles at four sections. (●) Experiments, (—) LEMLES with DTSE and (- - -) TANN-LEMLES. Experiments and LEMLES from (88).	185
85	Flow chart for the stand-alone LEM code.	205

NOMENCLATURE

Roman Symbols

A	pre-exponential factor
\mathbf{A}	reaction mapping gradient
b	temperature exponent
b_i	ANN bias value
c	speed of sound
$c_{p,k}$	specific heat at constant pressure per unit mass for the k -th species
$c_{v,k}$	specific heat at constant volume per unit mass for the k -th species
C_{EBU}	model coefficient for the Eddy Break-Up model
C_ϵ	model coefficient for subgrid dissipation
C_λ	scalar diffusivity
C_ν	model coefficient for turbulent viscosity
C_ϕ	IEM model coefficient
D	mixture diffusivity
Da	Damkohler number
D_C	vortex size
d_i	desired value for ANN training
D_e	conditional moment closure model coefficient
D_k^t	thermal diffusion coefficient
\mathcal{D}_{ik}	binary diffusion coefficient
D_{kj}	multi-component diffusion coefficient of the species k and j
D_{km}	mixture averaged diffusion coefficient for species k
D^{sgs}	dissipation of turbulent kinetic energy

e	internal energy per mass
E	total energy
E_a	activation energy
$E[k]$	artificial neural network training error at k -th iteration
\mathbf{F}	flux vector
$F_{k, stir}$	turbulent stirring for k -th species conservation equation
$F_{k, stir}$	turbulent stirring for temperature equation
\mathbf{F}_{LS}	supergrid scale flux vector
\mathbf{F}_{sgs}	subgrid scale flux vector
$g()$	artificial neural network activation function
H_i	enthalpy flux
h_k	specific enthalpy per unit mass of the k -th species
i, j, k	computational grid indices
\mathbf{J}	Jacobian matrix
J_{ik}	diffusion flux
k	turbulent kinetics energy
k^{sgs}	sub-grid turbulent kinetic energy
k_B	Boltzmann constant
k_{bi}	backward rate coefficient of the i -th chemical reaction
k_{fi}	forward rate coefficient of the i -th chemical reaction
l	integral length scale
Le	Lewis number
\mathcal{L}_i	amplitude of the characteristic waves
L_F	laminar flame thickness
$L_{i,j}$	Leonard's stress
m_{jk}	reduced molecular mass of the species pair j and k
N_s	number of species

N_{test}	total number of test samples used for ANN
\mathcal{P}	probability that a collision leads to reaction
p	pressure
P	probability density function
P^{sgs}	production term for the subgrid turbulent kinetics energy
Pr	Prandtl number
\mathbf{Q}	conserved variable vector
q_i	rate of progress variable of the i -th chemical reaction
Q_i	conditional pdf of species mass fractions
$\mathbf{R}(\phi)$	reaction mapping for the scalar vector
Re	Reynold's number
Re_{Δ}	subgrid Reynold's number
R_u	universal gas constant
S	rate of strain
\mathbf{S}	source vector
S_L	laminar flame speed
t	time
T	temperature
t_j	non-dimensional time
u, v, w, u_i	Cartesian velocity vector components
u'	<i>rms</i> velocity
u'_{sgs}	subgrid scale turbulence intensity
$U_{C,max}$	maximum velocity induced by the vortex
V	volume
V_c	diffusion correction velocity
$V_{i,k}$	k -th species diffusion velocity in i -th direction
W_k	species molecular weight

W_{mix}	molecular weight of the mixture
W_{im}	ANN weight coefficient
y_m	output of the m -th neuron
Y_k	k -th species mass fraction
Y_F	fuel mass fraction
x, y, z	Cartesian coordinate directions
X_k	k -th species mole fraction
Z	collision frequency
Z	mixture fraction

Greek Symbols

$\alpha_{i,j}$	momentum coefficient between processing elements i and j
χ	scalar dissipation rate based on mixture fraction
χ_k	scalar dissipation rate based on k -th species
χ_k	scalar dissipation rate at the stoichiometric mixture fraction
δ_{ij}	Kronecker delta
$\bar{\Delta}$	large eddy simulation grid cut-off scale
$\Delta h_{f,k}$	enthalpy of formation per unit mass for the k -th species
Δt	time step size
Δt_{LES}	large eddy simulation time step size
Δt_{stir}	stirring time step size
Δt_{diff}	diffusion time step size
ϵ	dissipation of turbulent kinetic energy
η	Kolmogorov length scale
η_k	k -th species pure viscosity
$\eta_{i,j}$	learning rate coefficient between processing elements i and j

γ	ratio of specific heats
Γ	eigenvalue vector
κ	thermal conductivity
κ_1, κ_2	artificial neural networks model coefficients
λ	stirring frequency
Λ	eigenvector matrix
μ	mixture viscosity
ν_{kr}'	stoichiometric coefficient of the k -th species in r -th reaction
ν_t	turbulent viscosity
$\dot{\omega}_{kin}$	chemical reaction rate
$\dot{\omega}_{mix}$	mixing reaction rate
$\dot{\omega}_k$	chemical reaction rate of the k -th species
$\dot{\omega}_T$	chemical heat release due to combustion
$\Omega^{(1,1)}$	correction factor
Φ	equivalence ratio
$\phi_{i,j}$	gradient of training error with respect to the weight coefficient
$\Phi_{i,m}$	convective mass flux of species m
ψ	scalar field state vector
ρ	density
σ	wave reflection coefficient
σ_{ij}	viscous work
τ_c	chemical time scale
τ_t	turbulent time scale
τ_{ij}	viscous stress tensor
$\theta_{i,m}$	diffusive flux of species m
ξ, η, ζ	spatial directions in computational space

Subscripts

cgs	cm-gram-second measurement system
i, j, k	Cartesian tensor indices or species indices
k	species index
L	laminar
m	chemical index
n	time step index
t, T	turbulent quantity
u	unburned
∞	quantity at infinity downstream

Superscripts

0	reference quantity
LEM	quantity at the LEM level
sgs	subgrid scale
$stir$	stirring
$test$	test filter scale

Other Symbols

∂	partial derivative operator
∇	gradient operator
$\nabla \cdot$	divergence operator
\sum	summation operator
Δ	difference operator
\mathcal{M}	Mach number

\sim	Favre spatial filter
$\hat{}$	test filter
$-$	space average
$'$, $''$	fluctuating quantity

Abbreviations

<i>AGDR</i>	Adaptive Gradient Descent Rule
<i>ANN</i>	Artificial Neural Network
<i>CMC</i>	Conditional Moment Closure
<i>CFD</i>	Computational Fluid Dynamics
<i>CFL</i>	Courant-Friedrichs-Lewy number
<i>CPU</i>	Central Processing Unit
<i>DI</i>	Direct Integration
<i>DNS</i>	Direct Numerical Simulation
<i>DSTE</i>	Direct Source Term Estimation
<i>DVODE</i>	Double Precision Variable Coefficients Ordinary Differential Equations
<i>EBU</i>	Eddy Break-Up
<i>EBU-LES</i>	Eddy Break-Up with Large Eddy Simulation
<i>EDBD</i>	Extended Delta Bar Delta
<i>F-ANN</i>	ANN Trained on Flame Vortex Interaction
<i>FVI</i>	Flame Vortex Interaction
<i>FFT</i>	Fast Fourier Analysis
<i>FTI</i>	Flame Turbulence Interaction
<i>GDR</i>	Gradient Descent Rule
<i>LANN</i>	Laminar Artificial Neural Network
<i>LDKM</i>	Localized Dynamic k -equation Model

<i>LEM</i>	Linear Eddy Mixing model
<i>LES</i>	Large Eddy Simulation
<i>LEMLES</i>	Large Eddy Simulation with Linear Eddy Mixing model
<i>LODI</i>	Locally One-Dimensional Inviscid
<i>MA</i>	Mixture Averaged
<i>MER</i>	Multiple Equivalence Ratio
<i>MLP</i>	Multi Layer Perceptron
<i>MPI</i>	Message Passing Interface
<i>ODE</i>	Ordinary Differential Equation
<i>P-ANN</i>	ANN Trained on Laminar Premixed Flame
<i>PE</i>	Processing Element
<i>PDE</i>	Partial Differential Equation
<i>PDF</i>	Probability Distribution Function
<i>RANS</i>	Reynolds Averaged Navier - Stokes
<i>SER</i>	Single Equivalence Ratio
<i>SPRF</i>	Stagnation Point Reverse Flow
<i>TANN</i>	Turbulent Artificial Neural Network
<i>TRZ</i>	Thin Reaction Zone
<i>TKE</i>	Turbulent Kinetic Energy
<i>RMS</i>	Root Mean Square, Variance

SUMMARY

Computational analysis of turbulent reactive flow applications requires resolution of the wide range of scales both in time and space from a flow modeling perspective. From a thermo-chemistry point of view, information regarding the radical chemical species is needed in order to capture flame-turbulence interactions accurately. A detailed investigation of all of these processes is time consuming. Thus, there is a need for speeding-up the computations by using the state-of-the-art modeling capabilities. This study seeks to answer this problem and focuses in particular on the chemical kinetics calculations. The new approach proposed here is based on incorporating the artificial neural network (ANN) based modeling of the chemical kinetics into the large eddy simulation (LES) of reactive flows.

Two separate and new ANN based modeling approaches relevant to the LES are proposed within the thesis work. Here, the first approach depends on employing ANN to predict the species instantaneous reaction rates as a function of the thermo-chemical state vector ($\dot{\omega}_i = ANN(Y_k, T)$). The second one is based on using ANN specifically to predict the spatially filtered chemical source terms in the LES modeling as a function of the filtered thermo-chemical state vector and flow quantities ($\bar{\dot{\omega}}_i = ANN(\tilde{Y}_k, \tilde{T}, Re_\Delta, \frac{\partial \tilde{Y}_i}{\partial x})$).

First part of the thesis work dealt with testing different thermo-chemical tabulation techniques that can be used in connection with the ANN approach for the LES. Basically, three distinct methods (and tools) are developed here: thermo-chemical tables based on (i) laminar flames, (ii) laminar flame-vortex interactions (FVI) and (iii) laminar flame-turbulence interactions (FTI). Results based on premixed flame-vortex-turbulence interaction simulations showed that the tables generated based on the

second and third approaches are capable of representing the actual thermo-chemical state-space accessed by the LES.

Once the tabulation procedure and the ANN training is achieved, ANN is first validated against direct numerical simulation (DNS) of a temporally evolving planar jet flame, which is reported to exhibit complex extinction and re-ignition type of physics. The flame physics are also investigated for this flame, and it is observed that the scalar dissipation rate has a weak sensitivity to extinction and re-ignition, than it is reported in the literature. As a second test case, comparisons against experimental and previous computational data are provided for a practical combustor simulation. Overall for all simulations considered here, the results indicated that the ANN works as a combustion mode independent model and provides fairly accurate results with considerable amount of speed-up and memory savings.

CHAPTER I

INTRODUCTION AND OBJECTIVES

1.1 Turbulent Combustion Modeling and Chemical Kinetics: An Overview

Turbulent combustion is described as the continuous distortion of the local flame front by eddies distributed over a wide range of length and time scales (63). The response of the flame front depends on the combined effect of molecular diffusion, turbulent transport, and chemical reaction occurring across the flame, without any clear scale separation. Eventually, the flame may experience complex, unsteady, local and/or global features such as extinction, re-ignition and quenching.

Turbulent combustion typically occurs within the combustion chambers of gas turbine engines. Here, the incoming flow is highly turbulent in order to enhance both mixing and combustion. In this manner, a shorter flame length can be ensured, which lead to a more compact combustor with low NO_x levels. Accurate prediction of the scalar and the vectoral fields inside the combustion chamber of a gas turbine engine is a challenging task and requires the solution of a three dimensional, highly unsteady, turbulent reactive flow problem. Direct numerical simulation (DNS) of the high Reynolds number flows is not affordable yet, since the grid resolution dictated by the solution methodology exceeds the current computer capabilities (22). In the realm of reactive flow computations, great effort has been spent to capture the time-dependent processes by large eddy simulation (LES), where the small scale processes are modeled, and large scale processes are resolved directly

The representation of the chemical kinetics is, however, a problem for both DNS and LES. Precise knowledge of the time rate of change of fuel/radicals/product mass

fraction is required to predict ignition, extinction, and pollutant formation (5). In order to calculate the changes in the species composition due to the chemical reactions, an ODE system must be solved. The size of the equation system is determined by the number of species simulated. On the extreme end, a full chemical kinetics mechanism may be used to represent the thermo-chemical state space, such as GRI-Mech 3.0, with 53 species and 325 elementary reactions optimized for methane combustion (86). Apart from the difficulty of solving 53 individual conservation equations; calculating species reaction rates through 325 reactions under reasonable computational time may not be practical even for LES. Also, since the radical and major species have a wide range of time scales, the solution procedure requires employing stiff ODE solvers, which add further computational burden. Thus, for a detailed reaction mechanism, the chemical kinetics calculations are very time consuming, and their application to the engineering problems may be limited similar to DNS due to the need for enormous computational resources. One common approach used to solve this problem is to reduce the order of the chemical kinetics mechanism by identifying the partial equilibrium reactions and steady-state species (56; 31). However, this derivation may lead to several difficulties, i.e., the final mechanism may be even stiffer than the original one, the initialization may be troublesome, and most importantly, the assumptions may hold only for certain conditions, which may not even be valid for the particular turbulent flame of interest (63).

Tabulation based methodologies, such as intrinsic low-dimensional manifolds (ILDMM) (45) and *in-situ* adaptive tabulation (ISAT) (65) are used typically in the literature to decrease the computational time required to calculate the species reaction rates. Here, ILDM requires generation of a multi dimensional look-up table prior to starting the flow computations. The number of resolved states by ILDM should be sufficient enough to include all the possible states that may be accessed during the actual flow simulation. Since this information is not known *a priori*, huge tables can be generated,

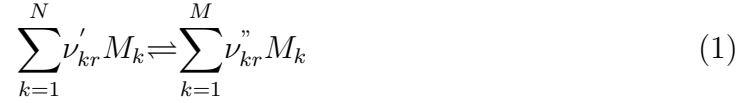
which would require large memory allocations (77). ISAT, on the other hand, is no different than direct integration of the chemical equation system in the early stages of the simulation, since the look-up table is generated as the simulation proceeds.

All models that use a tabulation strategy has to employ an interpolation scheme, since it is not possible to fill the table with all the possible states available. However, it has been previously reported that the search-interpolate-retrieve type of procedure from a multi-dimensional table may slow down the actual flow simulation and may induce interpolation errors (34). Furthermore, the dimensions of the pre look-up tables should be decreased by achieving parameterization with respect to few key variables, as large multi-dimensional structured tables would exceed the memory limit of the computers.

Another solution is the artificial neural networks (ANN) (47) methodology, which is a relatively new technique in the area of chemical kinetics and to date its applicability has not been tested fully for turbulent reactive flow applications. ANN is widely used for function approximation, classification, time series prediction, filtering, data association, and optimization (16). It is a computing system composed of a number of simple, highly interconnected, processing elements (PEs) -neurons-, which process information by dynamic state response to external inputs (27). Contrary to the conventional computer modeling approach, which relies on solving the equations, ANN learns by example and provides predictions into new states. The current thesis work is investigating the implementation of the ANN methodology into the LES of the reactive flows to speed-up the chemical kinetics calculations. The next sections will provide a more detailed description of the concepts (i.e., DNS, LES, ILDM, ISAT, ANN, etc.) introduced briefly in this section.

1.2 Chemical Kinetics

Combustion is defined as rapid oxidation generating heat, or both light and heat (86). The oxidation process and heat generation typically occur due to the chemical reactions between different species. The consumption, or production of a given species due to the chemical reactions, so-called species reaction rates ($\dot{\omega}_k$), are computed by applying the basic laws of chemical kinetics. The calculation procedure requires information regarding the set of chemical reactions occurring for the given thermodynamic state vector (Y_k, T, P). Let us consider the following set of elementary reactions R containing an arbitrary number of reactants: N , and products M :



for $r = 1, \dots, R$. Here, M_k denotes the chemical symbol for species k . ν'_{kr} and ν''_{kr} are the stoichiometric coefficients of the forward and backward reactions, respectively. Based on the given reaction mechanism, the net rate at which species M_k is produced and/or consumed, the chemical reaction rate, is given by using the following formula:

$$\dot{\omega}_k = \sum_{i=1}^R \nu_{ki} q_i \quad (2)$$

where q_i is the rate-of-progress variable and calculated as:

$$q_i = k_{fi} \prod_{k=1}^N [X_k]^{\nu_{ki}'} - k_{bi} \prod_{k=1}^M [X_k]^{\nu_{ki}''} \quad (3)$$

and $\nu_{ki} = (\nu_{ki}'' - \nu_{ki}')$. The rate coefficients of the forward and backward reactions, k_f and k_b , are functions of temperature, and are derived mostly from the kinetic theory of gases. In principle, they represent the collision frequency between the molecules (Z) and the probability that a collision will lead to a chemical reaction (\mathcal{P}), and is formulated as (86)

$$k \approx Z\mathcal{P} \quad (4)$$

The probability \mathcal{P} is expressed as the multiplication of two factors:

$$\mathcal{P} \approx \exp\left(\frac{-E_A}{R_u T}\right) p \quad (5)$$

where E_A , R_u , and p are the activation energy, universal gas constant, and the steric factor, respectively. The activation energy corresponds to the energy barrier that must be overcome during the reaction, and the collisions that can pass this threshold can lead to a reaction (91). The steric factor, on the other hand, accounts for the molecular collision geometry. (86). Thus, only collisions that have the required energy and the correct orientation result in reactions. It must be noted that kinetic theory explains the mechanism for a reaction to occur, but cannot provide answers for the exact values of the E_A and p , leaving them to be found empirically. The final form of the rate coefficient is expressed in the "modified" Arrhenius form as:

$$k = AT^b \exp\left(-\frac{E_A}{R_u T}\right) \quad (6)$$

where A and b are the pre-exponential factor, and temperature exponent, respectively. The values of A , b , and E_A for the given reaction mechanism are found through combined experimental and computational studies and are tabulated.

1.3 Turbulent Combustion Modeling

From a computational point of view, the governing equations for the conservation of mass, momentum, energy, and species need to be solved together with the equation of state to investigate the combustion physics. Here, it should be noted that most of the practical reactive flow applications occur under turbulent conditions in order to enhance the combustion process. Turbulence can be roughly described as irregular, unsteady, multi-scale, three-dimensional fluid motion. Turbulent flow is essentially a collection of range of scales, and these turbulent structures interact with the flame front in the turbulent combustion process. The largest turbulent scale (integral length scale (l)) can be considered as equal to the size of the combustion device and is of the

order of 0.1-1 m. The smallest length scale (Kolmogorov length scale (η)), however, is determined by the Reynolds number and can be as small as 10^{-6} m. Turbulent mixing occurs on the Batchelor length scale, which is even smaller than the η .

Turbulent combustion modeling has to deal with the modeling of turbulence, combustion, and their interaction with each other. Combustion, compared to the turbulence, occurs mostly on the small scales and has a much wider range of time scales. Thus, the physics of the interaction process is quite complex and computational models used for the simulations need to be validated carefully to provide an answer into the problems.

1.3.1 Turbulent Flow Modeling

1.3.1.1 Direct Numerical Simulation

In DNS, the governing set of equations are solved exactly without using any modeling. DNS provides the most accurate results to the turbulent combustion, since processes occurring at all length and time scales are directly resolved. In order to achieve this solution, however, the grid size that is used for simulation should be small enough to resolve even the smallest turbulent structure to provide a solution at all length scales. The range of scales in a turbulent flow is a function of the Reynolds number. As noted earlier, practical combustion devices operate at high Reynolds numbers. The ratio between l and η is roughly given as $Re^{3/4}$ (84). Hence, as the Reynolds number increases, for the same device (constant l), η becomes much smaller. This leads to the DNS grid resolution in 3D scale with $Re^{9/4}$. From a computational point of view, a decrease in η yields a smaller time step size between consecutive iterations, since maximum step size is proportional to the square of the grid size (93). Overall, the computational requirement for the DNS of a reactive flow increases by the fourth power of the Reynolds number (66). Hence, DNS is not yet computationally affordable in order to be used for practical combustion applications.

1.3.1.2 Reynolds Averaged Navier Stokes

RANS is based on the assumption that turbulence is statistically stationary, and any given quantity (e.g., u_k , T , etc.) can be represented as a time average mean and instantaneous fluctuation (94). Based on this assumption, the governing set of equations are time averaged and solved on a much coarser grid than the DNS. In RANS, only the mean flow is resolved, hence, no turbulent motion is explicitly captured, since all scales are modeled. The averaging procedure leads to new terms (so-called Reynolds stresses) in the governing equations, which need closure. There exists several techniques in the literature used to calculate the Reynolds stresses (i.e. Spallart-Allmaras, k - ϵ , k - ω , Reynolds stress model, etc. (94)).

1.3.1.3 Large Eddy Simulations

Fundamental studies in the field of turbulence reveal that the large scale structures are coherent and geometry dependent, whereas small scale structures are universal. Also, large scale structures are continuously broken into smaller structures up to a scale where viscous effects are dominant over the inertial processes (66). At this scale, the eddies are dissipated by the action of the viscosity. In the LES framework, based on this hypothesis, a cut-off scale is defined, where scales larger than this scale are resolved directly similar to the DNS, and smaller scales are subsequently modeled, as they are universal and geometry independent. This is achieved by applying a spatial filtering operator to the governing set of equations, which leads to unclosed terms similar to the RANS. However, for LES, the interpretation of these terms are fundamentally different. They represent the processes that occur at the scales smaller than the applied cut-off.

One of the important advantages of the LES over RANS is that, LES does not invoke any explicit assumption regarding the time variation of the turbulent structures. The unsteady evolution of the turbulent structures is calculated effectively.

This is especially important for the reactive flow applications, where the local heat release is very sensitive to the unsteady evolution of the turbulent structures. This unsteady interaction process leads to many important physics such as acoustic flame instabilities, extinction, and flash-back, which can be captured by LES, but not by the RANS.

1.3.2 Flame Turbulence Interaction Modeling

The above noted methodologies are essentially developed for modeling *turbulent flows*, and they provide information on how to solve (or model) the turbulent structures. For example, the subgrid modeling in LES relies on the observation that the small scales are mostly responsible for providing dissipation to the energy budget of the flow. Hence, an eddy viscosity type of closure is widely used for sub-grid representation of the momentum. However combustion is essentially a small scale phenomena, where molecular diffusion, turbulent stirring and chemical reaction all occur at the small scales (which is modeled in LES) in an unsteady manner (which is not the case in RANS). Handling combustion in LES and RANS, so-called flame-turbulence interaction, is a challenge for the modeling of reactive flows. There exists many models in the literature to answer this issue. These models were first developed for the RANS applications and were later turned into forms that can be used in the LES as well. The most widely used flame-turbulence interaction models will be presented next in the LES context.

1.3.2.1 Eddy Break-Up and Eddy Dissipation Models

Eddy break-up (EBU) is one of the simplest turbulent combustion models and is essentially used to calculate the filtered reaction rate as a function of the known turbulent quantities. It was initially developed for RANS applications (79; 80) and is later extended to the LES. EBU views the reaction zone as a collection of fresh and burnt gas pockets, and treats the combustion process as a mixing problem, rather

than as a reaction problem. The basic assumption behind the EBU is that both the Re and Damkohler (Da) numbers are considerably high. In other words, the chemical time scale is much smaller than the turbulent mixing time scale ($\tau_c \ll \tau_t$). Hence, combustion proceeds as long as the turbulence allows for species come together and react with each other, leading to the result that τ_t is the controlling parameter. As a result, the filtered reaction rate is calculated as:

$$\bar{\omega}_F = -C_{EBU} \frac{\rho}{\tau_t} \widetilde{Y_F^n}^{1/2} \quad (7)$$

Here, the turbulent time scale is usually given as $\tau_t = k/\epsilon$. In terms of calculating the filtered reaction rate, the EBU model is one of the simplest models available in the literature. It is very easy to implement EBU into existing LES and/or RANS codes. However, it has a couple of drawbacks. First, since the model highly depends on the turbulence quantities, it tends to overestimate the reaction rates in highly strained regions where k/ϵ is very high. Also, the results are highly sensitive to the model coefficient (C_{EBU}), and different results can be obtained based on slight changes of C_{EBU} (63). The model is originally proposed for a single-step reaction, and its extension to detailed kinetics is also problematic, since radical species evolution cannot be quantified based merely on the turbulent quantities, without considering the chemical reactions. It should be noted that, the detailed kinetics is important only when there is unsteady flame dynamics (i.e., extinction, quenching, re-ignition), in which case the Da number is low and EBU is not valid anyway.

The eddy dissipation model (EDM) (46) is a derivative of the EBU. EBU model (46) in its original form is based on the "mixed is burnt" assumption. In EDM it is assumed that the chemical reactions occur very rapidly compared to the turbulent mixing process if the turbulence level is high. Also, in EDM, in contrast to EBU, variance of the product mass fraction ($\widetilde{Y_F^n}^{1/2}$) is replaced with the mean mass fraction of the deficient species (Y_k). In this manner it is more general and can be applied to multi-step kinetics as well. Also, both kinetic and mixing rates are calculated at a

given point within the computational domain, and among them the fastest (smallest) one is selected. In this manner, the source term of the species equation switches between the mixing and kinetic rates depending on the level of turbulence.

The mixing rate in EDM for LES is selected as:

$$\bar{\omega}_{mix} = \min\left(\frac{\Delta x}{\sqrt{k^{sgs}}} C_{EBU} \widetilde{Y_{R_{min}}}, \frac{\Delta x}{\sqrt{k^{sgs}}} C_{EBU} \widetilde{Y_{P_{min}}}\right) \quad (8)$$

where Δx , $\widetilde{Y_{R_{min}}}$, $\widetilde{Y_{P_{min}}}$ denote the LES grid spacing, the deficient species mass fraction in the reactants and products, respectively.

The kinetic rate is calculated based on the given reaction mechanism and the thermodynamic state vector ($\bar{\omega}_{kin} = f(\widetilde{Y}_k, \widetilde{T}, \widetilde{p})$). Finally the overall rate is given by:

$$\bar{\omega}_k = \min(\bar{\omega}_{mix}, \bar{\omega}_{kin}) \quad (9)$$

In this manner, at the shear layers, where k^{sgs} is typically high, the EDM model tends to pick the mixing rate. Near the walls, where k^{sgs} may acquire unphysically high values, the reactions tend to be overpredicted by this model, and a limiter should be used.

Both the EBU (completely) and EDM (partially) reject the chemical rate with the "mixed is burnt" assumption. This is valid only for the cases where the turbulent time scale is much smaller than the chemical time scale. For most of the practical applications, however, there are certain cases where these two are comparable to each other. EDM, basically calculates both of these time scales and uses the rate limiting one. This model will be explained further in the next chapter.

1.3.2.2 Laminar Flamelets with presumed PDF

The flamelet model is valid for moderately high Damkohler (Da) number flames. The basic assumption behind the model is that the reaction zone is thin and is distorted by the flow field, whereas its internal structure is not strongly affected by the turbulence since the flame thickness is much smaller than the turbulent structures (57). Hence,

(i) the structure of the reaction zone remains laminar ("flamelet") and (ii) diffusive transport occurs in the direction normal to the surface of the stoichiometric mixture (59). Under these conditions, the species evolution can be re-cast into the following form:

$$\rho \frac{\partial Y_k}{\partial t} = \frac{1}{2} \rho D \chi \frac{\partial^2 Y_k}{\partial Z^2} + \dot{\omega}_k \quad (10)$$

Here, D is the mixture diffusivity, Z is the mixture fraction and χ is the scalar dissipation rate calculated as $\chi = (\partial Z / \partial x_i)(\partial Z / \partial x_i)$. It should be noted that the same form of the equation can be derived for the temperature as well. As a result, the scalar field is a function of Z and χ only, for the given boundary conditions. Hence, flamelets allows a lower-dimensional representation of the scalar field. In this manner, instead of solving the conservation equations for all species in the LES, the scalar field is provided through pre-computed flamelet tables ($Y_k = f(Z, \chi)$). However, it should be noted that LES requires the filtered quantities, which necessitates the use of presumed PDF in connection with the flamelet tables. The filtered scalar field is obtained by using:

$$\bar{\rho} \tilde{Y}_k = \int_0^\infty \int_0^1 \rho Y_k(Z, \chi_{st}) P(Z, \chi_{st}) dZ d\chi_{st} \quad (11)$$

Here, the Joint PDF of the scalar dissipation rate and the mixture fraction is required for the integration, which is not known. To proceed with the computation, Z and χ_{st} are assumed to be statistically independent from each other, which allows the representation of the joint PDF as two separate single PDFs ($P(Z, \chi_{st}) = P(Z)P(\chi_{st})$). The DNS studies show that the PDF of scalar dissipation rate is log-normal. The PDF of mixture fraction, however, is presumed using β -function, which requires the calculation of the mean and variance of the mixture fraction (\tilde{Z} , $\widetilde{Z''^2}$). The filtered scalar dissipation rate ($\tilde{\chi}$) in the LES solver is calculated as $\tilde{\chi} = C\epsilon \widetilde{Z''^2} / k$. The link between χ and χ_{st} is given by

$$\tilde{\chi} = \tilde{\chi}_{st} \int_0^1 \frac{F(z)}{F(z_{st})} p(z) dz \quad (12)$$

where $F(z)$ is

$$F(z) = \exp\left(-2 \left[\operatorname{erf}^{-1}(2z - 1)\right]^2\right) \quad (13)$$

To sum up the whole procedure: (i) a flamelet table is constructed by solving Eq. (10) for a range of Z and χ_{st} , (ii) the states in the flamelet table are integrated by using Eq. (11), with $P(Z)$ and $P(\chi_{st})$ modeled as β and log-normal distributions, respectively. (iii) Hence, the final look-up table tabulates filtered states (i.e. $\bar{\rho}\tilde{Y}_k$) with respect to the \tilde{Z} , $\widetilde{Z''^2}$, $\tilde{\chi}_{st}$. (iv) Here, additional equations for \tilde{Z} and $\widetilde{Z''^2}$ are solved, where as $\tilde{\chi}$ is modeled.

The main advantage of the flamelet modeling is that the scalar field is tabulated with respect to \tilde{Z} , $\widetilde{Z''^2}$, $\tilde{\chi}$. Hence, there is no need to solve species equations explicitly in the LES solver. As a result, a considerable amount of computational saving is achieved compared to directly solving the species equations. Furthermore, detailed multi-step kinetics can still be used during the flamelet table generation, which may not be affordable for most of the turbulent combustion models. On the other hand, the assumption that the flame front is laminar with respect to the flow field, may not be correct when turbulent eddies can penetrate into the reaction zone. This is a typical case when there is local extinction (57). Also, the flame may be under a high scalar dissipation rate only for a short period of time, in which case the flame may not go under extinction. Recently, unsteady flamelets have been used to overcome this unsteady issue (58).

1.3.2.3 Conditional Moment Closure with Presumed PDF

The Conditional Moment Closure (CMC) method was developed independently by Klimenko (1990) and Bilger (1993). The main idea in CMC modeling is to find how the reactive scalars depend on the mixture fraction ($\rho Y_k|Z$). Here, $|$ denotes the conditioning: $(\rho Y_k|Z)$ is the value of ρY_k for the given mixture fraction (Z). Hence, in a sense, CMC bears resemblance to the flamelet method. The main difference

between flamelets and CMC is that the latter solves the exact balance equation of the conditional species mass fractions, rather than tabulating them as it is done in flamelet models. In the CMC method, starting from the species conservation equation, the following form of the conditional species mass fraction equation is derived:

$$\frac{\partial Q_i}{\partial t} = \langle \widetilde{u_j|\eta} \rangle \frac{\partial Q_i}{\partial x_i} + \frac{\langle \widetilde{\chi|\eta} \rangle}{2} \frac{\partial^2 Q_i}{\partial \eta^2} + \langle \widetilde{\dot{\omega}_k|\eta} \rangle + \frac{\partial}{\partial x_j} \left[\langle \widetilde{D_e|\eta} \rangle \frac{\partial Q_i}{\partial x_i} \right] \quad (14)$$

Here, $Q_i = \langle \widetilde{Y_k|\eta} \rangle$, with η representing the sample space for the mixture fraction. This equation is solved both in the physical (x_i) and the mixture fraction (η) space. Assuming that the Q_i is not changing strongly within the computational domain, a second and much coarser grid in the physical space (CMC grid) is used for the solution. It should be noted that this is valid only when there is no extinction (90). Also, the number of the mixture fraction layers of which the equation is solved should be selected so as to achieve good results. Another problem associated with the CMC is that all terms on the right hand side of Eq. (14) ((i) turbulent transport, (ii) micromixing, and (iii) chemical source) need closure. To achieve turbulent transport and micromixing modeling, the conditionally filtered values are approximated by the conditional average of filtered values over the CMC cells ($\langle \widetilde{u_j|\eta} \rangle = \langle \widetilde{u_j|\eta} \rangle$, $\langle \widetilde{\chi|\eta} \rangle = \langle \widetilde{\chi|\eta} \rangle$). The fluctuations of chemical source term in the mixture fraction space is neglected, which leads to

$$\langle \widetilde{\dot{\omega}_k|\eta} \rangle = \dot{\omega}_k(Y_k|Z) \quad (15)$$

Thus, there is no need to provide any extra closure for the reaction rate. It should be noted that this transformation is valid only in the case of fluctuations in the conditional pdf is smaller than the fluctuations in the physical space (LES). This is again valid when the flame is in equilibrium with the flow field. For the cases when there is highly unsteady flame physics, this assumption is questionable. Finally, similar to that was done for flamelets (Eq. (11)), the link between the LES and CMC

is achieved by:

$$\bar{\rho}\tilde{Y}_k = \int_0^1 Q_i P(Z) dZ \quad (16)$$

Here, $P(Z)$ is assumed as a β distribution, which requires solution of additional equations for \tilde{Z} and $\widetilde{Z''^2}$ on the LES grid.

1.3.2.4 Linear Eddy Mixing

Linear Eddy Mixing (LEM) is a stochastic, Lagrangian-Eulerian coupled model that simulates the unsteady scalar field evolution on one-dimension. It can be used as a subgrid scale combustion model within the LES framework as well (LEMLES). In the LEMLES, the species equation is split into two parts denoting the small scale (molecular mixing, turbulent stirring, reaction) and large scale (advection) processes. Assuming that the turbulence is essentially isotropic on the sub-grid (which is a central assumption for the LES), the small scale structures are solved on 1-D lines embedded within each LES grid. Hence, the number of grid points is increased for solving the reactive scalar field evolution. Diffusion and reaction are treated deterministically, where as turbulent stirring is modeled in a stochastic manner (*triplet-maps*). LEMLES allows the use of detailed kinetics, since species reaction rates appear in the closed form in the small-scale equation. Also, it is possible to employ multi-component diffusion on the sub-grid. The details of the LEM formulation and its implementation into an LES code are given in more details in Sections 2.2.2 and 3.3, respectively.

1.3.2.5 PDF Transport Model

Both the flamelet and the CMC models require the PDF of mixture fraction ($P(Z)$), which is not known, and usually presumed by a beta function(63). Also for the flamelets, the joint PDF of Z and χ is required, which is again unknown. From a computational point of view, instead of presuming the PDF and using it in connection with models, it is possible to directly solve the following balance equation for the full

joint PDF (63), and use it as a turbulent combustion model by itself:

$$\begin{aligned}
& \rho \frac{\partial \bar{P}}{\partial t} + \bar{\rho} \tilde{u}_k \frac{\partial \bar{P}}{\partial x_k} = \\
& - \frac{\partial}{\partial x_k} [\bar{\rho} \langle u_k'' | \psi \rangle \bar{P}] - \bar{\rho} \sum_{i=1}^N \frac{\partial}{\partial \psi_i} \left[\left\langle \frac{1}{\rho} \frac{\partial}{\partial x_k} \left(\rho D \frac{\partial Y_i}{\partial x_k} \right) | \psi \right\rangle \bar{P} \right] - \bar{\rho} \sum_{i=1}^N \frac{\partial}{\partial \psi_i} \left(\frac{1}{\bar{\rho}} \dot{\omega}_i \bar{P} \right)
\end{aligned} \tag{17}$$

Here, ψ denotes the scalar field state-vector, and P is its joint PDF. In Eq. (17), the first and third terms on the right hand side represents the turbulent convection and the chemical reaction, respectively, and they are in the closed form. Hence, the PDF transport model has the potential to incorporate detailed chemical kinetics, since it does not require any filtering for the chemical reaction term. However, the molecular diffusion (*micromixing*) is unclosed, and needs to be modeled (64). Equation (17) is solved by using the Monte-Carlo method, which is ideal for high-dimensional equations, since the computational cost is linearly dependent on the dimensionality of the system. In this method, the Lagrangian particles evolve randomly both in the physical and compositional space due to the turbulent convection, molecular diffusion and reaction (66). The motion due to the turbulent convection is implemented as:

$$x_i^1 = x_i^0 + \frac{1}{2} u_i^0 \Delta t \tag{18}$$

The change in the composition due to the molecular diffusion, however, needs to be modeled. Among these models, the modified curl method uses the following relation to update the scalar field:

$$\begin{aligned}
\psi^{(i,new)} &= \psi^i + \frac{1}{2} a (\psi^j - \psi^i) \\
\psi^{(j,new)} &= \psi^j + \frac{1}{2} a (\psi^i - \psi^j)
\end{aligned} \tag{19}$$

In this formulation, a pair of state vectors (ψ^i and ψ^j) are selected randomly from an ensemble of states, and are changed with respect to their difference. Here, a is a random number, which is uniformly distributed in $[0,1]$. The interaction with

Table 1: Handling species equation with different flame-turbulence interaction models.

	# of Equations	Scalar field solved on
EBU	Nspeci	LES grid
Flamelet & PPDF	2 ($\tilde{Z}, \widetilde{Z'^2}$)	LES grid
CMC & PPDF	Nspeci	Physical:CMC grid (coarser than LES) Compositional:Mixture Fraction grid
LEM	Nspeci	LEM grid (finer than LES)
PDF Transport	Nspeci	Monte-Carlo particles

exchange (IEM) method, on the other hand, relates the molecular diffusion to the turbulent quantities, and modifies the given stat vector as:

$$\frac{d\phi^n}{dt} = -\frac{1}{2}C_\phi \frac{\epsilon}{k} (\psi^n - \tilde{\psi}) \quad (20)$$

Here, C_ϕ is the model coefficient, which needs to be calibrated.

As mentioned earlier, the main advantage of solving the PDF transport equation is that, unlike LES, the reaction rate and the turbulent convection is in a closed form. However, this advantage is offset by the fact that reactants are brought to the reaction zone by diffusion, and the *micromixing* term remains unclosed and requires modeling. Also, the total number of equations solved is equal to the number of species plus two, which may not be affordable for very large mechanisms. Lastly, large number of Lagrangian particles must be used in order to avoid statistical errors.

The comparison of the models described in this section (EBU, Flamelet with presumed PDF (PPDF), CMC with PPDF, LEM and PDF transport) in terms of the way they handle the scalar field equations are given in Tables 1 and 2. Here, Table 1 shows the number of additional equations required to solve the scalar field evolution. Table 2, demonstrates how each different term in the scalar field equation is handled.

Table 2: Sub-models used to handle chemistry, diffusion and turbulent stirring by different flame-turbulence interaction models.

	Chemistry	Species Diffusion	Turbulent Stirring
EBU	N/A	LES Modeled	LES Modeled
Flamelet & PPDF	Offline kinetics	Offline diffusion	LES Modeled
CMC & PPDF	Online kinetics	Presumed PDF	LES Modeled
LEM	Online kinetics	Exact	<i>triplet-map</i>
PDF Transport	Online kinetics	Model (i.e. IEM)	Exact

1.3.3 Chemical Kinetics Modeling

For the given reaction mechanism and Arrhenius model coefficients, the rate laws for the species can be represented as

$$\frac{dY_k}{dt} = F_k(Y_1, Y_2, \dots, Y_{N_s}, T, p) = \dot{\omega}_k \quad (21)$$

which is essentially a first-order ordinary differential equation system. It is possible to calculate the time rate of change of a given species at a given instant through Eq. 21. However, in actual CFD calculations the rate of change of species in a given time interval (chemical source term) is needed. It should be noted that a change in Y_k leads to changes in $\dot{\omega}_k$ as well. Hence, the resulting ODE system needs to be solved with the given initial conditions. Detailed reaction mechanisms are typically composed of tens of species, all having different time scales. Starting from an initial state of perfectly mixed reactants, the radical species (i.e., H, C_2H_2) may reach to their equilibrium values in $10^{-5} \sim 10^{-8}$ seconds. On the other hand, $10^{-1} \sim 10^{-3}$ seconds may be needed for the major species (i.e., CO_2, NO) to reach their equilibrium values. Thus, stiff ODE solvers are needed to calculate the chemical source terms. As the order of the chemical kinetics mechanism continues to increase, more radical species with shorter time scales are added to the system and the degree of stiffness increases. As a result, the stiff ODE solver becomes very time consuming, which acts as a bottleneck in the CFD simulations (19). Typical solutions used to overcome this difficulty are outlined

in the following sections.

1.3.3.1 *Low-Order Chemical Kinetics Mechanisms*

For most CFD applications, the order of the detailed reaction mechanisms are reduced by using steady-state and partial equilibrium assumptions (93). Careful investigation of the reaction mechanisms reveals that a certain number of intermediate *species* are responsible for the occurrence of slow reactions. Also, it is observed that the backward and forward reaction rates of certain number of *reactions* are almost equal. Hence, assuming steady-state assumption for particular species ($dY_k/dt = 0$) and equilibrating the forward and backward reaction rates of the certain reactions reduces the order of the system of ODE. In this way, the new system of equations that needs to be solved becomes a relatively smaller set of ODEs than the original form with additional algebraic equations. It should be noted that the reduction process requires extensive knowledge on the behavior of the species and reactions for the given particular mechanism (45). Also, the assumptions are only valid for the given range of conditions (i.e., high/low temperature, pressure, etc.). Finally, it has been reported that the order reduction may lead to mechanisms stiffer than their original forms (63).

1.3.3.2 *Intrinsic Low Dimensional Manifolds*

The intrinsic low dimensional manifolds method is used to reduce the order of the reaction mechanisms automatically without *a-priori* knowledge of the chemical processes. For an isobaric, adiabatic system with constant element composition, all trajectories that are started at distinct points in the compositional state-space eventually lead to the equilibrium point. ILDM is based on the fact that at a certain portion of the chemical state-space all trajectories tend to bunch (45). At this lower dimensional attractor, slow processes are more important than faster ones (44). The identification of this attractor is achieved by the perturbation analysis. Eq. 21 can be linearized in

the neighborhood of Y_k^0 by using the Taylor series expansion as:

$$\frac{dY_k}{dt} = F(Y_k^0) + \mathbf{J}(Y_k - Y_k^0) \quad (22)$$

where \mathbf{J} is the Jacobian matrix given by the following formula:

$$\mathbf{J} = \begin{bmatrix} \frac{dF_1}{dY_1} & \frac{dF_1}{dY_2} & \cdots & \frac{dF_1}{dY_{N_s}} \\ \frac{dF_2}{dY_1} & \frac{dF_2}{dY_2} & \cdots & \frac{dF_2}{dY_{N_s}} \\ \cdots & \cdots & \cdots & \cdots \\ \frac{dF_{N_s}}{dY_1} & \frac{dF_{N_s}}{dY_2} & \cdots & \frac{dF_{N_s}}{dY_{N_s}} \end{bmatrix} \quad (23)$$

The Schur decomposition of the Jacobian matrix leads to

$$\mathbf{J} = \Gamma \Lambda \Gamma^{-1} \quad (24)$$

where Γ is the eigenvalues vector, and Λ is the corresponding eigenvector matrix. The first advantage of this decomposition is that the ODE system is now transformed into uncoupled form. Second, it gives a clear explanation to the behavior of the system to different perturbations. If the system is perturbed, the processes with positive eigenvalues diverge whereas processes with negative eigenvalues converge to the low-dimensional attractor in the compositional state-space in the direction of their corresponding eigenvector (45). In the ILDM methodology, all but a few eigenvalues are replaced by zeros. In this manner, given state vector (Y_k, T) is projected onto a lower dimensional attractor (manifold) in the compositional state-space where slow processes are important. The states that correspond to zero eigenvalues are no longer needed since they are represented by slow processes. Hence, the dimensions of the system of equations are drastically reduced to 1-3 from N_s . In this manner, starting from a detailed reaction mechanism, ILDM can reduced the degree of freedom effectively with the assumption that only slow processes are important.

One of the most important difficulty associated with this methodology is that the ILDM assumes that only slow processes that are close to the equilibrium are

important (63). This is strictly true for steady flames. However, flame extinction or re-ignition the chemistry is not governed with slow processes. To capture these effects, the dimension of the ILDM has to be increased. Also, the identification of the lower dimensional attractor can be troublesome especially for high hydrocarbon fuels such as *heptane*. A hierarchical reconstruction scheme is proposed to overcome this problem, which depends on creating the ILDM surfaces by starting from simple fuels and extending towards more complex ones (9; 71; 39).

1.3.3.3 *In-situ Adaptive Tabulation*

ILDM methodology requires construction of look-up tables to be used in the CFD simulations. However, the portion of the compositional state-space that will be accessed by the flow solver is not known *a-priori*. Hence, huge structural tables must be generated for the ILDM reduced set of reaction progress variables. The size of the look-up tables is restricted by the memory capacity of the computer clusters. This difficulty is overcome by using ISAT, where the look-up tables are generated during the actual CFD simulation (65). Unlike ILDM, ISAT does not provide any reduction on the order of the reaction mechanism. Hence, ISAT can be used by both detailed and reduced reaction mechanisms effectively.

The formulation for the ISAT model can be described based on the reaction mapping, $\mathbf{R}(\Phi^0)$, which is obtained by integrating Eq. 21 between t_0 and $t_0 + \Delta t$. The ISAT table is populated with the Φ^0 , $\mathbf{R}(\Phi^0)$ and the mapping gradient $\mathbf{A} = \partial \mathbf{R}_i(\Phi) / \partial \Phi_j$. The mapping gradient measures the sensitivity of the reaction mapping to changes in the composition and provides coefficients that will be used for linear interpolations (63). For each entry in the ISAT table there exists a parameter that shows the size of the region of accuracy. For a new state that lie within this region (i.e., Φ^q), there is no need to use a stiff ODE solver during the simulation, and

the reaction mapping can be calculated by:

$$\mathbf{R}(\Phi^q) = \mathbf{R}(\Phi^0) + \mathbf{A}(\Phi^0)(\Phi^q - \Phi^0) \tag{25}$$

When the reaction mapping for a state that is outside the area of accuracy for the existing states in ISAT table is required, a stiff ODE solver is used. The resulting reaction mapping is compared with the one that is calculated by Eq. 25. If the error between two mappings is larger than a given tolerance ϵ , the new state is added to the table. If the error is smaller, the size of the region of accuracy for the existing state in the table is increased. In this manner, all states that lie between the existing state and the newly calculated state can be represented by the ISAT table without using the stiff ODE solver.

ISAT, as mentioned earlier, is no different than using a stiff ODE solver on the early stages of the simulation. Also, the speed-up highly depends on the selection of the ϵ . A large ϵ would provide speed-up with poor accuracy, whereas small ϵ would yield the code to calculate the reaction mapping by using stiff ODE solvers at most of the time. There exists no well-established methodology to select an optimum value for the ϵ .

1.4 Neural Networks

Living organisms solve problems in a completely different manner than the computers. A computer program can find the exact trajectory for the movement of a stone which is thrown at $t = 0$ with a known initial velocity and direction. The movement is governed by the laws of physics, which is known to the architect who writes the program and is solved exactly by the computer. Even if the initial velocity and direction are not known exactly, the computer can provide different trajectories with respect to the given different initial conditions, so that the path can be predicted from these results. The human brain, however, does not solve equations. Nonetheless, a person watching someone throw a stone can know (or predict) the trajectory as well. This is achieved

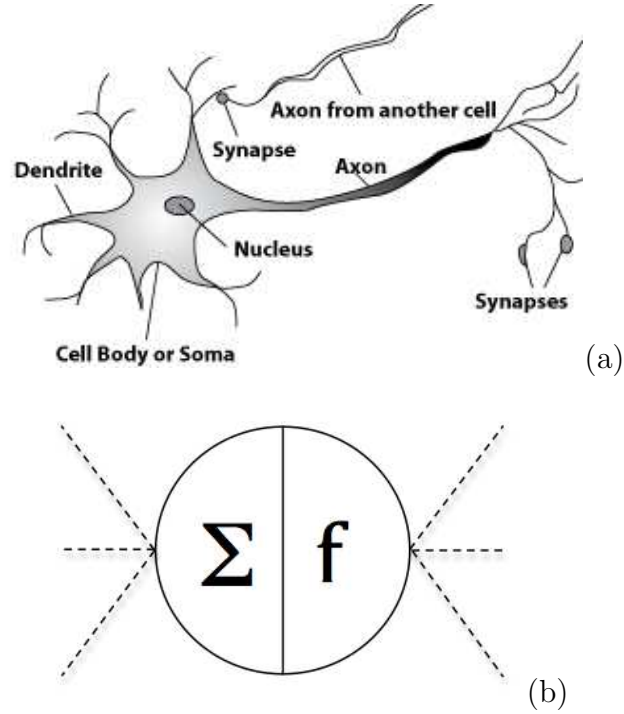


Figure 1: Schematics of (a) biological (53) and (b) artificial neurons.

by a *learning* process through given examples. The processors in the brain that let us think, the neurons, are organized in dense, complex network architectures, and they perform sophisticated information processing tasks through an inter-communication procedure (47). The communication is achieved through neurotransmitters, which generate electrical signals within the somatosensory system. The strength of the electrical signal, and the pattern of which neurons communicate with each other is formed by this *learning* stage.

The ANNs are modeled after their biological counterparts and they emerge as an alternative way to conventional computer modeling to provide answers into certain tasks in a much faster manner. Next sections will provide a detailed discussion for the biological and artificial neurons.

1.4.1 Biological Neurons

A neuron is the fundamental cellular unit of the nervous system, and can essentially be thought of as a single microprocessor unit. Fig. 1 (a) shows a typical sketch of a biological neuron (BN). The basic structure of a neuron consists of a cell body (soma), a long tail somewhat similar to an electrical cable (axon) and finally branch like structures both around the cell body (dendrites) and at the end of the axon (axon terminals) (47). The axon is covered with a myelin sheath which is mainly for insulation purposes. The dendrites are used to receive electrical signals, whereas the axon terminal transmits signals to the dendrites of other neurons.

A typical BN rests with a net negative electric potential around -70 mV compared to the fluid surrounding it (40). When a pre-synaptic neuron releases neurotransmitters, they bind to the receptors of the post-synaptic neuron in its dendrites. This action causes the ion pumps and controllable ion channels of the post-synaptic neuron to release either positively or negatively charged ions (i.e. Na^+ , K^+ , Cl^-) (40). Based on the released ions, the pre-synaptic neuron may either increase (excitatory) or decrease (inhibitory) the electric potential. It should be noted that not all the signals may excite the neuron. The net electrical signal needs to pass the threshold at the axon hillock, which is the part of the BN that merges the soma to the axon. Once the threshold is passed, the excitatory signals are transmitted through the axon to the axon terminals. Then, the axon terminals release neurotransmitters to the dendrites of the neighboring neurons so that the electrical signal sweeps through the somatosensory system.

The receiving neuron fires its own neurotransmitters depending on the cumulative effect of all excitatory and inhibitory signals arriving from all neurons. The electric potential threshold of each neuron is different than the each other. Also, the ion pumps release different ions based on the incoming neurotransmitters leading to a different type of response (and effect) to the neighboring neurons. All of these

parameters are adjusted by a life-long training procedure.

1.4.2 Artificial Neurons

Artificial neurons (AN) are modeled after their biological counterparts. A typical sketch of an AN is given in Fig. 1 (b). Similar to a BN, an AN has a processing element (soma) which processes the information coming through communication channels (dendrites) from other ANs that it is connected in the complex ANN architecture. The AN fires a signal if the cumulative effect of all signals coming from other ANs are larger than a given threshold (axon hillock). This signal is transmitted to other neurons (axon and axon terminals), so that the given initial data (stimulus) can proceed through the ANN (somatosensory system), which leads to the final answer (reaction).

In an ANN architecture each connection between a particular AN pair (i and j) has a certain synaptic efficiency, the *weight coefficient* W_{ji} . Basically, this coefficient defines the strength of the connection between all AN pairs. The combined effect of all pre-synaptic neurons on the given AN i and an input vector (net_i) is:

$$net_i = \sum_{j=0}^J W_{ij}[k]y_j - b_i \quad (26)$$

where y_j is the signal fired from AN j to i and W_{ij} is the respective weight coefficient. Here, b_i represents the internal threshold for the AN i . The net output of this AN is

$$y_i = g(net_i) \quad (27)$$

where g is an activation function.

For a given ANN architecture and the input/output pairs, the problem is then to find the values of W_{im} , which provide the correct output for a given input (16). This is achieved by the so-called training (learning) process. The training can be either in a supervised or unsupervised mode. In the supervised mode, an external *teacher* exists, who has the capability to identify the error made by the current

distribution of the weight coefficients for the given input vector. Then, through an weight adaptation technique (i.e. gradient descent, conjugate gradients etc.) the weights are modified so that the ANN provides the optimum answer to the given input vector. In the unsupervised learning, however, there is no external *teacher* to quantify the error made by the given ANN. The unsupervised learning is typically used for the problems, where the inputs are not known, but are rather latent (47). The ANN learning in this case is achieved by providing a measure of the quality of the representation that is aimed to be learned.

The activation function (g , see Eq. (27)) represents the rate of firing for the given AN based on the activity level of the input vector. There are couple of well known functions used typically for the ANN computations. Among these functions, the threshold function is the most simplistic one, which assumes that the AN fires if the cumulative effect of the excitation is above than a given value. Otherwise the AN rests. The sigmoid function is, however, by far the most commonly used activation function (16), which is an increasing function that saturates to 0 and 1 at the extreme values of the excitation. Unlike the threshold function, sigmoids are differentiable, which makes it a very effective function for the existing learning rules. The output range of the AN can be increased by using tangent hyperbolic functions. The output for this function varies between ± 1 .

The BNs are much slower than the ANs as it is shown in Table 4. Typical processing speed for an AN is of the order of $\sim 10^2$ Hz, whereas it is $\sim 10^9$ Hz for a BN. However, the brain compensates the relatively slow rate of operation of the BNs by having a huge number of neurons with massive number inter connections between them. It is estimated that there are of the order of 10 billion neurons in the human cortex with 60 trillion connections (40). The learning for an AN takes typically 1-2 days, whereas BNs are trained during a life time. Hence, they are more adaptable compared to the ANs.

Table 3: Comparison of Biological and Artificial Neurons

	Artificial Neurons	Biological Neurons
Operation Frequency	$\sim 10^9$ Hz	$\sim 10^2$ Hz
Signal Velocity	$\sim 10^8$ m/s	~ 1 m/s
Connections	~ 10	$\sim 10^4$
Operation	Sequential/Parallel	Sequential/Parallel
Training	~ 1 day	$\sim 1-10^3$ days

Table 4: Comparison of Biological and Artificial Neurons

	LEMLES	LANN-LEMLES	TANN-LES
Subgrid Turbulence	LDKM	LDKM	LDKM
Subgrid Combustion	LEM	LEM	TANN
Subgrid Chemistry	DI	LANN	—

1.4.3 ANN for Chemical Kinetics Calculations

ANN for the reactive flow computations has been used by different research groups in the past. Blasco et al. (7) performed one of the first attempts to incorporate ANN into chemical kinetics calculations, where the accuracy of the proposed model was tested in a plug flow reactor calculation. A speed-up of 2700 with ANN was obtained when compared to direct integration (DI). In a later study (8), time step size was included as an additional parameter, and it was reported that the memory requirement for such an ANN computation requires only 24 kbytes as opposed to 19934 kbytes for tabulated chemistry calculations. Choi and Chen (15) trained ANN for ignition delay time calculations and coupled it with a well-mixed reactor solver. A speed-up of 600 was obtained. Finally, an integration of ISAT with ANN for a partially stirred reactor computation was studied by Chen et al. (14), where ANN was trained based on an already existing ISAT table. Same approach was later revisited by Kapoor et al. (32) and applied to unsteady scalar field evolution within LEM approach.

In more recent studies, ANN has been used within the LES computations of reactive flows. The work by Kempf et al. (34) investigated the structure of the SANDIA Flame D (1) by LES, where ANN was used to store a steady flamelet library to provide species mass fractions, density and viscosity. They reported that the ANN reduces the storage size of the chemistry library by three orders of magnitude having almost same efficiency with a linear interpolation scheme. Ihme and co-workers (29) used ANN to store a flamelet library and applied it to a bluff body stabilized flame. A general strategy to optimize ANNs (O-ANN) for the given number of layers and neurons per layers was also proposed. The ANN performance with respect to accuracy, data retrieval time and storage requirements was compared with the structured tabulation methods, and it was shown that ANN yielded comparable accuracy with considerably lower storage and computational time.

Previous work by Kempf et al. (34) and Ihme et al. (29) used ANN to store flamelet libraries in connection with the presumed PDF approach, where the thermo-chemistry is not computed directly within the LES, but rather obtained from the ANN. In this approach, flamelet itself already provides a considerable amount of speed-up compared to directly simulating the scalar field, and the merit of using ANN mostly lies in the memory savings. An alternative approach is to use ANN to directly represent the multi-step kinetics within the LES approach, and this has been recently investigated by Sen and Menon (76). Here, a series of simulations of the *unsteady* evolution of flame-vortex interactions (FVI) were used to extract the thermo-chemical information for ANN training table construction. These simulations of FVI showed that, although the computations are started for a single large scale vortex, actually a large number of scales are present over the entire simulation period. Hence, each test case with an initial single vortex of a given size provided additional data over a much wider range of scales. The ANN was later used to replace the DI based on a 14-species, 11-steps reduced chemical kinetics mechanism within the LES

sub-grid calculations of premixed, syngas/air flames. A speed-up factor of around 11 with considerable amount of memory savings was reported.

1.5 Fundamental Flame-Turbulence Interaction Studies

For premixed turbulent combustion studies, the main idea is to investigate the effect of differential diffusion, flame curvature-strain and unsteady ignition effects on the turbulent flame speed and flame dynamics. Baum et al. (2) performed a series of DNS studies to investigate the validity of the flamelet assumption in a premixed H_2 -Air flame with a detailed reaction mechanism. For each DNS case they changed the equivalence ratio. The u'/S_L and l/L_F was roughly kept constant in order to limit the flames in the wrinkled flames (flamelets) regime of the turbulent combustion diagram. It was observed that for lean flames the local flame structure correlates with the curvature, whereas for rich flames with the strain rate. Later, Im and Chen (30) performed a similar study to further investigate the effect of stretch on the overall burning rate for an H_2 -Air flame with detailed kinetics. They also included preferential diffusion in their simulations. It was concluded that for rich-rich flame interactions the radical pool exhibits an overshoot instantaneously. The heat release, interestingly, remained unaffected in those instants exhibiting a smooth profile. This phenomenon was not observed in lean-lean flame interactions.

Echekki and Chen (18) extended these studies to investigate the CH_4 -Air flames. As a first step in this effort, a relatively low order chemical kinetics mechanism with four steps and seven species was used to calculate the chemical reaction rates. Here, the correlation of radical species with strain rate and curvature was extracted, and it was found that diffusive species (i.e. H and H_2) are well correlated with the curvature, whereas less diffusive species (i.e. CO) are affected more by the unsteady strain rate. The same observation was also made by DNS studies using higher order reduced mechanisms as well (4; 5). Bell et al. (4) used a 20 species and 84 reactions CH_4 -Air

mechanism for their DNS study. They investigated the effect of varying levels of turbulent intensity on the flame area and laminar flame speed. They concluded that the flame speed increases faster than the increase in the flame surface area. In a later study, Bell et al. (5) performed the DNS of a laboratory-scale turbulent slot flame and provided comparisons with an experimental study, which showed good prediction of the flame height, global consumption speed and the overall time averaged flame shape.

The flame dynamics is strongly affected by the effect of wrinkling of the flame front through turbulent eddies. This effect is different for each different fuel and equivalence ratio. Bell et al. (3) investigated this effect on two-dimensional DNS studies of turbulent, lean premixed H_2 /Air, C_3H_8 /Air and CH_4 /Air flames. The results indicated that for methane flames the local burning rate is relatively insensitive to the flame curvature, whereas hydrogen and propane flames exhibit an increased level of sensitivity. For propane flames the burning is enhanced in regions of large negative curvature, and the flames are thermo-diffusively stable.

The non-premixed DNS studies in general focus on investigating the extinction and re-ignition behavior in strained flames. Sripakagorn et al. (81) examined this process in an isotropic decaying turbulence using a one step global reaction mechanism. Here it was argued that the extinction mainly occurs due to the locally strong fluctuations of the scalar dissipation rate. For the flame reignition, three major scenarios were identified: independent flame, re-ignition with edge flame propagation and through engulfment by a hot neighborhood. Pantano (54) investigated the same process for a CH_4 /Air flame with a four step reduced mechanism. The joint PDF of the three dimensional edge velocity and the scalar dissipation rate was extracted and it was observed that the flame edge propagates with a velocity controlled by the scalar dissipation range.

Hawkes et al. (26) provided discussion for the extinction and re-ignition of non-premixed syngas/air flames with a relatively detailed 21 steps, 11 species reduced mechanism. The PDF of the scalar dissipation rate conditioned on the mixture fraction was found to be log-normal with a slight negative skewness. Also, the mechanical-to-scalar mixing timescale ratio calculated for the mixture fraction was found to be independent of the Reynolds number. On the other hand, the mechanical-to-scalar mixing timescale ratio calculated for the reactive species was found to be strongly affected by the Schmidt number and the chemical reactions.

Soot formation in non-premixed flames is also an important issue which needs to be investigated in details. The DNS study by Lingell et al. (41) examined this process in 2-D for an ethylene flame with a 15 steps, 19-species chemical kinetics mechanism. The relative motion between flame and soot particles was found to be resulting in a wide spread of the soot in the mixture fraction state-space. The relative motion in general occurs due to the change of flame motion as a result of the flame curvature.

All the aforementioned DNS work used mixture averaged species transport formulations. It is well known that this is valid only under certain assumptions, and multi-component diffusivities should be used for proper flame computations. Recently Grear et al. (25) studied the effect of using mixture averaged formulation against multi-component diffusivity in a turbulent premixed H_2 /Air flame computation. Here it was pointed out that the DNS with multi-component diffusivity indicated an increased level of extinction. Also, the flame exhibits more local pockets of hot products compared with the results obtained by mixture averaged formulations.

1.6 Objectives

The main motivation for this thesis study is to seek a way to use ANN based modeling for speeding up LES of turbulent reactive flows. ANN code development and incorporation of the new ANN based modeling capabilities into an existing LES solver is the primary goal. In contrast to the previous LES studies using ANN, the main purpose here, which is new, is to use ANN to directly represent the multi-step kinetics within the subgrid LES. The ANN training database is constructed by using stand-alone LEM computations. Hence, the thermo-chemical state-space is predicted without requiring any knowledge on the actual geometry of interest, which is also new. The objectives in details are follows:

Objective 1 *Develop a Tabulation Strategy for Instantaneous Reaction Rates*

The chemical source terms ($\dot{\omega}_k$) associated with the species conservation equation need to be calculated during the reactive flow computations. The system of equations for chemical kinetics calculations is non-linear, coupled and most importantly stiff which require the use of stiff ODE solvers. The solution procedure based on stiff ODE solvers is very time consuming and acts as a bottleneck for the reactive flow computations. Tabulation based models (i.e., ILDM, ISAT) are widely used in the literature for speeding up the computations. These models have their own drawbacks, which were explained in the previous sections. The current thesis study is seeking a way to develop a new tabulation strategy that can be used in the LES of reactive flows. Within this work, three different tabulation strategies based on the (i) laminar flames, (ii) laminar flame-vortex interaction and (iii) laminar flame-turbulence interaction have been developed.

Objective 2 *Develop an ANN Methodology in Connection with the First Objective for Instantaneous Reaction Rates (LANN)*

One of the main problem associated with the tabulation based models is the memory requirement. The look-up table size is restricted by the memory capacity

of the supercomputer used for the computations. Hence, usually sparse tables are used in connection with search and interpolation algorithms. Searching the closest states and interpolating them to find the reaction rate corresponding to the state calculated by the flow solver may be time consuming and yield interpolation errors. ANN is used within this thesis work to overcome this problem. ANNs can be trained on relatively huge tables and can store the information on a much memory efficient manner. Also, ANNs provide relatively smooth and faster interpolated data compared to the conventional interpolation schemes. ANN, in this respect, can be used as a tool to replace computationally expensive chemical kinetics calculations in the LES. It is possible to assume ANN as a "black box", which maps the inputs (Temperature, species mass fractions) to the output (the reaction rate):

$$\dot{\omega}_i = f(Y_k, T) \quad (28)$$

Once the training is achieved, it can be used for predictions into new states requiring neither any extensive computational power nor memory.

Objective 3 *Evaluate LANN in Premixed Flame-Turbulence-Vortex Interaction Problem*

The developed tabulation procedures in connection with the ANN methodology is tested in an LES of premixed flame-turbulence-vortex interaction problem. The scalar field is initialized based on a laminar flame simulation. An isotropic background turbulence and a pair of counter rotating coherent vortices are used to simulate the small and large scale flame wrinkling that occurs typically in gas turbine combustors. The results provide comparison for the accuracy of the proposed LANN model against the stiff ODE solvers.

Objective 4 *Evaluate LANN by a Nonpremixed Flame Exhibiting Extinction-Reignition Physics*

The LANN methodology is tested further on a nonpremixed temporarily evolving

jet flame. The test case is selected based on a DNS study that exists in the literature (26). The species conditional PDFs are extracted from the LANN-LEMLES to provide comparison with the DNS study. The PDFs of the scalar dissipation rate calculated based on the mixture fraction and species are also calculated and their evolution during extinction and reignition phases is investigated.

Objective 5 *Develop a Tabulation Strategy for Filtered Reaction Rates (TANN)*

The conventional LES approach is to solve the filtered species equation on the resolved level. This approach requires the calculation of the filtered reaction rate which is not only a function of the filtered mass fractions and temperature, but also the turbulent quantities. The common approach to calculate the filtered reaction rates is to assume a locally laminar flame front with respect to the turbulent flow field (as in flamelets and CMC) and re-construct the subgrid species evolution based on the reduced dimensions, i.e., scalar dissipation rate, mixture fraction, etc. The current study proposes a new tabulation model for the filtered reaction rates, which does not convey any explicit assumption regarding the interaction of turbulence with the laminar flame front, but solves them directly on their respective time and length scales through the stand-alone LEM computations. The stand-alone LEM code developed for the LANN approach is used for filtered reaction rate tabulation by applying a spatial filter on the table obtained for instantaneous reaction rates. For this approach, the filtered reaction rate is obtained from the ANN as a function of the filtered mass fractions, temperature, subgrid Reynolds number and the filtered level species gradient:

$$\bar{\omega}_i = f(\tilde{Y}_k, \tilde{T}, Re_\Delta, \frac{\partial \tilde{Y}_i}{\partial x}) \quad (29)$$

Objective 6 *Evaluate TANN by a Nonpremixed Flame with Extinction-Reignition Physics*

The table generated for Objective 5 is used in connection with the ANN to replace the filtered reaction rate calculations on the test case used in Objective 4.

Objective 7 *Apply and Evaluate LANN and TANN for a Complex Combustor Flow*

The final objective is to use both the LANN and TANN approaches on a practical combustor simulation. The stagnation point reverse flow (SPRF) combustor, which is developed at the combustion lab of Georgia Institute of Technology is selected as the test case. The SPRF combustor was studied both computationally (88) and experimentally (24) before. The current study aims to examine the flame structures in the same combustor by using a relatively high order (16 species, 12 steps) skeletal chemical kinetics mechanism on a computationally much affordable way by using the LANN and TANN techniques.

To achieve these objectives, two major tools are developed within the thesis study:

Stand Alone LEM Solver Development

A stand-alone LEM code is developed, which solves the unsteady evolution of the scalar field on a one-dimensional line. Unlike the LEM subgrid model (LEMLES) , which simulates the scalar field on one dimensional lines embedded within each LES supergrid cells, the computational domain in the current approach extends across the whole flame front without using any LES cell. Thus, the LEM cells here are continuous throughout the flame front. The proposed model solves the governing equations for the species and temperature fields starting from an initially laminar flame simulation. In this manner it is possible to identify the unsteady interaction process between the laminar flame front and the turbulent structures. Hence, the current tabulation approach may be considered as an extension of the flamelets. The code that is developed can use mixture averaged and multi component diffusion formulations as well.

ANN Training Code Development

The look-up tables constructed through the developed approaches in the current thesis study are used with the ANN to achieve computational time and memory savings. An ANN training code is developed to learn the input/output pairs that exist

within the look-up table. The ANN code uses a backpropagation learning algorithm with gradient descent rule (GDR). An extension of the GDR is also developed and coded, which uses non-constant model coefficients during the computations. This new rule is called the adaptive gradient descent rule (AGDR). The ANN training code uses fully connected processing elements (PEs) with a tangent hyperbolic function.

The details of the both codes will be provided on the next chapters.

CHAPTER II

MATHEMATICAL FORMULATION

2.1 Gas Phase Governing Equations

The gas phase governing equations of continuity, momentum, energy and species in the conserved form are given as:

$$\begin{aligned}
 \frac{\partial \rho}{\partial t} + \frac{\partial \rho u_i}{\partial x_i} &= 0 \\
 \frac{\partial \rho u_i}{\partial t} + \frac{\partial}{\partial x_j} [\rho u_i u_j + p \delta_{ij} - \tau_{ij}] &= 0 \\
 \frac{\partial \rho E}{\partial t} + \frac{\partial}{\partial x_i} [(\rho E + p) u_i - u_j \tau_{ji} + q_i] &= 0 \\
 \frac{\partial \rho Y_k}{\partial t} + \frac{\partial}{\partial x_i} [\rho Y_k u_i + J_{ik}] &= \dot{\omega}_k
 \end{aligned} \tag{30}$$

In the above equations ρ is the density, u_i is the i -th velocity component, E is the total energy and Y_k is the k -th species mass fraction. The viscous stress tensor is computed as:

$$\tau_{ij} = \mu \left(\frac{\partial u_i}{\partial x_j} - \frac{\partial u_j}{\partial x_i} \right) - \frac{2}{3} \delta_{ij} \mu \frac{\partial u_k}{\partial x_k} \tag{31}$$

where δ_{ij} is the Kronecker function ($\delta_{ij} = 1$ if $i = j$; $\delta_{ij} = 0$ if otherwise), and μ is the dynamic viscosity. The total energy is given as:

$$E = e + \frac{1}{2} u_k u_k \tag{32}$$

In this formulation the internal energy per given mass is:

$$e = \sum_{k=1}^{Ns} Y_k h_k - \frac{p}{\rho} \tag{33}$$

The k -th species total enthalpy is calculated as the sum of the chemical and sensible enthalpies as:

$$h_k(T) = \Delta h_{f,k}^0 + \int_{T_0}^T c_{P,k}(T') dT' \tag{34}$$

Here, $\Delta h_{f,k}^0$ is the enthalpy of formation at a given reference temperature and pressure (T_0, P_0) , and represents the heat released or absorbed by the chemical reactions when simple substances combine into a more complex substance. The second term on the right hand side is the sensible enthalpy, which is temperature dependent. At the standard temperature and pressure the sensible enthalpy is zero, which leads to total enthalpy being equal to the enthalpy of formation. Finally, $c_{P,k}$ is the heat capacity at constant pressure for the k -th species.

In Eq. 30 the pressure is directly derived from the equation of state for a perfect gas:

$$p = \rho R_u T \sum_{k=1}^{N_s} \frac{Y_k}{W_k} \quad (35)$$

where R_u , N_s , W_k are the universal gas constant, number of species and molecular weight of k -th species, respectively.

The k -th species mass reaction rate per unit mass ($\dot{\omega}_k$) is calculated by solving the ODE system representing the evolution of the species mass fractions with respect to the given reaction mechanism. For the given initial values and a time step size, a variable coefficient ODE solver with fixed leading coefficient implementation is used to find the new scalar field. Then, the reaction rate is given by:

$$\dot{\omega}_k = \frac{(Y_k^{t+\Delta t} - Y_k^t)\rho}{\Delta t} \quad (36)$$

Heat flux (q_i), k -th species diffusion flux (J_{ik}) and the k -th species mass reaction rate per unit mass will be discussed in more details on the proceeding sections.

2.1.1 Transport Properties

The heat flux (q_i) and the k -th species diffusion flux (J_{ik}) introduced in the Eq. 30 require special handling for a multi-component mixture. In their general form, these terms are given as:

$$q_i = \sum_{k=1}^{N_s} J_{ik} h_k - \kappa \nabla T - \sum_{k=1}^{N_s} \frac{R_u T}{W_k X_k} D_k^T d_{ik} \quad (37)$$

$$J_{ik} = \rho Y_k V_{ik} \quad (38)$$

where D_k^T is the thermal diffusion coefficient and V_{ik} is the k -th species diffusion velocity. The species diffusion velocity is a complicated expression that takes into account mass diffusion as a result of concentration gradients (ordinary diffusion), temperature gradients (Soret diffusion) and pressure gradients. In a typical combustion system the pressure gradients are not significantly large (86), hence, the discussion here will be focusing mainly on the ordinary and Soret diffusion.

2.1.1.1 Multi-Component Formulation

For a multi-component mixture with negligible pressure gradients, the total diffusion velocity is:

$$V_{ik} = \frac{1}{X_k W_{mix}} \sum_{j \neq k}^{Ns} W_j D_{kj} \frac{\partial X_k}{\partial x_i} - \frac{D_k^T}{\rho Y_k T} \frac{\partial T}{\partial x_i} \quad (39)$$

Here, D_{kj} is the multi-component diffusion coefficient, D_k^T is the thermal diffusion coefficient and X_k is the k -th species mole fraction. The D_{kj} 's are derived from the kinetic theory, and given as:

$$D_{kj} = X_i \frac{16T}{25p} \frac{W_{mix}}{W_j} (F_{kj} - F_{kk}) \quad (40)$$

The F_{kk} and F_{kj} are the components of the F matrix ($[F]$). The $[F]$ is calculated by taking the inverse of the $[L]$. The components of the $[L]$ are given by:

$$L_{kj} = \frac{16T}{25P} \sum_{m=1}^{Ns} \frac{X_m}{W_k \mathcal{D}_{km}} [W_j X_j (1 - \delta_{km}) - W_k X_j (\delta_{kj} - \delta_{jm})] \quad (41)$$

In this equation, \mathcal{D}_{km} 's are the binary diffusion coefficients. It assumes a two component binary mixture, where species is k diffusing into species m . Based on the kinetic theory of gases, where the individual gas molecules are modeled as rigid spheres, the binary diffusion coefficients are found to be proportional to the mean velocity rigid spheres and the mean free path, which leads to

$$\mathcal{D}_{kj} = \frac{3}{16} \frac{\sqrt{2\pi k_B^3 T^3 / m_{jk}}}{p \pi \sigma_{jk}^2 \Omega^{(1,1)}} \quad (42)$$

Here k_B is the Boltzman constant, σ_{jk} is the mean diameter ($= (\sigma_{jk} + \sigma_{jk}) / 2$), and $\Omega^{(1,1)}$ is the correction factor used to modify the ideal gas law to account for the molecular interactions. The reduced mass m_{jk} is the reduced molecular mass of the species pair j, k , and is given by

$$m_{jk} = \frac{m_j m_k}{m_j + m_k} \quad (43)$$

2.1.1.2 Mixture-Averaged Formulation

The multi-component formulation introduced in the previous section is the correct and accurate way of addressing the diffusion phenomenon for a multi-species mixture. However, the calculation requires inverting an $N_s \times N_s$ matrix to find the D_{kj} 's. Furthermore, although it was not shown for the sake of brevity, for D_K^T and κ , a $3N_s \times 3N_s$ system of algebraic equations are needed to be solved. Hence, the multi-component diffusion formulations are avoided in the practical LES. Instead, computationally more efficient, but not as accurate models are employed. These models will be discussed in the current and proceeding sections.

The mixture averaged formulation derives the diffusion coefficients from pure species properties by mixture averaging rules. The mixture averaged formulations are correct strictly only (i) for binary mixtures and (ii) for mixtures where all species except one move with nearly the same diffusion velocity (33). Also, mass conservation is an issue and needs to be confirmed separately, which may be time consuming.

The diffusion velocity for a mixture averaged formulation is given as:

$$V_{ik} = -\frac{1}{X_k} D_{km} \frac{\partial X_k}{\partial x_i} - \frac{D_k^T}{\rho Y_k T} \frac{\partial T}{\partial x_i} \quad (44)$$

where the mixture diffusion coefficient for the k -th species is:

$$D_{km} = \frac{\sum_{j \neq k}^{N_s} X_j W_j}{W_m \sum_{j \neq k}^{N_s} X_j / \mathcal{D}_{jk}} \quad (45)$$

This formulation needs to be controlled to satisfy the net species diffusion flux to be zero ($\sum_{k=1}^{N_s} V_{ik} Y_k = 0$). For most of the cases this constraint is not satisfied, which leads to the violation of the conservation of mass in a given control volume. In a simple manner this can be corrected by ensuring that $\sum_{k=1}^{N_s} Y_k = 1$ and by adding (or subtracting) the deficient (or excess) species mass fractions from N_2 . It should be noted that this would only work if the system is premixed or highly diluted. Another solution is to add a correction velocity to the convective terms in the species conservation equation to account for the excess diffusion. The correction velocity is calculated as:

$$V_i^c = - \sum_{k=1}^{N_s} Y_k \left(\frac{1}{X_k} D_{km} \frac{\partial X_k}{\partial x_i} \right) \quad (46)$$

In this case the k -th species diffusion flux is calculated as:

$$J_{ik} = \rho Y_k (V_{ik} + V_i^c) \quad (47)$$

The mixture averaged viscosity is given by the Wilke's formula:

$$\mu = \sum_{k=1}^{N_s} \frac{X_k \eta_k}{\sum_{j=k}^{N_s} X_j \Phi_{kj}} \quad (48)$$

where

$$\Phi_{kj} = \frac{1}{\sqrt{8}} \left(1 + \frac{W_k}{W_j} \right)^{-\frac{1}{2}} \left(1 + \left(\frac{\eta_k}{\eta_j} \right)^{\frac{1}{2}} \left(\frac{W_j}{W_k} \right)^{\frac{1}{4}} \right)^2 \quad (49)$$

The η_i in this formulation represents the i -th species viscosity. In a similar manner the thermal conductivity is calculated by using the following formula:

$$\kappa = \frac{1}{2} \left(\sum_{k=1}^{N_s} X_k \lambda_k + \frac{1}{\sum_{k=1}^{N_s} X_k / \lambda_k} \right) \quad (50)$$

where λ_k is the pure species conductivity

2.1.1.3 Simplified Fickian transport

The diffusion coefficients (viscosity, thermal conductivity and species diffusion) can be calculated by excluding completely the effect of multi-component diffusion. For this case the viscosity is given by the Sutherland's rule as:

$$\mu = S_0 \frac{T^{3/2}}{T + S_1} \quad (51)$$

where S_1 is 110.4 K and S_0 is:

$$S_0 = \frac{\mu_{ref}}{T_{ref}^{3/2}}(T_{ref} + S_1) \quad (52)$$

Here μ_{ref} is the reference viscosity at the reference temperature (T_{ref}). Once the viscosity is known, the mixture thermal conductivity and diffusion coefficients are calculated based on the unity Lewis numbers and the given Schmidt number as follows:

$$D_{km} = \mu / S_{Ck}; \kappa = \rho C_p D_{km} \quad (53)$$

Apparently this is the most computationally efficient model among the ones listed in this section. However, this approach completely rejects the multi-component diffusion and calculates the mixture thermal conductivity and the species diffusion coefficients based on non-dimensional numbers and the mixture viscosity calculated for air.

2.2 LES Modeling

An LES approach is employed to solve the fully compressible, reacting, multi species, Favre averaged form of the conservation equations. In the LES methodology large scale structures are fully resolved whereas small scale structures (subgrid-scale) are modeled by using appropriate subgrid momentum and combustion models (94; 66). In the current approach a spatial top hat Favre filter is used with a kernel size equal to the grid spacing (Δx). All flow variables are decomposed into the resolved and un-resolved components as a result of the filtering operation as $f = \tilde{f} + f''$, where (\sim) represents

resolved scales (which is Favre filtered) and ($\tilde{\cdot}$) denotes the unresolved subgrid scale quantities. Since the kernel size is equal to the grid spacing, the separation between large and small scales is determined with Δx . Thus, modeling is applied only for scales smaller than Δx . The following Favre-filtered form of the Navier Stokes equations for continuity, momentum, total energy and species conservation are solved for the current computations:

$$\begin{aligned}
\frac{\partial \bar{\rho}}{\partial t} + \frac{\partial \bar{\rho} \tilde{u}_i}{\partial x_i} &= 0 \\
\frac{\partial \bar{\rho} \tilde{u}_i}{\partial t} + \frac{\partial}{\partial x_j} [\bar{\rho} \tilde{u}_i \tilde{u}_j + \bar{p} \delta_{ij} - \bar{\tau}_{ij} + \tau_{ij}^{sgs}] &= 0 \\
\frac{\partial \bar{\rho} \tilde{E}}{\partial t} + \frac{\partial}{\partial x_i} [(\bar{\rho} \tilde{E} + \bar{p}) \tilde{u}_i + \bar{q}_i - \tilde{u}_j \bar{\tau}_{ji} + H_i^{sgs} + \sigma_i^{sgs}] &= 0 \\
\frac{\partial \bar{\rho} \tilde{Y}_k}{\partial t} + \frac{\partial}{\partial x_i} [\bar{\rho} \tilde{Y}_k \tilde{u}_i + \bar{\rho} \tilde{Y}_k \tilde{V}_{i,k} + \phi_{i,k}^{sgs} + \theta_{i,k}^{sgs}] &= \bar{\omega}_k
\end{aligned} \tag{54}$$

Any Favre filtered quantity (i.e. \tilde{f}) is calculated as $(\overline{\rho f / \bar{\rho}})$, where the overbar stands for spatial filtering using the top-hat filter. Here, $\tilde{\rho}$, \tilde{u}_i , \tilde{E} , and \tilde{Y}_k are the Favre filtered mixture density, velocity, total energy and k -th species mass fraction, respectively. The total energy is given as $\tilde{E} = \tilde{e} + \frac{1}{2} \tilde{u}_k \tilde{u}_k + k^{sgs}$, where \tilde{e} is the filtered internal energy and k^{sgs} is the subgrid scale kinetic energy. The filtered pressure is calculated by the filtered equation of state as $\bar{p} = \bar{\rho} R \tilde{T} + P^{sgs}$, where R is the mixture gas constant. Past studies suggested that P^{sgs} can be neglected (21), and this is assumed here as well. $\tilde{V}_{i,k}$ is the diffusion velocity of the k th species and based on the mixture averaged transport formulation, is given as:

$$\tilde{V}_{ik} = - \frac{D_{km}^-}{\tilde{X}_k} \frac{\partial \tilde{X}_k}{\partial x_i} + \tilde{V}_i^C \tag{55}$$

where \tilde{X}_k is the k th species mole fraction and $D_{k,m}^-$ is the mixture averaged species diffusivity. \tilde{V}_C is the correction velocity as given in Eq. 46. Finally, the filtered heat-flux vector is given by

$$\tilde{q}_i = -\bar{\kappa} \frac{\partial \tilde{T}}{\partial x_i} + \bar{\rho} \sum_{k=1}^{N_s} \tilde{h}_k \tilde{Y}_k \tilde{V}_{i,k} + \sum_{k=1}^{N_s} q_{i,k}^{sgs} \quad (56)$$

with \tilde{h}_k and $\bar{\kappa}$ denoting the Favre filtered k th species enthalpy and thermal conductivity. The unresolved subgrid-scale terms arising due to the filtering approach on the conservation equations are denoted with *sgs* and they need to be modeled. These terms are the subgrid shear stress (τ_{ij}^{sgs}), subgrid viscous work (H_i^{sgs}), subgrid viscous stress (σ_i^{sgs}), subgrid mass flux ($\phi_{i,k}^{sgs}$), subgrid diffusive mass flux (θ_{jm}^{sgs}), and subgrid heat transfer via turbulent convection of species $q_{i,k}^{sgs}$. In details they are represented as:

$$\begin{aligned} \tau_{ij}^{sgs} &= \bar{\rho} [\widetilde{u_i u_j} - \tilde{u}_i \tilde{u}_j] \\ H_i^{sgs} &= \bar{\rho} [\widetilde{E u_i} - \tilde{E} \tilde{u}_i] + [\overline{p u_i} - \bar{p} \tilde{u}_i] \\ \sigma_i^{sgs} &= [\widetilde{u_i \tau_{j,i}} - \tilde{u}_i \tilde{\tau}_{j,i}] \\ \phi_{i,k}^{sgs} &= \bar{\rho} [\widetilde{Y_k u_j} - \tilde{Y}_k \tilde{u}_j] \\ \theta_{jm}^{sgs} &= \bar{\rho} [\widetilde{Y_k V_{j,k}} - \tilde{Y}_k \tilde{V}_{j,k}] \\ q_{i,k}^{sgs} &= \left[\overline{h_k D_k \frac{\partial Y_k}{\partial x_i}} - \tilde{h}_k \tilde{D}_{km} \frac{\partial \tilde{Y}_k}{\partial x_i} \right] \end{aligned} \quad (57)$$

Next, the sgs models selected to represent these unclosed terms for momentum and combustion will be explained.

2.2.1 Subgrid Momentum Modeling

For the momentum and the energy transport, the major effect of the small scales is to provide dissipation to the energy budget of the flow. Therefore, an eddy viscosity type subgrid model is suitable for the calculation of subgrid stresses, τ_{ij}^{sgs} and the enthalpy flux, H_i^{sgs} . The sub-grid stress tensor is modeled as:

$$\tau_{ij}^{sgs} = -2\bar{\rho}\nu_t(\tilde{S}_{ij} - \frac{1}{3}\tilde{S}_{kk}\delta_{ij}) + \frac{2}{3}\bar{\rho}k^{sgs}\delta_{ij} \quad (58)$$

where resolved strain-rate is given as $\tilde{S}_{ij} = (\frac{1}{2})[(\frac{\partial \tilde{u}_i}{\partial x_j}) + (\frac{\partial \tilde{u}_j}{\partial x_i})]$. This expression is closed if ν_t and k^{sgs} are known. The subgrid scale eddy viscosity is calculated as $\nu_t = C_\nu(k^{sgs})^{\frac{1}{2}}\bar{\Delta}$, where $\bar{\Delta}$ is the grid cut-off scale ($\bar{\Delta} = (\Delta x \Delta y \Delta z)^{\frac{1}{3}}$). An additional transport equation for the subgrid scale kinetic energy k^{sgs} is solved, which is in the form of:

$$\frac{\partial \bar{\rho} k^{sgs}}{\partial t} + \frac{\partial}{\partial x_i}(\bar{\rho} \tilde{u}_i k^{sgs}) = P^{sgs} - D^{sgs} + \frac{\partial}{\partial x_i}(\frac{\bar{\rho} \nu_t}{Pr_t} \frac{\partial k^{sgs}}{\partial x_i}) \quad (59)$$

where $P^{sgs} = -\tau_{ij}^{sgs} \frac{\partial \tilde{u}_i}{\partial x_j}$, and $D^{sgs} = C_\epsilon \bar{\rho} (\tilde{k}^{sgs})^{\frac{3}{2}} / \bar{\Delta}$, are the production and the dissipation of the k^{sgs} , respectively. In this equation, $Pr_t = 1$, and the two coefficients, C_ν and C_ϵ have constant value of 0.067 and 0.916, based on an earlier calibration (12).

The current study uses a dynamic approach to compute the model coefficients C_ν and C_ϵ , as a part of the solution procedure. The dynamic approach (LDKM (37; 52; 48; 38; 20; 55) hereafter), assumes that the resolved and the unresolved small scales behave in a similar manner and, thus, the model coefficients can be computed using similarity relations. It has been previously reported based on the experimental observations of high Reynolds number flows that the subgrid stress (τ_{ij}^{sgs}) at the grid filter level $\bar{\Delta}$ and the Leonard's stress (L_{ij}) at the test filter level $\hat{\Delta} (= 2\bar{\Delta})$ are self-similar. Here, L_{ij} is given by the following expression

$$L_{ij} = [\langle \bar{\rho} \tilde{u}_i \tilde{u}_j \rangle - \langle \bar{\rho} \tilde{u}_i \rangle \langle \bar{\rho} \tilde{u}_j \rangle] / \hat{\rho} \quad (60)$$

However, a simple scale model of the form $\tau_{ij}^{sgs} = C_L L_{ij}$ for the given model coefficient C_L is found to be not providing the proper turbulent dissipation (43), and a better approach is needed.

LDKM extends this observation by assuming that the L_{ij} and the sub-grid stress at the test filter level ($\hat{\tau}_{ij}^{sgs}$) are also similar (i.e., $\hat{\tau}_{ij}^{sgs} = \hat{C}_L L_{ij}$). Then, $\hat{\tau}_{ij}^{sgs}$ is modeled using the same form used for τ_{ij}^{sgs} with all variables defined at the test filter level. This would give a new expression for the L_{ij} as

$$L_{ij} = \frac{\widehat{\tau}_{ij}^{sgs}}{\widehat{C}_L} = 2\widehat{\rho}\frac{C_\nu}{\widehat{C}_L}\sqrt{k_{test}}\widehat{\Delta}(\langle\tilde{S}_{ij}\rangle - \frac{1}{3}\langle\tilde{S}_{kk}\rangle\delta_{ij}) + \frac{2}{3}\frac{1}{\widehat{C}_L}\widehat{\rho}k_{test}\delta_{ij} \quad (61)$$

Assuming $\widehat{C}_L = 1$, C_ν can be determined using a least-square method of Lilly (42)

$$C_\nu = -\frac{L'_{ij}M_{ij}}{2M_{ij}M_{ij}} \quad (62)$$

In the above expression, $L'_{ij} = L_{ij} - \frac{2}{3}\widehat{\rho}k_{test}\delta_{ij}$, and $M_{ij} = \widehat{\rho}\sqrt{k_{test}}\widehat{\Delta}(\langle\tilde{S}_{ij}\rangle - \frac{1}{3}\langle\tilde{S}_{kk}\rangle\delta_{ij})$.

The expression is closed by using the original definition of the Leonard's stress Eq. (60). A similar approach is used to obtain the dissipation coefficient C_ϵ such that:

$$C_\epsilon = \frac{\widehat{\Delta}(\bar{\mu} + \mu_t)}{\widehat{\rho}k_{test}^{3/2}}[\langle\widetilde{T}_{ij}\frac{\partial\tilde{u}_j}{\partial x_i}\rangle - \widehat{T}_{ij}\frac{\partial\widehat{u}_j}{\partial x_i}] \quad (63)$$

where $\mu_t = \bar{\rho}\nu_t$, the tensor \widetilde{T}_{ij} is $[\frac{\partial\tilde{u}_i}{\partial x_j} + \frac{\partial\tilde{u}_j}{\partial x_i} - \frac{2}{3}\frac{\partial\tilde{u}_k}{\partial x_k}\delta_{ij}]$, and \widehat{T}_{ij} is the tensor at the test-filter level.

In general, seven realizability conditions need to be satisfied (92) for a sub-grid scale stress tensor to guarantee a realizable solution. Those conditions are:

$$(1-3) \tau_{ii} \geq 0, \text{ where } i = 1, 2, 3;$$

$$(4-6) |\tau_{ij}| \leq \sqrt{\tau_{ii}\tau_{jj}}, \text{ where } i \neq j;$$

$$(7) \det(\tau_{ij}) \geq 0.$$

The LDKM approach is ensured to satisfy all the realizability conditions (70) at majority of grid points even in complex reacting flows. Subgrid viscous work (H_i^{sgs}) is handled in a similar manner with the subgrid shear/viscous stress terms. Starting from the definition of the total energy ($\tilde{E} = \tilde{e} + \frac{1}{2}\tilde{u}_k\tilde{u}_k + k^{sgs}$), and the thermodynamic relation between the enthalpy and internal energy ($h = e + P/\rho$), (H_i^{sgs}) can be rewritten in the following form

$$H_i^{sgs} = \rho[\widetilde{hu}_i - \tilde{h}\tilde{u}_i] + \rho[\widetilde{u_k u_k u_i} - \widetilde{u_k u_k} \tilde{u}_i] + \rho[\widetilde{k^{sgs} u_i} - \widetilde{k^{sgs}} \tilde{u}_i] \quad (64)$$

This term is usually modeled in combination with the subgrid shear stress (σ_i^{sgs}) as:

$$H_i^{sgs} + \sigma_i^{sgs} = -\rho \frac{\nu_T}{Pr_T} C_p \frac{\partial \tilde{T}}{\partial \tilde{x}_i} + \tau_{i,j}^{sgs} \tilde{u}_i - \left(\rho \frac{\nu_T}{Pr_T} + \mu \right) \frac{\partial k^{sgs}}{\partial x_i} \quad (65)$$

where Pr_T is the turbulent Prandtl number ($Pr_T = 0.6$).

2.2.2 Subgrid Combustion Modeling

The subgrid mass flux, $\phi_{i,k}^{sgs}$, the subgrid diffusive flux $\theta_{i,k}^{sgs}$, and the filtered reaction rate $\bar{\omega}_k$ all require closure as well. However, a closure at the resolved scale (as done for momentum and energy transport) is not appropriate since combustion, heat release, volumetric expansion and small-scale turbulent stirring all occur at the small scales, which are not resolved in a conventional LES approach. To address this important physics, in this thesis work a subgrid combustion model based on the LEM (35) model is used to account for the combustion occurring within the LES cells (called LEMLES, hereafter). With this approach, there is no need to provide explicit closure for ϕ_{jm}^{sgs} , θ_{jm}^{sgs} , and $\bar{\omega}_k$, since a more accurate and exact closure is implemented within the subgrid scales.

LEM is a stochastic, Monte-Carlo simulation of the unsteady scalar field evolution in a turbulent flow. It is based on solving the unsteady reaction-diffusion equation on a one-dimensional domain, and treating the turbulent convection separately at its own time scale. The computational domain is aligned with the direction of the steepest scalar gradient, and the resolution is the smallest turbulent length scale (η), so that it is possible to resolve all length scales ranging from integral length scale (L) to η . The main LEM assumption is that the turbulent field is isotropic and with no boundaries and/or body forces. This simplifies the turbulence representation by using the well-established inertial range and scaling laws (78). Hence, the problem can be treated as a one-dimensional front propagation. In LEM, the molecular diffusion and chemical reaction evolve deterministically (and in an exact manner) from an initial

scalar field by the solution of the thermo-chemical equations. Past studies of stand-alone LEM computations (35; 78; 13) have clearly demonstrated the appropriateness of this model and its ability to capture high Re, Sc, and Da scaling.

Consider the following exact transport equation for the k th scalar Y_k , where there is no spatial filtering:

$$\rho \frac{\partial Y_k}{\partial t} = -\rho[\tilde{u}_i + (u'_i)^R + (u'_i)^S] \frac{\partial Y_k}{\partial x_i} - \frac{\partial}{\partial x_i}(\rho Y_k (V_{i,k} + V_i^C)) + \dot{\omega}_k \quad (66)$$

The convective velocity here is separated into three parts as: $\tilde{u}_i + (u'_i)^R + (u'_i)^S$ that represent respectively, the LES resolved velocity field, the LES resolved subgrid fluctuation (obtained from k^{sgs}), and the unresolved subgrid fluctuation. Using this definition, Eq. (66) can be recast into the following two-step numerical form (49):

$$\rho \frac{\partial Y_k}{\partial t} = -[(\tilde{u}_i + u'_i)^R] \frac{\partial Y_k}{\partial x_i} \quad (67)$$

$$\rho \frac{\partial Y_k}{\partial t} = \rho (u'_i)^S \frac{\partial Y_k}{\partial x_i} + \frac{\partial}{\partial x_i}(\rho Y_k (V_{i,k} - V_i^C)) - \dot{\omega}_k \quad (68)$$

Here, Eqs. (67) and (68) represent large-scale and small-scale processes, respectively. The large-scale step (Eq. 67) advects the subgrid scalar gradient using a 3D Lagrangian process that ensures strict mass conservation and preserves the small-scale scalar structure. Within each LES cell the subgrid scale processes (Eq. (68)) represent respectively, the small-scale turbulent stirring, molecular diffusion and reaction kinetics. Eq. (68) is solved on a 1D line embedded inside each LES cells with a subgrid resolution that is fine enough to resolve the Kolmogorov scale, η . With such a resolution, both molecular diffusion and reaction rate are closed in an exact sense and this is one of the major strengths of the LEMLES strategy. The 1D line is aligned in the flame normal or the maximum scalar gradient direction and thus, does not represent any physical Cartesian direction.

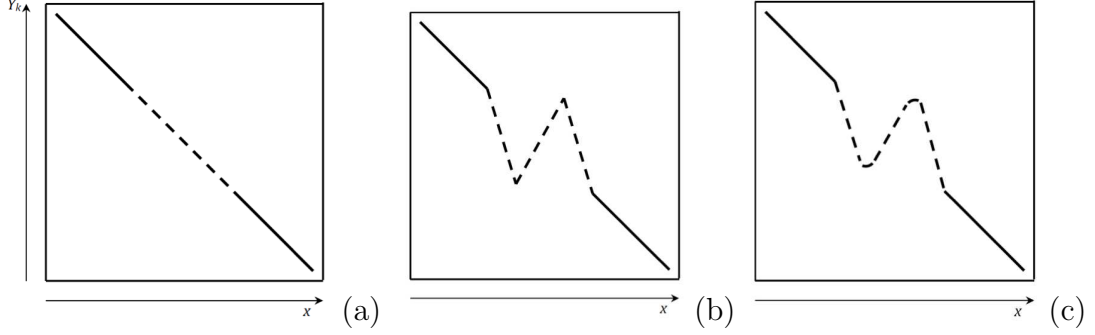


Figure 2: Scalar field evolution with LEM. (a) initial field, (b) after triplet map and (c) after solving the diffusion-reaction equation

Based on this approach, in the LEMLES model (or in the stand-alone LEM solver as well) the following reaction-diffusion equation system is solved on the 1D LEM level:

$$\begin{aligned} \rho \frac{\partial Y_k}{\partial t} &= F_{k, stir} - \frac{\partial}{\partial s} (\rho Y_k (V_{k,s} - V_k^C)) + \dot{\omega}_k \\ \rho C_p \frac{\partial T}{\partial t} &= F_{T, stir} - \rho \frac{\partial T}{\partial s} \left(\sum_{k=1}^{N_s} C_{p,k} Y_k (V_{k,s} - V_s^C) \right) + \frac{\partial}{\partial s} \left(\kappa \frac{\partial T}{\partial s} \right) + \dot{\omega}_T \end{aligned} \quad (69)$$

In the LEMLES, the equation system is solved on 1D LEM lines embedded within each LES cells. In the stand-alone LEM, the 1D LEM line extends through the entire flame in the flame normal direction. In this equation, heat release due to combustion is calculated as $\dot{\omega}_T = -\sum_{k=1}^{N_s} h_k \dot{\omega}_k W_k$. Here, the subgrid field within each LES supergrid is resolved by N_{LEM} number of LEM cells along the local coordinate s , which is aligned in the direction of the steepest gradient.

2.2.2.1 Small Scales: Turbulent Stirring

Within the LEM concept, turbulent stirring is not solved deterministically, but is rather handled explicitly by a numerical analogus using re-arrangement events (*triplet-maps*) (35). This is represented symbolically as $F_{k, stir}$ and $F_{T, stir}$ in Eq. (69). The central assumption behind the stirring model is that the effect of the turbulent eddies

on the scalar field is to stochastically re-distribute the concentration gradients, without changing the scalar values, but by only increasing the scalar gradients. Therefore, for the given initial scalar profile, the turbulent advection increases the gradients by the re-distribution process whereas molecular diffusion competes with it by smoothing out these gradients.

The action of a turbulent eddy on a given hypothetical concentration gradient through triplet map is seen in Fig. 2. Once the location and the length scale for the eddy is selected, the given segment of the concentration gradient is divided into three sub-segments. The gradients in each sub-segment is increased by a factor of three and the middle one is inverted. The final profile is replaced with the original one to finish up the stirring process. Mathematically, applying the above mapping sequence to the segment $[x_o, x_o + l]$ at time t_o , transforms $\psi(x, t_o)$ to $\hat{\psi}(x, t_o)$ according to:

$$\hat{\psi}(x, t_o) = \begin{cases} \psi(3x - 2x_o, t_o) & x_o \leq x \leq x_o + \frac{l}{3} \\ \psi(-3x + 4x_o + 2l, t_o) & x_o + \frac{l}{3} \leq x \leq x_o + \frac{2l}{3} \\ \psi(3x - 2x_o - 2l, t_o) & x_o + \frac{2l}{3} \leq x \leq x_o + l \\ \psi(x, t_o) & otherwise \end{cases} \quad (70)$$

Triplet map implementation necessities the number of LEM cells used in the simulation to be a multiple of three. At the minimum, nine LEM cells are used to resolve one turbulent eddy. Hence, to resolve a Kolmogorov eddy (smallest length scale), the LEM domain resolution should be equal to $\eta/6$.

The location of stirring event is chosen from a uniform distribution and the frequency of stirring is derived from 3D inertial range scaling laws derived from Kolmogorov's hypothesis as (36):

$$\lambda = \frac{54 \nu Re_{\bar{\Delta}} [(\frac{\bar{\Delta}}{\eta})^{\frac{5}{3}} - 1]}{5 C_{\lambda} \bar{\Delta}^3 [1 - (\frac{\eta}{\bar{\Delta}})^{\frac{4}{3}}]} \quad (71)$$

where, $C_{\lambda} = 0.067$ (13). The eddy size (l) is picked randomly from an eddy size distribution $f(l)$ ranging from $\bar{\Delta}$ to η :

$$f(l) = \frac{5}{3} \frac{l^{-\frac{8}{3}}}{\eta^{\frac{5}{3}} - \Delta^{\frac{5}{3}}} \quad (72)$$

where $\eta = N_\eta \bar{\Delta} Re_{\bar{\Delta}}^{-3/4}$, and $Re_{\bar{\Delta}} = u' \Delta / \nu$ is the subgrid Reynolds number.

2.2.2.2 Large Scales: Advection

Once the subgrid evolution has occurred, large-scale advection (Eq. 67) is implemented by a 3D Lagrangian process that determines the amount of mass to be advected and explicitly advecting this amount (and the accompanying subgrid scalar fields) across the LES cell faces. Further details of this process will be outlined in the next chapter.

2.2.2.3 Volumetric Expansion

In LEM, volumetric expansion due to heat release is implemented locally within the subgrid by expanding the LEM domain. Although not required, re-gridding is employed to keep the total number of LEM cells constant throughout the simulation to reduce programmatic complexity. Re-gridding can introduce some numerical diffusion that is shown to be negligible in compressible flow simulations using an explicit time step Δt_{LES} (which is limited by acoustic time scale).

2.3 Artificial Neural Networks

ANN is a highly interconnected computing system made up of a number of processing elements (PEs) connected through uni-communication channels. ANNs can be used to model the relationships between inputs and outputs of a system through a training approach. The ANN code used in the study is based on a back-propagation learning with gradient descent rule (GDR) (16). The back-propagation algorithm is considered much simpler and to require less memory compared to conjugate gradient based algorithms. Its validity has been shown elsewhere (73). The training algorithm basically consists of two parts: (i) forward propagating the input and (ii) backward

propagating the error. For the given ANN architecture, the output of a single neuron i at iteration number k is calculated as:

$$y_i[k] = g(\text{net}_i[k]) \quad (73)$$

for

$$g(z) = (e^z - e^{-z}) / (e^z + e^{-z}) \quad (74)$$

where $g()$ is the hyperbolic-tangent activation function

In Eq. (73), net_i represents the effect of the all PEs that are connected to the PE i . It can be calculated by using the following formula:

$$\text{net}_i[k] = \sum_{m=0}^M W_{im}[k] y_m[k] - b_i[k] \quad (75)$$

Here, $W_{im}[k]$ is the weight coefficient between PEs i and m , $y_m[k]$ is the output of the neuron m , $b_i[k]$ is the internal threshold for the PE i , and M is the number of PEs connected to the PE i . Once the output is calculated for all PEs, the global error ($E[k]$) for the current weight distribution is the difference between the desired (d_i) and the calculated ($y_i[k]$) value at the output layer:

$$E[k] = \frac{1}{2} \sum_{i=1}^I [d_i - y_i[k]]^2 \quad (76)$$

with I denoting number of PEs at the output layer. The error at the output layer is backpropagated to all the previous PEs to calculate the new weight coefficients by using the GDR. This is achieved by adjusting the weights of all connections according to the gradient of the local error across each connection as:

$$W_{i,j}[k+1] = W_{i,j}[k] - \eta \frac{dE[k]}{dW_{i,j}[k]} \quad (77)$$

where η is the global learning coefficient which is constant and same for all PE's and iterations. Thus, the main idea behind gradient descent rule is to find a particular weight distribution among all connections, which would minimize the global error. In a perfect case this would provide $dE[k]/dW_{i,j}[k] = 0$ and the algorithm would

converge. Equation (77) requires calculation of the gradient of the global error with respect to the individual weights. Considering the fact that the error function at the output layer is differentiable, with a help of little algebra, the derivative of the local error with respect to the connection coefficient can be obtained for a connection between the output and a hidden layer as:

$$\frac{dE[k]}{dW_{i,j}[k]} = -[d_i - y_i[k]]g'(net_i[k])y_j[k] \quad (78)$$

and for the rest of the connections as:

$$\frac{dE[k]}{dW_{i,j}[k]} = -[\sum_{m=1}^M \delta_m[k]W_{m,i}[k]]g'(net_i[k])y_j[k] \quad (79)$$

Here, $\delta_m[k]$ is the local error term of the PE m . Its value depends if the PE m is in the output or in one of the hidden layers is given by the following formula

$$\delta_m[k] = \begin{cases} [d_m - y_m[k]]g'(net_m[k]) & \text{if output layer} \\ g'(net_m[k]) \cdot \sum_{z=0}^Z W_{z,m}[k]\delta_z[k] & \text{if hidden layers} \end{cases} \quad (80)$$

There are couple of drawbacks of the standart GDR rule (16). The use of a non-linear activation function leads to a complex error surface topology with respect to the connection weights that has several local minima. Selecting constant model coefficients may lead the GDR to be trapped in one of the local minima. Also, the model coefficients may need to be calibrated for all new cases, and modified during the course of the training to enhance the stability and the convergence. Hence, there is need to change dynamically the model coefficients. To overcome these problems, a new learning algorithm (AGDR) based on the extended delta-bar-delta model has been proposed (76). AGDR essentially uses the following (instead of Equation (77)) to update the weights:

$$W_{i,j}[k+1] = W_{i,j}[k] - \eta_{i,j} \frac{dE[k]}{dW_{i,j}[k]} + \alpha_{i,j} \Delta w_{i,j}[k-1] \quad (81)$$

The proposed model is based on the fact that all PE's have their own model parameters ($\eta_{i,j}$ and $\alpha_{i,j}$) and they are updated at every ANN iterations based on the history

of the global error as

$$\begin{aligned}\eta_{i,j}[k+1] &= \eta_{i,j}[k] + \Delta\eta_{i,j}[k] \\ \alpha_{i,j}[k+1] &= \alpha_{i,j}[k] + \Delta\alpha_{i,j}[k]\end{aligned}\tag{82}$$

with $\Delta\eta_{i,j}[k]$, and $\Delta\alpha_{i,j}[k]$ given as

$$\begin{aligned}\Delta\eta_{i,j}[k] &= \begin{cases} \kappa_1\lambda\eta_{i,j} & \text{if } \phi_{i,j}[k]\bar{\phi}_{i,j}[k-1] > 0 \\ -\kappa_1\lambda\eta_{i,j} & \text{if } \phi_{i,j}[k]\bar{\phi}_{i,j}[k-1] < 0 \\ 0 & \text{if } \phi_{i,j}[k]\bar{\phi}_{i,j}[k-1] = 0 \end{cases} \\ \Delta\alpha_{i,j}[k] &= \begin{cases} \kappa_1\lambda\alpha_{i,j} & \text{if } \phi_{i,j}[k]\bar{\phi}_{i,j}[k-1] > 0 \\ -\kappa_1\lambda\alpha_{i,j} & \text{if } \phi_{i,j}[k]\bar{\phi}_{i,j}[k-1] < 0 \\ 0 & \text{if } \phi_{i,j}[k]\bar{\phi}_{i,j}[k-1] = 0 \end{cases}\end{aligned}\tag{83}$$

Here, $\lambda = (1 - \exp(-\kappa_2\phi_{i,j}[k]))$, $\phi_{i,j}[k] = \frac{\partial E[k]}{\partial W_{i,j}}$, and $\bar{\phi}_{i,j}[k] = (1 - \theta)\phi_{i,j}[k-1] + \theta\phi_{i,j}[k]$. Also, κ_1 and κ_2 are the second-order model coefficients selected to be 0.1 and 0.01, respectively based on numerical studies. In the current study, this new approach (76) is employed for the training process.

Memorization is one of the problems associated with the ANN training, and it needs to be handled in care. The goal of the ANN training is to minimize the global error so that the ANN can provide the correct output when it is asked. It is reported in the literature (16) that the ANNs trained perfectly well on given training data points usually fail to provide answers for the points that they are not trained for. This is called the *generalization* problem and is a direct consequence of data memorization. The ANN training needs to be stopped at an iteration, after which the ANN starts to memorize the training data and loose its generality. Usually this can be avoided by controlling the evolution of the ANN error during the training (16). If the error is not decreasing for consecutive number of iterations, the training is stopped. This approach is used in the current work to ascertain the ANN generality.

There are three key differences between the EDBD (16) and the current model.

The first one is that the model coefficients are increased and decreased by using the same formula so as to avoid any bias that may arise due to the use of a different formulation. The second difference is that the model coefficients are updated only after introducing the whole training table. The batch update as done in the EDBD causes wild oscillations of the model coefficients, since the input output pairs are selected randomly. In the current method, the global error for the whole training table is calculated along with the total change of the weights, so that the $dE[k]/dW_{i,j}[k]$ term is no longer a local but a global quantity. Finally, the third difference is that in the EDBD method momentum coefficient is decreased for $\phi_{i,j}[k]\bar{\phi}_{i,j}[k-1] > 0$, which is directly opposite to our formulation. The argument in the EDBD model for this selection is to increase the numerical stability of the learning algorithm. In our new model, however, the momentum coefficient is increased along with the learning coefficients in order to perform a very quick search in the error space so as to find the closest point to the global minimum. Once the learning algorithm diverges, the code reverts back to the point where the error was minimum and further decreases the model coefficients, so that convergence is stabilized again.

CHAPTER III

NUMERICAL IMPLEMENTATION

3.1 Discretization of the Governing Equations

3.1.1 The Finite Volume Formulation

The LES filtered Navier-Stokes equations are solved with a finite volume scheme. Finite volume is typically employed in CFD applications since it ensures strictly the mass conservation, which is not the case for finite difference methods. The basic idea in the finite volume approach is to solve the governing set of equations in the integral form. The divergence terms in this form are converted into surface integrals. These terms are evaluated as fluxes at the surfaces of each finite volume. Another advantage of finite volume against finite difference is that it can handle skewed grids in a better way.

More specifically, in the finite volume approach, the governing LES filtered Navier-Stokes equations are solved in the following integral form:

$$\frac{\partial}{\partial t} \int_V \mathbf{Q} dV + \oint_A (\mathbf{F} dA_x) = \int_V \mathbf{S} dV \quad (84)$$

where V is the control volume delimited by surface A . For the given control volume, this equation is converted as

$$\vec{Q} + \frac{1}{V} \sum_{i=1}^6 \vec{F} \cdot \vec{A}_i = \vec{S} \quad (85)$$

where, the \sum operator is used to calculate the fluxes across the surfaces (A_i) of the control volume (V). In this equation, \vec{Q} , \vec{F} , \vec{S} represent the conserved variables, flux of \vec{Q} across the cell control surface and the source terms, respectively. The flux vector (\vec{F}) is actually given as the summation of the inviscid flux, viscous flux (\vec{F}_{LS}) and the subgrid flux term (\vec{F}_{sgs}).

Here, \mathbf{Q} is given as:

$$\vec{Q} = \left\{ \begin{array}{c} \bar{\rho} \\ \bar{\rho}\tilde{u} \\ \bar{\rho}\tilde{v} \\ \bar{\rho}\tilde{w} \\ \bar{\rho}\tilde{E} \\ \bar{\rho}k^{sgs} \\ \bar{\rho}\tilde{Y}_m \end{array} \right\} \quad (86)$$

In LES, the flux vector is calculated as the sum of the large scale \vec{F}_{LS} and subgrid scale flux (\vec{F}_{sgs}):

$$F_{x,LS} = \left\{ \begin{array}{c} \bar{\rho}\tilde{u} \\ \bar{\rho}\tilde{u}\tilde{u} + \bar{p} \\ \bar{\rho}\tilde{u}\tilde{v} \\ \bar{\rho}\tilde{u}\tilde{w} \\ \bar{\rho}\tilde{u}(\tilde{E} + \bar{p}) \\ \bar{\rho}\tilde{u}k^{sgs} \\ \bar{\rho}\tilde{u}\tilde{Y}_k \end{array} \right\} - \left\{ \begin{array}{c} 0 \\ \bar{\tau}_{xx} \\ \bar{\tau}_{xy} \\ \bar{\tau}_{xz} \\ \bar{\sigma}_x - \bar{q}_x \\ 0 \\ \bar{\rho}\tilde{Y}_k\tilde{V}_{xk} \end{array} \right\} \quad (87)$$

$$F_{y,LS} = \left\{ \begin{array}{c} \bar{\rho}\tilde{v} \\ \bar{\rho}\tilde{v}\tilde{u} + \bar{p} \\ \bar{\rho}\tilde{v}\tilde{v} \\ \bar{\rho}\tilde{v}\tilde{w} \\ \bar{\rho}\tilde{v}(\tilde{E} + \bar{p}) \\ \bar{\rho}\tilde{v}k^{sgs} \\ \bar{\rho}\tilde{v}\tilde{Y}_k \end{array} \right\} - \left\{ \begin{array}{c} 0 \\ \bar{\tau}_{yx} \\ \bar{\tau}_{yy} \\ \bar{\tau}_{yz} \\ \bar{\sigma}_y - \bar{q}_y \\ 0 \\ \bar{\rho}\tilde{Y}_k\tilde{V}_{yk} \end{array} \right\} \quad (88)$$

$$F_{z,LS} = \left\{ \begin{array}{l} \bar{\rho}\tilde{w} \\ \bar{\rho}\tilde{w}\tilde{u} + \bar{p} \\ \bar{\rho}\tilde{w}\tilde{v} \\ \bar{\rho}\tilde{w}\tilde{w} \\ \bar{\rho}\tilde{w}(\tilde{E} + \bar{p}) \\ \bar{\rho}\tilde{w}k^{sgs} \\ \bar{\rho}\tilde{w}\tilde{Y}_k \end{array} \right\} - \left\{ \begin{array}{l} 0 \\ \bar{\tau}_{zx} \\ \bar{\tau}_{zy} \\ \bar{\tau}_{zz} \\ \bar{\sigma}_z - \bar{q}_z \\ 0 \\ \bar{\rho}\tilde{Y}_k\tilde{V}_{zk} \end{array} \right\} \quad (89)$$

$$F_{x,sgs} = \left\{ \begin{array}{l} 0 \\ \bar{\tau}_{xx}^{sgs} \\ \bar{\tau}_{xy}^{sgs} \\ \bar{\tau}_{xz}^{sgs} \\ -\rho\frac{\nu_T}{Pr_t}(C_p\frac{\partial\tilde{T}}{\partial\tilde{x}} + \frac{\partial\tilde{k}^{sgs}}{\partial\tilde{x}}) + (\tau_{xx}^{sgs} + \tau_{xy}^{sgs} + \tau_{xz}^{sgs})\tilde{u} \\ \frac{\bar{\rho}(\nu+\nu_t)}{Pr_t}\frac{\partial\tilde{k}^{sgs}}{\partial\tilde{x}} \\ \frac{\tilde{W}_k}{W_{mix}}\bar{\rho}D_t\frac{\partial\tilde{X}_k}{\partial\tilde{x}} \end{array} \right\} \quad (90)$$

$$F_{y,sgs} = \left\{ \begin{array}{l} 0 \\ \bar{\tau}_{yx}^{sgs} \\ \bar{\tau}_{yy}^{sgs} \\ \bar{\tau}_{yz}^{sgs} \\ -\rho\frac{\nu_T}{Pr_t}(C_p\frac{\partial\tilde{T}}{\partial\tilde{y}} + \frac{\partial\tilde{k}^{sgs}}{\partial\tilde{y}}) + (\tau_{yx}^{sgs} + \tau_{yy}^{sgs} + \tau_{yz}^{sgs})\tilde{v} \\ \frac{\bar{\rho}(\nu+\nu_t)}{Pr_t}\frac{\partial\tilde{k}^{sgs}}{\partial\tilde{y}} \\ \frac{\tilde{W}_k}{W_{mix}}\bar{\rho}D_t\frac{\partial\tilde{Y}_k}{\partial\tilde{y}} \end{array} \right\} \quad (91)$$

$$F_{z,sgs} = \left\{ \begin{array}{l} 0 \\ \overline{\tau}_{zx}^{sgs} \\ \overline{\tau}_{zy}^{sgs} \\ \overline{\tau}_{zz}^{sgs} \\ -\rho \frac{\nu_T}{Pr_t} (C_p \frac{\partial \tilde{T}}{\partial \tilde{z}} + \frac{\partial k^{sgs}}{\partial x}) + (\tau_{zx}^{sgs} + \tau_{zy}^{sgs} + \tau_{zz}^{sgs}) \tilde{w} \\ \frac{\overline{\rho}(\nu + \nu_t)}{Pr_t} \frac{\partial k^{sgs}}{\partial z} \\ \frac{\overline{W}_k}{W_{mix}} \overline{\rho} D_t \frac{\partial \tilde{Y}_k}{\partial z} \end{array} \right\} \quad (92)$$

Finally, the source terms are:

$$\vec{S} = \left\{ \begin{array}{l} 0 \\ 0 \\ 0 \\ 0 \\ 0 \\ P^{sgs} - D^{sgs} \\ \tilde{\omega}_k \end{array} \right\} \quad (93)$$

3.1.2 Domain Discretization

The numerical simulations presented herein are carried out on structured, three-dimensional, Cartesian grids. In this approach, the physical space (x, y, z) is transformed into a computational space (ξ, η, ζ) of uniform unity length by:

$$\left\{ \begin{array}{l} \frac{\partial}{\partial x} = \xi_x \frac{\partial}{\partial \xi} + \eta_x \frac{\partial}{\partial \eta} + \zeta_x \frac{\partial}{\partial \zeta} \\ \frac{\partial}{\partial y} = \xi_y \frac{\partial}{\partial \xi} + \eta_y \frac{\partial}{\partial \eta} + \zeta_y \frac{\partial}{\partial \zeta} \\ \frac{\partial}{\partial z} = \xi_z \frac{\partial}{\partial \xi} + \eta_z \frac{\partial}{\partial \eta} + \zeta_z \frac{\partial}{\partial \zeta} \end{array} \right. \quad (94)$$

where $\xi_x, \eta_x, \zeta_x, \xi_y, \eta_y, \zeta_y, \xi_z, \eta_z, \zeta_z$ are the grid metrics.

Applying this transformation to the integral form yields the following equation:

$$\int_V \frac{\partial}{\partial t} \mathbf{Q}' dV + \int_V \left(\frac{\partial \mathbf{F}'}{\partial \xi} + \frac{\partial \mathbf{G}'}{\partial \eta} + \frac{\partial \mathbf{H}'}{\partial \zeta} \right) dV = \int_V \Phi dV \quad (95)$$

where:

$$\begin{cases} \mathbf{Q}' = \frac{1}{J} \mathbf{Q} \\ \mathbf{F}' = \frac{1}{J} (\xi_x \mathbf{F} + \xi_y \mathbf{G} + \xi_z \mathbf{H}) \\ \mathbf{G}' = \frac{1}{J} (\eta_x \mathbf{F} + \eta_y \mathbf{G} + \eta_z \mathbf{H}) \\ \mathbf{H}' = \frac{1}{J} (\zeta_x \mathbf{F} + \zeta_y \mathbf{G} + \zeta_z \mathbf{H}) \end{cases} \quad (96)$$

Here, J is the Jacobian of the coordinate transformation:

$$J = \frac{1}{\frac{\partial x}{\partial \xi} \frac{\partial y}{\partial \eta} \frac{\partial z}{\partial \zeta} + \frac{\partial x}{\partial \zeta} \frac{\partial y}{\partial \xi} \frac{\partial z}{\partial \eta} + \frac{\partial x}{\partial \eta} \frac{\partial y}{\partial \zeta} \frac{\partial z}{\partial \xi} - \frac{\partial x}{\partial \xi} \frac{\partial y}{\partial \zeta} \frac{\partial z}{\partial \eta} - \frac{\partial x}{\partial \eta} \frac{\partial y}{\partial \xi} \frac{\partial z}{\partial \zeta} - \frac{\partial x}{\partial \zeta} \frac{\partial y}{\partial \eta} \frac{\partial z}{\partial \xi}} \quad (97)$$

3.1.3 Time Integration

The governing equations are integrated in time by using an explicit scheme. Explicit schemes update the variables at a new time step based on the information of the current step. It is very easy to code and parallelize compared to the implicit schemes. However, the time step size required for the explicit schemes is often almost 4-5 order of magnitude less than that is for the implicit schemes due to the stability issues. This is, however, desired for the current study presented in the thesis, since complex flame physics occur at scales already on the order of $10^{-5} \sim 10^{-9}$ s. It should be noted that the time step size gap between the explicit and implicit schemes is highly dependent on the grid resolution used in the computations. This will be discussed further on the next paragraphs.

A two step, predictor-corrector type of MacCormack time integration scheme is used for the current study. The combination of the two steps leads to a scheme second order in time. In this method, the time integration in the predictor step is achieved as:

$$\vec{Q}^* = \vec{Q}^n + d\vec{Q}^n \Delta t \quad (98)$$

and in the corrector step as:

$$\overrightarrow{Q^{n+1}} = \frac{1}{2} \left[\overrightarrow{Q^n} + \overrightarrow{Q^*} + d\overrightarrow{Q^*} \Delta t \right] \quad (99)$$

In the predictor and corrector steps, the variables are updated as:

$$\overrightarrow{Q^*} = -\Delta t \left[\frac{1}{V} \sum_{i=1}^6 \left(\overrightarrow{F_i^{-,*}} \cdot d\overrightarrow{A}_i \right) - \overrightarrow{S^*} \right] \quad (100)$$

$$\overrightarrow{Q^n} = -\Delta t \left[\frac{1}{V} \sum_{i=1}^6 \left(\overrightarrow{F_i^{+,n}} \cdot d\overrightarrow{A}_i \right) - \overrightarrow{S^n} \right] \quad (101)$$

Here in this formulation, $\overrightarrow{F_i^{+,n}}$ and $\overrightarrow{F_i^{-,*}}$ represent the fluxes at the surface i , at time step n , which are evaluated using a forward and backward difference method, respectively. The alternating is used in order to avoid bias that is a result of using a specific differencing for fluxes at time integration.

The explicit schemes are conditionally stable when the integration time step size is smaller than the time that a sound wave travels between adjacent grid points. This is well the known *Courant – Friedrichs – Lewy* (CFL) condition, which is used as a convergence criteria for certain partial differential equations, such as the Navier-Stokes. Basically the CFL condition reads:

$$\Delta t < CFL \frac{\Delta x}{U_{prop}} \quad (102)$$

where Δx is the grid spacing and the u is the wave propagation speed. The grid spacing in the current implementation is calculated as $V/|d\overrightarrow{A}|$, where V is the volume of the given cell. For the case of Navier-Stokes equations, U_{prop} should include the convective (V_c), acoustic (V_a) and diffusion (V_d) velocities:

$$\begin{aligned} V_c &= u\vec{i} + v\vec{j} + w\vec{k} \\ V_a &= a \\ V_d &= \frac{2\gamma\mu}{\bar{\rho}Pr} \frac{|d\overrightarrow{A}|^2}{V_{i,j,k}} \\ U_{prop} &= v_{tot} = V_a + V_c + V_d \end{aligned} \quad (103)$$

where a is the speed of sound. Hence, the time step size is given as

$$\Delta t = CFL \cdot \min_D \left(\frac{V}{|\vec{d}\vec{A}| \cdot U_{prop}} \right) \quad (104)$$

Here $\min_D(\phi)$ operator calculates the minimum value of the given variable ϕ within the computational domain D . With a little bit of algebra, this expression is transformed into the following final equation:

$$\Delta t = \min_D \left[\frac{CFL}{\frac{|u|}{\Delta x} + \frac{|v|}{\Delta y} + \frac{|w|}{\Delta z} + a \sqrt{\frac{1}{(\Delta x)^2} + \frac{1}{(\Delta y)^2} + \frac{1}{(\Delta z)^2}} + \frac{2\gamma\nu}{\bar{\rho}Pr} \left(\frac{1}{(\Delta x)^2} + \frac{1}{(\Delta y)^2} + \frac{1}{(\Delta z)^2} \right)} \right] \quad (105)$$

3.2 Characteristic Boundary Conditions

Using an explicit time integration scheme with a compressible formulation necessitates the proper description of the wave reflection at the boundaries. It is well known that flow stability and the flame-acoustic interactions highly depend on the accurately handling waves at the boundaries. In the LES, the numerical viscosity is often eliminated, or very low, so that the acoustic waves within the computational domain do not vanish. Thus, the numerical simulations need to consider the acoustic waves at the boundaries and ensure some acoustic conditions such as impedance or amplitude of the incoming wave (63). Also, apart from the wave reflection, another problem is that in most of the cases the number of physical boundary conditions known at the boundaries is less than it should be. Hence, there is a need for a numerical approach which accounts for the wave reflection and provide information for the unknown quantities at the boundaries. The well known characteristic boundary conditions of Poinso and Lele (so-called Navier Stokes characteristic boundary conditions (NSCBC)) (62) are used in this study to answer these problems. This method essentially uses relations based on the analysis of the different waves crossing the domain boundary. This method is an extension of the Euler characteristic boundary conditions (ECBC) (63),

which uses relations derived from the Euler equations. The current approach extends ECBC by including the viscous terms as well.

In the NSCBC method the set of the filtered Navier-Stokes equations are re-written as:

$$\left\{ \begin{array}{l} \frac{\partial \bar{p}}{\partial t} + d_1 + \frac{\partial \bar{p} \tilde{u}_2}{\partial x_2} = 0 \\ \frac{\partial \bar{p} \tilde{u}_1}{\partial t} + \tilde{u}_1 d_1 + \bar{\rho} d_3 + \frac{\partial \bar{p} \tilde{u}_1 \tilde{u}_2}{\partial x_2} + \frac{\partial \bar{p} \tilde{u}_1 \tilde{u}_3}{\partial x_3} = \frac{\partial \tau_{1j}}{\partial x_j} \\ \frac{\partial \bar{p} \tilde{u}_2}{\partial t} + \tilde{u}_2 d_1 + \bar{\rho} d_4 + \frac{\partial \bar{p} \tilde{u}_2 \tilde{u}_2}{\partial x_2} + \frac{\partial \bar{p} \tilde{u}_2 \tilde{u}_3}{\partial x_3} = \frac{\partial \tau_{2j}}{\partial x_j} \\ \frac{\partial \bar{p} \tilde{u}_3}{\partial t} + \tilde{u}_3 d_1 + \bar{\rho} d_5 + \frac{\partial \bar{p} \tilde{u}_3 \tilde{u}_2}{\partial x_2} + \frac{\partial \bar{p} \tilde{u}_3 \tilde{u}_3}{\partial x_3} = \frac{\partial \tau_{3j}}{\partial x_j} \\ \frac{\partial \bar{p} \tilde{E}}{\partial t} + \bar{\rho} \tilde{u}_1 d_3 + \bar{\rho} \tilde{u}_2 d_4 + \bar{\rho} \tilde{u}_3 d_5 + \frac{1}{2} \left(\frac{\partial (\tilde{u}_1 \tilde{u}_1)}{\partial x_1} + \frac{\partial (\tilde{u}_2 \tilde{u}_2)}{\partial x_2} + \frac{\partial (\tilde{u}_3 \tilde{u}_3)}{\partial x_3} \right) \\ + \frac{d_2}{\gamma-1} + \frac{\partial}{\partial x_2} (\bar{\rho} \tilde{E} + \bar{p}) \tilde{u}_2 + \frac{\partial}{\partial x_3} (\bar{\rho} \tilde{E} + \bar{p}) \tilde{u}_3 + \left[\left(\tilde{e} - \frac{a^2}{\gamma(\gamma-1)} \right) d_1 \right] \\ + \sum_{m=1}^N \bar{\rho} d_{6+m} \left[\tilde{e}_m - \frac{\tilde{R}_u \tilde{T}}{MW_m(\gamma-1)} \right] = -\frac{\partial q_j}{\partial x_j} + \frac{\partial (\tilde{u}_i \tilde{\tau}_{ij})}{\partial x_j} \\ \frac{\partial \bar{p} k^{sgs}}{\partial t} + k^{sgs} d_1 + \bar{\rho} d_6 + \frac{\partial (\bar{p} \tilde{u}_2 k^{sgs})}{\partial x_2} + \frac{\partial (\bar{p} \tilde{u}_3 k^{sgs})}{\partial x_3} = \\ \frac{\partial}{\partial x_j} \left(\bar{\rho} \nu_t \frac{\partial k^{sgs}}{\partial x_j} \right) + P^{sgs} - D^{sgs} \\ \frac{\partial \bar{p} \tilde{Y}_m}{\partial t} + \tilde{Y}_m d_1 + \bar{\rho} d_{6+m} + \frac{\partial (\bar{p} \tilde{u}_2 \tilde{Y}_m)}{\partial x_2} + \frac{\partial (\bar{p} \tilde{u}_3 \tilde{Y}_m)}{\partial x_3} = \\ \frac{\partial}{\partial x_j} \left(\bar{\rho} D_m \frac{\partial \tilde{Y}_m}{\partial x_j} \right) + \bar{\rho} \tilde{w}_m, m = 1, N \end{array} \right. \quad (106)$$

where d_i are the various partial derivatives with respect to the $x_1 - th$ direction:

$$\vec{d} = \begin{pmatrix} d_1 \\ d_2 \\ d_3 \\ d_4 \\ d_5 \\ d_6 \\ d_{6+m} \end{pmatrix} = \begin{pmatrix} \frac{\partial \bar{p} \tilde{u}_1}{\partial x_1} \\ \bar{\rho} c^2 \frac{\partial \tilde{u}_1}{\partial x_1} + \tilde{u}_1 \frac{\partial \bar{p}}{\partial x_1} \\ \tilde{u}_1 \frac{\partial \tilde{u}_1}{\partial x_1} + \frac{1}{\bar{\rho}} \frac{\partial \bar{p}}{\partial x_1} \\ \tilde{u}_1 \frac{\partial \tilde{u}_2}{\partial x_1} \\ \tilde{u}_1 \frac{\partial \tilde{u}_3}{\partial x_1} \\ \tilde{u}_1 \frac{\partial k^{sgs}}{\partial x_1} \\ \tilde{u}_1 \frac{\partial \tilde{Y}_m}{\partial x_1} \end{pmatrix} = \begin{pmatrix} \frac{1}{c^2} \left[\mathcal{L} + \frac{1}{2} (\mathcal{L}_5 + \mathcal{L}_1) \right] \\ \frac{1}{2} (\mathcal{L}_5 + \mathcal{L}_1) \\ \frac{1}{2\bar{\rho}c} (\mathcal{L}_5 - \mathcal{L}_1) \\ \mathcal{L}_3 \\ \mathcal{L}_4 \\ \mathcal{L}_6 \\ \mathcal{L}_{6+m} \end{pmatrix} \quad (107)$$

In this formulation \mathcal{L}_i 's represent the characteristic waves amplitude associated with the eigenvalue λ_i :

$$\vec{\lambda} = \begin{pmatrix} \lambda_1 \\ \lambda_2 \\ \lambda_3 \\ \lambda_4 \\ \lambda_5 \\ \lambda_6 \\ \lambda_{6+m} \end{pmatrix} = \begin{pmatrix} \tilde{u}_1 - c \\ \tilde{u}_1 \\ \tilde{u}_1 \\ \tilde{u}_1 \\ \tilde{u}_1 + c \\ \tilde{u}_1 \\ \tilde{u}_1 \end{pmatrix} \quad (108)$$

with c denoting the speed of sound ($c = \sqrt{\gamma \tilde{R}_u \tilde{T}}$). Here, the λ_i 's represent the following:

- λ_1 is the velocity of the positive sound wave;
- λ_2 is the velocity of the entropy wave (convection velocity);
- λ_3 is the velocity of \tilde{u}_2 advection in the x_1 -direction;
- λ_4 is the velocity of \tilde{u}_3 advection in the x_1 -direction;
- λ_5 is the velocity of the negative sound wave;
- λ_6 is the velocity of k^{sgs} advection in the x_1 -direction;
- λ_{6+m} is the velocity of \tilde{Y}_m advection in the x_1 -direction, where m goes from 1 to the number of chemical species considered in the problem. .

The amplitudes of the characteristic waves, \mathcal{L}_i are:

$$\begin{pmatrix} \mathcal{L}_1 \\ \mathcal{L}_2 \\ \mathcal{L}_3 \\ \mathcal{L}_4 \\ \mathcal{L}_5 \\ \mathcal{L}_6 \\ \mathcal{L}_{6+m} \end{pmatrix} = \begin{pmatrix} \lambda_1 \left(\frac{\partial \bar{p}}{\partial x_1} - \bar{\rho} c \frac{\partial \widetilde{u}_1}{\partial x_1} \right) \\ \lambda_2 \left(c^2 \frac{\partial \bar{p}}{\partial x_1} - \frac{\partial \bar{p}}{\partial x_1} \right) \\ \lambda_3 \frac{\partial \widetilde{u}_2}{\partial x_1} \\ \lambda_4 \frac{\partial \widetilde{u}_3}{\partial x_1} \\ \lambda_5 \left(\frac{\partial \bar{p}}{\partial x_1} + \bar{\rho} c \frac{\partial \widetilde{u}_1}{\partial x_1} \right) \\ \lambda_6 \frac{\partial k^{sgs}}{\partial x_1} \\ \lambda_{6+m} \frac{\partial \widetilde{Y}_m}{\partial x_1} \end{pmatrix} \quad (109)$$

From the analysis of the above equations, the Local One-Dimensional Inviscid (*LODI*) relations can be determined (61) and values of the wave amplitude variations in the viscous, three-dimensional Navier-Stokes equations can be inferred:

$$\begin{aligned}
\frac{\partial \bar{p}}{\partial t} + \frac{1}{c^2} \left[\mathcal{L}_2 + \frac{1}{2} (\mathcal{L}_5 + \mathcal{L}_1) \right] &= 0 \\
\frac{\partial \bar{p}}{\partial t} + \frac{1}{2} (\mathcal{L}_5 + \mathcal{L}_1) &= 0 \\
\frac{\partial \widetilde{u}_1}{\partial t} + \frac{1}{2\bar{\rho}c} (\mathcal{L}_5 - \mathcal{L}_1) &= 0 \\
\frac{\partial \widetilde{u}_2}{\partial t} + \mathcal{L}_3 &= 0 \\
\frac{\partial \widetilde{u}_3}{\partial t} + \mathcal{L}_4 &= 0
\end{aligned} \quad (110)$$

Based on the LODI equations (Eq. 110) various types of characteristic boundary conditions can be derived (61). For the purposes of this work, only two such boundary condition types were needed and will be described in the following.

3.2.0.1 Subsonic Inflow Boundary Conditions

For the inflow, the gas density is computed based on the flow information, while all other values are specified. The inflow boundary condition employed in this study required the a-priori specification of the velocity components, u_1 , u_2 and u_3 as well as of the inflow temperature T and pressure, p and of the chemical composition of the incoming fluid, Y_m . For a subsonic, three dimensional, N -species reacting flow,

$5 + N$ characteristic waves, $\mathcal{L}_2, \mathcal{L}_3, \mathcal{L}_4, \mathcal{L}_5, \mathcal{L}_6$ and \mathcal{L}_{6+N} enter the domain and \mathcal{L}_1 leaves the domain at $\lambda_1 = u_1 - c$.

Since u_1, u_2, u_3, T and Y_m are known at the inflow, the second, third and fourth relation from Eq. 106 become irrelevant and can be discarded. The characteristic boundary condition determines the temporal change in the incoming fluid density, ρ as follows:

Using the known quantities mentioned earlier, the wave amplitudes can be determined:

$$\mathcal{L}_1 = (u_1 - c) \left(\frac{\partial \bar{p}}{\partial x_1} - \bar{\rho} c \frac{\partial \tilde{u}_1}{\partial x_1} \right) \quad (111)$$

$$\mathcal{L}_5 = \mathcal{L}_1 - \frac{1}{2} \bar{\rho} c \frac{\partial \tilde{u}_1}{\partial t} \quad (112)$$

$$\mathcal{L}_2 = \frac{1}{2} (\gamma - 1) (\mathcal{L}_5 + \mathcal{L}_1) + c^2 \frac{\partial \bar{p}}{\partial t} \quad (113)$$

where

$$\frac{\partial \bar{p}}{\partial t} = \frac{\bar{\rho}}{\bar{T}} \frac{\partial \tilde{T}}{\partial t} \quad (114)$$

Finally, d_1 can be now determined as:

$$d_1 = \frac{1}{c^2} \left[\mathcal{L}_2 + \frac{1}{2} (\mathcal{L}_1 + \mathcal{L}_5) \right] \quad (115)$$

and:

$$d\bar{p} = -d_1 * \Delta t \quad (116)$$

3.2.0.2 Partially Reflecting Subsonic Outflow

At the outflow, second order accurate, partially reflecting conditions are enforced by allowing a pressure wave coming from downstream to enter the computational domain. For the conditions of this study, the pressure is imposed downstream of the outflow, as p_∞ . Using this, the amplitude variation of in going wave, \mathcal{L}_1 , can be

determined. Thus, if the current outflow pressure \bar{p} is different from p_∞ , reflected waves will enter the domain to bring the pressure back to p_∞ . Therefore:

$$\mathcal{L}_1 = \beta(\bar{p} - p_\infty) \quad (117)$$

where:

$$\beta = \sigma(1 - \mathcal{M}^2) \frac{c}{L} \quad (118)$$

and \mathcal{M} is the maximum Mach number in the flow, L is a characteristic length scale chosen in this study to be equal to the length of the computational domain and σ is the reflection coefficient chosen for this study to be 0.15 (62).

3.3 Linear Eddy Mixing Model Implementation

3.3.1 The Reaction Diffusion Equation

The reaction-diffusion equation introduced in the previous chapter (see Eq. 69) is solved with an explicit scheme. The time integration is achieved by using an operator splitting technique, which is based on identifying the different physical process and updating the given scalar field separately with respect to the time scale of the each individual process. Basically there exists four distinct physical processes and time scales in the LEM subgrid model. These are namely, the molecular diffusion, chemistry, and thermal expansion, turbulent stirring.

The diffusion time step is calculated as:

$$\Delta t_{diff} = C_{diff} \frac{\Delta s^2}{\max(D_k)} \quad (119)$$

The minimum of the D_k is selected to calculate the Δt_{diff} in order to ascertain the stability of the diffusion process for the lightest species. The C_{diff} in the equation is a model constant, set here to 0.25 for reasons of numerical stability (69). For mixture averaged formulation, Δt_{diff} is typically the largest time scale among all physical processes considered here. For multi-component diffusion formulation, however, this

value can be as small as the chemical time scale, which increases the number of diffusion sub-iterations beyond its practical limit.

The chemical time step size is determined with the stiffness of the reduced mechanism used in the computations. The stiffness increases as the number of radical species in a chemical kinetics mechanism increases. It is well known that the chemical time step size varies typically in a range of 10^{-2} to 10^{-10} , with the largest being NO production and the smallest as the radical recombination (86). In the current LEM implementation the chemistry is integrated for the given time step size of Δt_{diff} . A stiff ODE solver, which uses adaptive time step size is employed for the integration process so that each different chemical processes are resolved in their respective time scales. This approach, nevertheless, is very time consuming, and the current thesis is providing discussion for implementing ANN based modeling for chemistry integration. This will be further discussed on the coming chapters.

The thermal expansion time scale is associated with the volumetric expansion induced by the increase in temperature through chemical heat release. In the current implementation it is assumed that, the heat release in the fast chemistry limit is controlled by the molecular mixing (69), therefore:

$$\Delta t_{expansion} = \Delta t_{diffusion} \quad (120)$$

The turbulent stirring, which is mimicked using *triplet-maps* is implemented as discrete time events within the given chemistry-diffusion time integration. The time step size between each triplet map is calculated as:

$$\tau_{stir}(x) = \frac{1}{\lambda \Delta} \quad (121)$$

where λ is the turbulent stirring frequency, given by Eq. 71.

To sum up with the integration process, for the given diffusion time step size the chemistry is integrated. Then, the diffusion equation is solved for the species

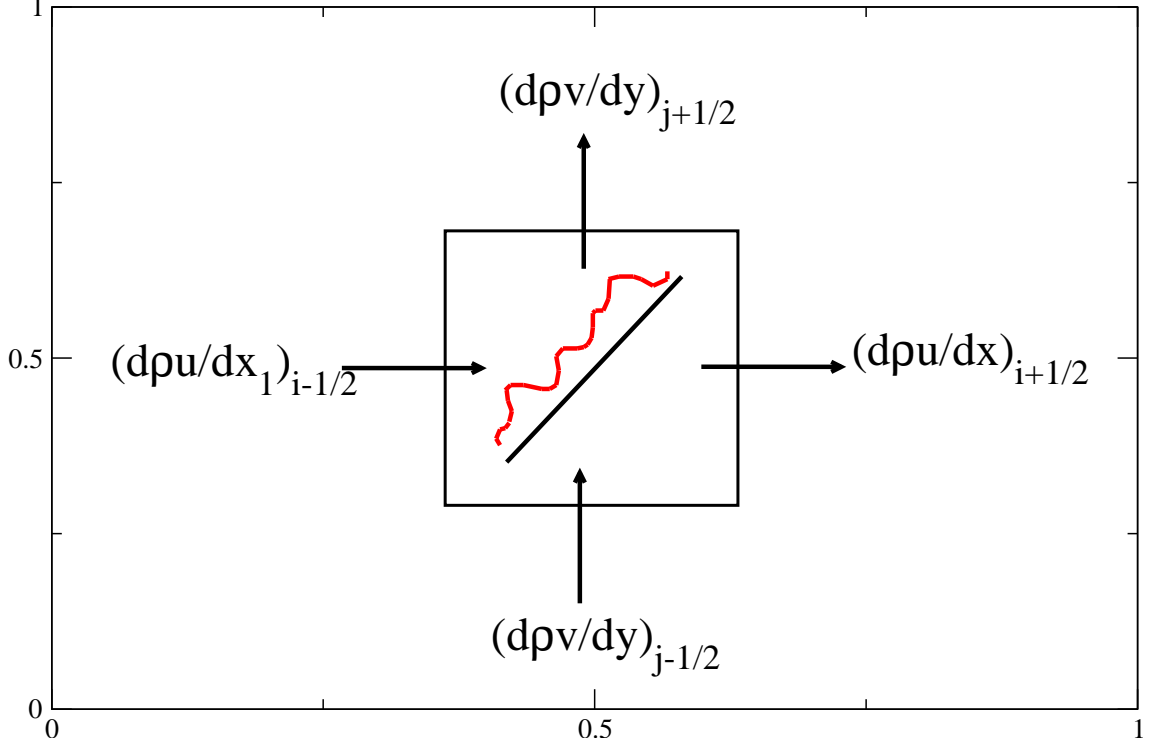


Figure 3: Scalar field on the LEM level and LES cell fluxes for a hypothetical example

and temperature equations. This process is repeated until the total diffusion time equals to the LES time step size coming from the CFL condition. The turbulent stirring, on the other hand, is performed as discrete number of events by interrupting the time integration of the diffusion-reaction equation at a time step size of Δt_{stir} . Overall, for the given LES time step size, the number of stirrings events equal to $N_{stir} = \Delta t_{LES}/\Delta t_{stir}$.

3.3.2 The Splicing Algorithm

The large scale advection is implemented in a Lagrangian sense with the splicing algorithm. Once the subgrid evolution of the scalar field as a result of the turbulent stirring, diffusion, reaction and thermal expansion is achieved, the splicing algorithm is used to advect the scalar field between the LES cells. The advection, from a computational point of view is implemented as carrying partial LEM cells between

the adjacent LES cells by the fluxes at the interfaces. The current splicing algorithm works based on the following rules:

- Splicing is done once in every spatial direction.
- Splicing is performed using an upwind scheme.
- The absolute value and the sign of the term $\frac{\partial \bar{\rho} \tilde{u}_i}{\partial x_i}$ determines the order in which splicing is performed. The largest negative flux will be the first one to exit the LES cell, while the largest positive flux will be the last one to enter the LES cell.

Let's look at a hypothetical 2D example, as illustrated in Fig. 58, and assume the following order between the magnitudes of the face fluxes:

$$\left. \frac{\partial \bar{\rho} \tilde{u}}{\partial x} \right|_{(i-\frac{1}{2})} < \left. \frac{\partial \bar{\rho} \tilde{u}}{\partial x} \right|_{(i+\frac{1}{2})} < 0 < \left. \frac{\partial \bar{\rho} \tilde{v}}{\partial y} \right|_{(j-\frac{1}{2})} < \left. \frac{\partial \bar{\rho} \tilde{v}}{\partial y} \right|_{(j+\frac{1}{2})} \quad (122)$$

Based on this assumption, the volume which needs to be transferred between the adjacent LES cells (δm) is calculated as:

$$\begin{aligned} \frac{1}{\delta t_{LES}} \frac{\delta m_1}{V^{LES}} &= F_i^0 = \left. \frac{\partial \bar{\rho} \tilde{u}}{\partial x} \right|_{(i-\frac{1}{2})} \\ \frac{1}{\delta t_{LES}} \frac{\delta m_2}{V^{LES}} &= F_i^1 = \left. \frac{\partial \bar{\rho} \tilde{u}}{\partial x} \right|_{(i+\frac{1}{2})} \\ \frac{1}{\delta t_{LES}} \frac{\delta m_3}{V^{LES}} &= F_j^0 = \left. \frac{\partial \bar{\rho} \tilde{u}}{\partial y} \right|_{(j-\frac{1}{2})} \\ \frac{1}{\delta t_{LES}} \frac{\delta m_4}{V^{LES}} &= F_j^1 = \left. \frac{\partial \bar{\rho} \tilde{u}}{\partial y} \right|_{(j+\frac{1}{2})} \end{aligned} \quad (123)$$

In this case, δm kg from the donor LEM cell is transferred to the receiver. Here it should be noted that the cell fluxes ($\partial \bar{\rho} \tilde{u}_i / \partial x_j$) contains the splicing information due to the mean flow. However, as it was given in Eq. 67, the large scale advection is a result of both the resolved large scale (\tilde{u}_i) and the modeled subgrid scale velocities

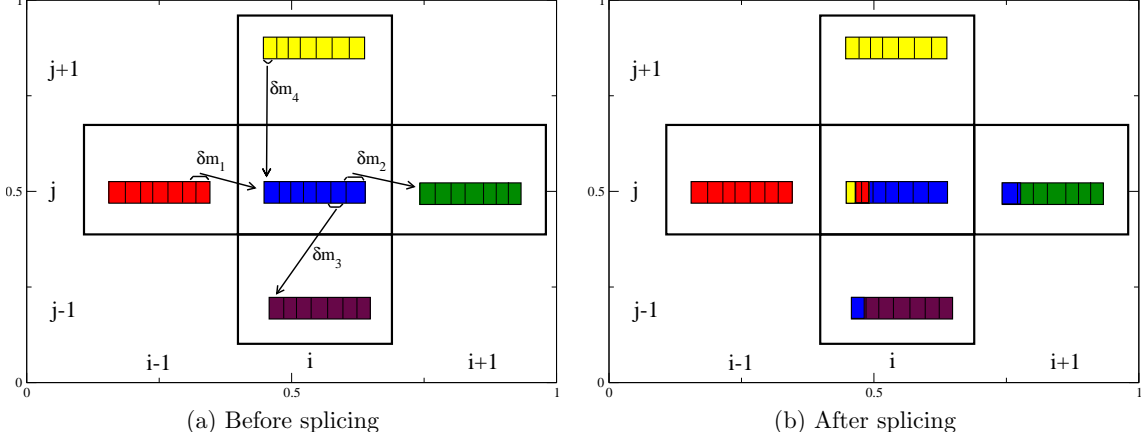


Figure 4: Species field before and after the splicing of the cell (i,j)

$((u'_i)^R)$. In the current implementation, based on the assumption that the velocity field is isotropic on the small scales, $(u'_i)^R$ is calculated as in the following form:

$$(u'_i)^R = \sqrt{\frac{2}{3}k_{sgs}} \quad (124)$$

In this formulation, it should be noted that unlike \tilde{u}_i , the direction of $(u'_i)^R$ is not known. Thus, the flux arising due to the $(u'_i)^R$ is added to the large scale flux by selecting the direction randomly. Since for most of the cases \tilde{u}_i is much larger than $(u'_i)^R$, the error made by selecting the direction randomly is not considered to be huge.

Once all the mass is transferred between the LES cells, the resulting LEM cells have more number of cells than that it had before the splicing started as shown in Fig. 4. Also, the volume of the cells are different from each other based on the transferred mass. Re-gridding is applied to uniformly divide all the mass between LEM cells. This process, apparently, results in an artificial diffusion for the advection, which is purely numerical and undesired. Earlier studies on this issue has concluded that this numerical diffusion is negligible when the LES time step size (thus, the spliced mass) is getting smaller.

CHAPTER IV

ANN VALIDATION

An ANN code which uses the formulation on Section 2.3 is developed within the context of this thesis work. The validation studies of this code is presented in the current chapter.

4.1 A-priori Testing of the GDR and AGDR

An activation function is used in the ANN formulation to calculate the output of the given processing element based on its input. The most simplistic activation function that can be selected to be used is the step function. Essentially, as it was explained in Section 2.3, the backpropagation algorithm searches for the minimum of the local error function with respect to the weight distribution. This requires that the activation function that is used on the training algorithm must be differentiable and continuous within its output range. The sigmoid and tangent hyperbolic activation functions satisfy these conditions and are used extensively in the ANN computations (53). Essentially the tangent hyperbolic activation function is the scaled version of the sigmoid function. The tangent hyperbolic has a much wider output range compared to the sigmoid ($[-1,+1]$ against $[0,+1]$), which makes it more sensitive to the changes in the input/output pairs, and hence, is used in the current study.

The fact that the activation function is differentiable and continuous poses another problem: The error surface topology is quite complex with several local minima and maxima (67). The backpropagation algorithm with the GDR can be captured in one of these local minima, after which the code ceases to update the weight coefficients. This is illustrated in Fig. 5 (a)-(c) for a hypothetical error surface, which varies with

respect to the W as in the following form:

$$\left\{ \begin{array}{ll} E(W) = -0.02W + 0.02\frac{\pi}{4} + \text{Cos}(\frac{\pi}{4}) & W < \frac{\pi}{4} \\ E(W) = \text{Cos}(W) & \frac{\pi}{4} \leq W < 2\pi \\ E(W) = 2\text{Cos}(W) - 1 & 2\pi \leq W < 4\pi \\ E(W) = 0.5\text{Cos}(W) + 0.5 & 4\pi \leq W < 6\pi \\ E(W) = 4\text{Cos}(W) - 3 & 6\pi \leq W < 8\pi \\ E(W) = \text{Cos}(W) & 8\pi \leq W < \frac{53\pi}{4} \\ E(W) = 0.02W - \frac{0.02 \times 53\pi}{4} + \text{Cos}(\frac{53\pi}{4}) & \end{array} \right. \quad (125)$$

Here W is the weight coefficient. Starting from an initial value of $W = \pi/4$, the GDR is tested to find the global minimum located at approximately $W = 7\pi$. As seen in the figure, the GDR is trapped in the first local minimum. This is mainly because of the way GDR updates the the weight coefficients:

$$W[k + 1] = W[k] - \eta \frac{dE[k]}{dW[k]} \quad (126)$$

In this formulation, whenever the GDR leads W to a local minimum, the gradient becomes zero ($dE[k]/dW[k] = 0$), and the algorithm stops updating W . This problem can be solved by using a momentum term to update W in the following form:

$$W[k + 1] = W[k] - \eta \frac{dE[k]}{dW[k]} + \alpha \Delta W[k - 1] \quad (127)$$

with

$$\Delta W[k - 1] = -\eta \frac{dE[k - 1]}{dW[k - 1]} + \alpha \Delta W[k - 2] \quad (128)$$

where $\Delta W[k - 1]$ is the last update applied on the W by the GDR. In this manner, even if a local minimum is encountered, the algorithm continues on updating the W . It should be noted that the addition of a momentum term does not guarantee the convergence of the algorithm. It may (or may not) converge depending on the values of the model coefficients, the learning rate (η) and the momentum coefficient (α). This is illustrated in Figs 5 (b) and (c) for the same hypothetical example as in Fig

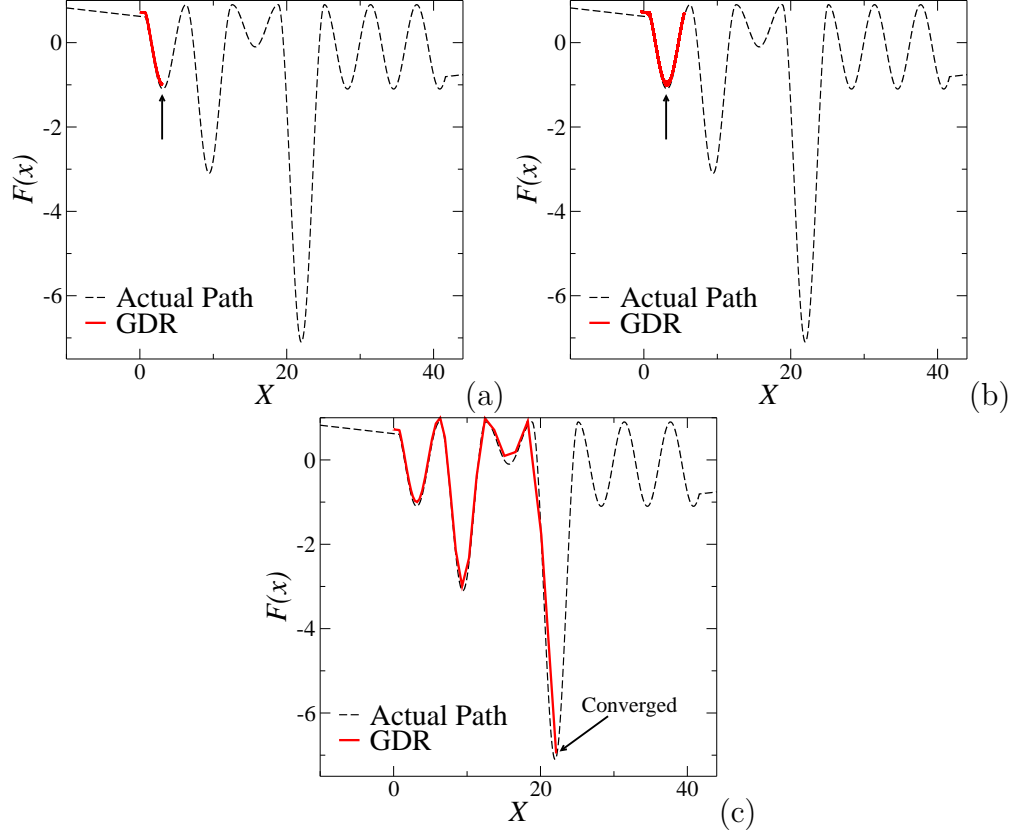


Figure 5: Testing GDR on a hypothetical example. (a) $\alpha = 0$, (b) $\alpha = 1$ and (c) $\alpha = 2$

5 (a). This time, the computations are repeated by using the momentum term. In Fig 5 (b), a momentum coefficient of 1 ($\alpha = 1$) is used for the calculations. Although the results seem to pass beyond the first local minimum, it eventually turns back and converges at $W = \pi$ similar to the no-momentum case. For $\alpha = 2$ case, however, as shown in Fig. 5 (c), the momentum is strong enough and surpasses the $-\eta(dE/dW)$ term, so that the peak value at 2π is passed and the global minimum can be found.

The original GDR method with the momentum term uses constant model coefficients: η and α are selected before the computations are started. As demonstrated on Figs 5 (a)-(c) for the hypothetical example considered here, based on the value of the momentum coefficient the algorithm may be trapped in a local minimum, or can converge to the global minimum. To overcome this difficulty, in the current thesis

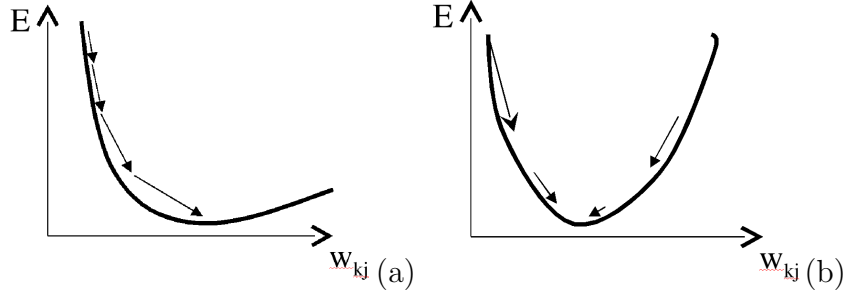
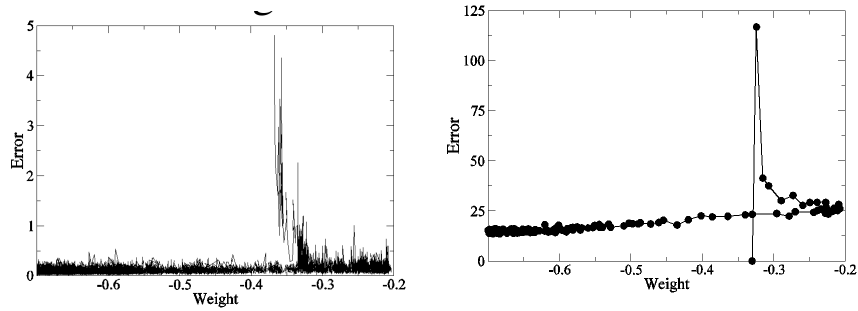


Figure 6: Variation of the step size with the AGDR method for a case with (a) the same sign and (b) alternating sign of the error gradient for consecutive iterations.



(a) Update model coefficients at ev- (b) Update model coefficients after in-ery iteration by using the EDBD rule producing the whole training dataset by using the AGDR

Figure 7: Variation of the global error with respect to the ANN iterations.

work an adaptive GDR (AGDR) method which works based on non-constant model coefficients (α, η) is developed. In this new model, the model coefficients are updated during the training process, by using the formulation introduced on Section 2.3. The effect of this approach is demonstrated in Fig. 6 schematically on a hypothetical example. Lets assume that the gradient of the local error with respect to the weight is having the same sign for consecutive iterations, which means that a minimum value is approached from one side. In this case both $\eta_{i,j}$ and $\alpha_{i,j}$ are increased to reach into the minimum point with fewer number of iterations than the standard GDR. However, if the gradient is alternating for consecutive iterations, then the GDR with constant coefficients would oscillate around this point and may not be able to converge properly at all if the initial model coefficients are large. The model coefficients

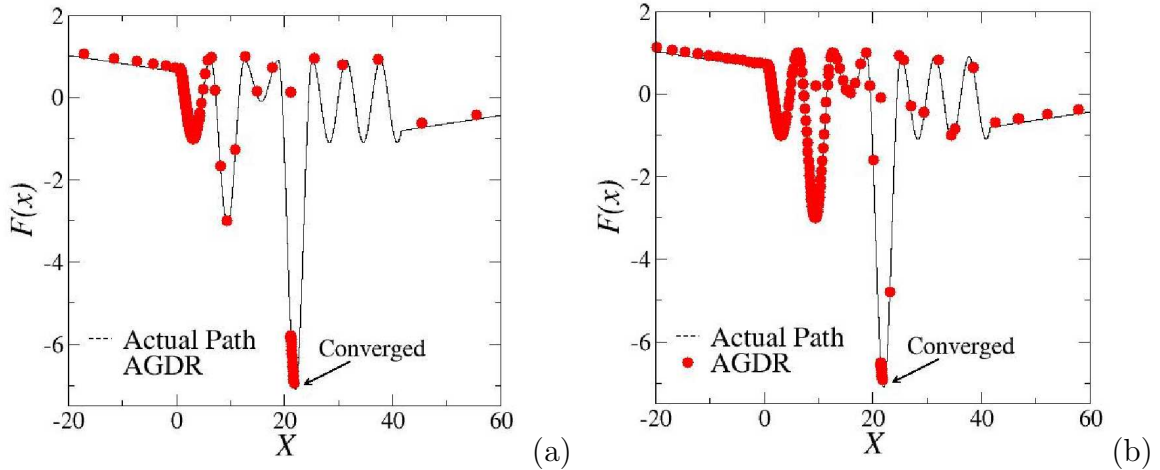


Figure 8: Testing AGDR on a hypothetical example. (a) $\alpha_{init} = 1$, and (b) $\alpha_{init} = 2$

in this case are decreased by the new rule, so as to enhance the convergence rate.

The new rule in general is similar to the EDBD rule (53). However, the way the coefficients are manipulated are different for both of the methodologies (see Eq. (83)). Also, the EDBD rule relies on updating the model coefficients after introducing each batch of input/output pairs. This is actually not a very efficient way. As shown in Fig. 7 (a), the error calculated for each batch highly oscillates during the training process. Thus, the error gradient with respect to the weight is also changing, which leads to wild oscillation of the model coefficients as well. In the new proposed algorithm, compared to the EDBD, the model coefficients are updated after introducing the whole training dataset, as shown in Fig. 7 (b). In this manner, the general trend can be captured in a better way, since the previous and current $\partial E/\partial W$ terms are actually more correlated.

The performance of the new model against the GDR is tested by a Sinus function. Starting from the same point and by using the same initial values of the model coefficients and weights, the GDR required 180 iterations to converge, where as the new rule converged only in 28 iterations.

For completeness, the performance of AGDR) on the same hypothetical example

used to test GDR is demonstrated next. The computations are started at $\pi/4$ similar to the previous case. The current run with AGDR uses the momentum coefficient by default, and its initial value is selected to be 1 ($\alpha = 1$). The GDR using the same momentum coefficient was demonstrated to be captured in a local minimum in Fig. 5 (b). With the AGDR method, however, the current computation can successfully wind the global minimum as shown in Fig. 8 (a). Here it should be noted that, the AGDR method is not as stable as the GDR. The model coefficients may grow beyond some value which may lead the weights to be unbounded. In this case, the model can never converge to a state but would oscillate. This is prevented by using *save-best* and *store* options. During the training, if a particular distribution of the weights and model coefficients correspond to an error less than that was obtained in the previous iterations, these ANN parameters are saved. Later, once the weights start to oscillate unboundedly, or if the error cannot be decreased for some number of iterations, the ANN parameters revert back to the last saved best result, and the model coefficients are decreased by a factor of two. In this manner, the algorithm starts from an initial point, performs a very quick sweep over all possible states, finds the position of the global minimum roughly, and saves the weight coefficients. Once the AGDR starts to oscillate, the code turns back to the point with minimum value of the error and continues with much finer step sizes. This is ensured by effectively decreasing the model coefficients. This process can be seen in Fig. 8 (a). Here, the AGDR method accesses values of X ranging from -20 to 60. Once the X starts to grow unboundedly, then the algorithm turns back to the point where $F(X)$ (which is representative of E for this case) is minimum. Then, the AGDR converges to the global minimum with small step sizes. This can be seen around $X = 20$. As the initial value of the momentum coefficient is increased to 2 ($\alpha = 2$), there is not much difference on the results as given in Fig. 8 (b).

Finally, the number of iterations required for convergence based on the initial

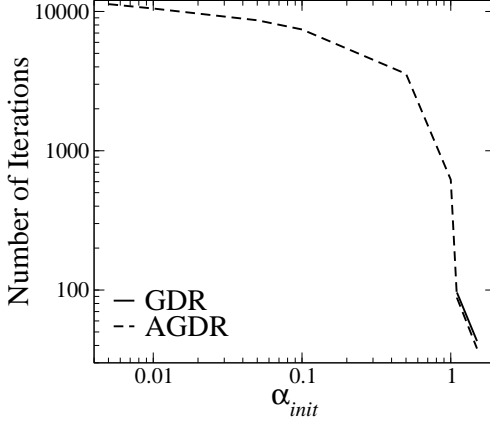
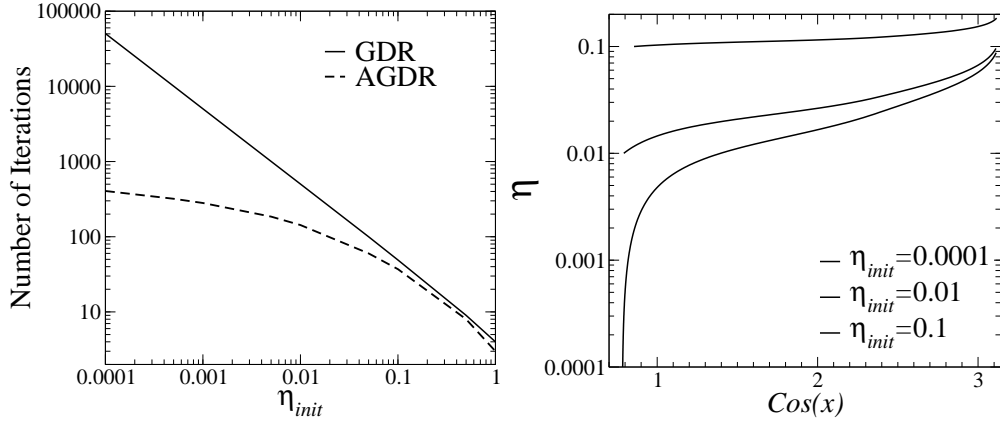


Figure 9: Number of iterations required for convergence based on the initial value of the momentum coefficient.

value of the momentum coefficient is given in Fig. 9. In consistent with our previous results, the GDR fails to converge for $\alpha_{init} < 1.1$. The AGDR can converge for even smaller values of the momentum coefficient. As seen in the graph, for $\alpha_{init} = 0.0001$, the number of iterations required for the AGDR method to converge is almost 10000. This value decreases as the α_{init} is increased for AGDR.

The evolution of the model coefficients are further tested for a second, and much simpler, hypothetical error surface topology, which changes as $E(W) = Cos(W)$. The reason for selecting a simpler function is to let GDR converge too, so that a better comparison can be obtained on a much wider range of model coefficients than it is shown in Fig. 9. The results obtained for this case are presented in Figs 10 (a)-(b). Here, the computations are started by using different initial values of the learning coefficients (η_{init}). Both GDR and AGDR are used for calculations to compare the number of iterations required for convergence. It is well known that for an initially very small η_{init} , the GDR converges in more number of iterations compared to a case with a higher value of η_{init} . This is because the η_{init} sets the step size that is used to update the weight coefficient. The AGDR, however, increases the step sizes substantially, which leads to a faster convergence. This can be seen in Fig 10 (a),



(a) Variation of the number of iterations (b) The evolution of the learning rate co- with respect to the initial value of the efficient during the ANN learning phase. learning rate coefficient.

Figure 10: AGDR method.

where the number of iterations required for convergence is plotted with respect to the η_{init} . For both GDR and AGDR the convergence is faster if η_{init} is high. Also, at relatively higher values of η_{init} (i.e. $\eta_{init} > 0.1$) the number of iterations required for the convergence is almost identical for both GDR and AGDR. The difference starts when η_{init} is getting much smaller than 0.1. As given on the figure, the AGDR can converge in 400 number of iterations at $\eta_{init} = 0.0001$, whereas GDR needs at least 40000 iterations, which is 100 times more than that is required for the AGDR. It is also interesting to note that the number of iterations required for convergence varies linearly with respect to the η_{init} for the GDR.

The variation of the η obtained by the AGDR as a function of the value of the error (which is already defined as $\text{Cos}(x)$) is given in Fig. 10 (b). As it is seen in the figure, the AGDR method increases the value of η substantially. Independent of the value of η_{init} , they all tend to attain values close to 0.1. The increase in η is more pronounced at $\text{Cos}(x) < 1$, since in this range the error surface gradient (dE/dW) is higher than that is $\text{Cos}(x) > 1$.

4.2 *Validating the ANN Training Code on Generic Functions*

The validity of the ANN training code is tested on a simple function. This is an important step which proves that the ANN code is working fine and can be used as a tool for chemical kinetics calculations. The function of interest is:

$$f(x) = \exp[-(x - 1)^2] + \exp[-(x + 1)^2] \quad (129)$$

which is a typical benchmark problem used in the literature for ANN validation (16; 17). The ANN training table has nine entries, Once the training is achieved, the ANN is used to predict the states that it was not trained for. Also, the points outside the training database are used to evaluate the ANN prediction capability further. The results are given in Fig. 11 (a)-(b). In ANN computations the training is achieved usually on a normalized set of variables so as to match the input/output space of the physical process with that of the ANN training function. For this study, the normalization is always achieved between [+1, -1], and the ANN output is between [+0.8, -0.8]. The actual value is later achieved by using a simple transformation. The results shown in Fig. 11 (a)-(b) represents the untransformed results.

Fig. 11 (a) shows the results obtained by using the GDR rule. The predictions obtained by using different ANN architectures is given in the figure. The smallest ANN architecture, with one hidden layer and 10 PEs (1/10/1), can predict the general trend of the function. However, the two peaks located at approximately $x = \pm 0.3$ cannot be detected. An increase in the number of PEs from 10 to 20 (1/20/1) leads to better predictions. After this, however, the ANN predictions seem to be insensitive to the increases in the number of PEs and hidden layers, and the tested ANNs more or less provide the same answer. The ANN predictions for the same function obtained by using AGDR is given in Fig. 11 (b). Similar to that was observed for GDR in Fig. 11 (a), the AGDR results obtained for 1/10/1 ANN architecture cannot capture the peaks. Interestingly for the AGDR results, however, as the number of PEs and

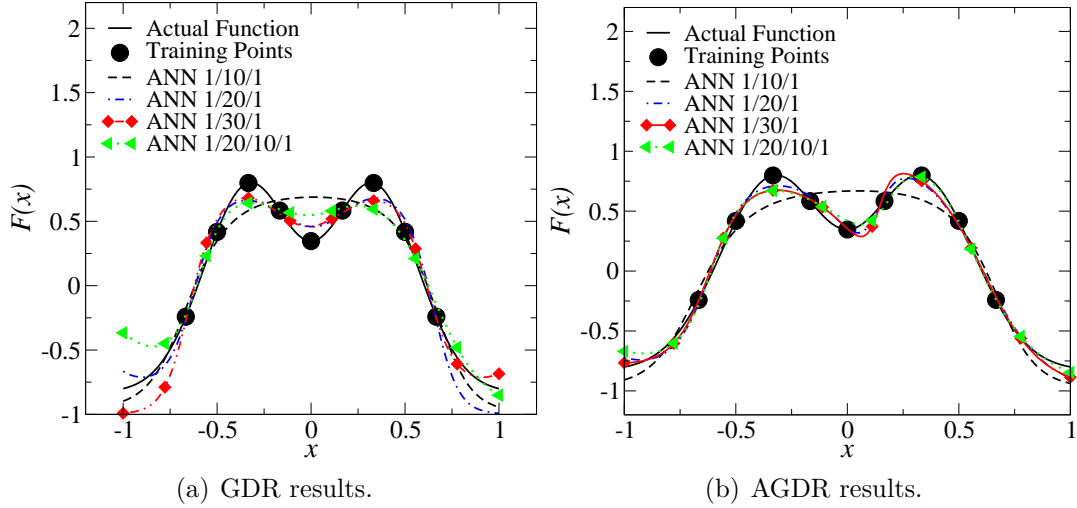


Figure 11: Function prediction by the GDR and AGDR methods.

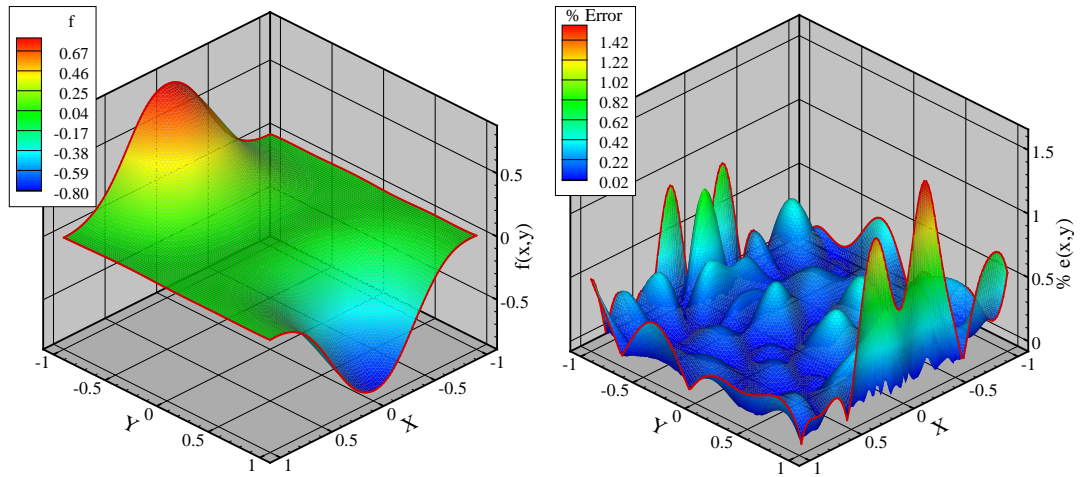
hidden layers are increased the ANN predictions differ, which is in contrast to the GDR. Another interesting observation is that, although more precise in predicting the actual value of the function on the training points, the AGDR results exhibits an asymmetric profile. Overall, the rms error obtained by the AGDR training is much better than that is obtained by the GDR.

The second function used for validating the current ANN approach is:

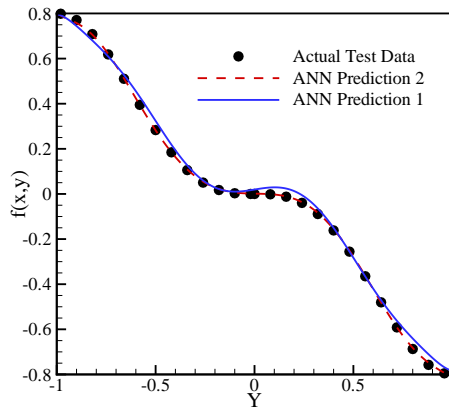
$$f(x, y) = \text{Sin}(\pi x)^3 \cdot \text{Cos}(\pi y)^3 \quad (130)$$

The ANN training is achieved by using two different training files. First training file is constructed by 100 points, 10 in x and 10 in y , where as the second one is for 2500 points, with 50 points for each variable. The ANN architecture comprises of 3 hidden layers with 15, 10 and 4 PEs at each layer. This specific distribution is achieved by experimenting over different architectures and checking the performance with the maximum root mean square (RMS) error. The AGDR is used for the training procedure. The trained nets are used later to predict the function at locations for which it was not trained and the surface that is calculated with ANN is given in Fig. 12 (a) for the net trained for 2500 points. Here, the general topology seems to be

accurately captured by the ANN without any significant errors. The absolute error surface, as seen in Fig. 12 (b) exhibits maximum values corresponding to the regions where the function reaches into its peak. For the rest of the regions, the error seem to be acceptable with a maximum value of 0.42 %. Fig. 12 (c) shows the variation of the actual data and ANN predictions on a cross section taken in a x constant plane. As it can be clearly seen in the figure, the net trained for 100 points fails to predict the exact profile especially on the center region where it should be flat. The other net that is trained for 2500 points, on the other hand, is very accurate and follows the correct profile in a better way.



(a) Surface plot of the prediction obtained by ANN (b) Error surface between the ANN prediction and the actual data



(c) Effect of the number of training data on predictions

Figure 12: Validation of the ANN code on a simple test function

CHAPTER V

EVALUATION OF DIFFERENT TABULATION STRATEGIES FOR ANN TRAINING

The objective of the current chapter is to propose different tabulation strategies for the chemical kinetics relevant to the LES of reactive flow applications, and use them in connection with the ANN methodology to achieve both computational speed-up and memory savings. The focus here is to use ANN for predicting the instantaneous (unfiltered) reaction rates. Hence, this methodology is applicable to laminar flames, DNS, CMCLES, LEMLES, and PDF transport method computations. It cannot be used to predict filtered reaction rates, which is needed when a conventional filtered species conservation equation is solved on the LES level. This will be investigated on the next chapters. Here, basically three different tabulation methodologies are proposed and used in connection with the ANN. These are: ANN trained on (i) laminar flames (Section 6.3), (ii) laminar flame-vortex interaction (Section 5.2) and (iii) laminar flame-turbulence interaction (Section 5.3). The proposed tabulation strategies are tested mostly on the LES of premixed flame-turbulence-vortex interaction computations. As a first step in evaluating the applicability of the ANN approach for non-premixed flames the last section provides *a-priori* testing of the proposed tabulation on stand-alone LEM computations as well, but, this will be investigated in more details on the next chapter.

5.1 ANN Trained on Laminar Flames

5.1.1 Laminar Premixed Flame Computation

Applicability of the ANN for substituting the chemical kinetics solver is first tested for a simple laminar 1-D premixed flame computation. A PSI syngas mixture (11) is used as the fuel which includes CO_2 and H_2O as diluents in a $CO-H_2$ fuel mixture. The main fuel components exhibit distinct reaction pathways. Hence, combustion simulations for syngas mixtures require relatively large chemical kinetics mechanisms to capture the correct physics (51), which increases the computational cost. ANN can be used to decrease the cost for these calculations.

The initial test/train data required for ANN procedure is generated by using PREMIX module of CHEMKIN for an equivalence ratio of 0.6, and a 14 species, 10 step reduced mechanism is used for representing the chemical kinetics. The mechanism is accurate for a wide range of operating conditions of syngas flames (50). Result obtained from the PREMIX calculation resolved the flame on 256 points. Although an exact definition for the number of train/test data is not given in the literature, it is advised that for an MLP-ANN to generalize properly, the number of independent weights need to be fewer by a factor of 10 than the number of input/output training points (16). Considering the fact that number of PEs used for most of the previous ANN-chemical kinetics calculations is on the order of 10, 5000 points for the current computation is appropriate for the training procedure. Thus, the profiles are populated to 5000 equi-distance data points and among these points randomly 70 % is selected for training and 30 % for testing. Similar to the selection of exact number of training points, the relative percentage of train and test data is also case dependent, and the range varies between 60-80 % in the literature (8; 15). The ANN architecture for this particular case consists of 15 inputs and 3 hidden layers with each having 20, 10 and 8 PEs, respectively. The optimum value for the architecture is defined by experimenting with different values of PEs at the hidden layers and checking the

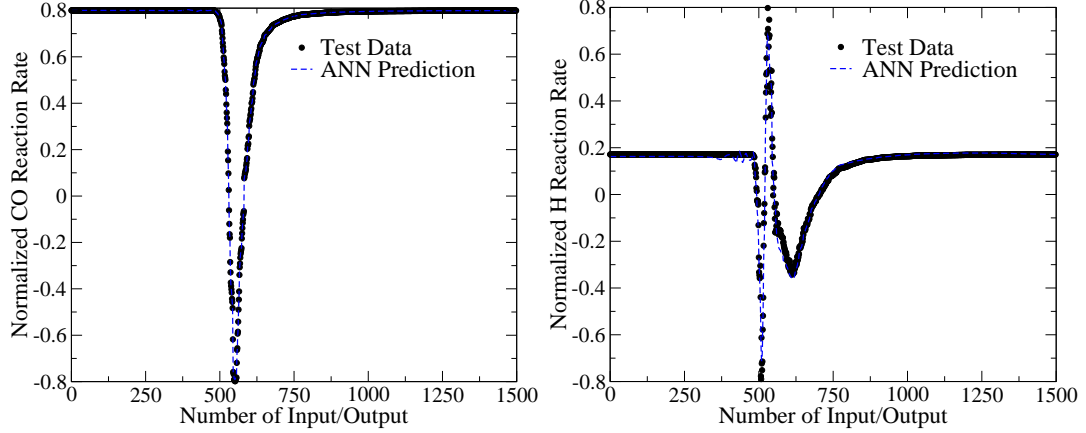


Figure 13: Actual test data and ANN predictions.

performance of the ANN for predicting the test data. The architecture used for this study corresponds to an RMS error at the output layer of 0.56 % at maximum for the OH radical. The errors associated with other species are less than this value, e.g., the maximum RMS error for H_2 is 0.073 %. 14 independent nets are generated for the reaction rates of each species. Following the information given in the literature (53), in order to avoid saturation at the output layer, the normalized reaction rate is scaled to vary between ± 0.8 as opposed to the normalized input, which is between ± 1 .

The comparison of the ANN predictions and the actual test data is shown in Fig. 13 (a) and (b). In general, reaction rates exhibit two distinct profiles depending on the species. Major species, such as CO , H_2 , CO_2 , H_2O for this particular case, are either consumed or produced at all in the flame region corresponding to a profile as given in Fig. 13 (a). The minor species, on the other hand, are consumed and produced in the flame region. A typical example for this kind of behavior is given in Fig. 13 (b). It is crucial and must be proved that ANN is able to predict both profiles correctly, which is the case for this calculation. For this purpose, the performance of the net has been tested on the data that it was not trained for as shown in Fig. 13 (a) and (b) with the dashed lines. For both of these species ANN successfully captures the correct profile,

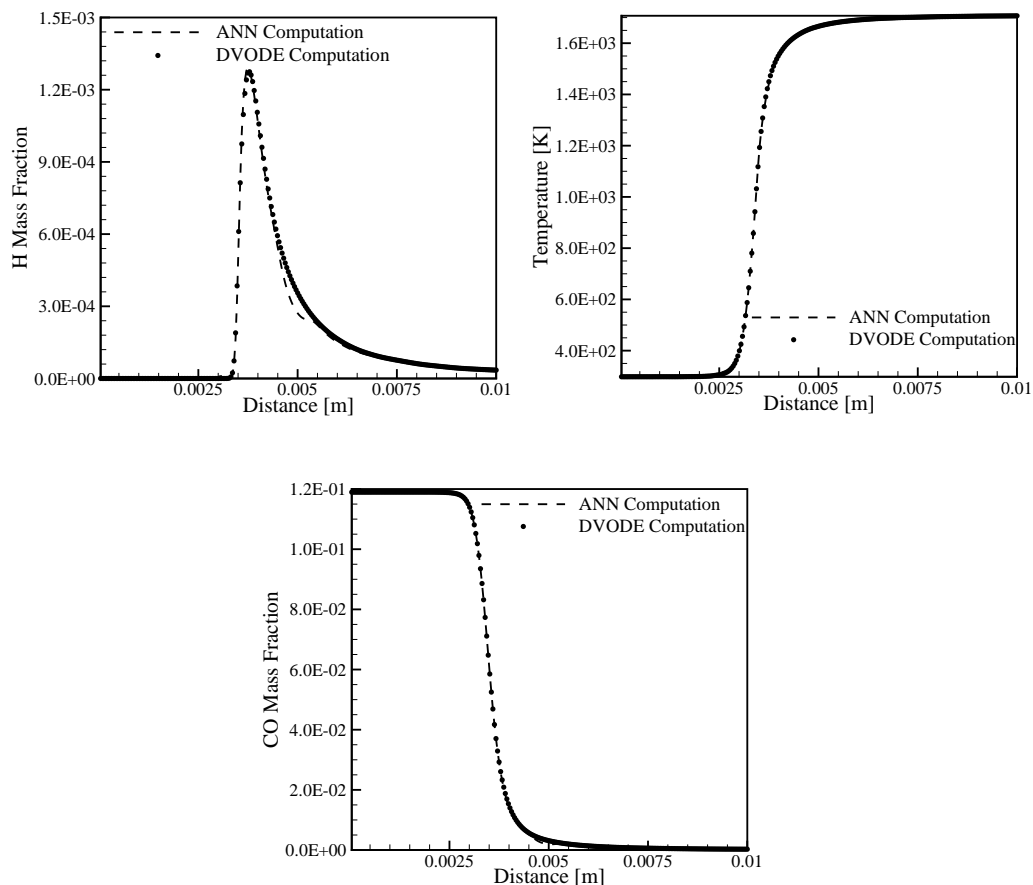


Figure 14: Application of ANN to a laminar, time dependent syngas-air flame.

except for small oscillations in H reaction rate right before it starts to decrease. This defect is very small and the RMS value averaged for all the input/output pairs at the at the output layer is less than 1 %, which is a good indicator of the accuracy of the ANN.

In order to further test the performance of the ANN, a time dependent computation is performed by creating an ANN module for chemical kinetics calculations in an existing flow solver. For this purpose, the profiles obtained by PREMIX calculation is used to initialize a 3-D computation. The initial PREMIX profile is linearly interpolated onto a uniform grid of 256 points in the x direction. The same profile is later replicated to all y locations, and the $x - y$ plane is copied to all z locations, resulting

a grid of 256x12x2 points in x, y and z directions, respectively. The profiles obtained by such a calculation is given in Fig. 14 (a)-(c) for H , CO mass fraction and temperature. As to yield a better comparison the DI calculations are also presented in the figures. The H mass fraction exhibits small discrepancy approximately at 0.005 m. Although not shown here, this defect shows itself for some other minor species too, but major species in general are free from this problem. The error does not impact the resolved flame, as shown in the temperature plot.

5.1.2 Turbulent Premixed Flame Computations

5.1.2.1 Methane-Air Flames

Computation for a simple steady-state, laminar case is carried out to demonstrate that the developed ANN model for chemical kinetics predictions is working. However, the realistic combustor applications are generally highly turbulent and unsteady problems. LES is widely used for the reactive flow analysis and the goal of the current section is to check the applicability of ANN to be used as a chemistry integrator for LES. For this purpose, following an earlier LES(68) and DNS(85) study that exist in the literature we consider a premixed methane-air flame front interacting with an initially generated isotropic turbulent flow field. Similar to the previous section, the LES is initialized by using the solution of PREMIX-CHEMKIN and the flame is at a lean condition ($\phi=0.8$) with the reactants initially preheated up to 570 K. Based on the initial turbulence level and the flame properties, the premixed flame is in the thin reaction zone (TRZ) regime. A 5 species ($CH_4, O_2, CO_2, H_2O, N_2$), 1 step reduced methane-air chemical kinetics mechanism is used for ANN training and LES. Following the earlier LES(68), the subgrid scale combustion processes are simulated with LEM by using 12 grid points inside each LES cell.

Two different ANN training procedure has been used for this section of the study. First one is based on generation of train/test data-set for a single equivalence ratio (SER), similar to what was done for the laminar computations. The second method,

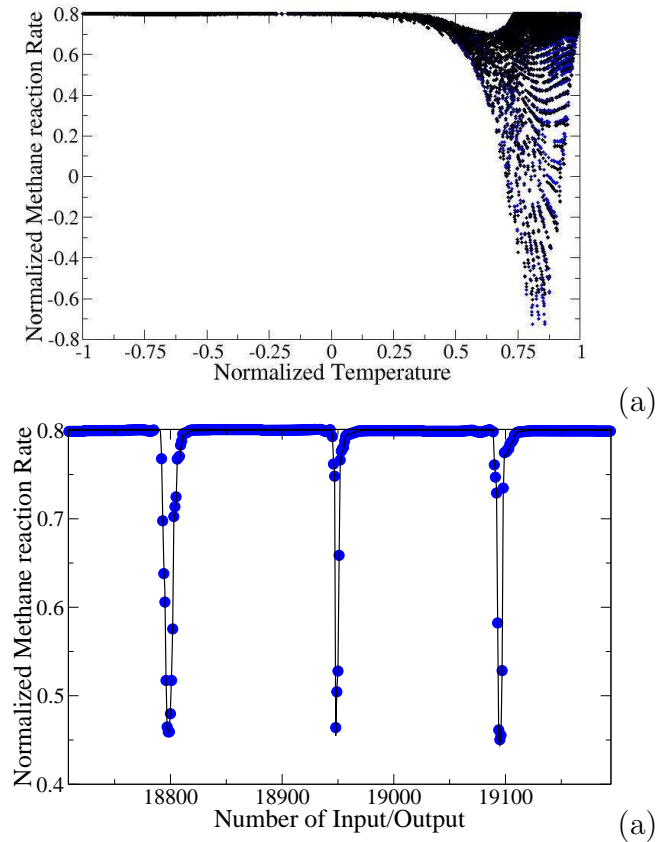


Figure 15: Actual test data and ANN predictions (a) for all equivalence ratios and (b) for close up view of three equivalence ratios. ANN-MER approach applied to a methane-air flame

on the other hand, relies on training ANN for multiple equivalence ratios (MER), so as to cover a larger portion of the chemical state space. This is particularly important for turbulence computations with thermally perfect and mixture transport properties, since small perturbations can change the composition space locally. The procedure of ANN training based on a SER is exactly similar to the procedure outlined in the previous section. The solution of PREMIX is populated to 1000 points and several ANN architectures are used to determine which one is better on predicting the test data. Although it is generally advised to employ 1 or 2 hidden layers at most (53), for this particular study 2 hidden layer configuration was the worst case and an ANN

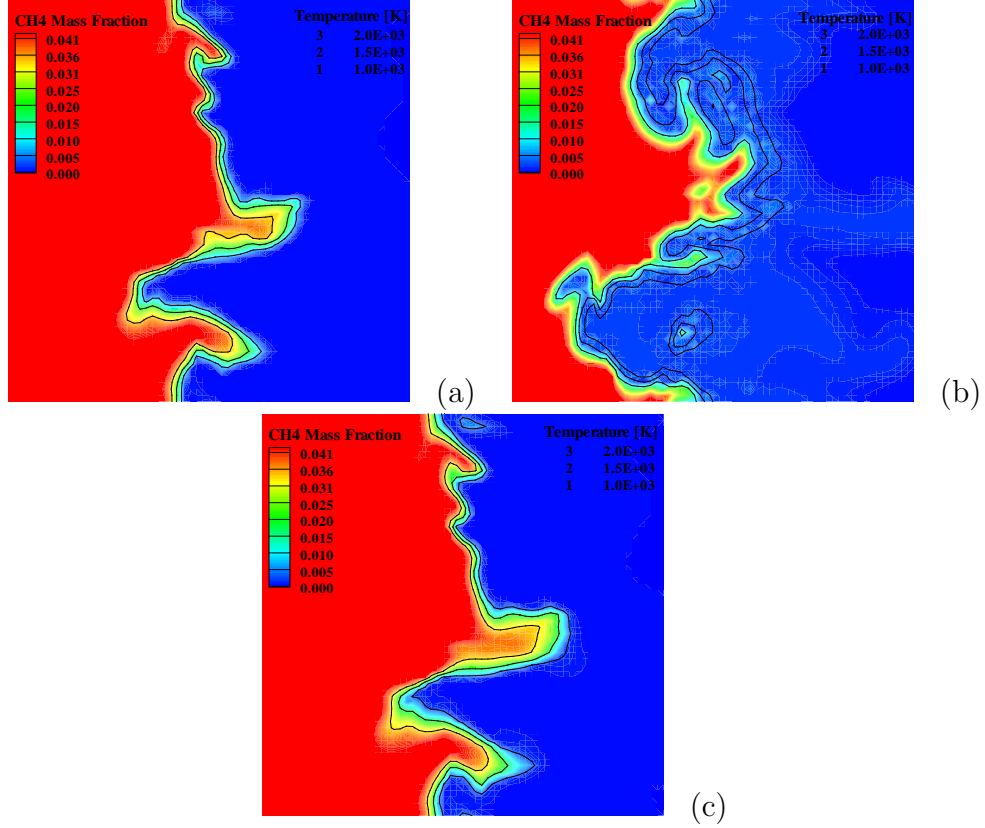


Figure 16: CH_4 mass fraction surface plot and temperature contours obtained with (a) DI, (b) ANN-SER and (c) ANN-MER

architecture with 1 input, 1 output and 3 hidden layers each having 8, 4 and 2 PEs, respectively, is constructed. Based on the second training approach, a database of 1-D laminar premixed flame solutions for equivalence ratios ranging from 0.60 to 0.9 with increments of 0.001 is generated. The PREMIX solution for each equivalence ratio comprises 50 points which is interpolated to 500. ANN results based on the test data which is a part of the training procedure is given in Fig. 15 (a)-(b). Fig. 15 (a), shows the ANN predictions and actual test data on the CH_4 reaction rate - Temperature hyperplane of the chemical state space. Here, the ANN predictions are comparable with the actual test data and it is not possible to distinguish between both of them for most of the region. The only considerable amount of discrepancy occurs at the region where reaction rate is at maximum. The reason for this is, this

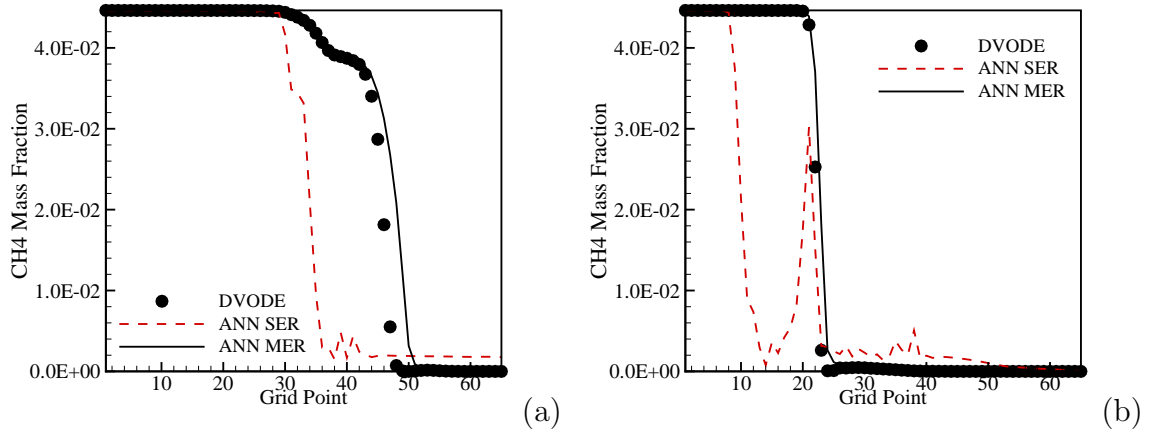


Figure 17: CH_4 mass fraction profile comparison at cross-sections (a) A-A and (b) B-B

region is accessed only by couple of equivalence ratios, thus, is not well populated. A comparison of the profiles with respect to the equivalence ratios is presented in Fig. 15 (b), where the agreement is quite accurate.

Results obtained by using DI, ANN-SER and ANN-MER computations after 4 flow through time is introduced in Fig. 16. Here, 1 flow through time is defined as l/u' , where l is the largest eddy size and u' is the turbulent fluctuation. The effect of different turbulent scales on the scalar field evolution is evident in the CH_4 mass fraction surface plot obtained by DI computations as shown in Fig. 16 (a). The temperature contours covers the maximum value of the CH_4 on a thin region indicating the flame zone. This feature is absent in the ANN-SER computations as given in Fig. 16 (b). The temperature contours seem to be spread out, covering a larger area across the flame front. Also, the flame topology seems to be very different than the DI calculations and do not exhibit any similar structure. On the other hand, ANN-MER computations predict a very similar flame topology with DI calculations as shown in Fig. 16 (c).

A better understanding of the effect of different ANN training approaches can be achieved by investigating the actual profiles along a cross section of the flame and is

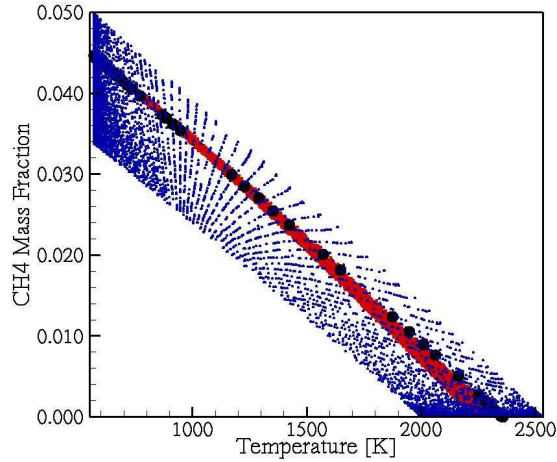


Figure 18: Composition state-space accessed by SER, MER training approaches and DI computations

introduced in Fig. 17 (a)-(b). The profiles are obtained across the flame front at $y=0.0125$ m and 0.0101 for Fig. 17 (a) and (b), respectively. These locations correspond to a convex and a concave region of the flame. The ANN-MER computation as seen in Fig. 17 (a), predicts a slightly larger flame region as opposed to DI. In Fig. 17 (b), on the other hand, the agreement is better. As it was observed in the surface plot, the predictions obtained by ANN-SER, is very different than the DI results and look unphysical. The region on the CH_4 mass fraction and temperature hyperplane of the chemical state-space that is accessed by DI computations and covered by the ANN-MER-SER training procedures is shown in Fig. 18. Here, the ANN-SER results are shown with black circles and it corresponds to a line on the state-space. The actual data obtained by DI computations is not a single line, but it covers a region within the state-space. The ANN-SER approach, therefore, can not provide predictions, since the region of interest is outside of its training region. The ANN-MER approach covers a larger space on the state-space which is more general and adapts itself to local perturbations in the composition state space in a better way.

Table 5: Simulation parameters for flame turbulence interaction problem

	u'/S_L	l/l_f	Regime [m]	Box Size [cm]
SYN-Case A	10	5	TRZ	3.0
SYN-Case B	5	5	TRZ	5.0

Table 6: Flame parameters used for flame turbulence interaction

	Fuel Composition	Equivalence R.	S_L [m/s]	l_f [m]
$H_2:CO:CO_2$	0.0678:0.113:0.0254	0.6	0.2105	8.755×10^{-4}
$H_2O:O_2:N_2$	0.0650:0.1507:0.5781			

5.1.2.2 Syngas-Air Flames

The applicability of ANN into flame-turbulence interaction computations by using LEMLES is studied further in a configuration with an embedded pair of coherent vortices in an isotropic background turbulence, where there is wrinkling of the flame surface both by large and small scales. More specifically a flame front interacting with a pair of spanwise vortices superimposed on an isotropic turbulent premixed mixture is of interest. This is more difficult test case as large scale wrinkling alters significantly the diffusion of the species across the flame front. $uc, max/S_L$ and D_c/l_f for this vortex pair is 50 and 5, respectively. The fuel composition and the size of the coherent structure are held constant, and in connection with an earlier study (72). Two different background turbulence levels are simulated, where the flames are in the thin-reaction-zone (TRZ) regime. A 64^3 grid is used for all cases, and the size of the computational domain is selected as to yield a minimum spacing of 3.3 times the Kolmogorov length scale. In the subgrid level within each LES cell, 12 LEM cells ($N_{LEM} = 12$) are used, which allows a resolution of 4 times smaller than η . The fuel composition is PSI as defined by General Electric (11). Simulation parameters and flame properties for FTI computations are summarized in Tables 5 and 6, respectively.

The LESLEM results obtained for both cases by employing ANN approach are

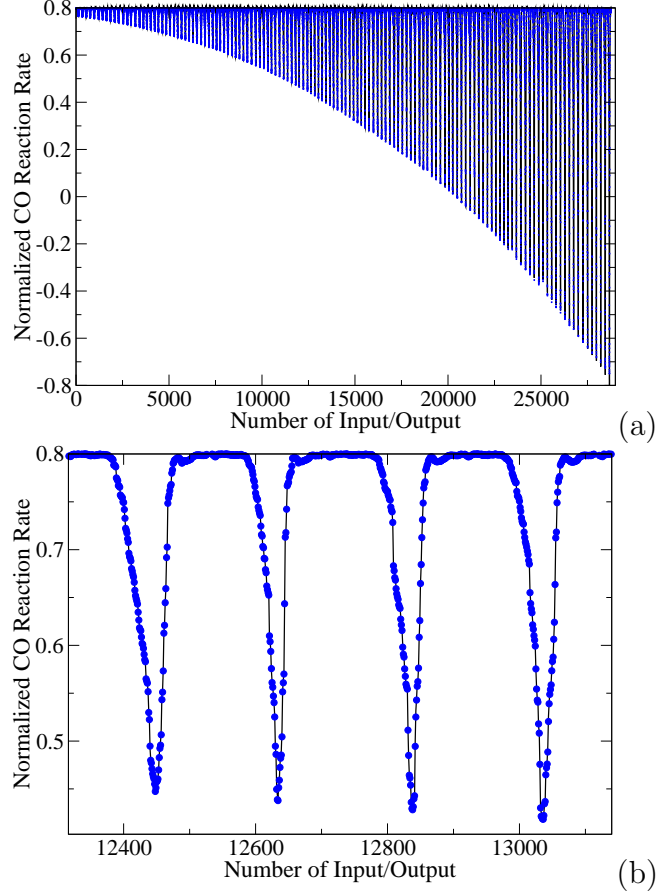


Figure 19: Actual test data and ANN predictions for an ANN-MER approach applied to a syngas-air flame. (a) general, (b) close-up view

given in Fig. 20 (a)-(b) at a non-dimensional time of 0.3. The time is non-dimensionalized with the characteristic time, which is calculated based on the background turbulence level as D_c/u' . Here, Figs. 20 (a) and (b) shows the contour plot of temperature superimposed on the vorticity surface plot. The flame front is wrinkled both by the large scale-coherent vortex pair and the small scale background isotropic turbulence. The small-scale vorticity in the

As it was shown in the previous section, since an ANN-MER approach is superior to ANN-SER, the ANN training approach here uses only the MER technique. The training data is constructed for equivalence ratios ranging from 0.45 to 1.10 with jumps of 0.005. Also, to avoid poor training due to the few number of data points

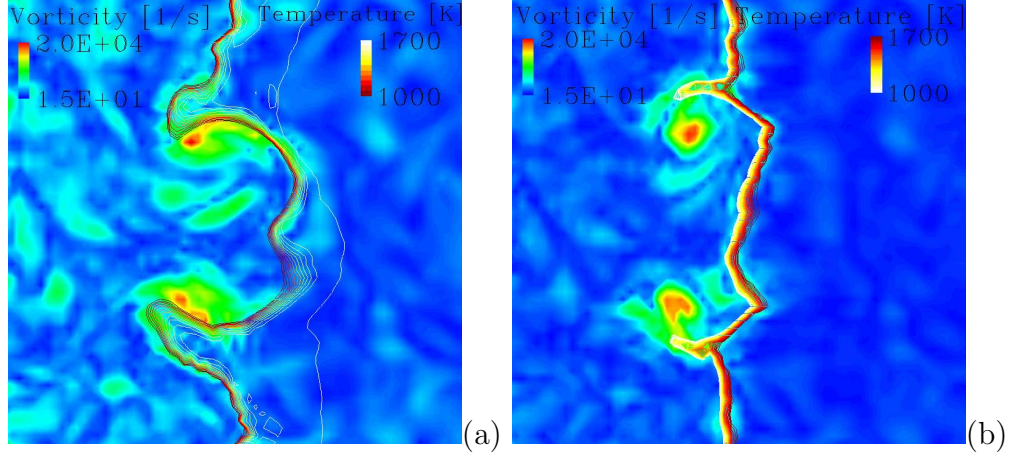


Figure 20: Application of ANN to a turbulent premixed syngas-air flame:(a) Case 1, (b) Case 2.

associated with each single equivalence ratio, the gridding sensitivity of PREMIX is increased by adding more grid points to sections where there are large gradients, which yielded approximately 700 points. In total, there is 67128 train and 28768 test data. The ANN architecture consists of 5 layers, having 3 hidden layers with 20, 10 and 8 PEs, respectively. The exact ANN architecture is constructed following the same logic that was outlined in the previous sections. The test data and the ANN predictions for the normalized CO reaction rate is given in Fig. 19 (a). The data corresponds to an almost non-smooth function of the reaction rate with respect to the equivalence ratio. The ANN can, however, predict the profile fairly well. A close-up look of the profiles reveal that as there are more train/test points for each equivalence ratio, the ANN predictions match with the actual data better than the earlier case. Although it can not be detected well in these figures, the only considerable amount of difference between ANN predictions and the test data is at the regions where there is not any reaction rate which corresponds to a value of 0.8 on the normalized data. ANN fails to predict an absolute zero value of reaction rate in the post and pre flame regions. This problem is overcome by adding a threshold to the ANN value, beyond which the reaction rates are considered to be zero.

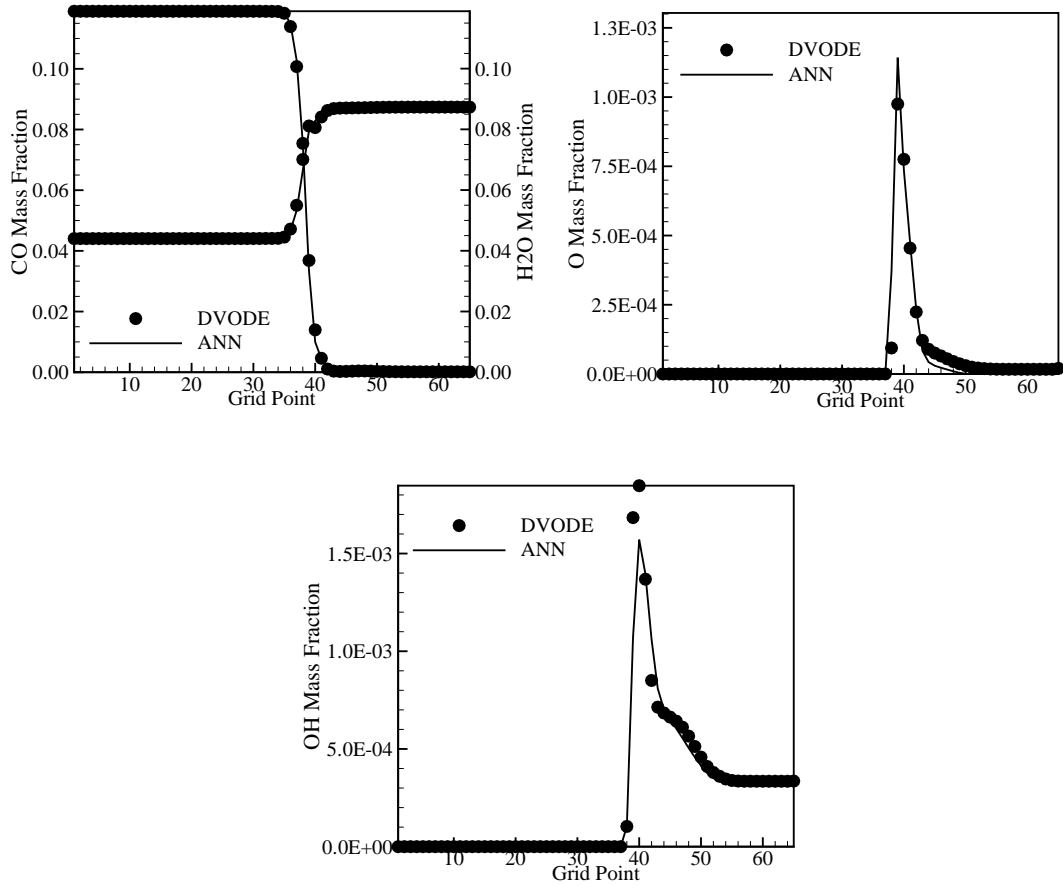


Figure 21: Comparison of species profiles obtained by DI and ANN approaches for turbulent, premixed syngas-air flame, Case 1. (a) CO and H_2O , (b) O , and (c) OH mass fraction.

incoming turbulent field dissipates across the flame and only the large structures exist in the burned side due to the high temperature values in this region. A detailed description of the interaction between the flame and the vortical structures is given elsewhere (72). The comparison of the computed profiles across the flame is given in Fig. 21 (a)-(c) for Case 1. The profiles obtained for major species CO and H_2O match well with the DI computations. The minor species, O and OH , show discrepancy near the peak region. The maximum error for both of the species is less than 18 %. However, both species mass fraction is on the order of 10^{-3} and the impact of their error is not very severe on the major features of the flame.

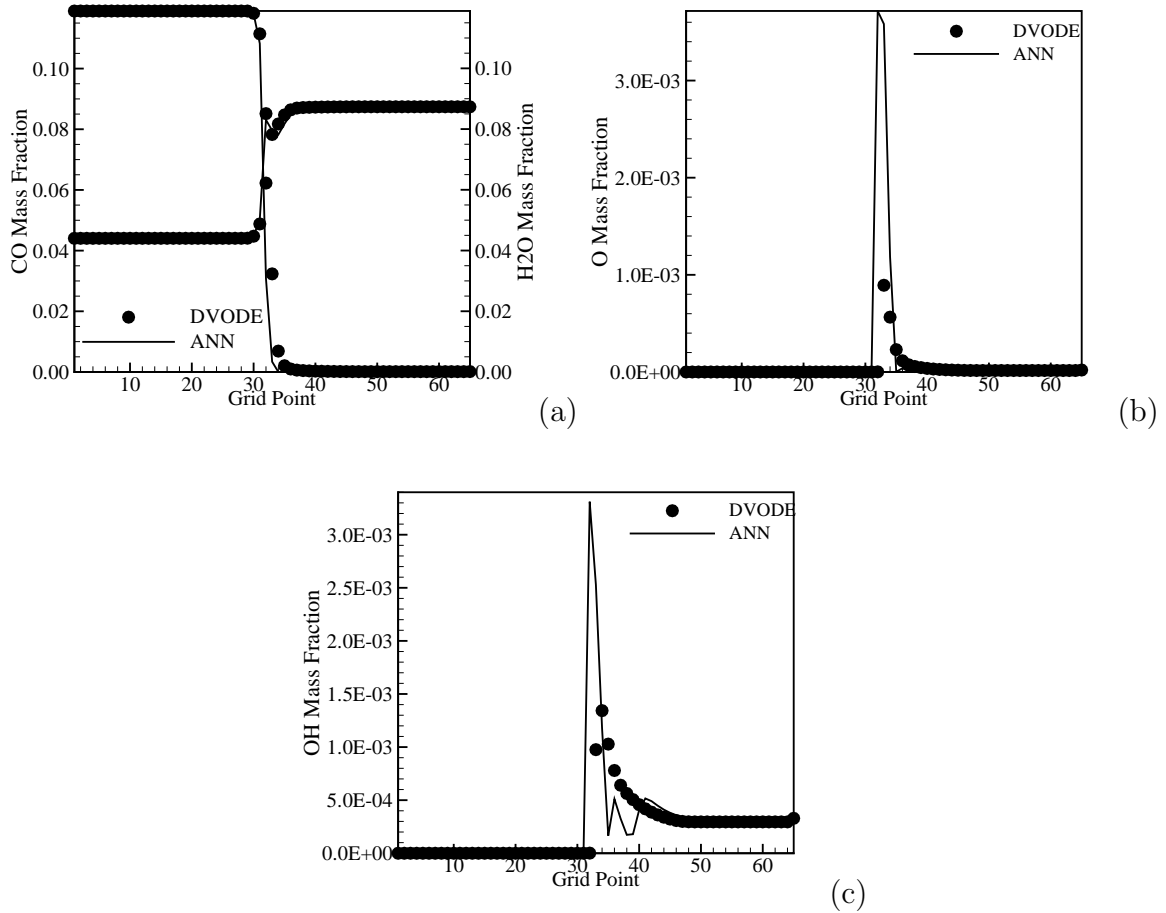


Figure 22: Comparison of species profiles obtained by DI and ANN approaches for turbulent, premixed syngas-air flame, Case 2. (a) CO and H_2O , (b) O , and (c) OH mass fraction.

The agreement between the profiles obtained for flame Case 2, as shown in Fig. 22 (a)-(c), however, is not as good as it is obtained for Case 1. CO starts to be consumed earlier than that is calculated with DI and the H_2O mass fraction exhibits a peak value within the flame zone. The maximum value of the minor species is overpredicted, almost 4 times for O and 2 times for OH . The profile for OH also corresponds to an oscillation which is not physical. In order to gain further insight into the effect of ANN on the LEMLES, the $CO_2 - OH$ hyperplane of the chemical state-space is presented in Fig. 23. Here, Fig. 23 (a) corresponds to the region that was accessed by DI, whereas Fig. 23 (b) is by the ANN calculations. In Fig. 23

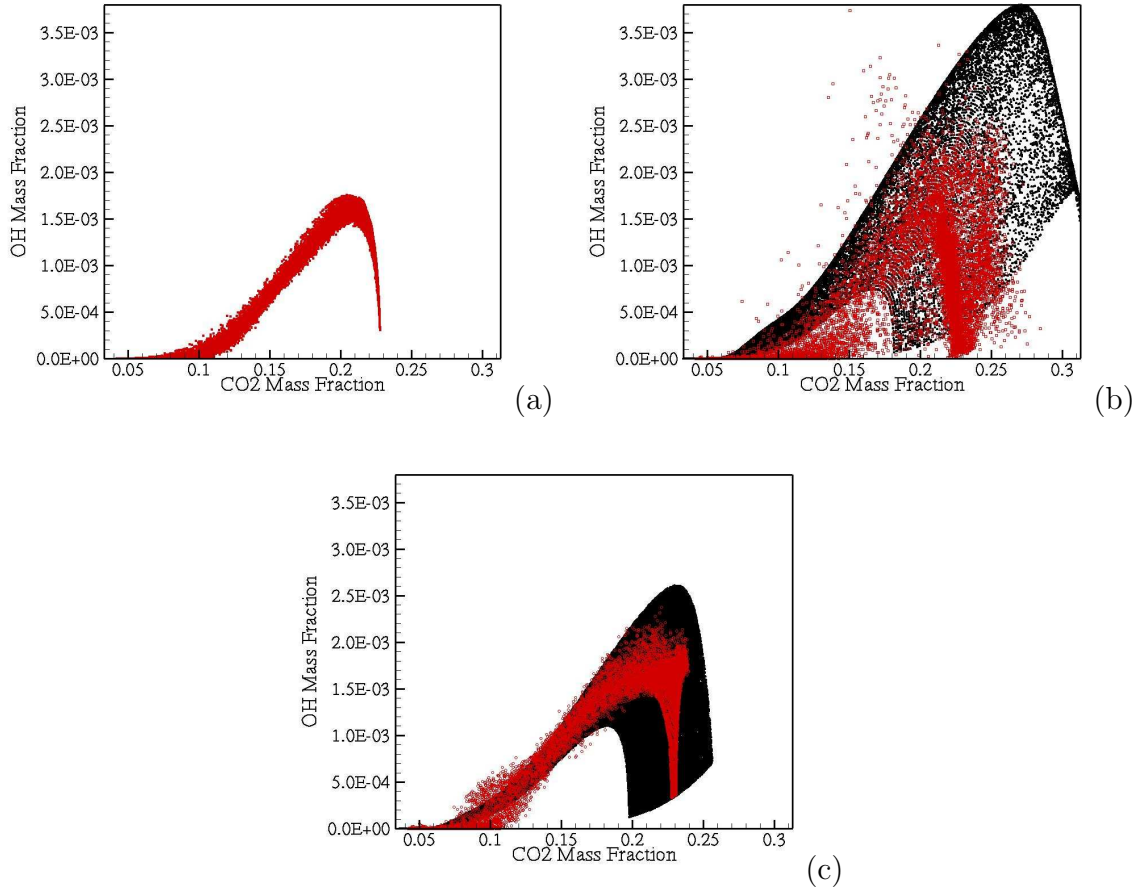
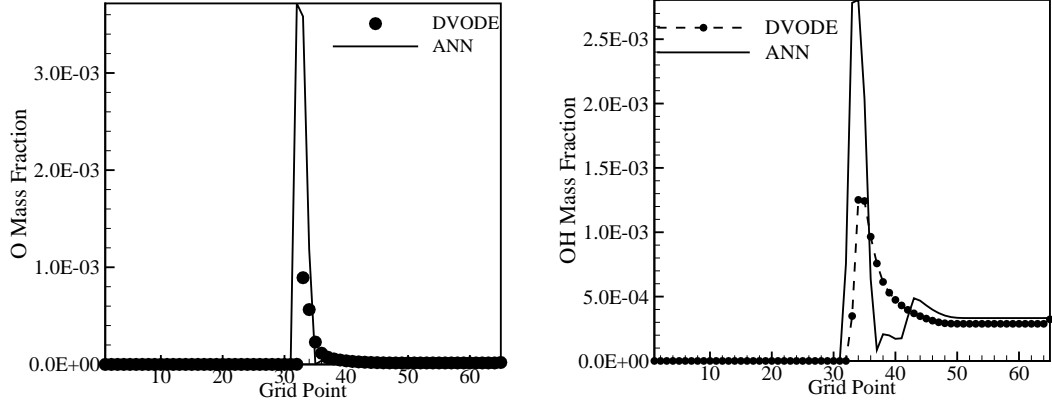


Figure 23: $CO_2 - OH$ Hyperplane Accessed by (a) DI-LES, (b) ANN training on coarse data and ANN-LES, and (c) ANN training on fine data and ANN-LES.

(b), the region that was covered within the initial ANN training phase is also given, and denoted with black dots. The DI computations, similar to that was obtained for earlier methane-air case, supports the idea why it is not possible to achieve training and expect accurate results for a SER computation. This time, the region is more complex and can not be represented by a SER, which would actually correspond to a single line on the hyper-plane. A direct comparison of the region covered by the ANN training phase and the actual region constructed by DI computations reveal that only a single portion of the state-space is actually accessed. Since the ANN is trained for a wide range, the accessed points with the ANN computation is spread



(a) O mass fraction profiles by DI and ANN computations for Case 2 (b) OH mass fraction profiles by DI and ANN computations for Case 2

Figure 24: Comparison of species profiles obtained by DI and ANN approaches for turbulent, premixed syngas-air flame, Case 2 with refined table

over the entire region. Moreover, the ANN training table is sparse in most of the region, which would avoid ANN to fully generalize on the training data.

In order to get better solution, a new ANN training table is produced for a smaller portion of the chemical state-space but with a finer resolution. The ANN is trained for a range of equivalence ratios from 0.5 to 0.7 with 0.001 increments. The CO_2-OH hyperplane representative of the region accessed through ANN training and LEMLES is given in Fig. 23 (c). The accessed region by LEMLES for this training file is very similar to the region covered by DI, as shown in Fig. 23 (a). For low values of the CO_2 , the region used for training becomes very thin and cannot cover the accessible region as predicted by DI calculations. Hence, the ANN prediction spreads over a relatively larger area compared to DI. The species profile as seen in Fig. 22. is much better than the results in Fig. 24. There is still an overestimation of the minor species maximum value, but the error is smaller than the previous case and most importantly the profiles do not exhibit any non-physical structure. Nevertheless this is going to be studied further for future study.

As it was outlined in the previous sections, most important merit of using ANN against stiff ODE solvers is its speed, and against ISAT and ILDM based look-up table approaches is its efficiency in terms of memory. The time required for one time step iteration for the laminar, premixed syngas-air flame simulation with DI is 0.21547 sec and for ANN is 0.06217, which corresponds to a speed up of 3.47. The size of the table that is used for the training procedure is 23.8 MB. For the turbulent syngas-air flame simulation, the time required for one iteration is 42.7969 sec for DI and 11.62101 sec for ANN, which approximately corresponds to the same amount of speed up, 3.68. For the turbulent flame simulation, compared to the laminar flame, the memory required for the ANN training is larger since a MER approach is employed. The table that is used for training is 522.6 MB and hence, using ANN saved a considerable amount of memory. Finally, for the turbulent methane-air flame a speed up of 1.98 is achieved. The reason why the amount of speed up decreased compared to the syngas-air flames is related with the reduced mechanism that is used. The chemical kinetics calculations for the methane-air calculations are made by using a small, 1 step 5 species reduced mechanism. Thus, the time required for the solution of the stiff ODE is not as huge as it is for the syngas flame. Still, ANN saves a 93.4 MB of memory.

5.1.3 Conclusions

In the current section it is showed that, in contrast to employing stiff ODE solvers, ANN is very time effective, and the memory requirement is not as large as it is for look-up table approach. Here, the focus is spent for the determinig the reliability of the ANN predictions, which is highly dependent on the training procedure. For premixed flames it is showed that the ANN can be trained based on the solution of a 1D laminar premixed flame. This approach, however, is not very effective for turbulent computations, since turbulence may perturb the composition state-space locally which would not let it to be represented simply by one equivalence ratio.

Training based on multiple equivalence approach yielded relatively better results as it is demonstrated for turbulent, premixed methane-air and syngas-air flames. Still, the accuracy is not as good as it is wanted and next sections will provide ANN comparisons obtained by different training approaches.

5.2 ANN trained on Laminar Flame-Vortex Interactions

The current section provides further discussion on evaluating the applicability of the ANN approach as a chemistry integrator for LES of reactive flows. Here, another way of generating ANN training tables independent of the computation of interest is proposed, which is based on the laminar flame vortex interactions (FVI). The training table is constructed with an independent flame study, and the trained networks are used in LES of laminar flame-vortex-turbulence interaction studies at different equivalence ratios and turbulence levels.

5.2.1 Training Table Generation

As noted earlier, the current approach is to train the ANN using a generic setup within the parameter space of interest, and then to use it for different cases. Therefore, the training table is constructed by DNS of a laminar flame vortex interaction (60; 72). A 10 step, 14 species chemical kinetics mechanism for syngas combustion is used. Since turbulence is a collection of vortices of different strengths, six cases are run with $U_{C,max}/S_L$ between 10 to 400. In all these cases $D_C/L_F=1$. Here, $U_{C,max}$ is the maximum velocity induced by the vortex and D_C is the vortex diameter. The range is chosen based on observations in large-scale LES of high-Re combustion in gas turbine engines (49). The grid is fine enough to resolve the laminar flame thickness by 11 points. Simulations are conducted using a parallel solver and a typical case requires only around 1.95 sec/iteration on a single processor Intel PC (3.2 GHz Xeon) and therefore, considered efficient. Simulations are run for 15 eddy turn-over time ($t^* = D_C/U_{C,max}$) after which it is observed that the initial vortex significantly diminishes. The compositional state-space at every $0.2t^*$ is recorded, merged for all cases, and used for the ANN training. As will be discussed later, this approach allows us to include a large number of vortex length and time scales even though the actual number of simulations is limited.

5.2.2 Test Cases

Table 7: Case table for the LES of flame-vortex-turbulence interaction

	u'/S_L	$U_{C,max}/S_L$	D_C/L_F	ϕ
Case 1	10	–	–	0.6
Case 2	5	50	5	0.6
Case 3	10	50	5	0.8

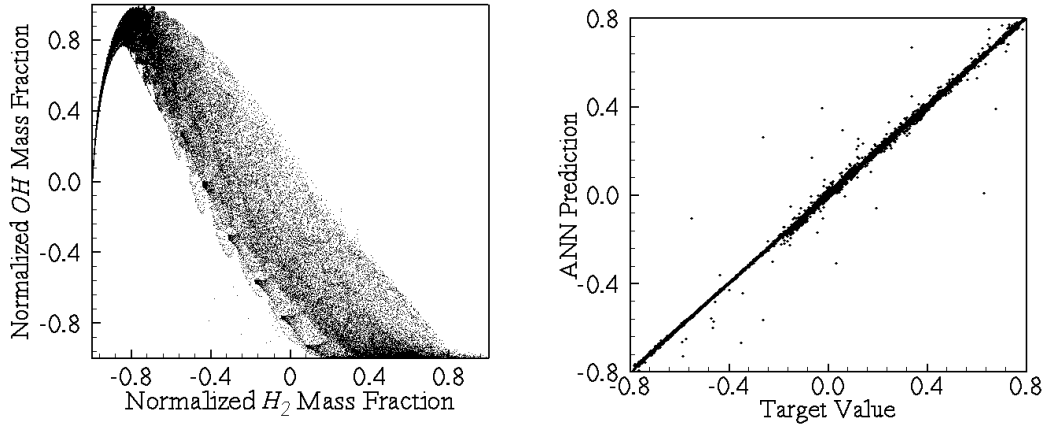
Table 8: Flame Parameters

Equivalence Ratio	S_L [m/s]	l_f [m]
0.6	0.2105	8.755×10^{-4}
0.8	0.3920	5.611×10^{-4}

The LES of premixed syngas (PSI (72))/air flame is conducted. A background isotropic turbulence is generated by using a prescribed spectrum with fixed u'/S_L and L_{11}/L_F , selected in accordance with earlier studies (85; 68). Here, L_{11} is the integral length scale. The flames are in the thin-reaction zone and the validity of the LEMLES on this regime has been shown earlier (68). We focus on three simulations (summarized in Tables 7 and 8), two of which with coherent vortex pair embedded in the background isotropic turbulence to mimic the effect of large scale wrinkling of the flame. A 64^3 grid is used for all cases, with an LES resolution 4 times larger than the Kolmogorov length scale. On the subgrid level, 12 LEM cells are used within each LES cell. Characteristic inflow/outflow boundary conditions are used in streamwise directions, and periodicity in the spanwise and the transverse directions is imposed. Mixture averaged transport coefficients are used with a thermally perfect gas equation of state.

5.2.3 Results and Discussion

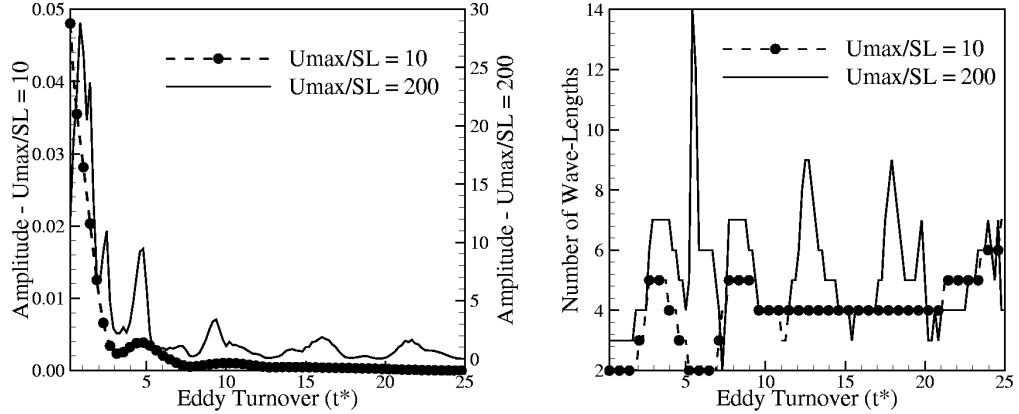
One hyperplane accessed by the training table is shown in Fig. 25 (a). Although each simulation is for a single equivalence ratio, the states accessed correspond to a certain region on the hyperplane. A fast Fourier transformation (FFT) analysis of the



(a) H_2 -OH Hyperplane Accessed by the Training Table. (b) Correlation between the target value and ANN prediction for all species obtained by the 10/5/4 ANN.

Figure 25: Training Phase.

u -velocity component obtained across the flame front is performed and the variation of the amplitude of the most energetic scale (the vortex) is given in Fig. 26 (a). The interaction represents a decaying process, and approximately after $5t^*$ the amplitude decreases by a factor of 10. The number of wave-lengths that contribute to the 80 % of the energy spectrum is given in Fig. 26 (b), and it is shown that large number of scales are present over the entire simulation period. Hence, each test case with an initial single vortex of a given size and strength provides additional data over a much wider range of scales. Therefore, the current strategy of simulating and storing data throughout the *unsteady* flame-vortex interaction process, coupled with the Lewis number effect (implicit in the multi-component mixture approach used here) allows us to include a broad region in the compositional state-space (as shown in Fig. 25). This method is found to be more suitable for generating training data compared to using PREMIX-CHEMKIN (73) which is *steady* in its nature and not suitable for LES. Although the training is not fully independent from the LES case, the flow features are not the same since the training is based on a laminar study. The LEM subgrid implementation allows us to use the laminar feature inside LES grid, and



(a) Variation of the amplitude of the most en- (b) Number of wave lengths that contribute
 ergetic wave length. 80 % of the energy spectrum.

Figure 26: FFT analysis of the flow across the flame front.

therefore this approach is a new strategy to account for turbulent mixing effects.

Table 9: Effect of number of hidden layers and PEs on the training phase

Case	ANN	Error (%)	Time/iteration
A	10	3.91	2.485
B	20	2.97	2.894
C	10/5	1.78	2.728
D	20/10	1.604	4.552
E	10/5/4	1.690	3.959
F	20/10/8	1.704	6.119

The table constructed for the ANN training procedure is around 200 MB. Two ANN architectures, one with 3 hidden layers (Case E, denoted 10/5/4 ANN) and the other one with 2 hidden layers (Case C, denoted 10/5 ANN) are discussed here. The selection of these ANNs for discussion is based on error and speed-up estimations of several different configurations (see Table 9). Overall, the smallest error is achieved for Cases E and D, but Case E is discussed here since it is almost 15 % faster than the latter. Case C is one of the fastest cases but with slightly higher error (compared to Case D), and is selected as a second case for discussion. The RMS error in the test phase is at most 3.4×10^{-3} for the 10/5/4 ANN and 1.3×10^{-3} for the 10/5 ANN, both observed for OH . H_2 exhibits the minimum RMS error of 3.0×10^{-4} and 2.8×10^{-4} for

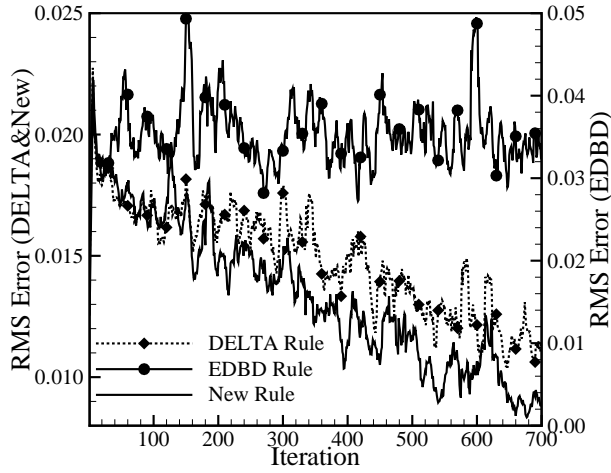
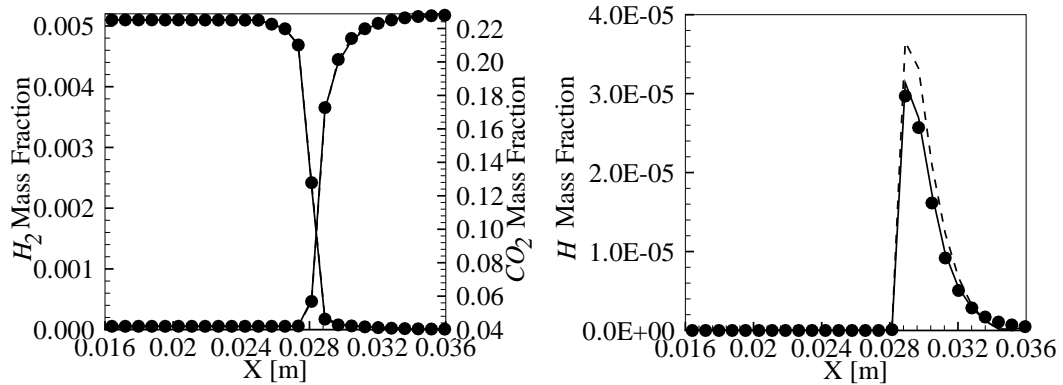


Figure 27: Convergence history.

10/5/4 and 10/5, respectively. Although the 10/5 ANN is almost 20 % faster than the 10/5/4 ANN, on the average, the training for one species takes approximately same amount of CPU time regardless of the number of hidden layers. Fig. 25 (b) shows the correlation curve obtained for the 10/5/4 ANN. The correlations for all the species collapse on top of each other, and demonstrate the overall accuracy during the training phase. The ANN predictions are highly correlated with the target value, except for some points. Considering that the plot shows almost 570,000 points, there are only few points outside the target values and they do not affect the overall performance.

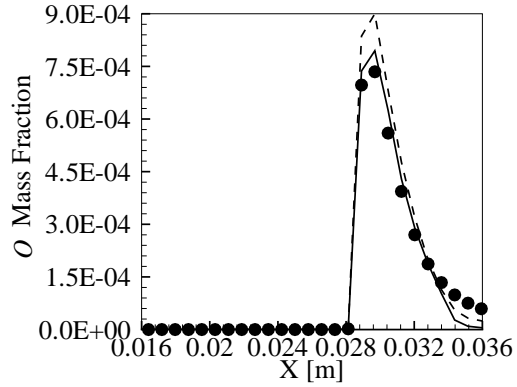
The new learning rule proposed within the paper is tested by comparing its performance with standard GDR and EDBD rules in Fig. 27. The EDBD rule has very poor learning compared to the other methods and does not exhibit a convergence, but stays almost flat. This is due to the dependance of the EDBD on the model coefficients, which need to be calibrated. The GDR and the new rules seem similar in the early stage, but as the number of iterations increases the new rule outperforms the GDR. Although not shown in the figure, the GDR eventually attains same value of RMS error with the new rule, but after a larger number of iterations.

To quantify the accuracy of the ANN, time averaged profiles across the flame are



(a) H_2 and CO_2

(b) H



(c) O

Figure 28: Comparison of the instantaneous species profiles obtained by the DVODE (\bullet), the 10/5 ANN (- - -) and, the 10/5/4 ANN (—) at $3t^*$ for Case 1.

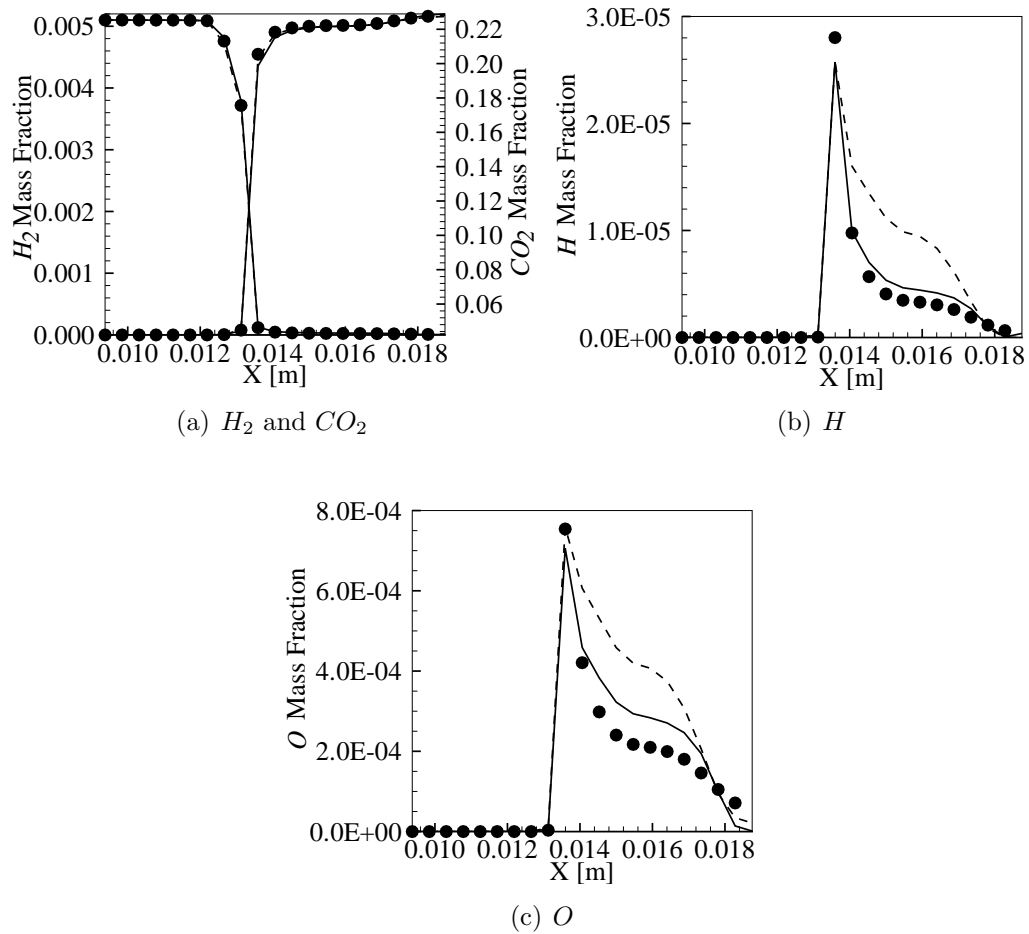


Figure 29: Comparison of the instantaneous species profiles obtained by the DVODE (\bullet), the 10/5 ANN (- - -) and, the 10/5/4 ANN (—) at $3t^*$ for Case 2.

Table 10: Speed-up obtained by ANN compared to DVODE

ANN	Connections	Speed-Up
20/10/8	986	4.71
10/5/4	390	7.62
10/5	274	11.22
DVODE	—	1.00

compared in Fig. 28. For the major species, (H_2 and CO_2), ANN and DVODE predicted profiles match very well. For minor species, H and O , the 10/5/4 ANN exhibits errors around 3 % and 5 %, respectively. The 10/5 ANN over-predicts the maximum value of some species, and this corresponds to an error of 22 % for H and 18 % for O at maximum even though the overall profiles are very similar. The instantaneous profiles across the flame also show similar errors and therefore, are not shown here. Fig. 29 shows the instantaneous profiles for flow Case 2. Note that, the same ANN and solver are employed and only the test conditions are changed. The major species are in good agreement with the DVODE predictions. The 10/5/4 ANN slightly under-predicts the maximum value of H within the flame zone. Overall, there is around maximum 10 % error for both ANNs. Some radicals show lower error, e.g., for O the error is around 5 % for the 10/5/4 ANN. The profiles obtained by the 10/5 ANN are not very accurate in the post flame region and over-predicts the DVODE computations for both of the species. The same ANN approach is used for a different equivalence ratio and turbulence level, and the results are presented in Fig. 30. Similar to the previous cases, the major species are in good agreement and not shown for brevity. For the minor species, H and O , the 10/5 ANN tend to broaden the reaction zone thickness, as shown in the figure. The 10/5/4 ANN on the other hand is more accurate. For both of the species, the 10/5 ANN overpredicts the maximum value as well. It is clear that the overall level of agreement is not changing with respect to the turbulence level or equivalence ratio.

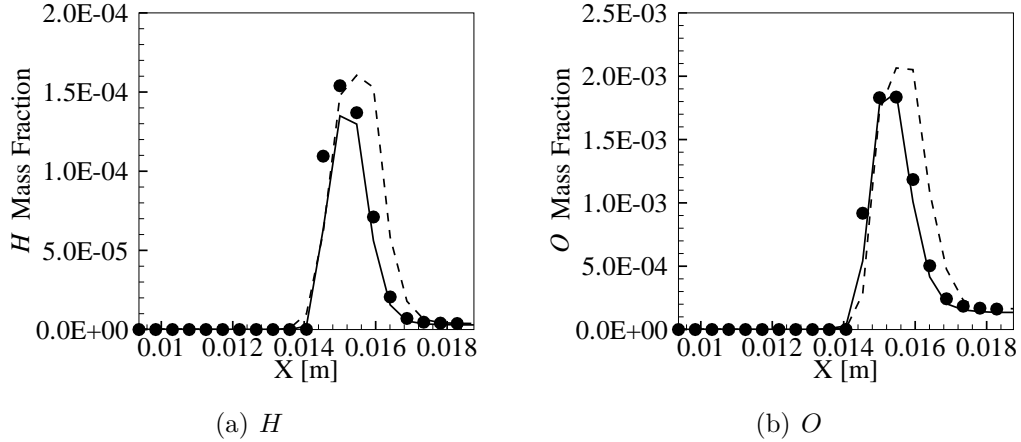


Figure 30: Comparison of the instantaneous species profiles obtained by the DVODE (\bullet), the 10/5 ANN (- - -), and the 10/5/4 ANN (—) at $3t^*$ for Case 3.

Table 11: Memory requirement for the look-up table approach and the ANN

ANN	Look-Up Table Size	ANN Size
20/10/8	212.6 MB	0.291 MB
10/5/4	212.6 MB	0.150 MB
10/5	212.6 MB	0.107 MB

5.2.4 ANN Speed-Up and Memory Savings

The speed-up achieved by using ANN and the memory requirement for LES of turbulent FVI are summarized in Tables 10 and 11, respectively. For the ANNs discussed here, we achieve around 7X speed-up for the 10/5/4 ANN and 11X speed-up for the 10/5 ANN compared to a stiff ODE solver. The attainable speed-up by ANN depends on the number of connections used in the selected architecture. Although the 10/5/4 ANN outperforms the 10/5 ANN both in the training and in the LEMLES, it uses 389 connections in comparison to 273, and is slower. Increasing the number of PEs to 20/10/8 reduces the speed-up to around 5X. It appears that the ratio of speed-up between different ANN architectures is roughly equal to the ratio of the number of connections, and this provides a potential design guideline (that will have to be verified with further studies). On the other hand, even though the training table size was large (around 200 MB), the actual ANN stores this information with less than

1 MB. Thus, storage is drastically reduced and this is very important on cheap PC parallel clusters where memory is limited.

5.2.5 Conclusions

The efficiency of ANN in terms of memory, time and accuracy for calculating chemical source terms (for a multi-species reduced kinetics) within LES of turbulent premixed flames is investigated. A new training table construction and ANN learning strategy is proposed in this section. The proposed training approach converges faster with a reasonable RMS error. The training strategy employs a simple flame-vortex test case but stores the entire *unsteady* database to provide a large range of time and length scales. The ANNs trained on this database are used without any change within the subgrid in the LEMLES and direct comparison with the DVODE evaluations show that the ANN can accurately predict the species profiles with an acceptable error. Furthermore, a speed-up of approximately 11 (for 10/5) is achieved, and the memory requirement is only around 0.1 MB of memory per processor.

5.3 ANN trained on Flame Turbulence Interaction

The final effort on using ANN to calculate instantaneous reaction rates within the LEMLES methodology deals with creating the ANN training tables based on the flame turbulence interactions. Since the DNS of this interaction is computationally expensive, a stand-alone LEM solver is developed and used to simulate the interaction process in a computationally much affordable manner. The thermo-chemistry is extracted by stand-alone linear eddy mixing (LEM) model simulations under both premixed and non-premixed conditions, where the *unsteady* interaction of turbulence with chemical kinetics is included as a part of the training database. The proposed methodology is tested in LES and in stand-alone LEM studies of three distinct test cases with different reduced mechanisms and conditions. LES of premixed flame-turbulence-vortex interaction provides direct comparison of the proposed ANN method against DI and ANNs trained on thermo-chemical database created using another type of tabulation method.

5.3.1 Training Table generation

The ANN training table is constructed by using stand-alone LEM computations for all cases presented in this section. The details of the tabulation process (i.e., reduced mechanism, range of Re_t and L , etc.) are different for each test case. The LEM computations start from an initially laminar profile, which is also different based on the type of the problem (i.e. premixed or non-premixed). The LEM domain for premixed cases extends from reactants to the products, whereas for non-premixed cases, it spans the oxidizer and fuel streams, as shown schematically in Fig. 31 as a 1D strip in a multi-dimensional domain. However, it should be noted that the basic structure of the tabulation and the capabilities of the stand-alone LEM computation are the same for all cases. These parameters will be identified with more details on the next sections.

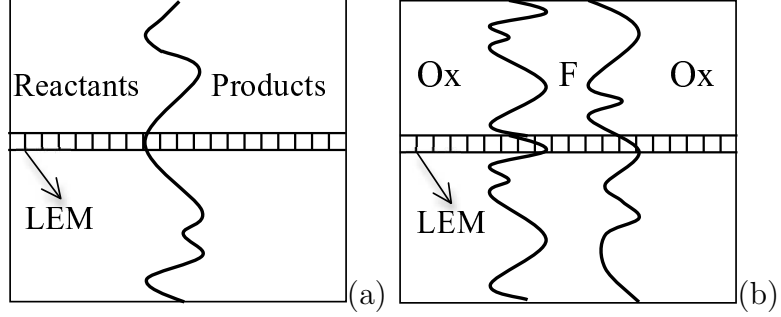


Figure 31: Schematics of the actual problem and the LEM sub-domain

Table 12: Test Cases

	Mode	ANN Testing	Reduced Mechanism
Case A	Premixed syngas/air	LES	10 steps, 14 species (skeletal)
Case B	Premixed methane/air	Stand-Alone LEM	12 steps, 16 species (skeletal)
Case C	Non-premixed syngas/air	Stand-Alone LEM	21 steps, 11 species

Table 13: LEMLES Test Cases

	u'/S_L	$U_{C,max}/S_L$	D_C/L_F	ϕ
Case A1	5	–	–	0.6
Case A2	5	50	5	0.6
Case A3	10	50	5	0.8
Case A4	10	50	5	0.6

Table 14: Flame Parameters for LEMLES Case A

Equivalence Ratio	S_L [m/s]	L_F [m]
0.6	0.2105	8.755×10^{-4}
0.8	0.3920	5.611×10^{-4}

5.3.2 Test Cases

The proposed methodology for thermo-chemical database construction and ANN accuracy is tested for three distinct reduced (or skeletal) mechanisms and test cases (Table 12). The first case (Case A) is essentially a series of LEMLES of flame-turbulence-vortex interaction computations (Table 13). For the LES cases, the ANNs trained on the thermo-chemical data extracted from stand-alone LEM computations are used to replace the stiff ODE solver to predict the instantaneous reaction rates at the sub-grid model [Eq. (66)]. The strategy for the remaining cases (Case B and C) is

to test the ANN capabilities within the stand-alone LEM computations for different flames and kinetics mechanisms. Similar to Case A, the thermo-chemical database is constructed with stand-alone LEM computations, and the ANNs are trained on the data-base. Once training is achieved, ANN is used to replace the DI technique to assess the ANN accuracy. Multiple test simulations are conducted in each of the test cases (Cases A-C).

Case A is a series of LEMLES conducted for a premixed syngas (PSI (72))/air flame. The LEMLES cases are listed in Table 13. The LES cases are selected so that they can be compared with the earlier study (76), where the ANNs were trained using tables extracted from the FVI simulation. Here, we compare the baseline LEMLES using (a) stiff ODE solver (DI), (b) ANN trained on FVI (F-ANN) (76), (c) ANN trained on stand-alone LEM (L-ANN) (74), and (d) ANN trained on laminar premixed flame simulations (P-ANN) (73). The flame properties for the flames considered in the LEMLES computations are given in (76). For all cases the integral length scale (L) to the laminar flame thickness (L_F) ratio and the coherent vortex diameter (D_C) to the laminar flame thickness ratios are kept constant, and are selected to be 5 ($L/L_F = D_C/L_F = 5$). Thus, all the flames are in the thin reaction zone regime.

The LES for all these cases is initialized by using a 1D, laminar, steady solution for a premixed flame. Then, a pair of counter-rotating vortices are superimposed on an isotropic background turbulence to induce both large and small scale wrinkling of the flame front. The details of the initialization process can be found in our earlier studies (72; 73; 76). A 64^3 grid is used for all cases, and the grid resolution is approximately four times larger than the Kolmogorov length scale ($\Delta x = 4\eta$). For sub-grid scalar field evolution, 24 LEM cells are used within each LES grid, allowing a resolution of turbulent eddy in the sub-grid approximately of the order of η . The chemical kinetics is represented by a 14-species, 11-steps reduced skeletal mechanism. Based on the u' and L selected for each of the cases, the thermo-chemistry is extracted by running

stand-alone LEM computations for a fixed L and varying Re_t . The process of creating the LEM tables is described in detail later in Section 5.3.3.1.

The second series of test cases (Case B) are selected to construct the thermochemical state-space occurring inside the stagnation point reverse flow (SPRF) combustor (?). Rather than performing the actual LES, here we perform stand-alone LEM computations for the SPRF conditions and evaluate the performance of the ANNs within the LEM framework. Characteristic eddy size (L), fluctuating velocity (u') and the local viscosity obtained in a separate LEMLES of this combustor (?) are used to find the maximum Re_t . The characteristic eddy size (integral length scale) is selected to be the radius of the whole injector assembly ($L = 8.25 \times 10^{-3} \text{m}$). Also, previous LEMLES studies of this configuration obtained $u' \sim 10 \text{ m/s}$ (?). The stand-alone LEM computations are performed for 20 ($N_{Re_t}=20$) different Re_t values ranging from 10 to 400 for a fixed L . For the each different Re_t , both η and λ are changing, so the initial scalar field experiences different level of interaction. This is similar to the process observed in turbulent flames. It is also found that, as the N_{Re_t} is further increased, the states accessed by the LEM computations become nearly identical for two consecutive simulations, thus $N_{Re_t}=20$ is found to be an optimum value for this particular case.

The last case (Case C) is based on a DNS of a temporally evolving, plane jet, syngas/air flame from the literature (26). Similar to case B, stand-alone LEM is performed here to evaluate the ANN performance. The maximum Re_t for this case is reported to be 175 in the DNS study. Also, the integral length scale is roughly $H/3$, with H denoting the initial width of the jet velocity (26). The stand-alone LEM computations are performed for 20 ($N_{Re_t}=20$) Re_t values ranging from 10 to 180, for a fixed L .

It is noted that LEMLES of Cases B-C using the ANNs developed in this study are currently being conducted and these results will be reported in the next chapters.

The current section aims to establish the tabulation based on stand-alone LEM on different combustion modes and configurations. Hence, we focus primarily on the development and use of ANN for these test cases.

5.3.3 Results and Discussion

5.3.3.1 Description of the LEM tabulation and ANN training

LEM tabulation

For the premixed cases (Case A and B) the initial profile is calculated as function of the equivalence ratio and the reactant temperature. For the non-premixed simulations, however, strain rate is an additional parameter to the thermodynamic variables. From the LEM perspective, once the non-premixed simulations are started from an initial strain rate, the small scale turbulent structures will change the straining locally resulting in different scalar field evolution based on the Re_t and L . Hence, non-premixed LEM computations (Case C) are initialized for a relatively lower strain-rate than the one used in the DNS computations (26). During the simulation it is expected that the database created with LEM computations will cover a broader range in the compositional state-space, compared to the case initialized by a strain rate very close to the extinction. As will be discussed later, an increase in Re_t results in flame extinction although the initial strain rate is very low.

Once the scalar field is initialized, the stand-alone LEM for all cases is run with a given time step size (Δt). Here it should be noted that, for the given Δt , both turbulent stirring and molecular diffusion proceeds with sub-iterations with their respective time steps (Δt_{stir} , Δt_{diff}). Thus, the LEM evolution is independent of Δt .

For two LEM computations with different Re_t , the number of stochastic turbulent stirring events per given time interval (Δt) is distinct, which results in a different level of flame-turbulence interaction process. Also, the diffusion process counteracts turbulent stirring at its own time and length scale. A typical picture demonstrating these

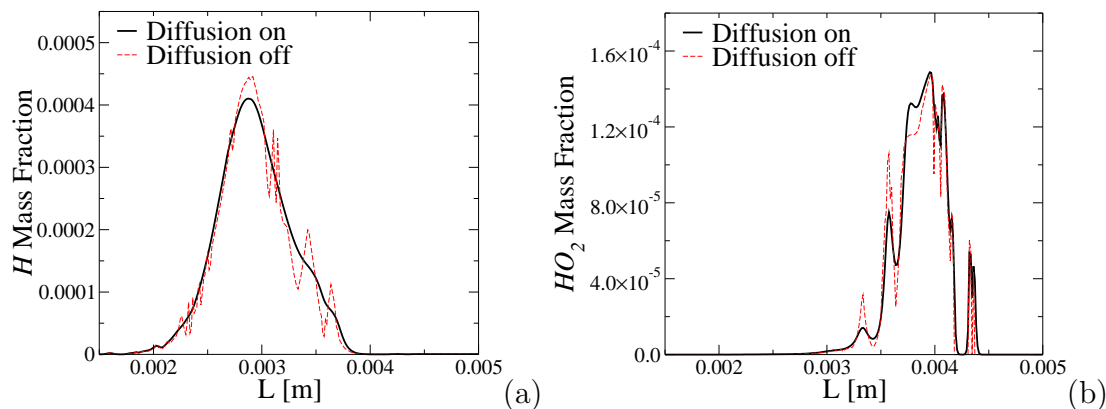


Figure 32: Effect of diffusivity for different species.

unsteady interactions is shown in Fig. 32 for Case C. For the given Re_t , the dashed lines represent the LEM result obtained without simulating the effect of diffusion. The LEM computation with diffusion turned on exhibits smooth variation for both of the species. Here, first thing to note is that the scalar profile obtained for HO_2 is highly wrinkled, whereas H seems almost not affected by the turbulent stirrings. This is a direct result of using non-equal diffusion coefficients for the species. Hence, HO_2 is more sensitive to the turbulent forcing, which can be captured through LEM diffusion sub-iterations.

ANN training

Once the LEM database is created, the instantaneous species reaction rates corresponding to each state are calculated and added to the look-up table, which is used for ANN training. Since each LEM iteration requires a certain number of diffusion and stirring sub-iterations, the generated database cannot be expected to contain all the available states. Such an attempt would require tabulation of a table of N_s dimensions, which is probably not affordable for large chemical mechanisms. However, if well trained, ANN has the potential to fill out the gaps between the existing states in the database and provide predictions to the states that it was not trained for. This is one of the goals of this section.

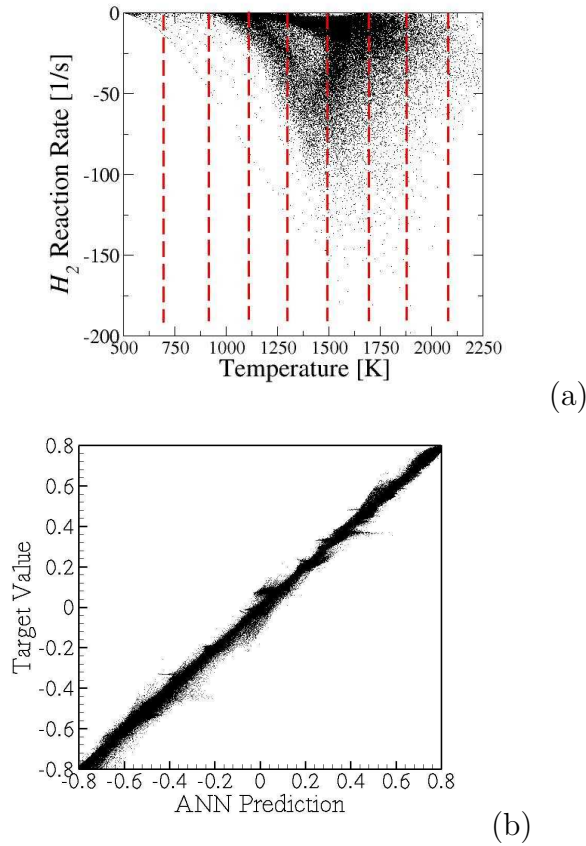


Figure 33: (a) Thermo-chemical database accessed by the 1D-LEM solver. (b) Correlation obtained by the ANN testing

The temperature- H_2 reaction rate hyperplane from the training table generated for test Case C is shown in Fig. 33 (a). There are approximately 5M states included within the training table. In order to increase the sensitivity of the reaction rate calculations with respect to the temperature, the whole database is divided into nine equi-distance temperature bins. The number of bins are selected so as to leave at least 100K datapoints at each bin to achieve a proper training. The boundaries of each temperature bin is shown with dashed lines in the figure. Once all states are divided into temperature bins, ANN training is achieved for each bin separately. A multi-layer perceptron type of ANN is used for the training with arbitrary number of hidden layers and PEs. The inputs for the ANNs are the species mass fractions and

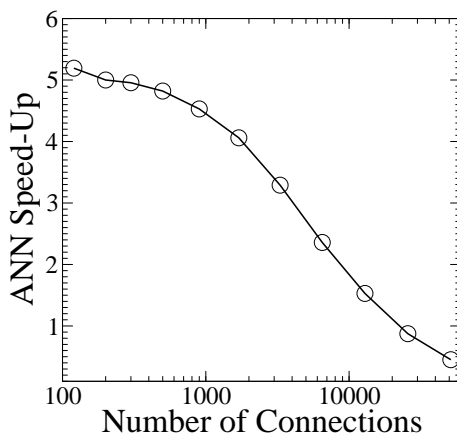


Figure 34: ANN speed-up with respect to the number of connections.

the temperature, whereas the output is the reaction rates of all species.

Approximately 85 % of the database is selected randomly and used for training the selected ANN architecture. The remaining 15 % of the database (test table) is then used for testing the ANN during the training phase. There is no general rule that exists to determine the exact proportions of the training to testing database, and different studies in the literature uses different values (see (32? ; 29)). For this particular study the aim is to use as much as data for ANN training as possible in order to increase the ANN sensitivity to the LEM created database. In order to avoid over-training, which would cause ANN to memorize the training data and may prevent it from being general, the training is stopped if there is no improvement for consecutive iterations. The selection of the number of hidden layers and number of PEs for each hidden layer is an important issue that has to be handled with care. In the current study, the optimum ANN is selected by experimenting with different ANNs based on the speed-up provided and the RMS error achieved.

A typical correlation curve obtained during the training phase is given in Fig. 33 (b). Here, the y axis is the actual value of the test data, whereas x axis denotes the ANN predictions. The figure shows the correlation obtained for all temperature bins, and for all the species, and proves that a good correlation is achieved on the

training phase. The correlation curve shown in Fig. 33 (b) is obtained for an ANN architecture with 5, 3, 2 number of PEs at each hidden layer, respectively (hereafter, identified as 5/3/2 ANN). The selection of the number of hidden layers and number of PEs for each hidden layer is an important issue that has to be handled in care. In the current section, the optimum ANN is selected with experimenting different ANNs based on the speed-up provided and the RMS error achieved.

It is known that the number of floating point operations for a given ANN is a function of the number of connections between each PE, as it was shown in Section ???. Figure 34 shows the ANN speed-up against using a stiff ODE solver with respect to the number of connections, and it is seen that the maximum speed-up that can be obtained for this particular reduced mechanism is slightly larger than 5. As the number of connections are increased, the speed-up decreases, and at 500 it is almost 4 % less than the ideal speed-up, which is still an acceptable value. Beyond 500, however, ANN speed-up seems to be more sensitive to the changes in the number of connections and it decreases exponentially. Eventually beyond 20K connections, ANN is slower than using a stiff ODE, which suggests that there should be a limit for the number of connections used in ANN computations. For this particular study, the limit is approximately 500, since it gives the best speed-up with respect to the number of connections. Nevertheless, the exact ANN architecture should be defined not only based on the ANN speed-up, but also the ANN training error. The selection of a limit for 500 connections would only be meaningful if the error associated with the ANNs having connections less than 500 correspond to an acceptable ANN training error.

The above approach is not optimal, since in general, the exact ANN architecture should be defined not only based on the ANN speed-up, but also the ANN training error. The selection of a limit for 500 connections would only be meaningful if the error associated with the ANNs having connections less than 500 correspond to an

acceptable ANN training error. The error and the number of connections for some of the tested ANNs are summarized in Table 15. Here, the ANN error is calculated as :

$$E = \log_{10} \left(\frac{1}{N_{test}} \sum_{k=1}^{N_{test}} \frac{1}{2I} \sum_{i=1}^I [d_i - y_i[k]]^2 \right) \quad (131)$$

which is an average over the number of PEs at the output layer (I) and number of test samples (N_{test}). As seen in the Table 15, the ANN training error (E) varies between -3.521 to -4.870, with the latter obtained for a 3 hidden layer ANN architecture with 20, 10, 5 number of PEs at each hidden layer, respectively (hereafter, identified as 20/10/5 ANN). However, the number of connections for this particular ANN is 1240, which is beyond the optimum limit obtained from speed-up analysis. It has been observed that the ANN error (Eq. (76)) for the architectures with more than 500 connections is less than -4. Among the ANNs tested in this study that has number of connections less than 500, this condition can only be satisfied for 1 hidden layer ANN with 20 PEs and 3 hidden layer ANN with 5, 3, 2 PEs at each hidden layer, respectively (5/3/2, hereafter). As the 5/3/2 ANN has less number of connections than the 20 ANN, it is selected as the optimum ANN for this test Case C.

Table 15: List of ANN architectures and their properties used for Case C

ANN	Error	Connections	Time/(Iter×Sample)
5	-3.521	230	1.922×10^{-5}
10	-3.801	340	2.021×10^{-5}
20	-4.056	460	2.279×10^{-5}
5/4	-3.889	358	2.058×10^{-5}
10/5	-3.920	500	2.199×10^{-5}
20/5	-4.114	770	2.437×10^{-5}
20/10	-4.619	1080	2.635×10^{-5}
5/3/2	-4.201	371	2.060×10^{-5}
10/5/2	-4.327	574	2.259×10^{-5}
20/10/5	-4.870	1240	2.813×10^{-5}

It is noted that recently an automatic way of defining the optimum number of PEs for the given hidden layers has been proposed in the literature (28; 29) (O-ANNs),

and the applicability of this approach with our new learning rule will be evaluated in the future for LEM based tabulation procedure. The approach used so far evaluated the ANN speed-up and the training error (E) for a certain number of candidates, and further optimization is possible. However, it should be noted that the ANN training error cannot be expected to be an absolute ANN error in the LES. It is rather a measure of how well the current ANN is predicting the states in the test table on an *average* sense. These states may never be accessed in the LES computations, or the LES may access a sub-space of the results where the ANN training error is locally large. Hence, as long as the training error for a given ANN architecture is less than a given value (i.e., -4.0 for this case) it is assumed that the ANN is trained well and fine tuning is not necessary. However, this is an issue for future studies.

The time required to do one training iteration per number of training and testing samples for the current ANN approach is given in Table 15. For the optimum case, with approximately 500K number of samples and 500 iterations (which is typical number of training iterations), it takes only 1.4 hours on a PC (Pentium 4, 2.40 GHz) to finish the training, which is considerably quite reasonable. Of course, this cost may change with larger skeletal mechanisms and is an issue currently being investigated.

5.3.3.2 Case A - LEMLES of turbulent flame-turbulence-vortex interaction

The LEMLES cases are selected based on our earlier study (76), and are listed in Table 13. For the each given test case, the LEMLES is carried out using different kinetics evaluation strategies (DI, F-ANN, L-ANN, and P-ANN). The F-ANN is identical to the one used in our earlier calculation (76), and the whole methodology of creating the data-base and ANN training is not repeated here for sake of brevity. The training table for P-ANN is constructed based on performing laminar, 1-D, premixed flame calculations for multiple equivalence ratios. Our previous observations on premixed flames revealed that the species mass fractions may locally deviate from that obtained

from the laminar flame calculations as a result of the unsteady mixing induced by the flame-turbulence interaction (73). Hence, rather than creating a table for a single equivalence ratio (Φ), the training table is formed for multiple-equivalence ratios, by changing Φ from 0.4 to 1.10, with a step size of 0.001 ($\Delta\Phi = 0.001$). The final training table includes approximately 482K total entries. For L-ANN, the training table is constructed similar to the way explained in Section 5.3.3.1. The stand-alone LEM code is run for a fixed L ($L = 5 \times L_f$) and varying Re_t , for the values given in Table 13. The optimum ANN based on F-ANN for this case was previously found to be a three hidden layer 10/5 architecture (76). It should be noted that the optimum ANN architecture depends highly on the training data, and should be different for each F-ANN, P-ANN and L-ANN. However, for comparison purposes, same ANN architecture is used for all ANN models considered in Case A.

The time-averaged and instantaneous species profiles obtained across the flame front at mid- y and z planes is used to evaluate the different ANN methodologies, and to compare them with the DI computations. The time averaged results for the variation of a major (H_2) and two intermediate species (H , O) across the flame front for Case A1 are presented in Figs. 35a-c. Other species show qualitatively similar trends and therefore not shown for brevity. Here, dots represent the LES results with DI, dashed lines P-ANN, dash-dot lines F-ANN and straight lines L-ANN. The agreement between all ANN models are acceptable for H_2 as seen in Fig. 35a. However, for H (Fig. 35b), the P-ANN exhibits the most error, with almost 1.5 times larger values than the DI predictions. P-ANN overpredicts the O mass fraction as well (Fig. 35c), suggesting that it is not very accurate for minor species prediction. The F-ANN successfully follows the same profile calculated by DI computations for all species with an acceptable error, which is in consistency with our previous observations (76). The L-ANN, on the other hand, is even better than F-ANN for this case, showing almost identical variation with DI.

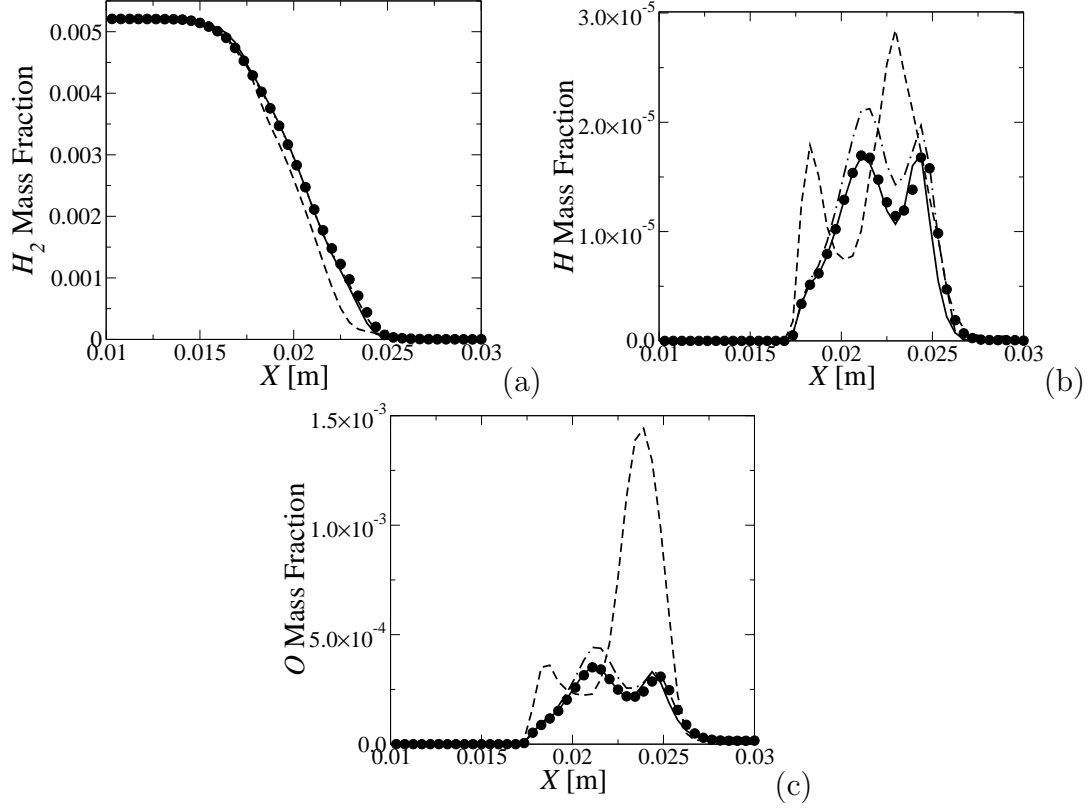


Figure 35: Comparison of the time-averaged species profiles obtained by the DI (\bullet), the P-ANN (---), F-ANN (- . - .), and L-ANN (—) for Case A1.

The corresponding instantaneous results for species H_2 , H and O at $t = 5t^*$ is shown in Figs. 36a-c for Case A2, respectively. The non-dimensional time (t^*) is calculated based on the maximum velocity induced by the initial coherent vortex and its size (u' , D_C). At this instant, the results obtained by P-ANN is not following the same trend even for the major species H_2 , and denotes an early consumption of the fuel (36a). This is supported by the fact that the peak value for H is reached at approximately 0.022, whereas DI results detect the peak at 0.028, as seen in Fig. 36b. P-ANN results are not shown for O mass fraction in Fig. 36c, since it exhibits large amount of error compared to the other ANN models. Similar to Case A1, the F-ANN and L-ANN results are comparable with each other with an acceptable error. The L-ANN results seem to be slightly shifted towards the reactants for both of the

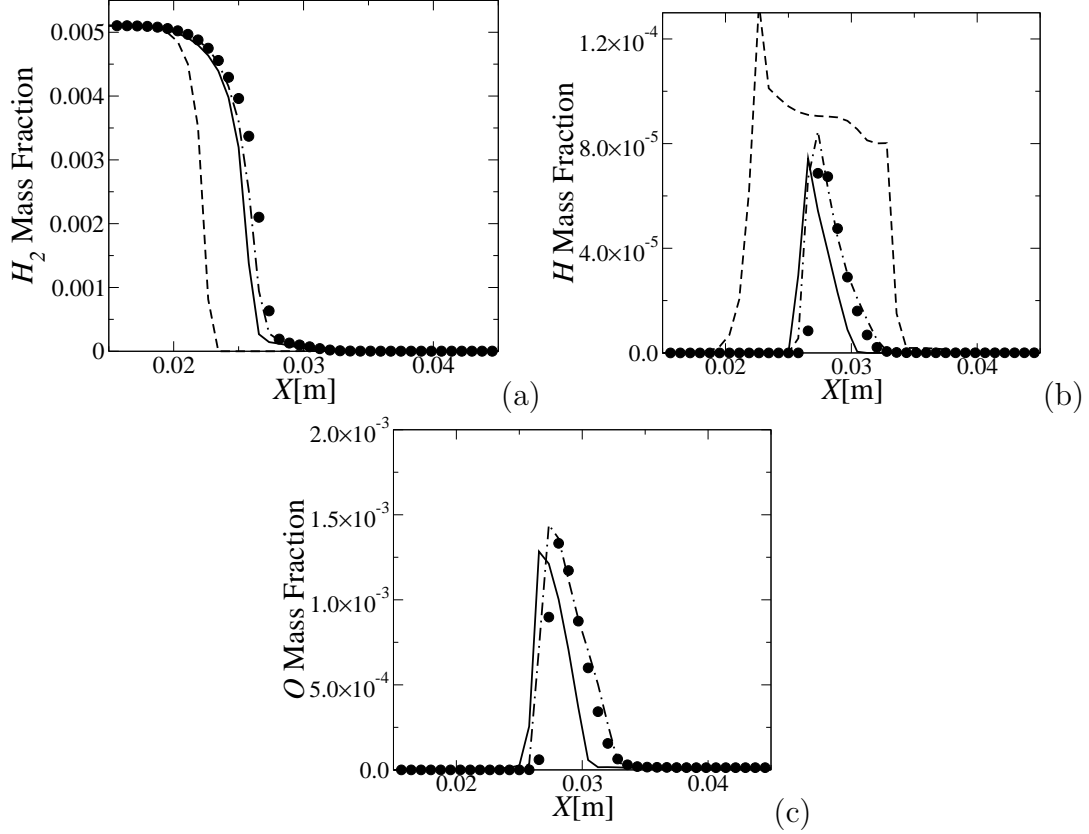


Figure 36: Comparison of the instantaneous species profiles obtained by the DI (\bullet), the P-ANN (---), F-ANN (- . - .), and L-ANN (—), at $t = 5t^*$ for Case A2.

minor species.

Figs. 37a-c (Case A3) shows the instantaneous species mass fraction profiles at $t = 5t^*$ for an equivalence ratio of 0.8, and a higher background turbulence intensity compared to Cases A1 and A2. The equivalence ratio is an indirect input to the F-ANN and L-ANN computations through the initial data profile used to run both 3D simulations and the stand-alone LEM. Hence, a different ANN is used for F-ANN and L-ANN in Case A3, than the previous cases, whereas P-ANN is not changed. Interestingly, the P-ANN underpredicts the actual profiles of the minor species as seen in Figs. 37a-c at $t = 5t^*$ for Case A3. This indicates a non-complete combustion process, which is supported by the H_2 plot (Fig. 37a) as well. The H_2 mass fraction exists at locations where it should have been consumed as calculated by the DI.

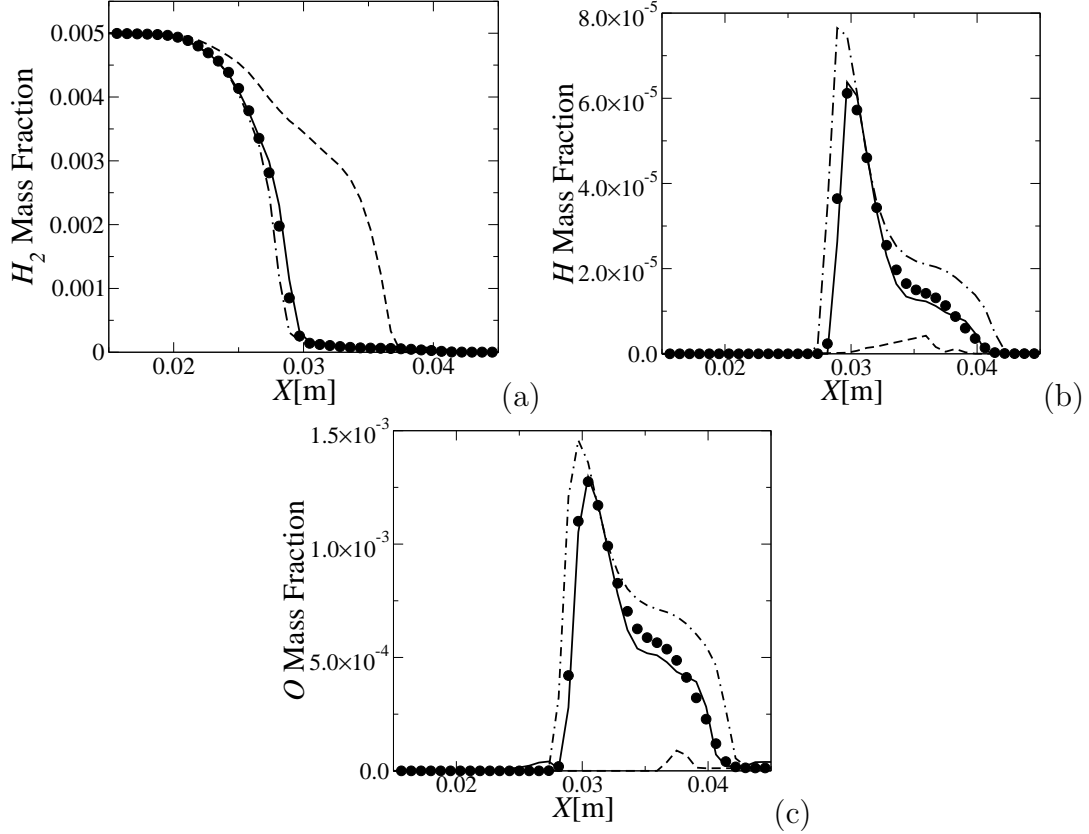


Figure 37: Comparison of the instantaneous species profiles obtained by the DI (\bullet), the P-ANN (---), F-ANN (- . - .), and L-ANN (—), at $t = 5t^*$ for Case A3.

Results obtained by F-ANN is very accurate in capturing the variation of H_2 , similar to the previous cases. The location of the reaction zone is also detected well, with a slight overprediction of the peak value of the mass fractions. The maximum deviation is 7 % for the O mass fraction. The L-ANN results for this case exhibit better agreement with the DI computations than the F-ANN.

Finally the instantaneous profiles for H_2 , H and O species obtained at $t = 5t^*$ for Case A4 are given in Figs. 38a-c. This case is for the same initial turbulence quantities with Case A3, but, for $\Phi = 0.8$. Hence, the same ANN used for cases A1 and A2 is used for A4. The increase in initial turbulent intensity resulted in flame thickening compared to case A2, as seen in the plots. Similar to that is observed in A3 (Figs. 37a-c), the P-ANN tends the underpredict the correct profiles, and is

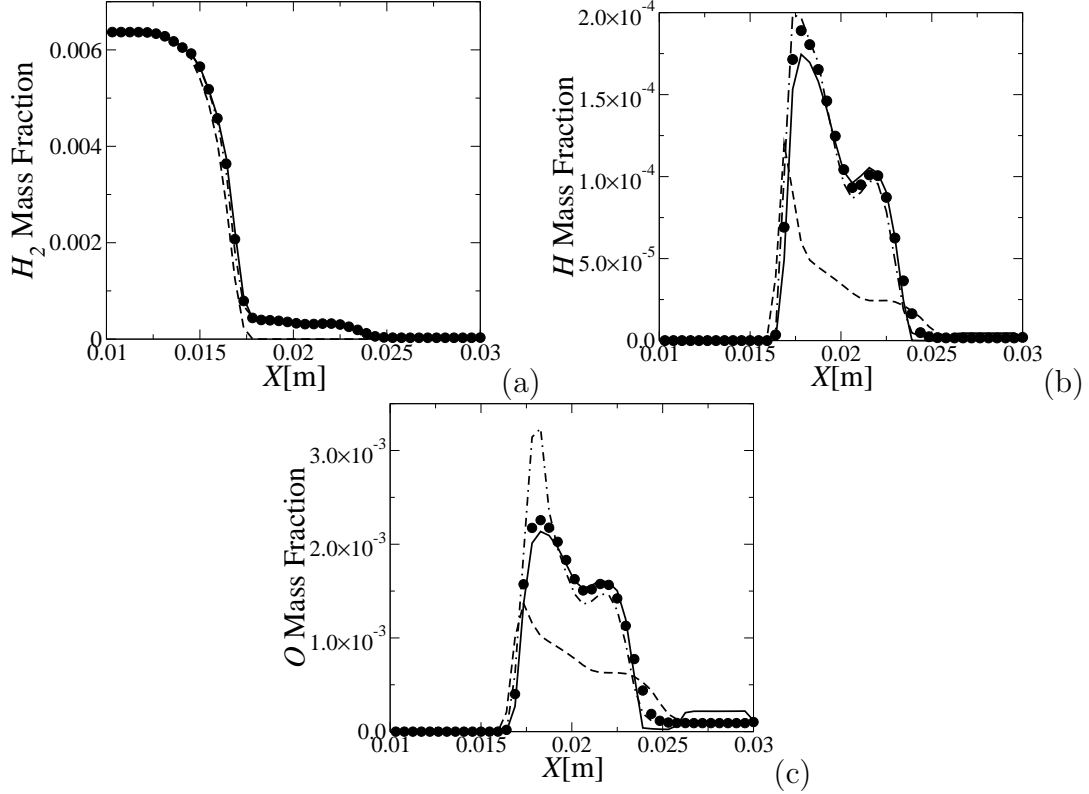


Figure 38: Comparison of the instantaneous species profiles obtained by the DI (\bullet), the P-ANN (- - -), F-ANN (- . - .), and L-ANN (—), at $t = 5t^*$ for Case A4.

wrong for all species.

5.3.3.3 Case B - LEM studies of premixed methane/air flames

The LEM is initialized based on the solution obtained from a steady, laminar, one-dimensional premixed methane/air flame computation at an equivalence ratio of 0.6. A 16-species, 12-step skeletal mechanism is employed for chemical kinetics calculations (83). The details of this mechanism is given in the Appendix. A database is constructed for a range of Re_t with a fixed integral length scale L . The recent LES data on the SPRF combustor (88) reveals that the maximum value of Re_t is of the order of 400. Hence, the Re_t is varied from 10 (diffusion dominated) to 400 (turbulent stirring dominated). The thermo-chemical state-space is recorded at every five iterations, and later the instantaneous species reaction-rates are calculated and stored in

a training table. The LEM computations are run for a number of iterations up to 1000 number of iterations ($N^* = 10$). The optimum ANN architecture is found to be a three hidden layer architecture with ten, eight and four (10/8/4) number of PEs at each hidden layer.

The comparison of the LEM results for species CH_4 , H_2O , OH and CO obtained by DI and ANN at $Re_t = 92$ is shown in Figs. 39a-d at $N = 15N^*$. The integral length scale for this case is larger than the laminar flame thickness of the premixed flame. Hence, for the given turbulent Reynolds number, the flame front is distributed more effectively by turbulent stirrings than Case C, as it is shown in Fig. 32. The turbulent stirrings create multiple flame crossings at each instant. The agreement between the ANN and DI predictions is fairly good within the flame brush. As it is seen in Fig. 39c, the only discrepancy is observed for OH mass fraction at approximately $L = 0.06$ m.

Figs 40a-d shows the profiles obtained by ANN and DI for CH_4 , H_2O , OH and CO at a higher turbulent Reynolds number ($Re_t = 290$). At this Re_t the number of grid points across the flame front increases, since η decreases. Consequently, the number of turbulent stirrings per time step increases with a decrease in the characteristic eddy size. Hence, the flame front exhibits more small scale flame wrinkling as shown in the figure. This causes a thicker turbulent flame brush compared to that of shown in Figs. 39a-d for a lower Re_t . Regardless, the agreement between ANN predicted and DI computed profiles is unaffected by Re_t

Finally, the evolution of the minor species mass fractions are given in Fig. 41 for $Re_t = 290$. Here, the results up to $N = 30N^*$ is shown to assess the ANN accuracy, which is well beyond the limit ($N = 30N^*$) used to extract the thermo-chemical state-space. As seen in the figures, the species mass fractions exhibit sudden jumps during the computations. This is a result of the turbulent stirring process. As it was mentioned before, the characteristic eddy size ($L = 0.008$ m) for Case B is larger than

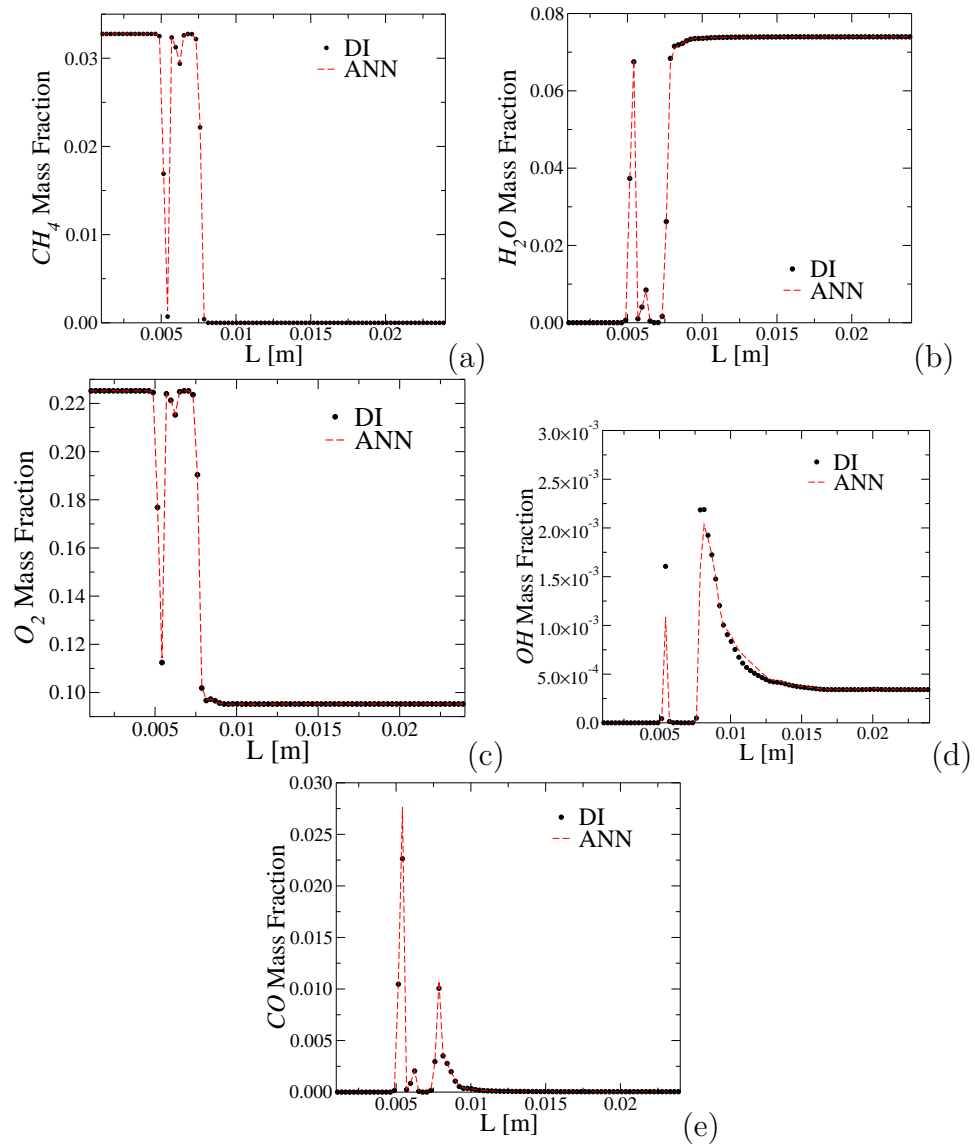


Figure 39: Instantaneous scalar profiles obtained for $Re_t = 90$ and at $N_{iter} = 15N^*$: Case B.

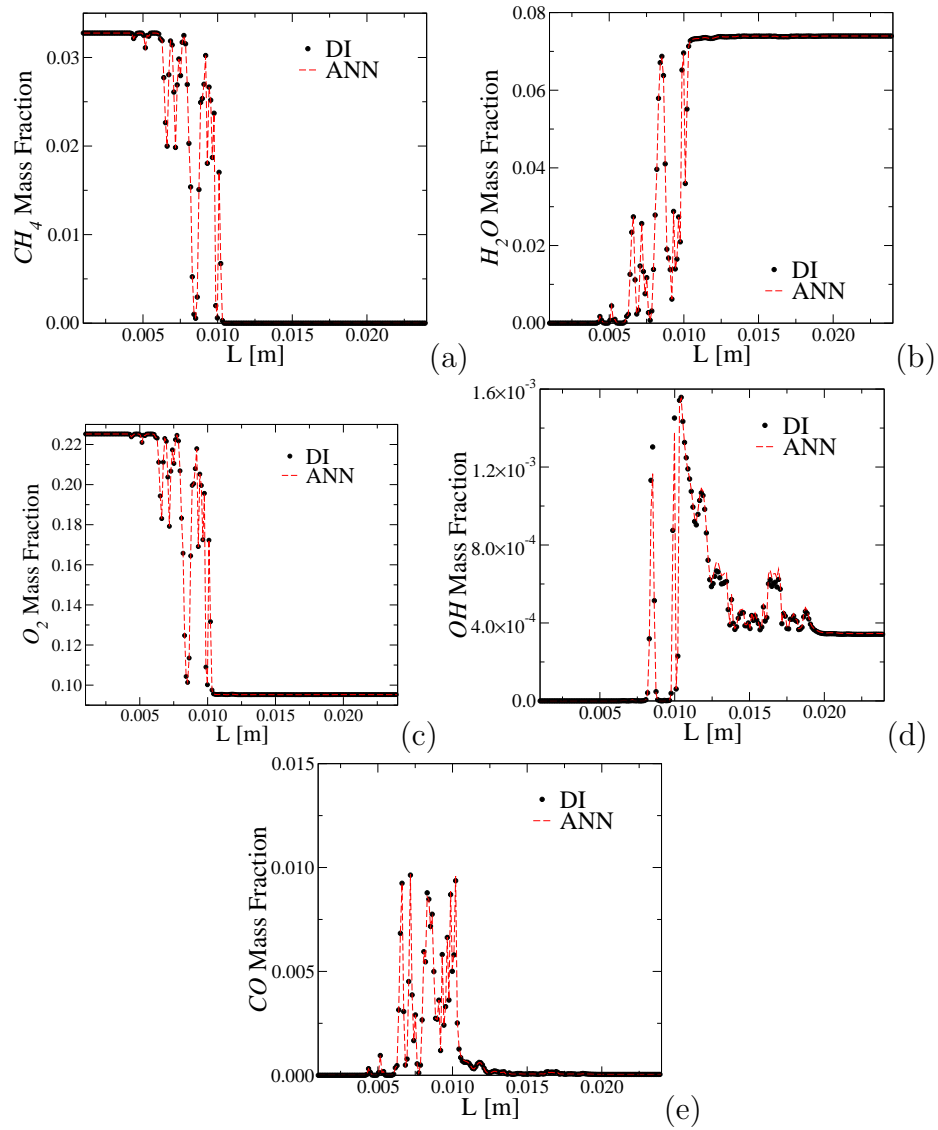


Figure 40: Instantaneous scalar profiles obtained for $Re_t = 290$ and at $N_{iter} = 5N^*$: Case B.

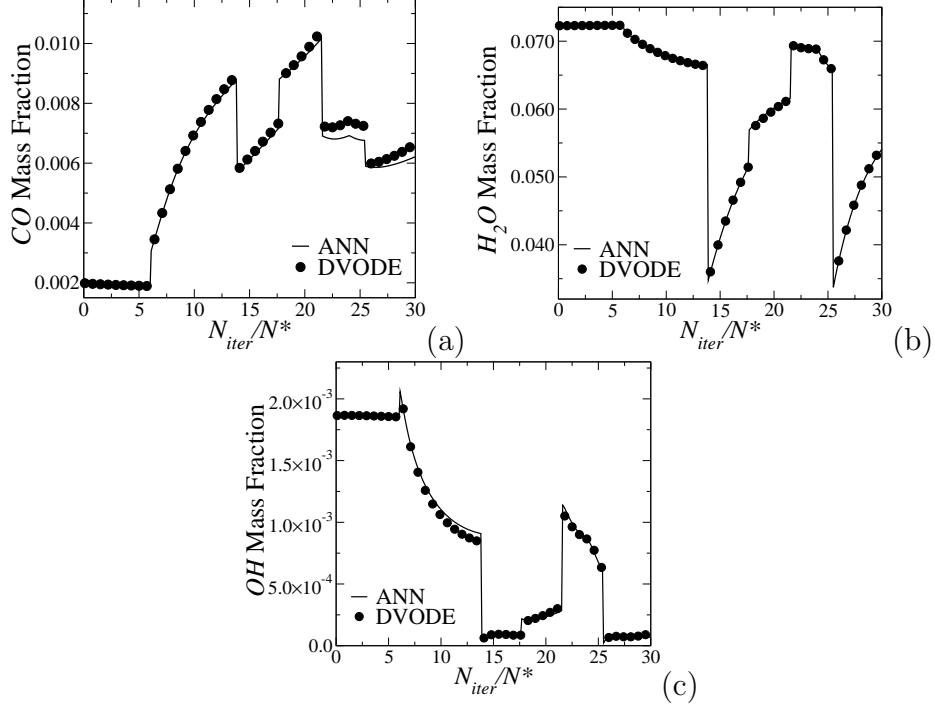


Figure 41: Time evolution of the scalar profiles for $Re_t = 290$

the laminar flame thickness, resulting in large scale mixing process within the flame region. Still, the ANN and DI profiles are matching quite well as seen in the figure.

5.3.3.4 Case C - LEM studies of non-premixed syngas/air flames

The initial scalar dissipation rate is selected to be $\chi = 0.50\chi_q$, with χ_q denoting the extinction scalar dissipation rate ($\chi_q = 2194\text{s}^{-1}$). Here, stand-alone LEM computations are run for 2000 iterations ($N_{iter} = 2000$) with a time step (Δt) size of 4.510^{-8} s ($t_j = 20$), at which, the DNS study reports considerable amount of local extinction occurs. Similar to the DNS study, the non-dimensional time (t_j) is calculated by using the width of the fuel slab (H) and the characteristic jet velocity U (26). Δt is selected in accordance with an LES study performed for the same case (74). As noted earlier, the LEM is independent of Δt as stirring and diffusion proceeds with their own time step sizes.

The mean value of the PDF of OH mass fraction conditioned on the mixture

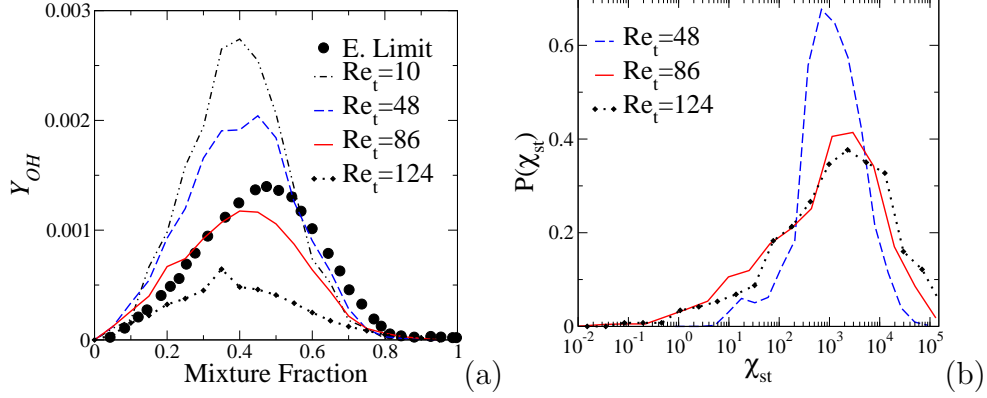


Figure 42: Conditional means of OH mass fraction and χ_{st} with respect to the mixture fraction for Case C.

fraction ($Y_{OH}|Z$) is shown in Fig. 42a for four different Re_t values at approximately $t = 20t_j$. The laminar flamelet value at extinction (extinction limit) (26) is also presented for comparison purposes. For a very low Re_t (i.e., $Re_t = 10$), the initial profile remains almost unaffected by the turbulence, which is consistent with our previous observations. As the turbulent Reynolds number increases, the flame is pushed towards extinction and the LEM data agrees well laminar flamelet at approximately $Re_t = 86$, denoting that LEM predicts extinction at this turbulent Reynolds number. As the Re_t is increased beyond 86, the LEM profiles demonstrate increased level of extinction. The PDF of the scalar dissipation rate at the stoichiometric mixture fraction $P(\chi_{st})$ is given in Fig. 42 (b) for the same conditions shown in Fig. 42 (a). Scalar dissipation rate is calculated as $\chi_{st} = 2D(\partial f/\partial s)(\partial f/\partial s)$, where f is the mixture fraction calculated by Bilger’s definition and D is the mixture diffusivity calculated with a unity Lewis number assumption (26). Here, it is seen that the tails of the PDF spreads-out as the Re_t is increased. Also, the mean value of $P(\chi_{st})$ shifts towards higher values of scalar dissipation rate as Re_t is increased, and is approximately 2300 s^{-1} for $Re_t = 86$. The DNS study reports that the extinction scalar dissipation rate is 2194 s^{-1} . The current LEM prediction is close to this value suggesting that some of the underlying physics has been captured in our LEM simulation.

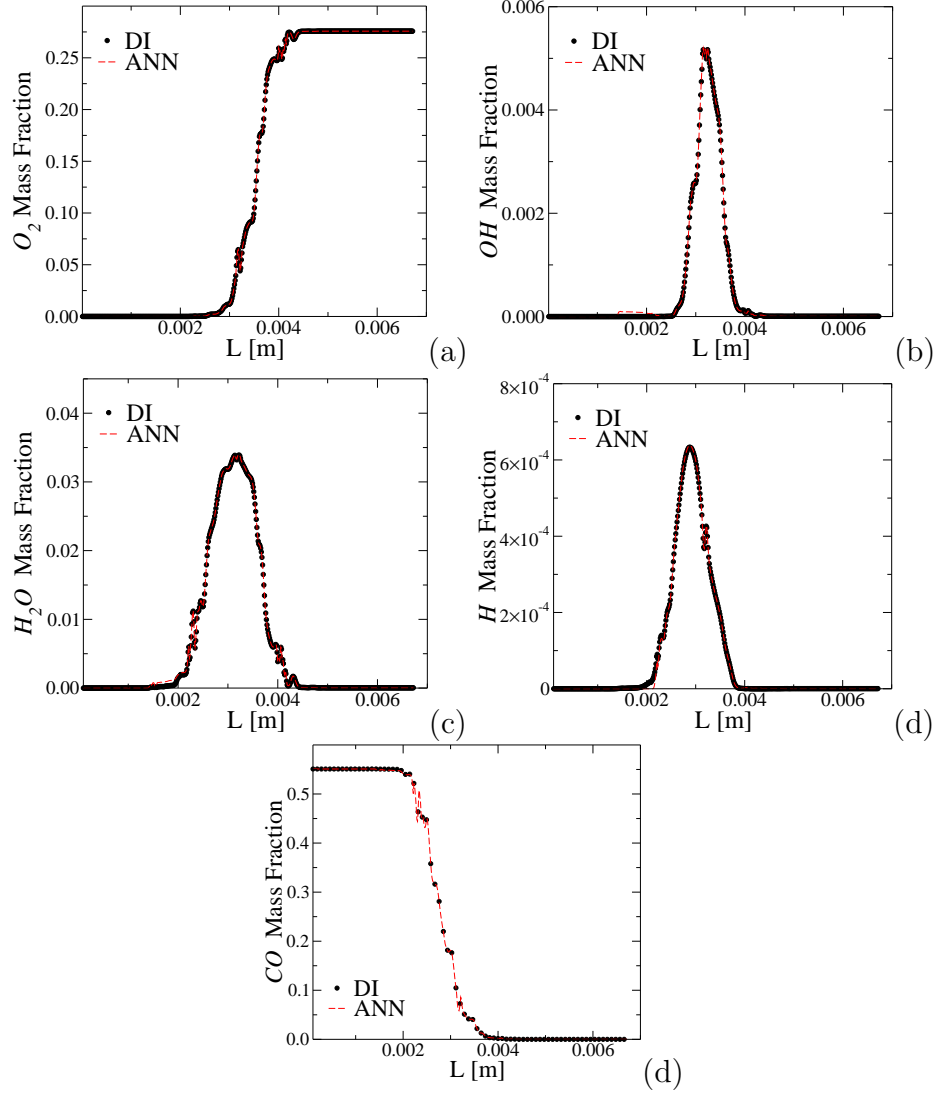


Figure 43: Instantaneous scalar profiles obtained for $Re_t = 20$ and at $t = 10t_j$: Case C.

In order to evaluate the generalization of the trained ANNs, the stand-alone LEM simulation is repeated, by using the trained ANN for the chemical-kinetics. The species profiles obtained for O_2 , OH , H_2O , and H are given in Figs. 43a-d, respectively, for $Re_t = 20$ at $t = 10t_j$. As demonstrated earlier, at $Re_t = 20$, the flame is diffusion dominated, and turbulence cannot cause an effective flame front wrinkling. The discrepancy between the ANN predictions and the DI calculations is indistinguishable from each other, which suggests that ANN is working excellently for this

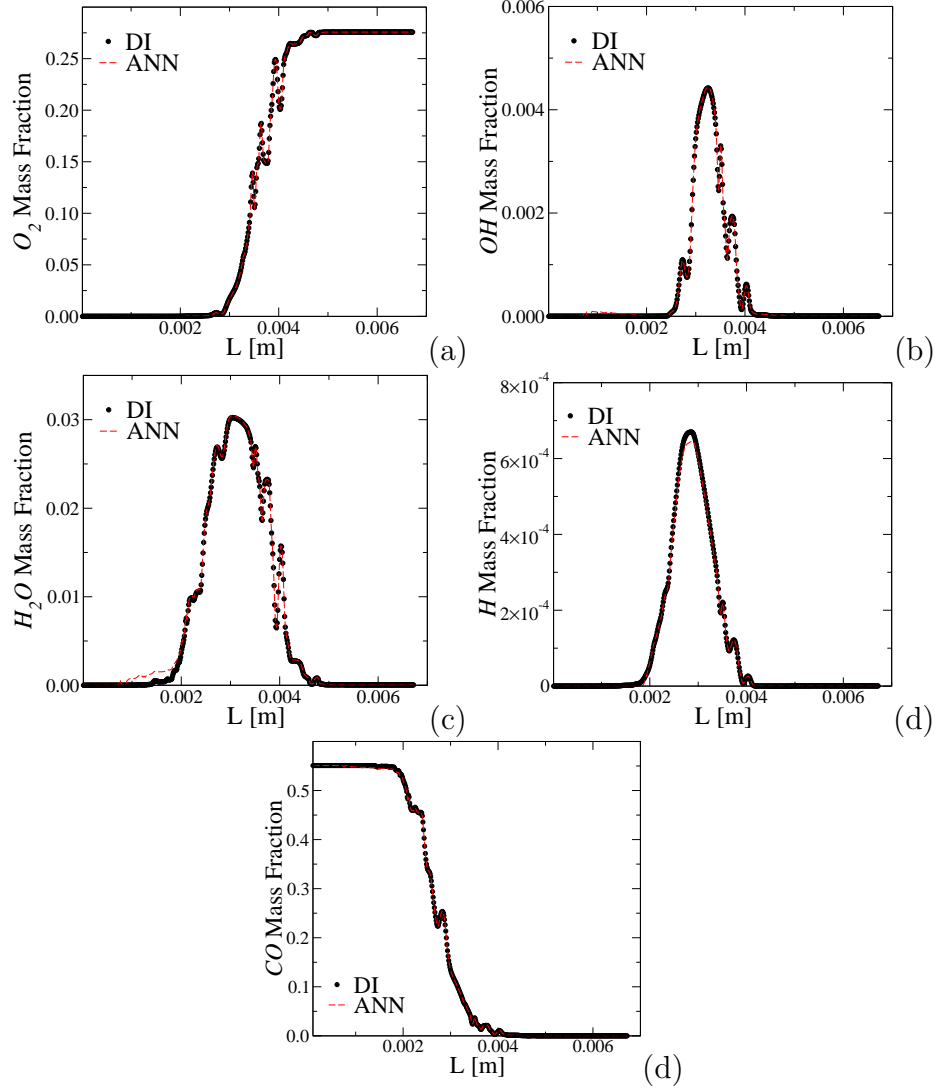


Figure 44: Instantaneous scalar profiles obtained for $Re_t = 20$ and at $t = 25t_j$: Case C.

relatively low Re_t . To test the ANN capacity, the number of iterations are further increased to 2500 ($t = 25t_j$), which is beyond the training database. As seen in Figs. 44a-d, small deviations tend to appear at this late time. This is most apparent especially at the peak value of H (Fig. 44d) and in the post flame region of H_2O (Fig. 44c).

For a higher turbulent Reynolds number ($Re_t = 80$) the time variation of some of the key minor species mass fraction (OH , H_2O , H) obtained by using DI and

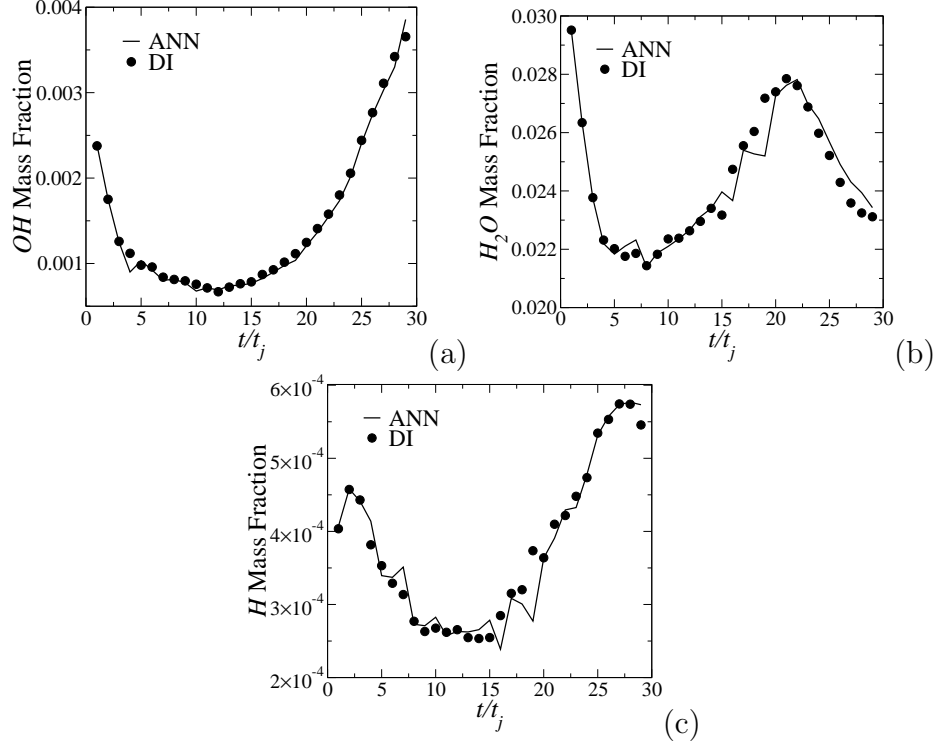


Figure 45: Time evolution of the scalar profiles for $Re_t = 80$ at a location within the flame zone : Case C.

ANN are in fair agreement. This is demonstrated in Figs. 45a-c at a location within the flame zone, where the reaction rates for the species are at their maximum value. Here, results at every 100 iterations are shown for both of the simulations. For t/t_j between 15 and 22 there is some discrepancy between the ANN and DI, although the error is less than 1 %. In order to understand if this discrepancy is systematically created and is enhanced by the ANN predictions or not, the time averaged results are shown in Figs. 46a-d for the same Re_t . The flame front exhibits smooth profiles for all species, since time averaging smoothens the small-scale wrinkling of the flame front. Overall, the agreement between the DI and ANN predicted results is quite good. This suggests that there can be small discrepancies in the instantaneous scalar profiles, but they do not provide major prediction errors on a time averaged sense. It still needs to be proved if this is a general conclusion or not, and will be investigated further in the future.

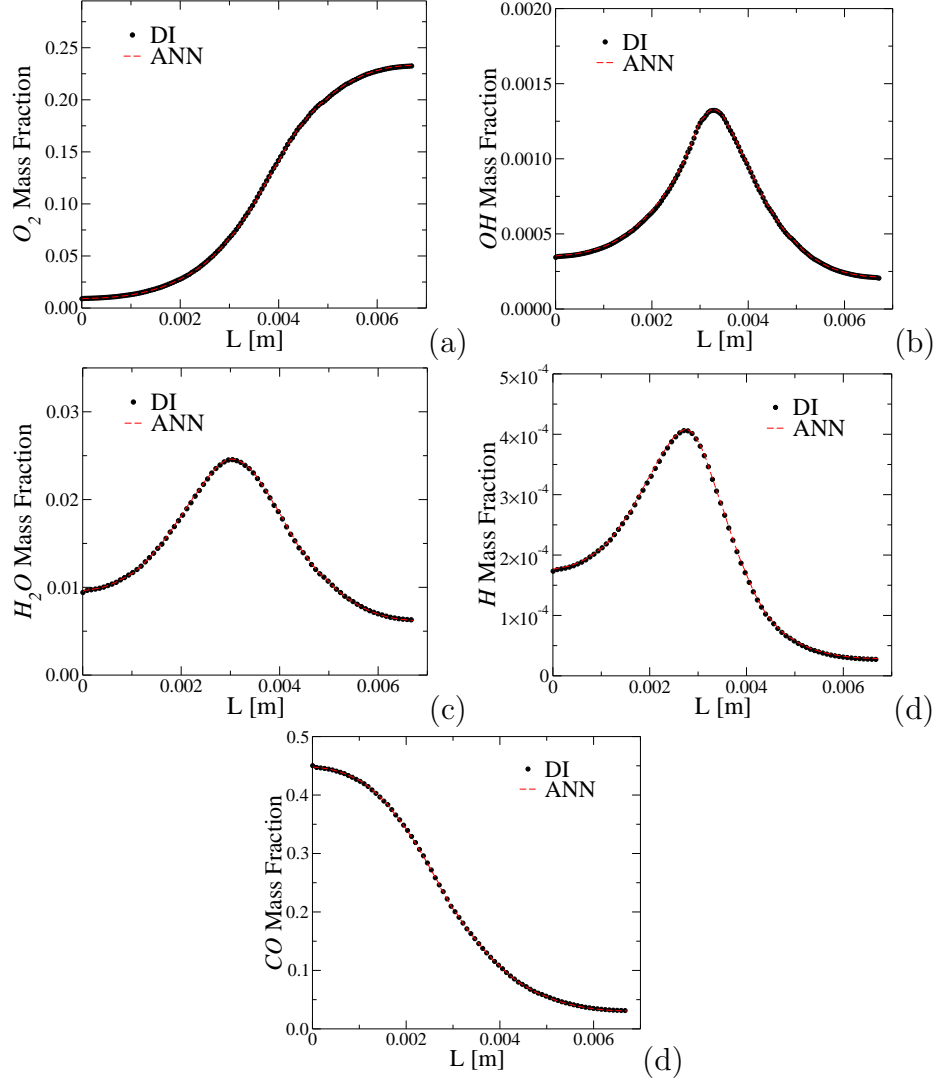


Figure 46: Time averaged scalar profiles obtained for $Re_t = 80$: Case C.

Finally, the accuracy of ANN at a turbulent Reynolds number that it was not trained for ($Re_t = 70$) is investigated, and the results are given in Figs. 47a-d for the same species at $t = 15t_j$. The results are overall very similar to what was observed for $Re_t = 20$ and $Re_t = 80$. There is substantial amount of small-scale flame wrinkling and spreading-out due to turbulence. The intermediate species exhibit increased level of mass fraction at $s = 0$ and L , respectively. The agreement between ANN and DI is still acceptable suggesting that ANN can provide predictions for a Re_t that was not in the training data-base.

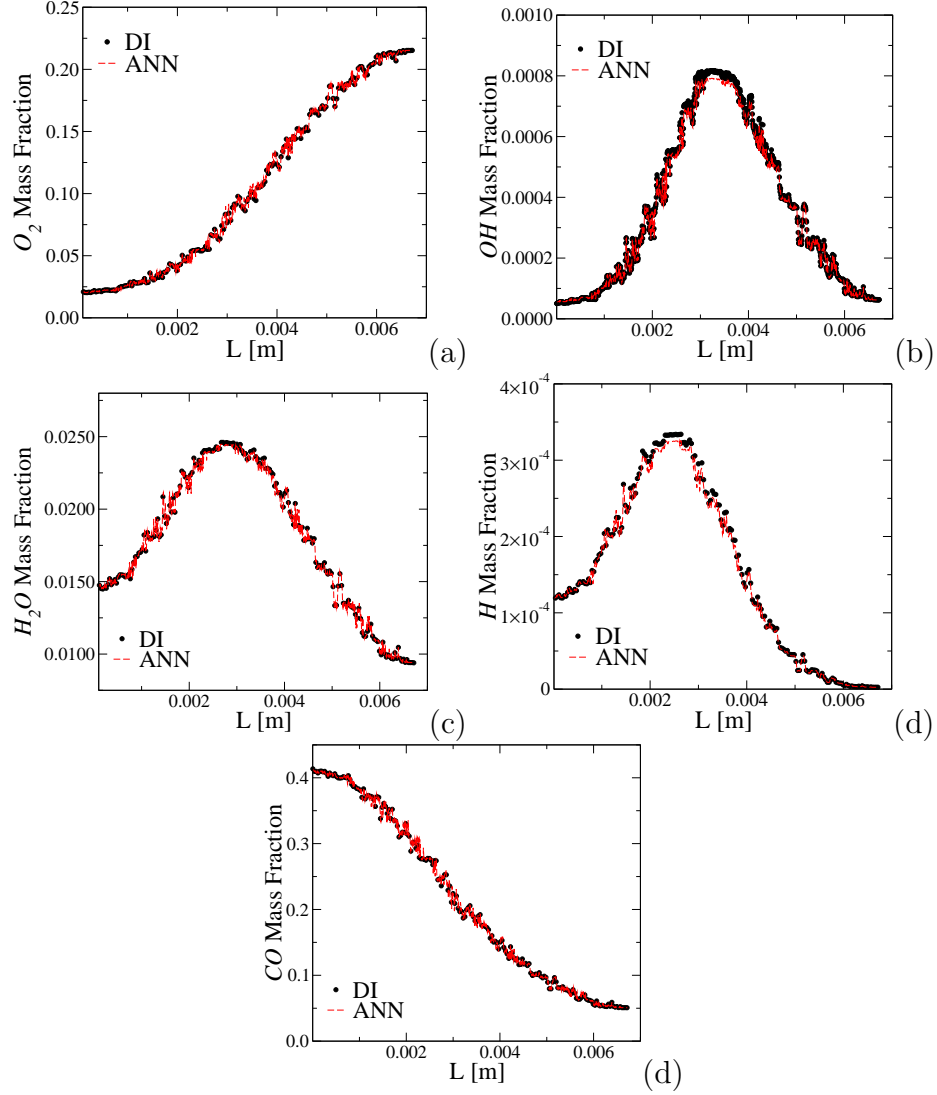


Figure 47: Instantaneous scalar profiles obtained for $Re_t = 70$ and at $t = 15t_j$ - Case C.

5.3.4 ANN Speed-Up and Memory Savings

The speed-up achieved by all ANNs considered for Case A is identical, and approximately 11X, since the same ANN architecture (10/5) is used for the LES cases. The memory saving is different for each distinct ANN method, since the training tables are different. As given in Table 16, there is considerable amount of memory saving achieved by using ANN. The tables used for training F-ANN and L-ANN have nearly

the same size. The table used for P-ANN training is, however, much smaller by almost 3 times than the ones used for F-ANN and L-ANN. So, the poor performance of P-ANN could be attributed to using a smaller training table size. However, the $\Delta\Phi$ used for generating the table is already very small, and the number of grid points has been increased extensively. Thus, for the range of Φ considered in the LES, increasing the training table size of P-ANN would be only possible by including states, which are very similar to those already in the table, and is therefore redundant. These observations suggest that there is an inherent limitation of the P-ANN approach compared to the F-ANN and L-ANN.

Table 16: Memory saving by ANN for Case A

	Look-up table size	ANN size
F-ANN	212.6 MB	0.107 MB
P-ANN	67.5 MB	0.107 MB
L-ANN	242.1 MB	0.107 MB

Table 17: Timing for Case B

	Time/(Step×Grid)
Stirring Only	5.66×10^{-5}
Diffusion Only (Le #)	4.52×10^{-4}
Diffusion Only (MA)	7.21×10^{-4}
Reaction Only	2.44×10^{-2} (7.02×10^{-4} with ANN)

Table 18: Timing for Case C

	Time/(Step×Grid)
Stirring Only	3.12×10^{-5}
Diffusion Only (Le #)	3.69×10^{-4}
Diffusion Only (MA)	7.22×10^{-4}
Reaction Only	2.35×10^{-3} (6.62×10^{-4} with ANN)

The time required to perform stirring, diffusion and reaction computations per number iterations and grid points on an Intel PC (Pentium 4, 2.40 GHz) is given in Table 17 for Case B. The least time consuming process is the turbulent stirring, since it is handled in a stochastic manner. The time required to do diffusion calculation is

approximately one order of magnitude larger than for stirring. The diffusion cost is increased further by using mixture averaged (MA) diffusivities for the species equation compared to the constant Lewis number assumption. Regardless, the reaction rate calculation by using a stiff ODE solver is the most time consuming process, which is 430 times more expensive than stirring, and approximately 30 times larger than the diffusion. The time required to calculate reaction rates through ANN computations is, however, of the same order with the diffusion calculations, and therefore, results in approximately 35X speed-up for the chosen ANN.

Table 18 lists the time required to perform stirring, diffusion and reaction rate calculations in the LEM simulation for Case C. The most important difference between Case B and Case C timing comparison is the reaction rate calculations. For the methane skeletal mechanism used in Case B, the chemical source term computation is approximately 30 times slower than the diffusion. For the syngas case, however, it is only 7 times slower than diffusion. It is well known, the syngas reaction mechanism is not as stiff as methane, since syngas combustion is a sub-set of the larger methane combustion (93). So, for this configuration and kinetics model, ANN is only 3.5 times faster than the DI. Regardless, there is still a speed-up in the computations. Finally, the ANN table used for training is 3.18 GB, whereas only 0.1 MB of memory is required to store the ANN coefficients used during the actual computation. Hence, there is considerable amount of memory saving, which is very beneficial for employing PC parallel clusters with limited memory. This result is expected to hold regardless of the mechanism itself.

5.3.5 Conclusions

The study discusses a new approach to calculate chemical source terms in multi-step, multi-species reaction kinetics mechanisms based on the ANN method. The ANN training is achieved by stand-alone LEM simulations, where the unsteady interaction

of small-scale structures with a laminar flame front is captured. The LEM scalar field is initialized based on the same composition as the LES. However, LEM is not carried-out for the same geometry as in the LES. Hence, this approach is new and offers a problem independent method to extract the thermo-chemical states, and therefore has the potential for developing ANNs independent of the geometry of interest.

The proposed methodology is evaluated for three distinct cases. The first test case (Case A) is a series of LEMLES of premixed syngas flame-turbulence-vortex interaction computations, where ANN is used to replace DI in the sub-grid LEM model. The simulations are carried out for four different cases with different equivalence ratios and turbulence levels. Cases B and C provide *a priori* ANN testing in the stand-alone LEM computations by evaluating the ANN predictions inside and outside the compositional state-space for which it was trained.

The LEMLES studies demonstrate that the current ANN approach is capable of detecting the correct variation calculated by the DI. Also, while results by L-ANN and F-ANN are comparable to each other, the P-ANN approach provides the worst predictions. This confirms that the ANN accuracy is strongly affected by the look-up table used for ANN training. The table constructed based on laminar flame calculations lacks the *unsteady* mixing effect caused by turbulent structures, and therefore, is not suitable for ANN training. This effect is included both in the 3D simulation of FVI and in the stand-alone LEM calculations, which leads to more accurate and reliable ANN predictions.

The thermo-chemical database constructed through LEM does not contain all the states accessed during the computation. Thus, the ANN's ability to predict states for which it is not trained (so-called *generality*) is addressed by both LEMLES and stand-alone LEM computations. As the composition is identical in cases A1, A2 and A4, exactly the same L-ANN is used for the computations. The results shows that the ANN predictions for these cases have almost the same accuracy. The stand-alone

LEM computations are also used to simulate conditions outside the training base of ANN. Results obtained by Case B for a premixed methane/air flame demonstrates that the LEM with ANN is indistinguishable from the LEM with DI. The same behavior is observed for a non-premixed syngas/air LEM simulation (Case C). The ANN's capability to predict the LEM evolution for a Re_t that is not included in the database is also addressed in Case C, and again, the results are satisfactory.

The ANN speed-up against DI is shown to be highly dependent on the stiffness of the reduced mechanism that is used to calculate the chemical source terms. For Case A, the ANN provided approximately 11X speed-up compared to DI, whereas for Case C, the speed-up is around 4~5X. This is related to the less stiff mechanism used for Case C. For the cases considered in this section, the maximum speed-up is obtained for Case B (35X), since the methane skeletal mechanism used here is much stiffer than the syngas mechanisms. Regardless of the speed-up, for all cases there is huge memory saving, e.g., for Case C, the look-up table size is 3.18 GB, whereas only 0.1 MB is needed for the ANN. These results show that in addition to memory saving, there is a possibility that a well trained ANN could be very cost effective for larger and stiffer mechanism. This observation has an important implication for LES of reacting flows with finite-rate kinetics, but more work is needed to fully demonstrate this advantage. Application of ANN in LEMLES for Cases B and C will be reported in the next chapters.

CHAPTER VI

LES OF EXTINCTION AND REIGNITION WITH ANN

6.1 Numerical setup and ANN training

A DNS of turbulent non-premixed combustion in a temporally evolving jet (Case M (26)) is chosen as a test case for the current LES study. This case corresponds to a Reynolds number of 4478 and a Damkohler number of 0.011. The DNS study showed that this case exhibits complex extinction and reignition during flow/flame interaction and evolution. The computational domain (L_x, L_y, L_z) is $(12H, 14H, 8H)$, where H denotes the initial width of the jet velocity, and $H = 0.96$ mm for Case M. The DNS employs 64 grid points along H , which implies a resolution of approximately 350 M grid points in total, with a minimum resolution of around 2η .

Two LES results are presented here: Cases M-1 and M-2, with $96 \times 112 \times 64$ and $192 \times 224 \times 128$ number of grid points in x , y and z directions, respectively. Both grids are clustered in the shear layer with smooth stretching towards the transverse boundaries. For Case M-1, the minimum LES resolution in the shear layer is 5η , whereas it is 2.5η for Case M-2. Thus, these resolution are similar to the DNS the grid in the other two periodic directions is much larger. 12 LEM cells are used within each LES cell to account for subgrid turbulence-chemistry interactions. The grid resolution for each of the cases is given in more details in Table 19. With this grid, the subgrid resolution is reasonable to capture flame-turbulence interaction. The LES is initialized identical to the original DNS study with a laminar flamelet solution at a scalar dissipation rate $\chi = 0.75\chi_q$. Here, χ_q is the extinction scalar dissipation rate, which is 2194 s^{-1} . The fuel is composed of 50 % CO , 10 % H_2 and 40 % N_2 , whereas the oxidizer is air. Isotropic background turbulence is added to trigger the evolution

of shear-generated turbulence. The initial turbulent integral length scale is $H/3$ and the turbulence intensity is $0.05U$. Characteristic perfectly non-reflecting outflow boundary conditions are used in the transverse direction, whereas in the streamwise and the spanwise directions periodicity condition is imposed. A 21 steps, 11 species ($H_2, O_2, O, OH, H_2O, H, HO_2, CO, CO_2, HCO, N_2$) reduced mechanism is used for the chemical kinetics calculations. Mixture averaged transport properties are used for the calculation of heat and species diffusion fluxes.

Table 19: Grid resolution used for Cases M-1 and M-2.

	Δx [m]	Δy [m]	Δz [m]	Δs (LEM) [m]
Case M-1	1.2×10^{-4}	max. 2.50×10^{-4} min. 0.70×10^{-4}	1.2×10^{-4}	max. 1.28×10^{-5} min. 0.84×10^{-5}
Case M-2	0.6×10^{-4}	max. 1.25×10^{-4} min. 0.35×10^{-4}	0.6×10^{-4}	max. 0.64×10^{-5} min. 0.42×10^{-5}

The ANN is trained on an *unsteady* thermo-chemical database constructed through stand-alone LEM computations. The further details of the table generation by stand-alone LEM, ANN training and architecture selection relevant to the conditions considered here are discussed in Section 5.3.3.1 and will not be repeated here for the sake of brevity.

6.2 LES with LANN

6.2.1 LANN Validation Against DI for Case M-1

Initially the validity of the ANN approach against using stiff ODE solver (DI hereafter) is assessed on the coarse LES grid. For this purpose the LEMLES is run first with DI (DI-LEMLES hereafter) and later with ANN (ANN-LEMLES hereafter). The comparison of the time averaged density, axial velocity, transverse velocity and temperature profiles obtained by both methodologies is given in Figs. 85 (a)-(d), respectively. Here, the time averaging is achieved on a time window of $t_j = [0 - 30]$, where t_j is the non-dimensional time given as $t_j = t/(H/U)$. H and U denote the

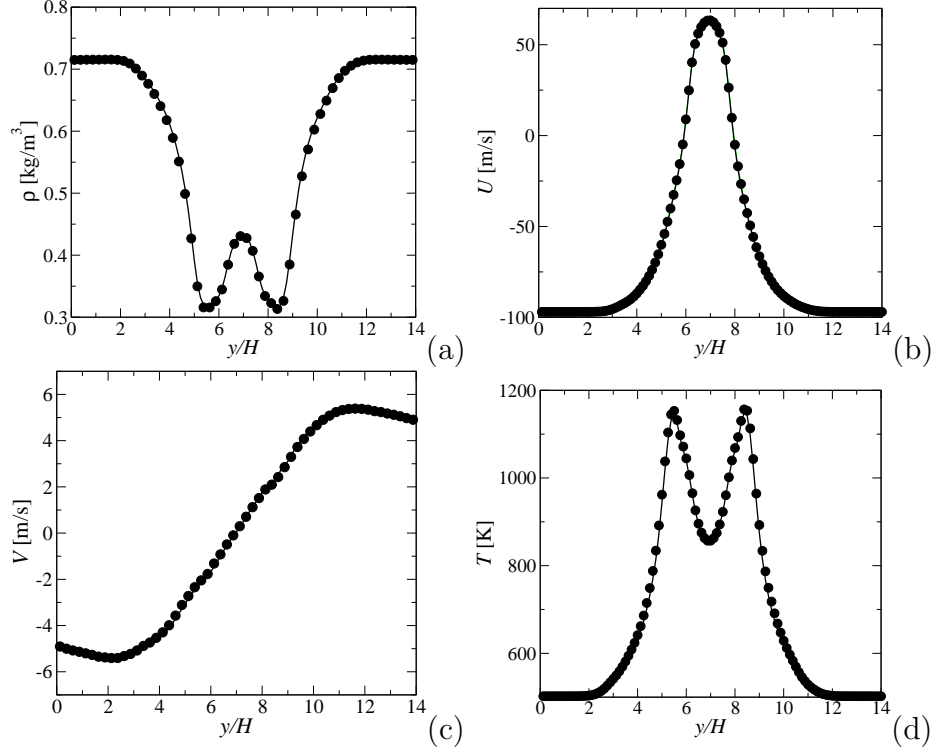


Figure 48: Comparison of the time-averaged data obtained for Case M-1 using DI-(●) and ANN-(—) LEMLES.

jet height and characteristic jet velocity, respectively (26). Averaging in the homogeneous x and z directions is also performed, which merged all the data to a single line.

The agreement between the DI- and ANN- LEMLES obtained profiles is satisfactory, as seen in the Figs. 85 (a)-(d). The density profile, given in Fig. 85 (a), starts from 0.7 kg/m^3 in the oxidizer stream ($y/H \lesssim 2$ and $y/H \gtrsim 12$) and decreases down to 0.3 kg/m^3 . Then it increases up to approximately 0.4 kg/m^3 in the fuel stream. The axial velocity indicates that on the average the fuel stream velocity at the center decreases to almost 50 m/s , whereas it was 100 m/s initially. Close to the upper and lower boundaries in the y direction, the oxidizer velocity stays almost constant at 100 m/s . The transverse velocity was initialized based on isotropic turbulence solution for the given length and velocity scales. Fig. 85 (c), however, shows that, the transverse

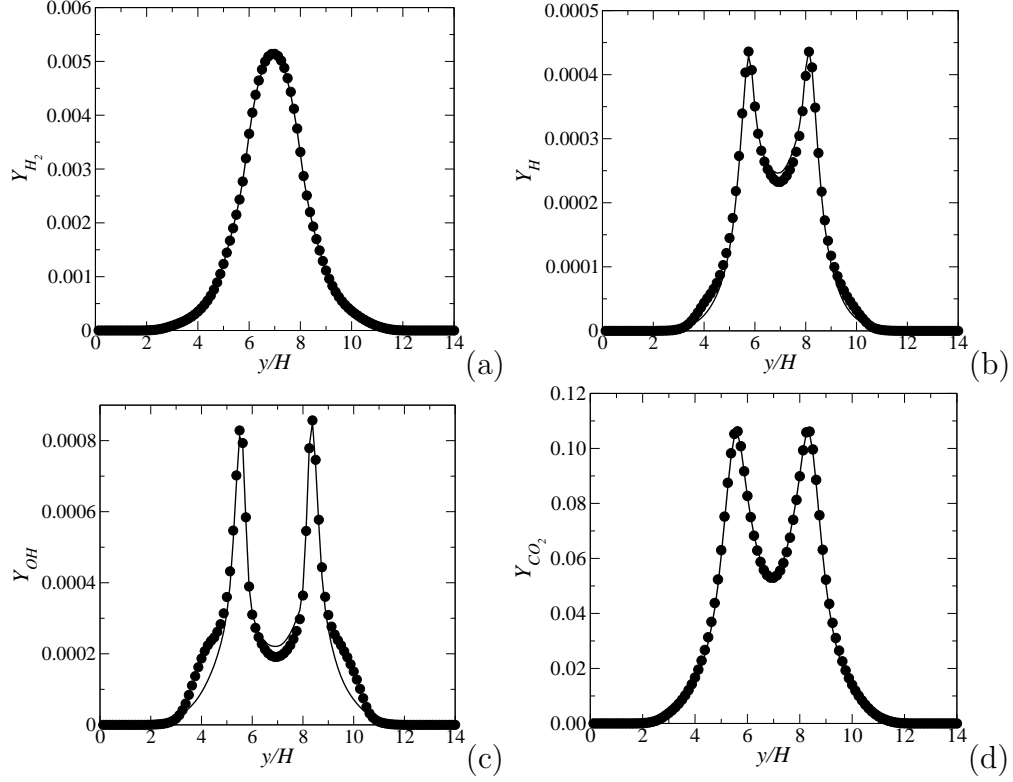


Figure 49: Comparison of the time-averaged scalar field obtained for Case M-1 using DI-(●) and ANN-(—) LEMLES.

velocity developed into a symmetric profile along the centerline. It is also seen that there is a net flux of flow from oxidizer stream to the fuel stream, which is essentially because of the combustion. The location of the reaction zone can be clearly seen on the temperature plot, Fig. 85 (d). According to the plot, the reaction zone is located approximately at $y/H \cong 4.5$ and $y/H \cong 8.5$, and at this location the temperature attains its maximum value, which is 1100 K on the average. It is noted that this value is less than the one used to initialize the flame indicating decreased temperature due to the extinction that occurred within the time window used for averaging.

The time and space averaged variation of the scalar field along the transverse direction is presented in Figs. 49 (a)-(d), for H_2 , H , OH and CO_2 , respectively. Similar to Fig. 85, the comparison between DI- and ANN- LEMLES is given in the figures. The initial value of the H_2 mass fraction in the reaction zone is 7.9×10^{-3} ,

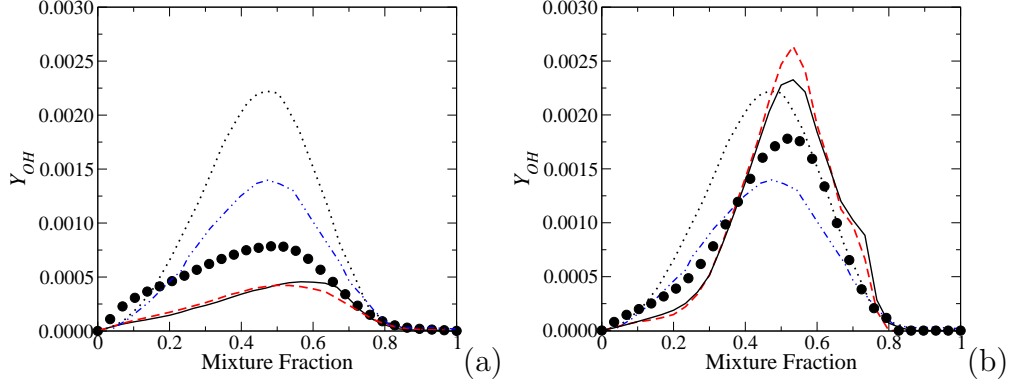


Figure 50: Comparison of the OH statistics obtained by the coarse and fine LEMLES at $t_j =$ (a) 20, (b) 40. (\bullet) DNS, (- -) Case M-1, (—) Case M-2, (...) initial data, and (- . -) laminar flamelet value at extinction.

whereas the time average data in Fig. 49 (b) shows that it dropped to approximately 5.5×10^{-3} . Both the H and OH mass fraction plots given in (b) and (c) indicate that there exists radical species within the fuel stream. This is both because of the species convection through mixing by the vortex roll-up in the shear layer, and the reactions occurring at this location coupled with the increased level of temperature, as it is evidenced in Fig. 85 (d). The agreement between the DI- and ANN-LEMLES is quite good for major species H_2 and CO_2 as seen in 49 (a) and (d). For the radicals, there exists small discrepancy at the centerline. Also, particularly for the OH , the ANN-LEMLES slightly overpredicts the DI-LEMLES results at $3 < y/H < 5$ and $11 < y/H < 11$. Overall, the agreement between both methodologies is acceptable, and the existing discrepancies do not seem to cause any major problem on understanding the physics of the problem.

6.2.2 Extinction and Reignition Predictions for Cases M-1 and M-2

The mean value of the probability density function (PDF) of OH mass fraction conditioned on mixture fraction obtained at non-dimensional times $t_j = 20$ and 40 by the cases M-1, M-2 and the DNS is shown in Figs. 50a-b, respectively. The time is non-dimensionalized by the reference time given as $t^* = H/U$, where H and U are

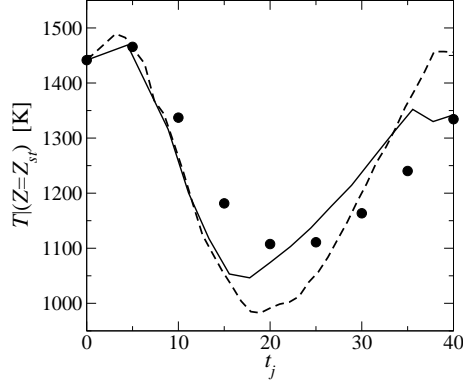


Figure 51: Variation of the mean temperature at the stoichiometric mixture fraction obtained by the DNS (●), Case M-1 (- -), and Case M-2 (—).

the initial width of the fuel slab and the characteristic jet velocity, respectively (26). The initial data at $t_j = 0$ used for all calculations, and the laminar flamelet value at extinction is also shown in the figures for comparison purposes. The flamelet value is given by the DNS study (26) and corresponds to the the solution obtained for the maximum strain rate without any extinction during the flamelet computations. At $t_j = 20$, as given in Fig 50 (a), the LES and DNS results starting from the initial profile drops below the extinction limit predicted by the laminar flamelet solution. Both LES results are very similar to each other at this time instant. They also get values less than the DNS at almost every mixture fraction, indicating that the LEMLES predicts more extinction. At reignition (Fig 50 (b)), all the profiles show increased level OH . Especially for mixture fraction values between 0.4 and 0.75, the OH mass fraction is greater than the extinction limit, clearly indicating the reignition process. The LES results, especially for Case M-1, exceed the initial data as well, and are substantially more than the DNS. Case M-2 solution is closer to the DNS data, as shown in the figure. Although there are differences, overall both of the LEMLES predict extinction and reignition at approximately the same instant as in the DNS with relatively good agreement in the trends.

The time variation of the mean value of PDF of temperature at the stoichiometric

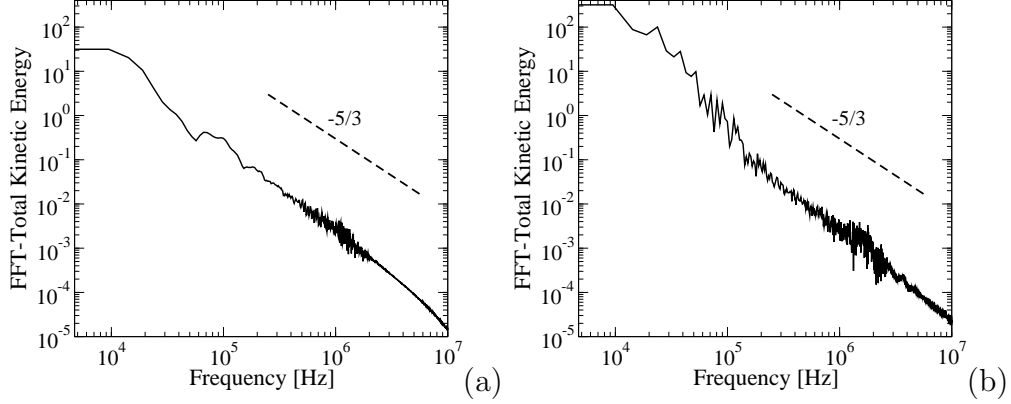


Figure 52: FFT of the mean flow total kinetic energy obtained by the fine LEMLES at a point located (a) $1H$ and (b) $4H$ away from the centerline.

mixture fraction is shown in Fig. 51. The DNS data starts initially at 1450 K, and then decreases down to approximately 1100 K at $t_j = 20$. After this time instant, the temperature starts to build up again, indicating the reignition process, and finally reaches 1300 K, which is less than its initial value. Both ANN-LEMLES exhibit a similar variation. However, similar to the observations made in Figs. 50 (a)-(b), the level of extinction and reignition is not captured precisely. Case M-1 indicates that the temperature at extinction is 1000 K, which is almost 100 K less than that is given by the DNS. On the other hand, the variation obtained by the Case M-2 is more similar to the DNS data. The discrepancy at $t_j = 20$ and 40 is almost insignificant. The Case M-2 simulation result denotes that the extinction occurs at $t_j = 18$, which is slightly earlier than the DNS. The discussion on the rest of the paper is provided for Case M-2, since it provides better prediction of the conditional OH statistics compared to the Case M-1.

As indicated earlier, the original DNS study (26) employed 350M grid points, whereas the current study uses approximately 700K and 5.5M nodes for the cases M-1 and M-2, respectively. This is considerably less than that was used for the DNS. In LES the main assumption is that the cut-off length scale is placed within the inertial range of the energy spectrum, preferably close to the η , so that the universal small

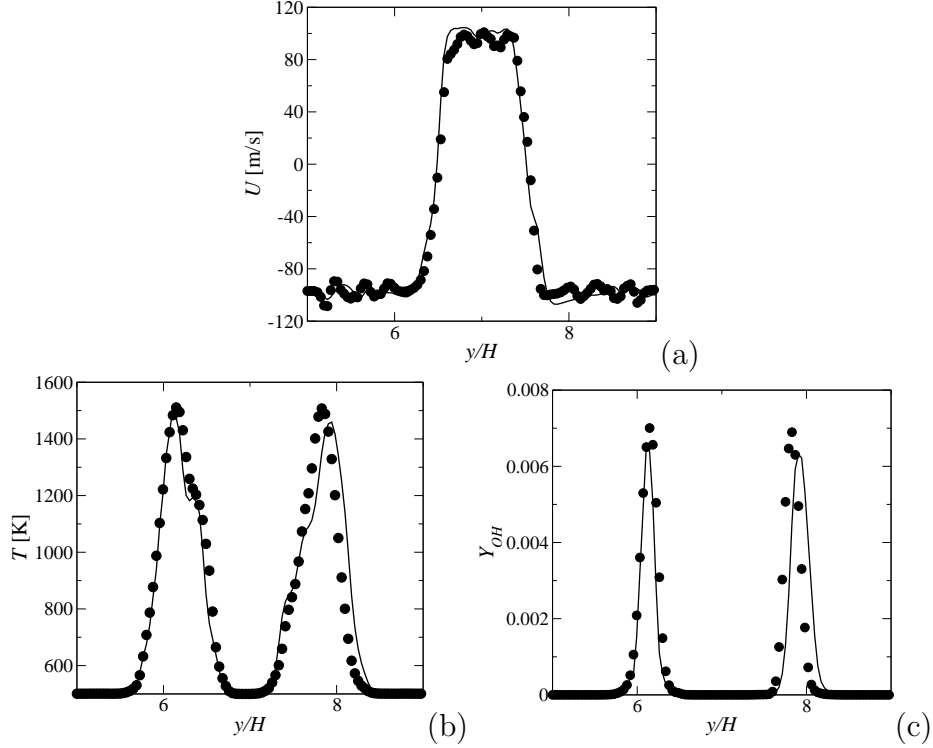


Figure 53: Comparison of the instantaneous data obtained by the fine LEMLES using DI (\bullet) and ANN ($—$) at $t_j=4.5$.

scale structures can be modeled by the sub-grid models. Figs 52a-b shows the FFT of the total velocity signal recorded at a location H and $4H$ away from the centerline. The FFT calculated for both of the points obeys the well known $-5/3$ scaling law of Kolmogorov at least for two decades. This denotes that the grid resolution for the current LES (Case M-2) is adequate to capture the inertial range of the turbulent spectrum.

Given the reasonable prediction of the flame structure and extinction/reignition characteristics obtained by the LEMLES, the LES using ANN (ANN-LEMLES, hereafter) is compared with the LES using stiff ODE solver (DI-LEMLES, hereafter) next for Case M-2 and the results are given in Figs. 53a-c. Here, the axial velocity, temperature and OH mass fraction comparisons are shown. The figure shows the

instantaneous data obtained at $t_j = 4.5$ at mid- $x - y$ and $y - z$ planes along the centerline. The accuracy of the ANN for this case is comparable to the DI. Here, the maximum value of the temperature within the reaction zone is predicted well. Also, the thickness of the reaction zone, as predicted based on both the temperature (Fig. 53 (b)) and OH mass fraction (Fig. 53 (c)) indicates that the ANN is working reasonably well. There is a slight mismatch in the peak value of the OH mass fraction, between the ANN- and DI- LEMLES. This mismatch is also observed for the axial velocity in particular at $y/H \cong 7$. However, it should be noted that the results cannot be expected to match perfectly well, since they are extracted at two time instants slightly different than each other. Regardless, the accuracy of the ANN-LEMLES is acceptable, and can be considered as representative for the actual DI-LEMLES. In the following, we primarily compare the ANN-LEMLES predictions against the DNS data in order to obtain a candid assessment of this approach.

6.2.3 Scalar Field Conditional Statistics

The mean value of the PDFs of H_2 and CO mass fraction conditioned on the mixture fraction at extinction ($t_j = 20$) and reignition ($t_j = 40$) are shown in Figs. 54a-d. The data used to initialize the LES and the laminar flamelet value at extinction are also shown in the figures. The DNS data shows that the conditional PDF of CO mass fraction varies almost linearly with respect to the mixture fraction at both $t_j = 20$ and $t_j = 40$, in Figs. 54 (a) and (b), respectively. The variation of the conditional PDF of H_2 mass fraction on the other hand exhibits different slopes with respect to the mixture fraction. Starting from the fuel stream ($Z = 1$), the PDF of H_2 mass fraction decreases with a much steeper slope than the CO (Fig. 54 (c)). This is a direct result of an early H_2 consumption within the fuel stream, which release H and OH radical species that play a key role in speeding up CO oxidation (86). Then, between $Z = 0.2$ and 0.6 , the H_2 consumption speed decreases and the variation of

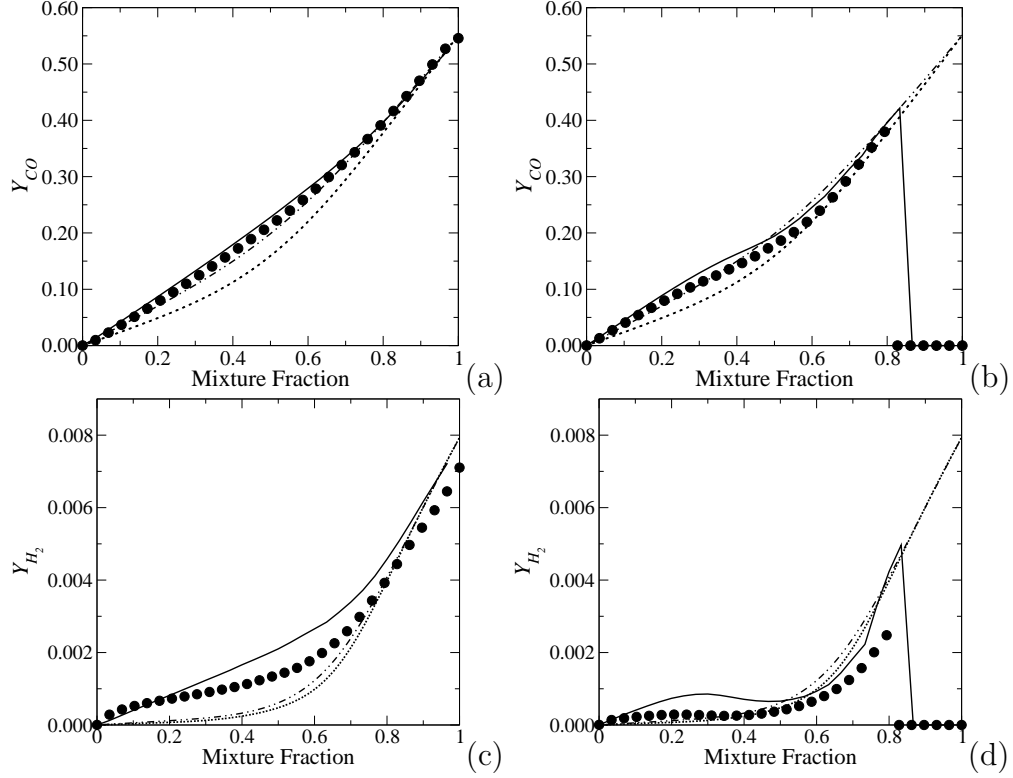


Figure 54: Conditional means of CO and H_2 at extinction (a, c) and reignition (b, d) obtained by ANN-LEMLES and DNS. (\bullet) DNS, (—) ANN-LEMLES, (...) initial data, and (- . -) laminar flamelet value at extinction.

the conditional statistics exhibits a relatively flat distribution, which is a result of the H_2 recombination reactions occurring within this range. At $t_j = 40$, Figs 54 (b) and (d) shows that there exists no CO and H_2 for $Z > 0.8$ indicating that the fuel is consumed at this time due to the reignition.

The means of the conditional PDFs obtained by ANN-LEMLES are given in Figs. 54 (a)-(d) along with the DNS data. The ANN predictions at both extinction and reignition for the CO statistics matches perfectly well with the DNS data as seen in 54 (a) and (b). For H_2 statistics, the profiles obtained by the ANN seem to capture the same trend as with the DNS. Fig. 54 (c) shows that the slope at $0.2 < Z < 0.6$ is, however, more than the DNS prediction. Also, at $t_j = 40$, as given in Fig. 54 (d), the value of H_2 at $Z = 0.8$ is higher than the DNS value. This indicates that in the

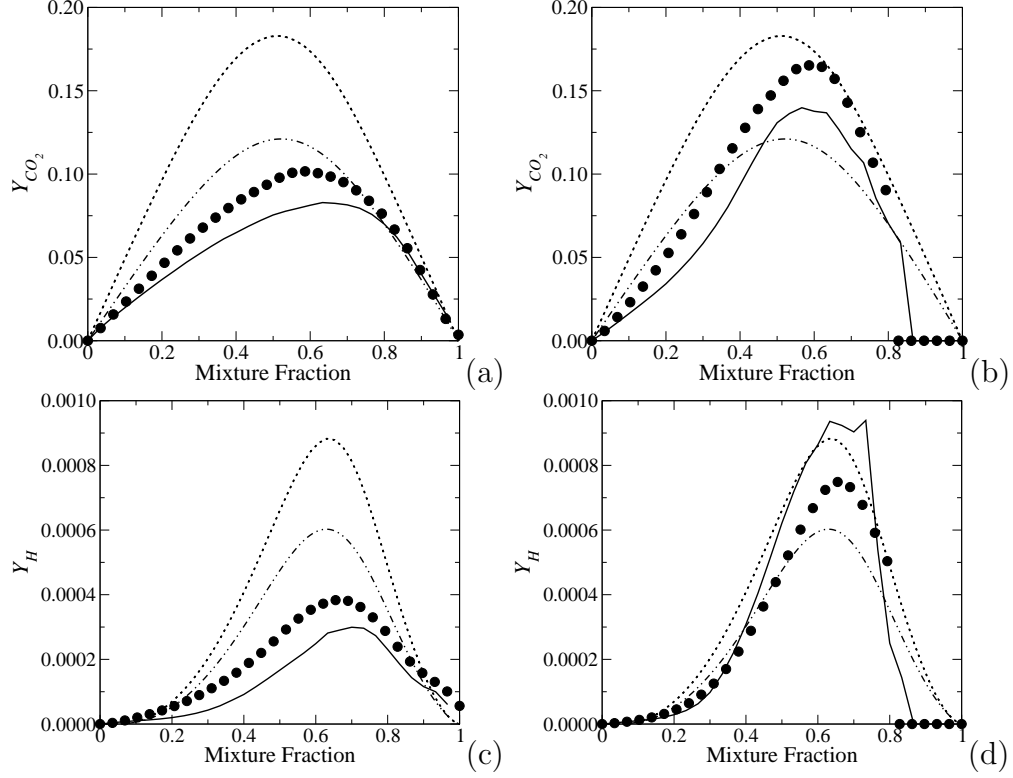


Figure 55: Conditional means of the CO_2 and H at extinction (a, c, e) and reignition (b, d, f) obtained by ANN-LEMLES and DNS. (●) DNS, (—) ANN-LEMLES, (...) initial data, and (- . -) laminar flamelet value at extinction.

current ANN-LEMLES the H_2 consumption is predicted slightly off, especially on the fuel rich side.

The mean value of the PDF of CO_2 mass fraction at $t_j = 20$ and $t_j = 40$ are compared in Figs. 55a-b. Similar to the OH mass fraction (as given in Fig. 50 (a)), the conditional CO_2 mass fraction exhibits smaller values than the laminar flamelet value at extinction. This feature can also be seen in Fig. 55 (c), where the mean of the PDF of H mass fraction conditioned on the mixture fraction is given at $t_j = 20$. All of these figures (Figs. 50 (a), 55 (a) and 55 (c)) indicate that the decrease in the conditional species mass fractions is not specific for only one species (i.e., OH), but is actually a general trend for all the species, except for the ones in the fuel mixture (CO and H_2). Both CO_2 and H ANN-LEMLES results follow the same trend as the

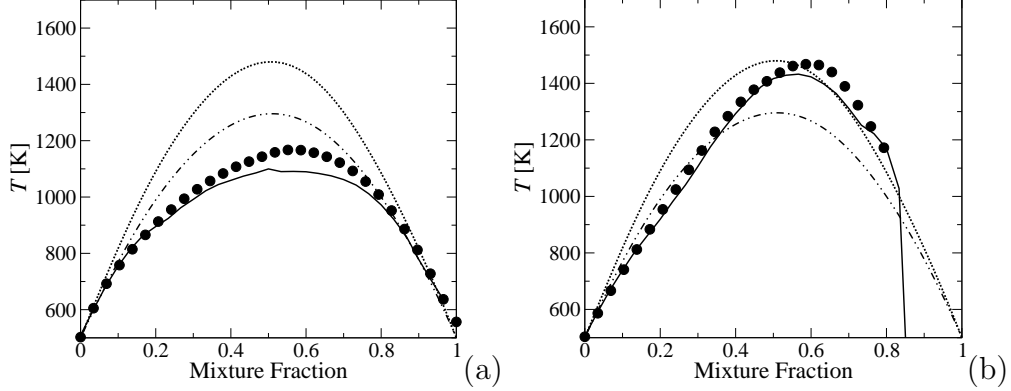


Figure 56: Conditional mean of the temperature at extinction (a) and reignition (b) obtained by ANN-LEMLES and DNS. (\bullet) DNS, (—) ANN-LEMLES, (...) initial data, and (- . -) laminar flamelet value at extinction.

DNS even though the former approach slightly underpredicts the DNS data especially at $0.4 < Z < 0.8$. Interestingly, the error is less than that is observed for the OH mass fraction.

At reignition ($t_j = 40$) in Fig. 55 (b), the mean of the PDF of CO_2 mass fraction conditioned on the mixture fraction shows increased levels compared to that of obtained at $t_j = 20$. The values at $t_j = 40$ for both species (CO_2 and H) and temperature are above the laminar flamelet values at extinction indicating reignition, consistent with the OH data shown in Fig. 50 (b). The CO_2 is slightly underpredicted, whereas the ANN-LEMLES calculated H is even greater than the initial data as seen in Fig. 55 (d). Still, the overall accuracy of the ANN-LEMLES is acceptable.

The variation of the mean value of the PDF of temperature conditioned on the mixture fraction at $t_j = 20$ is demonstrated in Fig. 56 (a). The maximum value of temperature at the stoichiometric surface at this time is approximately 1100 K, which is almost 300 K less than its initial value. At reignition (Fig. 56 (b)), the temperature recovers its initial value. The agreement between ANN-LEMLES and DNS is really good for the conditional PDF of the temperature indicating the accuracy of the current ANN methodology.

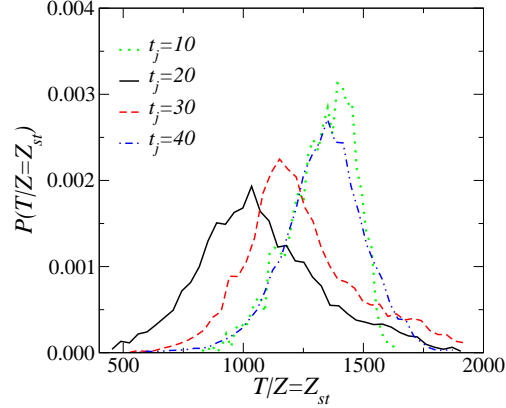


Figure 57: The time variation of the PDF of temperature at the stoichiometric surface obtained by the ANN-LEMLES.

The stoichiometric mixture fraction (Z_{st}) based on the Bilger’s definition (6) is approximately 0.43 for the current case. The stoichiometry refers to a perfect combustion where all the fuel is burned. Hence, typically, the scalar PDFs conditioned on the mixture fraction for temperature and the intermediate species peak at the stoichiometric mixture fraction value (95). For this particular study, however, it is interesting to note that both the DNS and ANN-LEMLES extracted PDFs exhibit the maximum temperature not at the stoichiometric value but at a slightly fuel rich side. The CO_2 mass fraction and temperature peaks at approximately $Z = 0.6$ as seen in Figs. 55 (a) and (e). The H mass fraction, on the other hand, peaks at $Z = 0.7$. At reignition, the peak of the PDFs are shifted towards the fuel rich side further. The main reason behind these observations is that the mixture fraction inherently assumes that the both the fuel and oxidizer has the same diffusion velocity. This is not correct for syngas flames, where the fuel mixture is composed of a relatively light (H_2) and heavy species (CO) which have different diffusion velocities. Hence, the results indicate that the mixture fraction formulation may not be an accurate modeling approach for syngas flames to parameterize thermochemical state-space in the LES applications. This is an issue that is being investigated.

The evolution of the PDF of temperature at the stoichiometric mixture fraction

is shown in Fig. 57. The PDF at $t_j = 10$ exhibits a narrow distribution, with a most probable state residing at 1300 K. This value decreases to 1000 K at $t_j = 20$. The probability of temperatures less than 1000 K also increases substantially compared to $t_j = 10$. This leads to a wider PDF, and the probability of the most probable state decreased from 0.03 to 0.02 at $t_j = 20$. The PDF at later instants shifts towards higher temperature values, denoting a most probable state of 1100 K and 1400 K at $t_j = 30$ and $t_j = 40$, respectively. The results shown on the figure indicates that the PDFs at the reignition and fully burnt cases are much narrower than the one at extinction.

6.2.4 Syngas Flame Structure

The surface plot of CO and H_2 mass fraction at $t_j = 20$ and $t_j = 40$ is shown in Figs. 58a-d. The stoichiometric mixture fraction ($Z_{st} = 0.43$) is also indicated in these figures. The mass fractions of both species show that from $t_j = 20$ ((a) and (c)) to $t_j = 40$ ((b) and (d)) the flame front is distributed over a finite region. Both CO and H_2 mass fractions decrease at $t_j = 40$ indicating consumption of the fuel. As seen in Figs. 58 (a)-(c), the stoichiometric mixture fraction at $t_j = 20$ looks like a boundary, after which both CO and H_2 cease to exist. At $t_j = 40$, however, the CO and H_2 mass fraction is spread over a much wider surface and the stoichiometric mixture fraction resides within this region.

Another interesting observation in Fig. 58 (a), at $t_j = 20$, is that the CO mass fraction is spread almost homogeneously, and its peak value is not changing much up to the stoichiometric mixture fraction. The H_2 mass fraction, on the other hand, exhibits peak values in pockets concentrated at the center part of the computational domain. Evidently, the H_2 is mostly consumed within the fuel stream, in contrast to CO , which is consumed at the stoichiometric surface. Similar to the earlier computational studies of the syngas flames (72), the current observations suggest that the

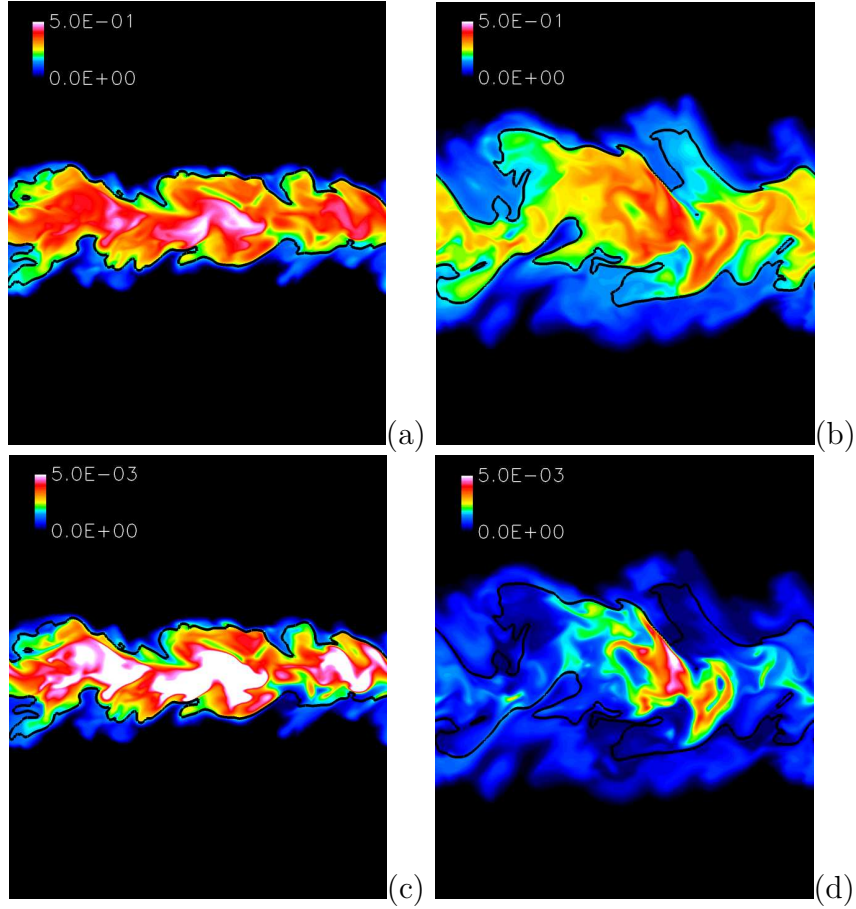


Figure 58: Surface plot of CO ((a)-(b)) and H_2 ((c)-(d)) mass fraction at $t_j = 20$ ((a)-(c)) and $t_j = 40$ ((b)-(d)).

syngas flames exhibit two reaction zones: An H_2 reaction zone which is followed by CO combustion. This is also consistent with our previous observations based on the conditional mean PDFs (i.e., Figs. 54 (a) and (c)).

In CO oxidation the main chain branching reaction is the $CO+OH\rightleftharpoons CO_2+H$ step (89). Hence, OH is a key species, which determines the oxidation rate of the CO in syngas combustion. The OH surface plot at $t_j = 20$ and $t_j = 40$ is given in Figs. 59 (a) and (b), respectively. In Fig. 59 (a), the OH mass fraction peaks at the fuel rich side of the stoichiometric surface. Comparing with H_2 surface plot shows that the OH is produced roughly around the H_2 pockets. Then, OH (and CO) is consumed through the chain branching reaction, and hence it vanishes near the stoichiometric

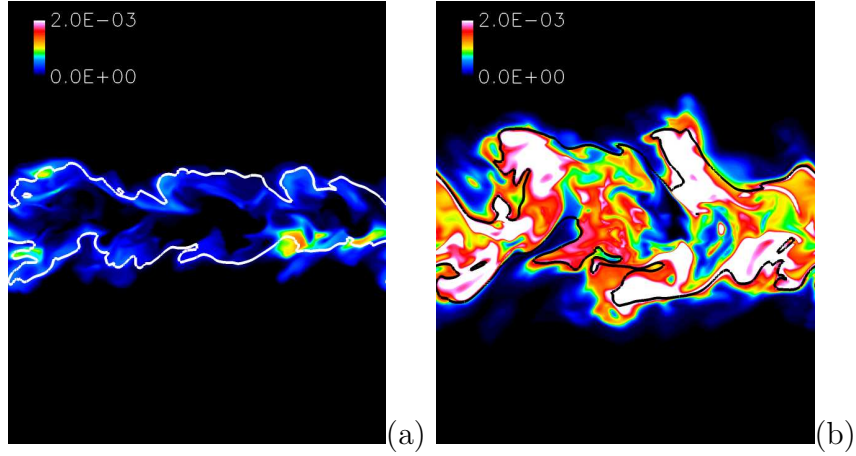


Figure 59: Surface plot of OH mass fraction at (a) $t_j = 20$ and (b) $t_j = 40$.

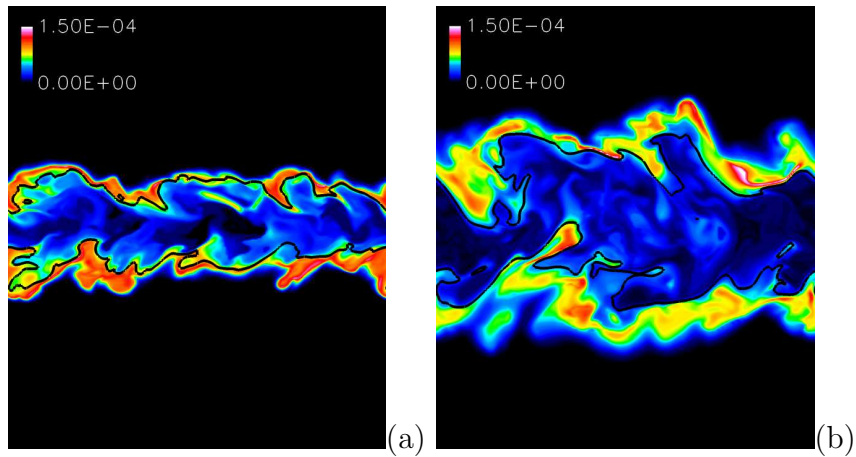


Figure 60: Surface plot of HO_2 mass fraction at (a) $t_j = 20$ and (b) $t_j = 40$.

surface. The OH mass fraction at $t_j = 40$ (Fig. 58 (c)) is not spread as much as the fuel mixture (CO and H_2) on the fuel lean side of the stoichiometric surface. There exists localized pocket-like structures with high OH content. This observation suggests that at this time instant the H_2 is mostly consumed by chemical reactions which leads to the formation of excessive amount of OH . This is also the reason for the decreased amount of H_2 within the center part of the computational domain as seen in Fig. 58 (d).

The surface plot of HO_2 radical species mass fraction at $t_j = 20$ and $t_j = 40$ is

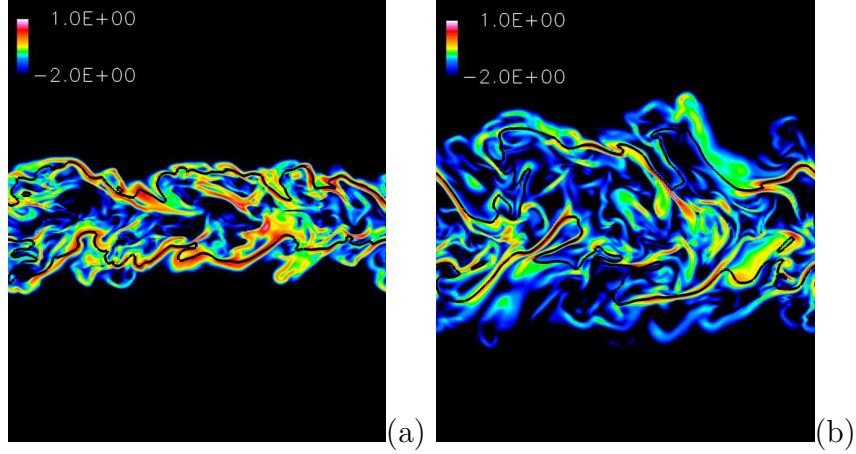


Figure 61: Surface plot of $\log_{10}(\chi_{st}/\chi_q)$ at (a) $t_j = 20$ and (b) $t_j = 40$.

shown in Figs. 60 (a) and (b), respectively. Unlike OH , the HO_2 species is mostly concentrated on the fuel rich side of the stoichiometric surface at both $t_j = 20$ and $t_j = 40$ as seen in the figures. Interestingly, the HO_2 mass fraction seems to be almost unaffected by the extinction process. In contrast to the rest of the species, the HO_2 exhibits a continuous and thin layer along the stoichiometric surface. At reignition (Fig. 60 (b)), the HO_2 layer is thicker than it is at extinction, $t_j = 20$. The maximum HO_2 mass fraction value at reignition is only slightly larger than what is observed at extinction. Here it should be noted that, although the peak value is larger at reignition, it can only be observed on a local sense. The HO_2 mass fraction at extinction on the overall is higher than that is for reignition. This indicates that at extinction the HO_2 exhibits a radical pool, whereas OH is decreasing. This needs to be studied further to come up with any conclusion and is a future work.

6.2.5 Scalar Dissipation Rate Statistics

Figures 61 (a) and (b) shows the surface plot of the logarithm of normalized scalar dissipation rate ($\log_{10}(\chi/\chi_q)$) at $t_j = 20$ and $t_j = 40$, respectively. At extinction (Fig. 61 (a)), the scalar dissipation rate is mostly concentrated around the stoichiometric surface. The variation clearly follows the stoichiometric line, since the gradient term

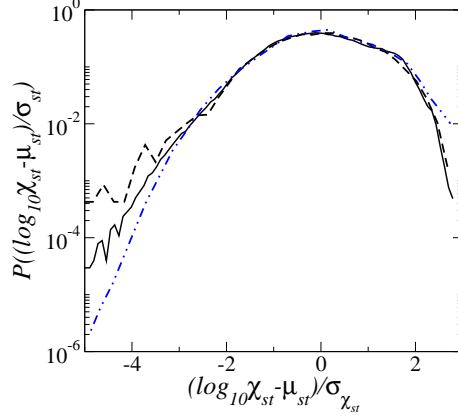


Figure 62: PDF of normalized logarithm of scalar dissipation rate at the stoichiometric mixture fraction at $t_j = 30$. (—) DNS, (- - -) ANN-LEMLES, (-...-.) log-normal distribution

(∇Z) attains its maximum value across the stoichiometric surface. At reignition (Fig. 61 (b)), the χ seem to be more distributed over the computational domain as in the form of thin sheets. Here, it should be noted that the maximum value of the χ is almost similar to that obtained at extinction. Also, the sheets of χ covers a much wider region in the computational domain, which suggests that, based on the χ information, same level of extinction should be expected at this instant similar to $t_j = 20$. This issue will be further discussed below.

The normalized PDF of the $\log_{10}\chi$ at the stoichiometric mixture fraction is given in Fig. 62 (a) at $t_j = 30$. The figure shows the PDFs obtained by the DNS study and the current ANN-LEMLES along with the log-normal distribution. The PDF extracted through ANN-LEMLES follows the same trend calculated by the DNS study. There are some minor discrepancies especially for the values of the normalized χ_{st} less than -3 . $((\log_{10}\chi_{st} - \mu_{st})/\sigma_{\chi_{st}} < -3)$. The ANN-LEMLES PDF tends to overpredict the DNS PDF at this range. Both the DNS and ANN-LEMLES PDFs exhibit a negative skewness with a log-normal distribution, which is consistent with the earlier studies (82). The results indicate that the DNS PDF can be matched by the LEMLES, since it does not carry out any assumption regarding the shape of the PDF. This is one of

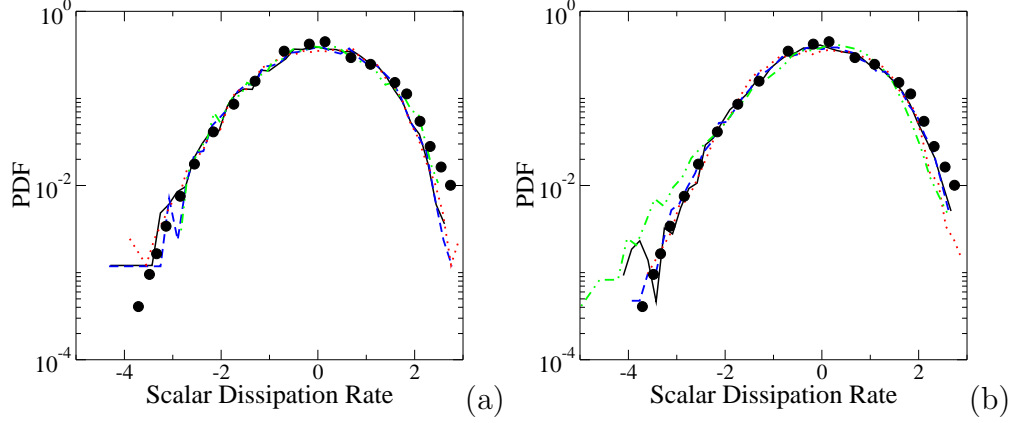


Figure 63: PDFs of normalized logarithm of scalar dissipation rate at the stoichiometric mixture fraction at (a) $t_j = 20$ and (b) $t_j = 40$. (●) log-normal distribution, (—) χ , (---) χ_{CO} , (-.-.-) χ_{OH} .

the unique ability of the LEMLES (with DI or ANN). The log-normal distribution tends to overpredict the correct PDF at higher and underpredict at lower values of χ_{st} , respectively for this case. The log-normal distribution is effectively used in flamelet approaches to model the PDF of the χ_{st} (81; 63). Both the DNS and ANN-LEMLES data show that the correct PDF differs from its model at the high and small values of χ_{st} . The results may point to possible modified model for flamelet type of simulations and is one of the being explored for the future.

The normalized PDF of the scalar dissipation rate at $t_j = 20$ and $t_j = 40$ obtained by the ANN-LEMLES is given in Figs. 63 (a) and (b). The scalar dissipation rate is typically calculated based on the mixture fraction (63). However, each species have their own scalar dissipation rates as well, and Figs. 63a-b show these PDFs calculated at different times of evolution. Here, in addition to the scalar dissipation rate calculated based on the mixture fraction (χ), the CO ($\chi_{CO} = 2D_{CO}\nabla Y_{CO}\cdot\nabla Y_{CO}$) and OH ($\chi_{OH} = 2D_{OH}\nabla Y_{OH}\cdot\nabla Y_{OH}$) scalar dissipation rates are also shown along with the log-normal distribution. For comparison purposes, all the PDFs are normalized based on their mean and variance. As seen in Fig. 63 (a), at $t_j = 20$ all PDFs follow

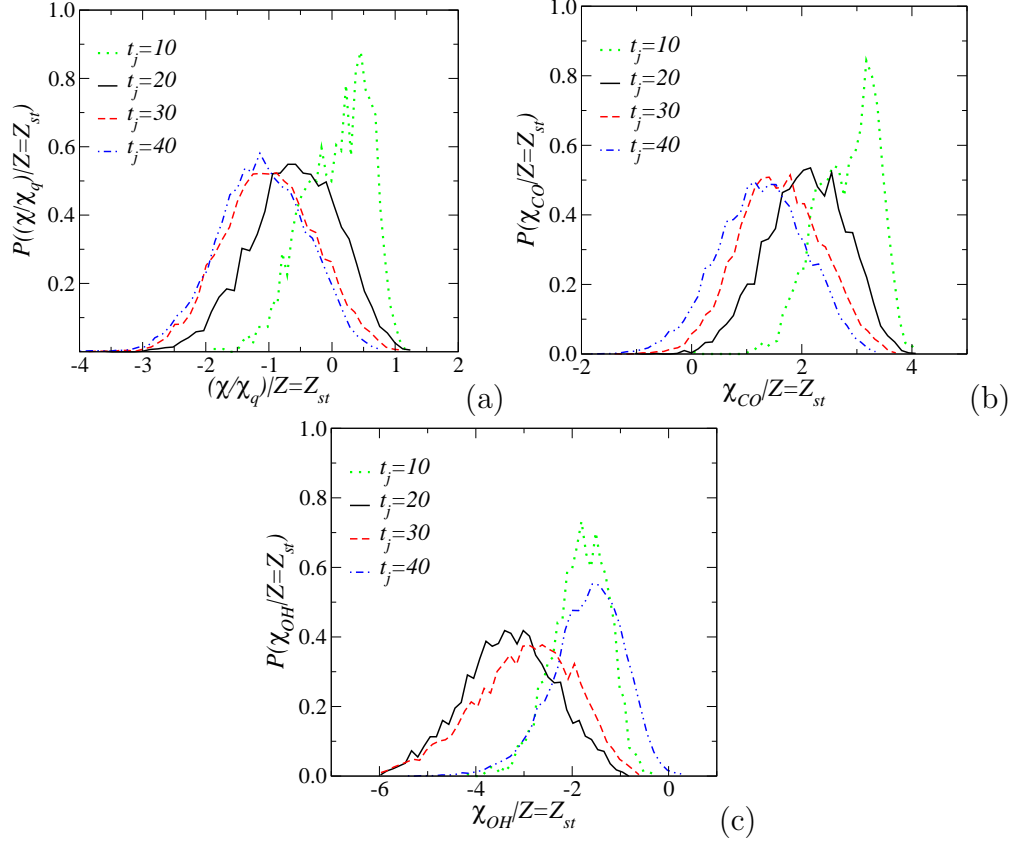


Figure 64: The time variation of the PDF of χ , χ_{CO} , χ_{OH} at the stoichiometric surface obtained by the ANN-LEMLES.

the log-normal distribution. Similar to that was observed in Fig. 62 (a), the computed PDFs attain lower values than the log-normal distribution at dissipation rate greater than 2. The PDFs obtained at reignition is given in Fig. 63 (b). Here, the discrepancy between the model and computed PDFs decreases at higher values of the scalar dissipation rate. The PDF of χ and χ_{CO} are indistinguishable from each other, and the log-normal distribution seems to be a proper function for modeling purposes. The PDF of χ_{OH} at lower values of the scalar dissipation rate tends to overpredict the log-normal distribution. It should be noted that this is not very important for the overall flow physics, since the model deviates more at very small values of the scalar dissipation rate.

Figs. 64 (a)-(c) shows the PDFs of χ , χ_{CO} and χ_{OH} at the stoichiometric surface

at different times. The scalar dissipation rate at the stoichiometric surface is an important quantity in modeling flame-turbulence interactions in LES (63), since it directly provides time scale information on the most reactive portion of the flame. A high χ at the stoichiometric surface leads to extinction, since local time scales are very short and the reactions cannot generate required amount of heat release (90). The variation of χ at $Z = Z_{st}$ as given in Fig. 64 (a), however, shows interesting results. Similar to the PDF of temperature, given in Fig. 57, the PDF of χ at $t_j = 10$ exhibits a narrow distribution, with its most probable state located at roughly 0.8. This indicates that at this time the χ acting on the flame is almost as high as the critical scalar dissipation rate obtained at extinction by the flamelets. At $t_j = 20$, the most probable state shifts towards lower values of χ compared to $t_j = 10$. Also, the tail of the PDF extends barely to 1, which indicates that the time scale at the stoichiometric surface is large enough for reactions to occur. However, as it was discussed in details previously, at $t_j = 20$ the flame goes through an extinction process. For $t_j = 30$ and 40, the χ decreases slightly and exhibits a similar shape.

The time variation of the PDF of χ_{CO} at the stoichiometric surface is given in Fig. 64 (b). Both χ_{CO} and χ shows almost exactly the same variation. It starts from a narrow pdf and at extinction decreases to more wider distribution. After this point, the shape of the PDF does not show any change, but it rather shifts towards smaller value of χ_{CO} . The χ_{OH} , on the other hand, is the only one that shows a change with respect to the time. At the initial stage ($t_j = 10$) and at reignition ($t_j = 40$), the PDF of the χ_{OH} shows a narrow and negatively skewed distribution. For both of the time instants, the χ_{OH} obtains a value of -1, with the probabilities of 0.8 and 0.6, respectively. The shape of the PDF at $t_j = 20$ and $t_j = 30$ is more like Gaussian. our previous computations (75).

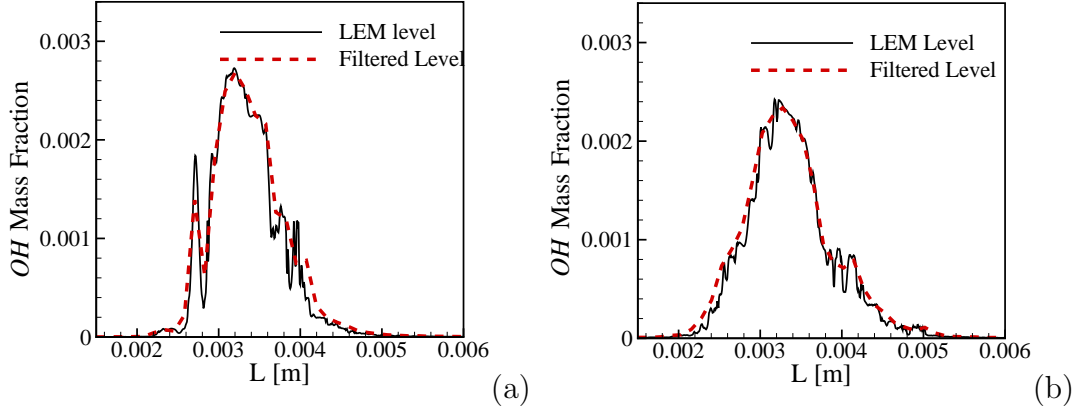


Figure 65: Y_{OH} profiles obtained by stand alone LEM computations (a)0.05 ms, (b) 0.1 ms

6.3 LES with TANN

6.3.1 TANN Model Description

Previous section dealt with using ANN to calculate the instantaneous reaction rates within the LEM framework. In this section, ANN will be used to predict the filtered reaction rates (so-called TANN approach) needed to solve the filtered species conservation equation *on* the LES grid. Here, the filtered reaction rate is parameterized with respect to the filtered species mass fractions, temperature, filtered level species gradient on the LEM domain and the subgrid Reynolds number:

$$\bar{\omega}_i = f(\tilde{Y}_k, \tilde{T}, Re_\Delta, \frac{\partial \tilde{Y}_i}{\partial x}) \quad (132)$$

The ANN training database for TANN is constructed by following the approach outlined in Section 5.3.3.1. The code is started from the same initial species profiles and is run for the same range of conditions (Re_t, L). The results are, however, filtered by a filter size equal to the grid spacing used in the LES (74). Fig. 65a-b shows the variation of the OH mass fraction along the 1D LEM domain obtained by using the stand-alone LEM code at two time instants. Here, the straight line represents the LEM level variation, whereas the dashed line is the filtered (representative of the LES) level variation. As seen in the figures, the LEM level is highly wrinkled due to

the turbulent stirring. On the filtered level, however, the profile is much smoother, since the spatial filtering process vanishes the effect of small scale wrinkling of the flame front on an average sense.

The subgrid Reynolds number in the LEMLES is calculated as:

$$Re_{\Delta} = \frac{u' \Delta}{\nu} \quad (133)$$

where $u' = (2/3)^{1/2} k^{sgs}$ and Δ is the LES grid filter. A transport equation for k^{sgs} is solved on the LES level, so that the subgrid velocity fluctuations u' can be calculated. In the current stand-alone LEM code, however, the velocity field is not simulated explicitly, and the effect of turbulent stirring is taken into account by using instantaneous re-distribution events. The k^{sgs} (and u' for that matter) is not known, and hence, Re_{Δ} cannot be computed explicitly with the current stand-alone LEM approach. To find the Re_{Δ} in this approach, the following additional equation for the variation of the k on the LEM domain is solved:

$$\frac{dk}{dt} = P_k - \epsilon \quad (134)$$

where P_k is the production term. Along the LEM domain, the k is initially assigned to be zero. Then, the u' on a segment of length l , where triplet-map (which is representative of the turbulent stirring) is applied can be calculated as:

$$u' = \frac{\nu Re_t}{l} \quad (135)$$

Here l is the characteristics eddy size used for turbulent stirring. Hence, whenever triplet-map is applied on the scalar field, the representative k is calculated as $3u'u'/2$ and this acts as the production term (P_k) which was shown in the Eq. 134. The rest of the equation (time variation and the dissipation) is solved on the 1D LEM domain similar to the reaction-diffusion equation. The dissipation term here is modeled as $\epsilon = (u')^3/\Delta s$. The main idea in Eq. 134 is that the turbulence is homogeneous, which leads to the form seen in the equation. This is in consistent with the basic LEM

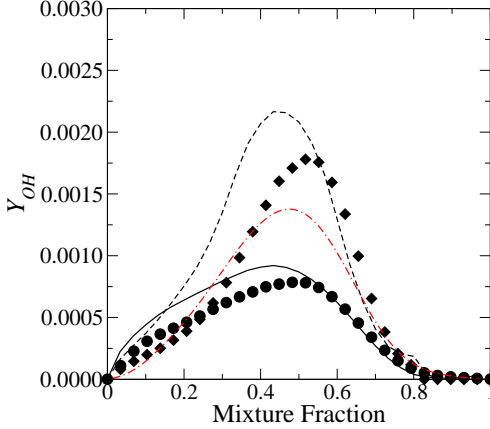


Figure 66: Conditional mean of OH mass fraction obtained by TANN-LES and DNS. (\bullet) DNS, (—) TANN-LES at $t_j = 20$; (\blacklozenge) DNS, (- - -) TANN-LES at $t_j = 40$; (- . -) laminar flamelet value at extinction.

assumption as well, hence the proposed way of calculating the k does not contradict with any of the assumptions already being made in the LEM formulation.

6.3.2 Results

The conditional mean of the OH mass fraction obtained by the TANN-LES is given in Fig. 66 at $t_j = 20$ and 40. The DNS data (shown by symbols) and the laminar flamelet value at extinction is also shown in the same figure for comparison purposes. The TANN-LES approach, as can be seen in the figure can detect the extinction (at $t_j = 20$) and reignition ($t_j = 40$) with an acceptable error. Unlike LANN-LEMLES results given in Fig. 50a-b, the TANN-LES tends to slightly overpredict the OH profile especially at oxidizer rich conditions. At reignition, the TANN-LES shows higher values of OH mass fraction within the computational domain. At this time, the variation of the OH mass fraction with respect to the mixture fraction seems to be skewed towards the oxidizer side compared to the DNS data as well. Still, the overall accuracy is considered to be acceptable.

The conditional means of the PDF of CO and H_2 mass fractions are given in Figs. 67a-b at $t_j = 20$ and 40. The results obtained by the TANN-LES approach

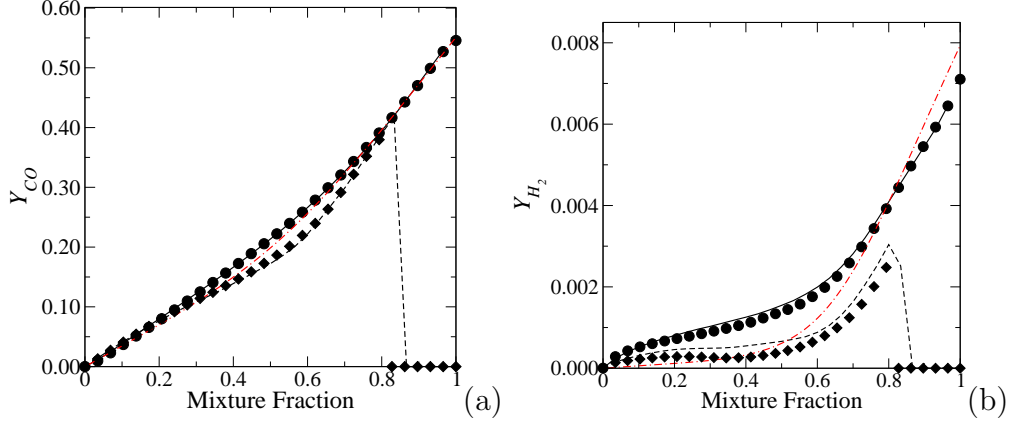


Figure 67: Conditional means of (a) CO and (b) H_2 mass fraction obtained by TANN-LES and DNS. (\bullet) DNS, (—) TANN-LES at $t_j = 20$; (\blacklozenge) DNS, (- - -) TANN-LES at $t_j = 40$; (- . -) laminar flamelet value at extinction.

show excellent agreement with the DNS data for conditional CO mass fraction both at extinction and reignition. Similar to the LANN-LEMLES data, the TANN-LES shows that at reignition, there is still fuel left in the computational domain at an equivalence ratio up to approximately 0.85. The DNS data shows that the fuel is consumed after an equivalence ratio of 0.8. The conditional H_2 mass fraction at extinction agrees well with the DNS data. At reignition, however there are two main differences. The first one is the maximum value of the mixture fraction up to which H_2 exists. This is similar to that of observed for CO mass fraction in Fig. 67a. The second difference is that the TANN-LES tends to overpredict the H_2 mass fraction at all mixture fraction values compared to the DNS data. Here it should be re-emphasized that although both CO and H_2 are fuel species, their conditional statistics represent different variations with respect to the mixture fraction. The CO is almost linear, where as H_2 is more curved. The curvature for H_2 statistics is changing with respect to time as seen in Fig. 67b. The TANN-LES seems to be capturing all of these features for both of the species.

The conditional statistics for mass fraction of a major product (CO_2) and a representative radical species (H) are shown in Figs. 68a-b. The laminar flamelet value

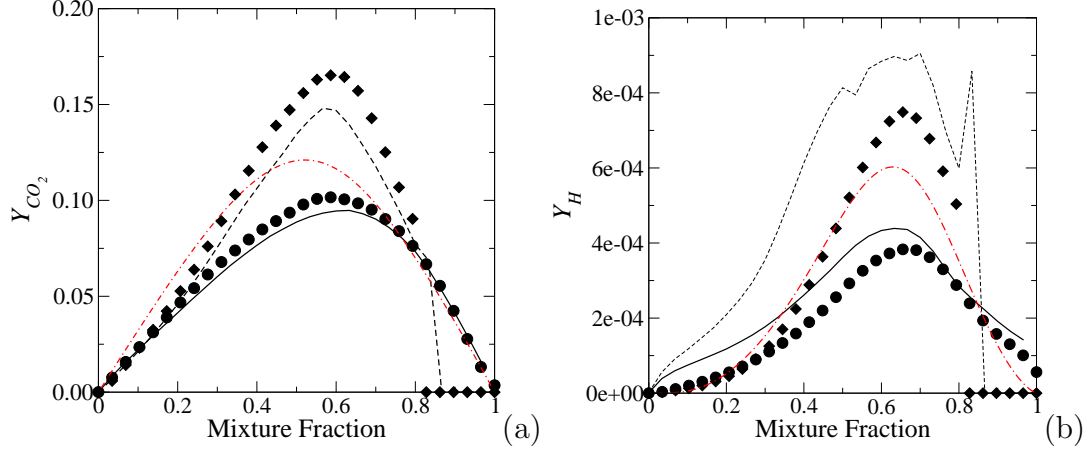


Figure 68: Conditional means of (a) CO_2 and (b) H mass fraction obtained by TANN-LES and DNS. (\bullet) DNS, (—) TANN-LES at $t_j = 20$; (\blacklozenge) DNS, (---) TANN-LES at $t_j = 40$; (- . -) laminar flamelet value at extinction.

at extinction is also shown in the figures. Both the CO_2 and OH statistics obtained by the TANN-LES exhibit good agreement with the DNS data at extinction. The accuracy for CO_2 is better than that is for H species. This is in consistency with the LANN-LEMLES results, and is expected to be a result of the overall ANN accuracy. Overall, the H mass fraction is slightly overpredicted by the TANN-LES approach especially at lean conditions, which is similar to the OH statistics. At reignition, the CO_2 mass fraction is underpredicted by the TANN-LES approach. However, it should be noted that the profile obtained by TANN-LES is still larger than the laminar flamelet value at extinction denoting that the TANN-LES can capture extinction and reignition. Although the results obtained for the H mass fraction shows the same trend, the TANN-LES tends to overpredict the DNS results. Also, at approximately a mixture fraction value approximately equal to 0.82, the conditional mean of H mass fraction obtained by the TANN-LES exhibits a peak value, which does not look physical. This may be an issue of the ANN training and the ANN coefficients for this species may need to be re-trained to obtain better results.

Fig. 69 shows the conditional mean of the temperature obtained at extinction and

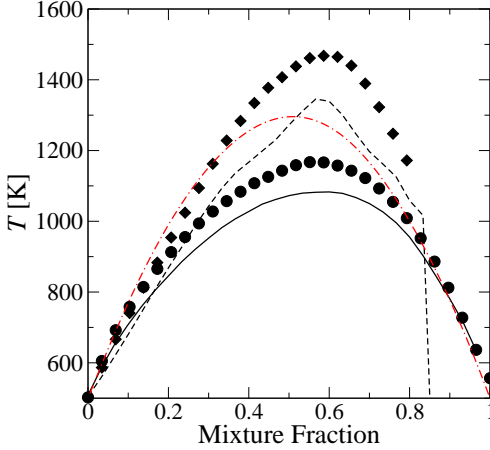


Figure 69: Conditional mean of T obtained by TANN-LES and DNS. (\bullet) DNS, (—) TANN-LES at $t_j = 20$; (\blacklozenge) DNS, (- - -) TANN-LES at $t_j = 40$; (- . -) laminar flamelet value at extinction.

reignition. The conditional mean obtained by the LANN-LEMLES for temperature, as seen in Fig. 56, shows good agreement with the DNS data. The TANN-LES, on the other, is not that accurate in predicting the correct variation. the temperature at both extinction and reignition is underpredicted by the TANN-LES. At reignition, the maximum value is predicted almost 150 K less than the DNS data. The DNS data shows that the conditional mean has almost the same variation (and level) with the laminar flamelet value at extinction, at $t_j = 40$, especially on the lean side, up to a mixture fraction value of 0.4. The TANN-LES results, on the other hand shows values less than the laminar flamelet value at extinction in this region. The fuel side predictions are better, and the data is above the extinction limit.

Finally the time variation of the mean temperature at the stoichiometric mixture fraction is given in Fig. 70. The TANN-LES results agrees well with the DNS data up to $t_j = 10$. After this time, the TANN-LES results tend to underpredict the variation obtained by the DNS. The discrepancy is maximum at $t_j = 40$, which is in consistent with our observations made based on the conditional statistics of the temperature at this time instant. Overall, the TANN-LES data tends to predict the same kind

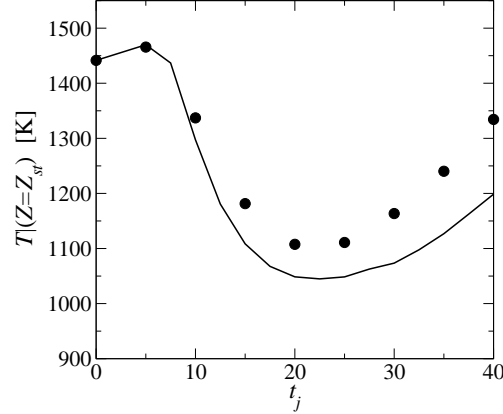


Figure 70: Variation of the mean temperature at the stoichiometric mixture fraction obtained by the DNS (●) and the TANN-LES (—).

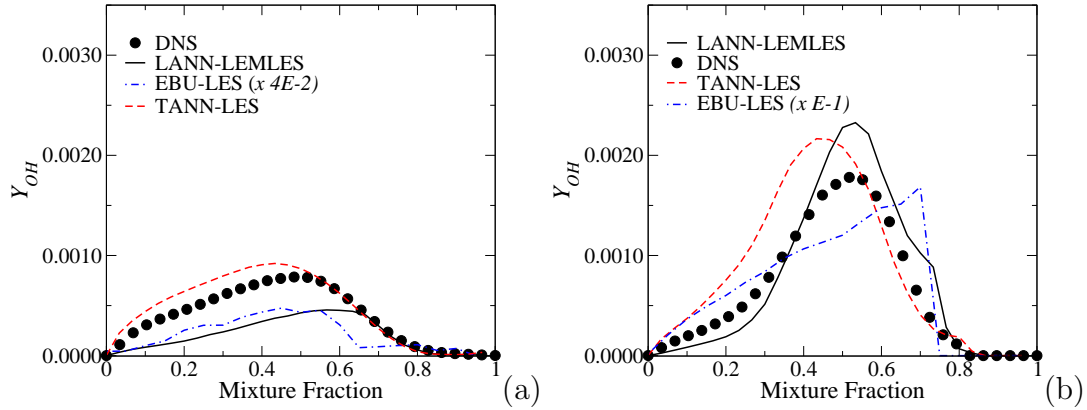


Figure 71: Mean value of the PDF of Y_{OH} conditioned on mixture fraction calculated by LANN-LES, TANN-LES and EBU-LES at $t_j =$ (a) 20 and (b) 40.

of extinction and reignition behavior with a less accuracy than LANN-LEMLES but with increased speed-up.

Fig. 71 shows the mean of the PDF of OH conditioned on mixture fraction calculated with LANN-LEMLES, TANN-LES and EBU-LES at $t_j = 20$ and 40. Among the models considered here, the EBU-LES gives the worst results. The LANN-LEMLES and TANN-LES, on the other hand provides results comparable with the DNS data. The LANN-LEMLES predicts more extinction compared to TANN-LES at $t_j = 20$. At $t_j = 40$, on the other hand, the LANN-LEMLES gives better agreement with the DNS data compared to the TANN-LES. The peak value obtained by the TANN-LES

at this time instant is shifted towards the fuel lean side.

The fact that LANN-LEMLES predicting more extinction than it should be can be attributed to the grid resolution. In LEMLES, the basic idea is to provide closure for turbulent stirring, molecular diffusion and reaction at their respective length scales. This is ascertained by solving the scalar field equations on the LEM level. For this particular case, however, the LES level grid resolution is already taken close to the DNS by clustering the grid through the shear layers. Hence, for this case especially at extinction, the LEMLES provides more extinction than it should be, since, more number of turbulent stirrings are performed than it should be per LES cell. On the other hand, the TANN-LES provides results similar to the DNS, since, as indicated before, the grid resolution is already close to DNS.

6.4 Time and Memory Savings

Each state obtained from the stand alone LEM computations is used as an entry on the thermo-chemical database used to train the LANN. The size of the whole database is 3.18 GB, which was saved entirely by the ANN training. The table constructed for TANN is 372 MB, much smaller than that of used for RR-ANN. Since filtered quantities are needed for LEM-ANN training, an averaging process was performed on each individual state, which resulted in a relatively smaller thermo-chemical database.

The computational time required to run one single iteration per number of grid points on a single processor INTEL PC (3.2 GHz Xeon) by LANN-LEMLES, TANN-LES, and DI-LEMLES using a stiff ODE solver is given in Table 20. Among the models considered here, the maximum amount of speed-up is obtained for the TANN-LES. The TANN-LES is almost 18 times faster than the conventional LEMLES approach. The LANN-LEMLES, on the other hand provides a speed-up of 5.5 times compared to the LEMLES using stiff ODE solver. Both the DI-LEMLES and LANN-LEMLES approaches solve the species equation within the subgrid, on one-dimensional lines

embedded within each LES cells. Hence, the number of grid points for the scalar field is increased drastically for these methods. The TANN-LES on the other hand, solves the species equation on the LES level. Hence, the speed-up obtained for this model is much higher than that is obtained for the LANN-LEMLES. The results showed that both of these models detected the extinction and reignition process with a good accuracy. It should be noted that the LANN-LEMLES is more accurate in detecting the correct physics compared to the TANN-LES.

Previous computations on premixed turbulent flames indicated almost 11 times speed-up based on LANN-LEMLES (74), which is not the case here. The stiffness of the reduced mechanism used for the premixed computation is one of the main reasons for this. Thus, the speed-up obtained by ANN highly depends on the reduced mechanism. This issue will be discussed in the next chapter.

Table 20: Speed-up obtained for 21 steps syngas mechanism

	Species Equation	Time/(step×cell)	Speed-Up
EBU-LES	LES level	0.36×10^{-2}	19.7
TANN-LES	LES level	0.39×10^{-2}	18.3
LANN-LEMLES	LEM level (12 cells/LES)	1.29×10^{-2}	5.5
DI-LEMLES	LEM level (12 cells/LES)	7.10×10^{-2}	1.0

CHAPTER VII

LES OF SPRF COMBUSTOR WITH ANN

The main objective of this chapter is to evaluate the speed-up and accuracy of the proposed ANN based methodologies in the LES of the SPRF combustor. Both LANN-LEMLES and TANN-LES are performed on the same grid as used in an earlier study (88). The details of the numerical set-up, ANN training and results are provided in the following sections.

7.1 Numerical Setup and ANN Training

SPRF combustor has recently been designed at the Georgia Tech to meet the lower emission regulations (10; 23; 87). It uses the exhaust gas re-circulation technique to reduce both the NO_x and CO emissions. The combustor can work both in premixed and non-premixed modes. Here, for the current computations, only the premixed mode is considered to demonstrate the ANN capabilities. It should be noted that the ANN can be extended for non-premixed cases as well, as it was discussed in the previous chapters. In the premixed mode, the Methane/Air mixture is injected into the combustion chamber at an effective equivalence ratio of 0.58. Flow enters and leaves the combustion chamber at the same plane, which provides extensive reactant preheating and mass entrainment across the shear layers. Thus, the reaction rates are enhanced and the flame can stabilize at very lean conditions. This phenomenon, which is known as the exhaust gas recirculation technique, allows feeding the *CO* leaving the combustor back into the incoming flow stream, so that any *CO* that may exist due to partial combustion can be subsequently burnt again.

The numerical set-up used in the current study is identical to that of used earlier by Undapalli and Menon (87; 88), and the schematics is given in Fig. 72. The

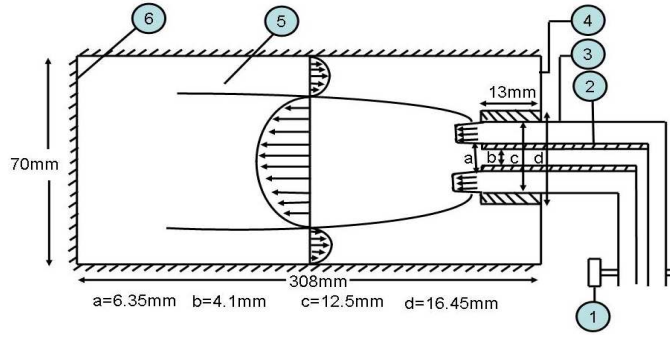


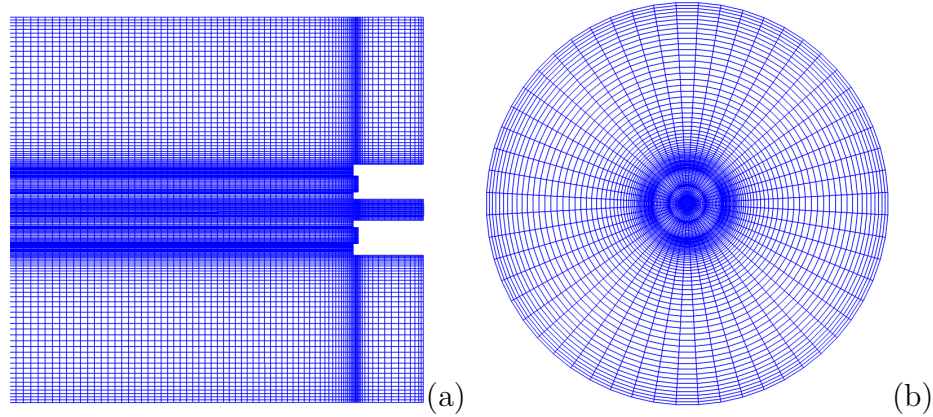
Figure 72: Schematics of the SPRF combustor (88).

combustion chamber (5) is enclosed with an end-plate (6) at one end. The outflow (4) is at the same plane with the injectors (2, 3). In the non-premixed mode the fuel (2) and the oxidizer (3) streams are introduced into the combustion chamber through different pipes. In the premixed mode, the central tube (2) is closed and the fuel/air mixture is discharged from the same pipe (3). The annular jet bulk velocity at the premixed mode is 122 m/s, whereas it is 104 m/s at the non-premixed mode. Also, the annular jet is preheated to 500 K at the premixed mode. Hence, the annular injector Reynolds number is 12,900 at the premixed mode, which is higher than that of for the non-premixed mode. A $1/8$ turbulent velocity profile is imposed as a boundary condition at the inlet with the mean velocity of 122 m/s. The boundary conditions are listed in details in Table 21. The chemical reaction rates are calculated based on a 12 steps, 16 species skeletal Methane/Air reaction mechanism (83). The details of the mechanism is given in Appendix B.3.

The grid used for the computations is shown in Fig. 73a-b. A two-domain butterfly type of grid, which comprises of a cartesian grid in the center of a cylindrical grid is used. Here, $194 \times 75 \times 57$ and $194 \times 15 \times 15$ number of nodes in x , y and z directions are used for the cylindrical and cartesian grids, respectively. The grid is clustered towards the dump plane and the shear layers in order to increase the quality of the LES in these regions. The validation of the selected grid is given in the previous

Table 21: Boundary conditions used for the LES (88).

	Reacting premixed	Reacting non-premixed
Annular jet flow rate [m^3/s]	0.00676	0.00638
Central jet flow rate [m^3/s]	-	0.00038
Annular jet temperature K	500	450
Central jet temperature K	-	300
Annular jet bulk velocity m/s	122	104
Equivalence ratio (ϕ)	0.58	0.58
Annular injector Re (Re_a)	12,900	10,160
Central jet Re (Re_c)	-	7,680
Subgrid Re (Re_Δ)	304	274

**Figure 73:** Side and cross-sectional views of the grid used for the LES.

studies (87; 88) and is not repeated here for the sake of brevity.

The ANN training table for this case is generated by using the stand-alone LEM code developed within the current thesis work. The database is constructed based on the conditions relevant to the SPRF combustor, i.e., the scalar field is initialized based on the laminar solution obtained for an equivalence ratio of 0.58, the Re_t is selected to vary between 10 to 400, etc. The details of this process are explained in Section 5.3.3.3. The same LEM table given in Section 5.3.3.3 is used in this part of the thesis work. The only difference lies in the fact that no temperature binning is performed for the training. Hence, each species have their own ANNs with a temperature ranging from 500 K to 1950 K.

7.2 *LES with LANN*

7.2.1 Instantaneous Reaction Rate Comparison

As an initial step, the LANN is tested against the DI and direct source term estimation (DSTE) methods to calculate the instantaneous reaction rates based on a given snapshot of the scalar field within the combustor at an arbitrary time instant. The DSTE method here calculates the species time evolution due to the chemical reactions on a given Δt_{LES} by performing sub iterations with a fixed chemistry integration time step. Hence, in contrast to the DI, which performs the integration with variable time step sizes based on the stiffness of the reaction mechanism, DSTE leads to a very simplistic and computationally affordable chemistry integration method (19). For the current computations, similar to the previous work performed by using the same reduced mechanism (87), 10 sub-iterations ($N_{si} = 10$) are performed for chemistry integration. It should be noted that the number of sub-iterations depend highly on the time step size (Δt) and the thermo-chemical conditions (Y_k, T, P). Hence, N_{si} needs to be validated (or re-calculated) for each distinct test case even though the same reduced mechanism is used. The results presented in Figs. 74, 75 and 76 are for three representative key species: the reaction rate of the fuel (CH_4), product (CO_2) and an intermediate species (CO), respectively.

Figure 74a shows the surface plot of the fuel reaction rate calculated by the (a) DI, (b) DSTE and (c) LANN. As seen in Fig. 74 (a), the flame front is highly wrinkled due to the existence of the small scale structures interacting with the flame. Close to the injector the fuel reaction rate exhibits a very thin zone. Further downstream there are pockets of fuel broken from the main flame and burning separately, which is evidenced by the island formations as seen in the figure. These features can also be detected by the DSTE and the ANN methods as given in Figs. 74b-c. The reaction rates calculated by the DSTE method exhibit a thicker reaction zone compared to the DI. The maximum value of the fuel destruction rate (in an absolute sense) has

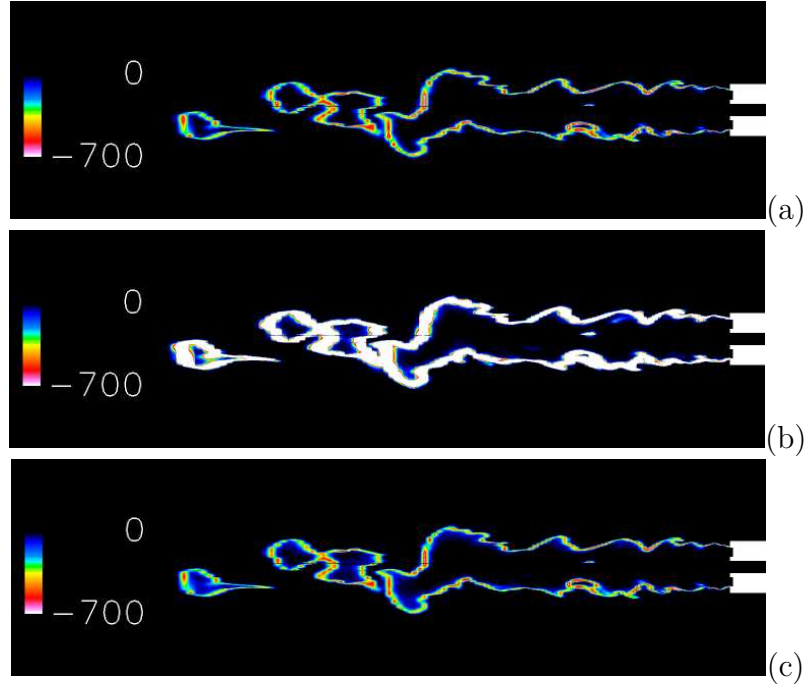


Figure 74: CH_4 reaction rate surface plot obtained by (a) DI, (b) DSTE and (c) LANN (in $1/s$).

also increased indicating that more fuel is burning with this method. ANN, on the other hand detects the same maximum value of the fuel destruction rate by the DI method as seen in Fig. 74c. The thickness of the reaction zone is also predicted well with the ANN method indicating that for this species it is working with an acceptable accuracy compared to the DI.

The reaction rate calculated for the CO_2 at the same arbitrary time instant with results shown in Figs. 74a-c is given in Figs. 75a-c. The previous figures showed that the fuel is destroyed close to the injector on a very thin region. It is interesting to note that the CO_2 reaction rate as calculated by the DI (Fig. 75a) exhibits a broken zone close to the injector. Although fuel is destroyed at this location, it cannot directly form CO_2 , since the chemical time scale is not sufficient enough for the reactions to reach the equilibrium point. This feature can be detected by relatively high order chemical kinetics mechanisms as it was explained in details in (87). Both the DI and

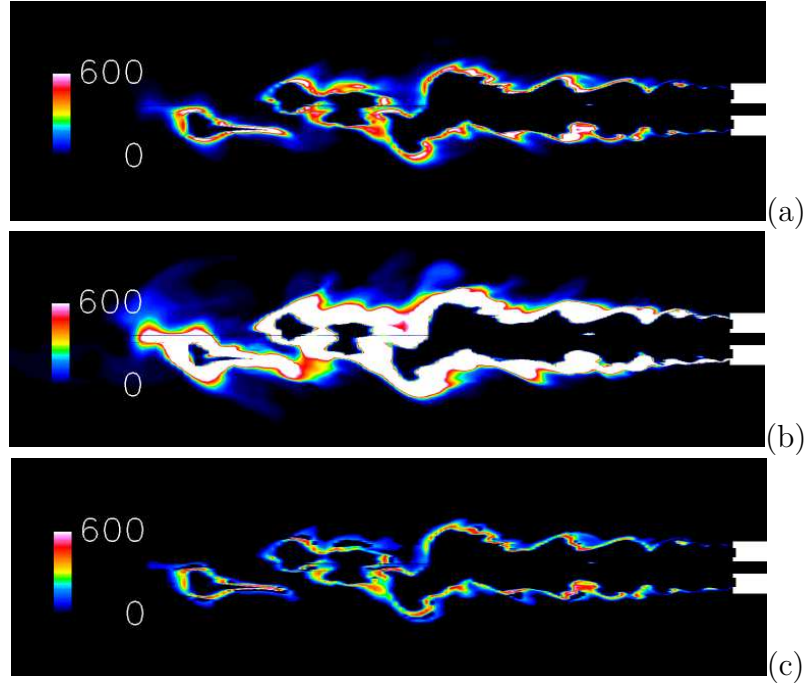


Figure 75: CO_2 reaction rate surface plot obtained by (a) DI, (b) DSTE and (c) LANN (in $1/s$).

LANN results lead to these observations consistently with each other. The DSTE results (Fig. 75b) shows increased level of reaction rate at this region. The CO_2 reaction zone is predicted much thicker than that of calculated by the DI and LANN. The LANN results as seen in Fig. 75c, tend to slightly underpredict the CO_2 reaction rate compared to the DI. This may lead to a decreased level of the CO_2 on an average sense within the combustor. This will be discussed in more details on the incoming sections.

Finally, the reaction rates obtained for CO is given in Figs. 76a-c. The intermediate species reaction rates, in general, tend to exhibit a two layer structure. At relatively low temperatures the radical species are produced, whereas they are consumed at high temperatures, which can also be seen in Figs. 76a-c. The CO mass fraction is produced within the inner layer of the flame zone as shown in Fig. 76a. Then, the whole flame is covered with negative reaction rate contours indicating that

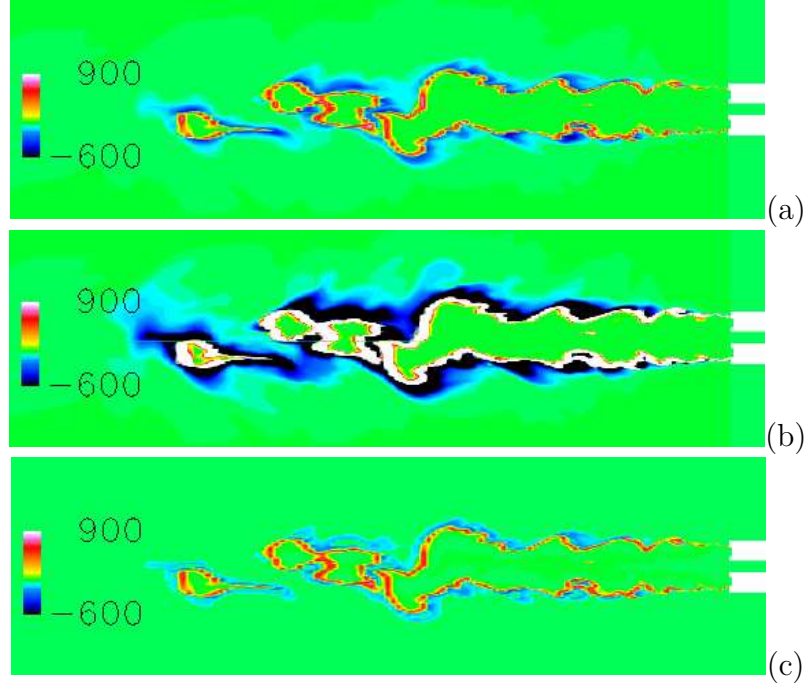


Figure 76: CO reaction rate surface plot obtained by (a) DI, (b) DSTE and (c) LANN (in $1/s$).

the CO is consumed on the outer layers. Both the DSTE and LANN methods successfully captured this feature (Figs. 76b-c). Similar to the observations made on the previous figures, the DSTE predicts higher level of consumption and/or production of the species with a thicker flame zone compared to both DI and LANN. The LANN shows similar flame structure with the DI. The production rate of the CO is predicted well by this method. Although the locations where the CO is consumed has been predicted well by the LANN, its magnitude shows that the consumption is not as strong as it is calculated by the DI.

7.2.2 Comparison of the Time Averaged Data

The current LANN-LEMLES is time averaged over a time window of 2τ . Here, τ is the characteristic time scale, and is the measure of the time required for a fluid particle that is discharged at the inlet to travel up to the stagnation plate, turn back and

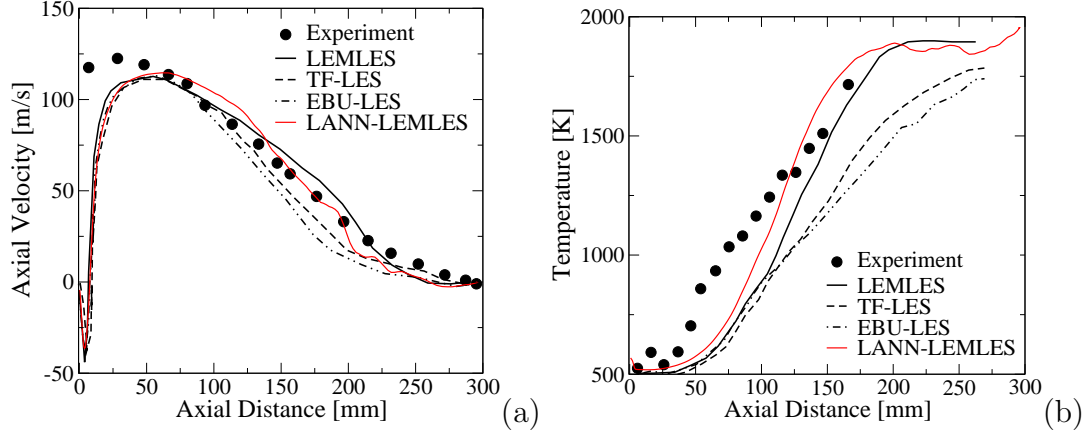


Figure 77: Comparison of the time-averaged (a) axial velocity and (b) temperature along the centerline. Experiment, LEMLES, TF-LES, and EBU-LES from (88).

leave the combustor. The variation of the time averaged axial velocity and temperature along the centerline is given in Figs. 77 (a) and (b), respectively. Here, results obtained earlier in (87) by using LES with LEM, TF and EBU subgrid combustion models are also shown for comparison purposes. The earlier LEMLES used DTSE method in combination with a four steps, seven species reduced mechanism to calculate the species instantaneous reaction rates. The axial velocity comparison (Fig. 77a) shows that both the LEMLES and LANN-LEMLES predicts the same variation of the axial velocity along the centerline. The LANN-LEMLES is particularly more accurate than the LEMLES in detecting the axial velocity at an axial distance starting from 100 mm and extending towards 200 mm. Both the TF-LES and EBU-LES tend to underpredict the time averaged axial velocity during this interval. All computational results show that there is a recirculation bubble located approximately at an axial distance value less than 25 mm. This feature cannot be detected by the experimental data. This is related with the BCs and the domain selected for the computations. The experimental set-up has a central tube which is used to inject the fuel in the non-premixed mode of the SPRF combustor. Although no flow is coming from this central tube in the premixed mode, from a computational point of view it

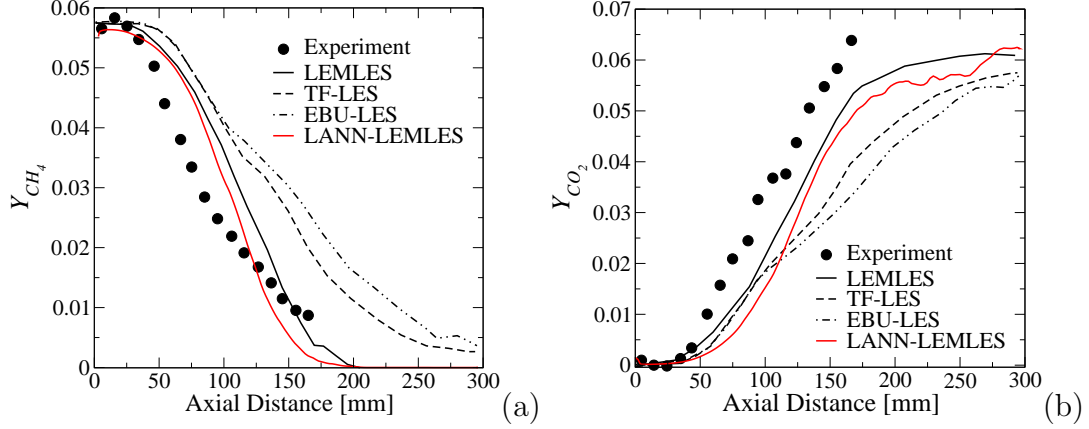


Figure 78: Comparison of the time-averaged (a) CH_4 and (b) CO_2 mole fraction along the centerline. Experiment, LEMLES, TF-LES and EBU-LES, from (88).

is still needed to be included in the LES, since it exists in the experimental set-up. In the experiments, this tube is connected to a valve in the further upstream. It is not possible to extend the central tube up to this valve in the current computations, and hence, a wall boundary condition is enforced after a much shorter distance in the upstream of the tube. This is believed to be the reason for detecting the small re-circulation bubble at the center part of the combustor. Nevertheless, the primary goal of the current section is to test the consistency between the LANN-LEMLES and the previous LEMLES, which is achieved successfully.

The temperature variation along the centerline is given in Fig. 77b. The experimental data indicates that the temperature increases up to 1000 K at an axial distance of approximately 80 mm. The computational results show that the time averaged temperature tend to increase with a slope less than that is for the experimental data. The LEMLES and LANN-LEMLES exhibit the same kind of behavior for temperature. The LANN-LEMLES tends to predict slightly higher values of temperature compared to the LEMLES. Overall they converge to the same maximum value of temperature, which is approximately 1900 K. The TF-LES and EBU-LES both show a temperature increase with a much smaller slope than that of obtained

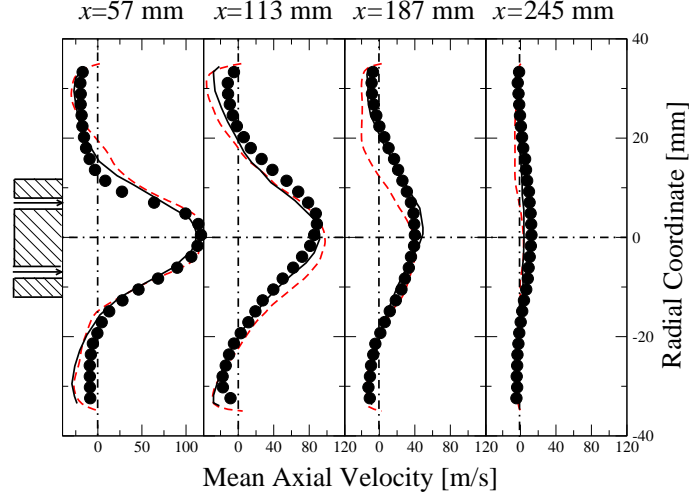


Figure 79: Comparison of the time-averaged axial velocity radial profiles at four sections. (●) Experiment, (—) LEMLES with DTSE and (- - -)LANN-LEMLES. Experiments and LEMLES from (88).

by LEMLES and LANN-LEMLES methodologies.

The comparison of the time averaged CH_4 and CO_2 mole fraction along the centerline are given in Figs. 78 (a) and (b), respectively. Here, TF-LES and EBU-LES methodologies predict that the fuel exists over a much longer distance along the combustor than it is calculated by the LEMLES based methodologies. They also indicate that there exists considerable amount of un-burnt fuel. As can be seen in the figure, close to the stagnation plate (at 300 mm) the fuel mole fraction is 0.05. The LEMLES and LANN-LEMLES, on the other hand, show that the fuel is actually consumed completely at an axial distance of 200 mm. The experimental data is recorded up to an axial distance of 175 mm. Hence, based on the data presented here it is not possible to conclude which model is predicting the correct physics in a better way. However, what is important is that both the LANN-LEMLES and LEMLES show the same flame physics. The variation of the CO_2 mole fraction along the axial distance is given in Fig 78b. Along the axial distance, from the injector tip to approximately 175 mm, the LEMLES based models provide the best results compared to the experimental data. The TF-LES and EBU-LES, again, predicts a longer flame. The

CO_2 for these computations build up with a much smaller slope compared to the experimental data.

The radial profiles of the time averaged axial velocity at four sections is given in Figs. 79. Here along with the experimental data, for the sake of clarity, only the computational results for LANN-LEMLES and LEMLES with DSTE are given. Here, it is interesting to note that almost at all cross-sections the experimental results are asymmetric. For instance, at the first section ($x = 57$ mm), for a radial distance greater than 20 mm the experimental data is almost -10 m/s, whereas it is much closer to 0 m/s at the other side. As a result of this asymmetry, the computational results seem to be mismatching with the experimental data at a radial distance greater than -20 mm. At the second section ($x = 113$ mm) the location of the peak axial velocity obtained by the experimental data is shifted to a radial distance of approximately 5 mm. At the same section the LEMLES results are also asymmetric, whereas LANN-LEMLES is not. At the third section, however, the LANN-LEMLES results are skewed. Overall the agreement between the experimental and computational results are satisfactory except for the asymmetry.

7.3 *LES with TANN*

In this section the results obtained by using the TANN-LES approach for the SPRF combustor are presented. For this part, the computations are run by using the same grid, initial and boundary conditions that of used in Section 7.1. The ANN training is achieved by using the output of the same calculation that was used to train the LANN in the previous section. This time, the output is spatially filtered with a characteristic filter size equal to the grid spacing used in the computations. The optimum ANN architecture is found to be a three hidden layer architecture with ten, eight and four (10/8/4) number of PEs at each hidden layer. For each species the inputs are the filtered species mass fractions, temperature, filtered level species gradient and subgrid

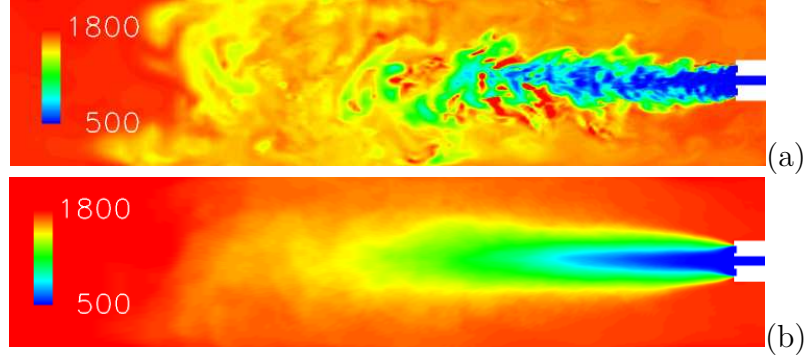


Figure 80: (a) Instantaneous and (b) time-averaged temperature surface plot.

Reynolds number.

The instantaneous and time averaged surface plots of the temperature are given in Figs. 80a-b. Similar to the results provided in the previous section, the time averaging here is obtained for 2τ . The variation of the instantaneous temperature within the combustion chamber exhibits a highly wrinkled flame front. Hot pockets of temperature exists within these structures indicating that the combustion is mainly occurring at these locations. On a time averaged sense, however, as seen in Fig 80b, these instantaneous fluctuations vanishes and the flame front becomes much smoother. The TANN-LES also shows that compared to the LANN-LEMLES, temperature is lower within the combustion chamber. The region close to the stagnation region exhibits the maximum temperature. The characteristic velocity at this location is much smaller than that of close to the injector, hence, it is much more difficult to obtain a statistical data at this region with the τ used to time average the results in the current study.

The instantaneous and time averaged surface plots of the CH_4 mass fraction are shown in Figs. 81a-b. The instantaneous picture shows that although the overall temperature level is decreasing within the combustor, this is not related with decrease in the overall consumption of the fuel. As seen in the figure, the fuel is consumed totally within the combustion chamber. The time averaged results are very smooth

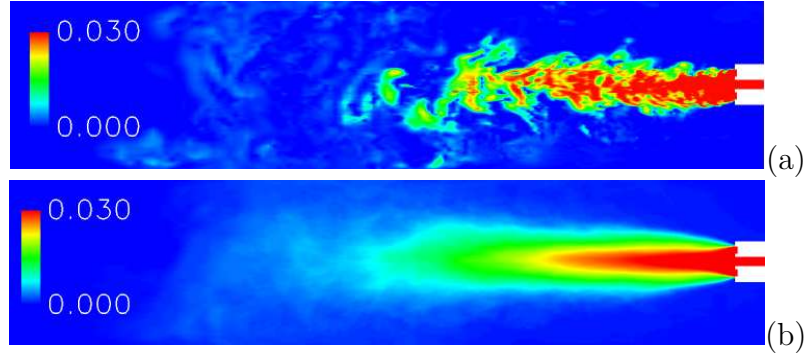


Figure 81: (a) Instantaneous and (b) time-averaged CH_4 mass fraction surface plot.

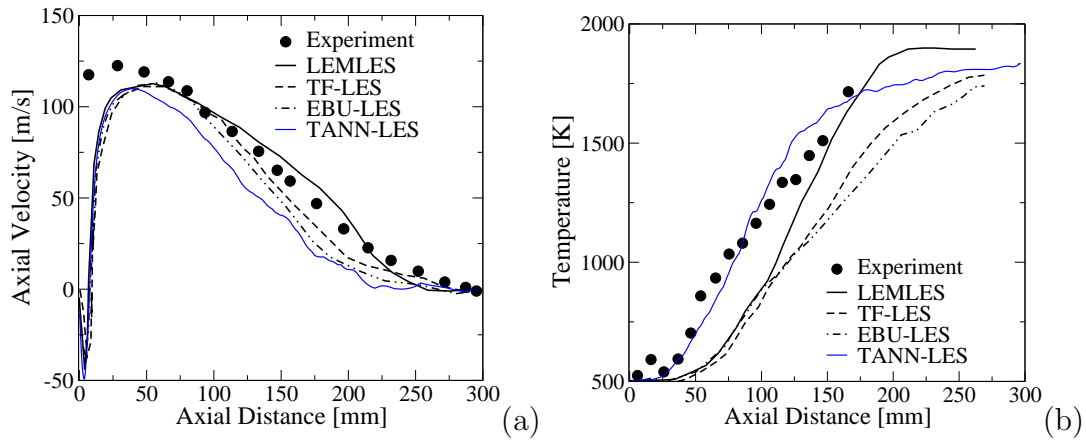


Figure 82: Comparison of the time-averaged (a) axial velocity and (b) temperature along the centerline.

close to the injector, whereas some oscillations can be seen close to the stagnation plate. Again, this is an issue of time averaging window used for the results, and more time instants are needed to reach statistically converged data at this region.

The comparison of the time averaged axial velocity and temperature are given in Figs. 82. The axial velocity surface plot shows that the current TANN-LES underpredicts the experimental data almost at all locations after an axial distance of 50 mm. The temperature plot, however, as shown in Fig. 82b indicates that the experimental data is captured with a good agreement compared to the results obtained by other computations. The time-averaged, axial variation of the temperature calculated by the TANN-LES indicates that the heat release is captured fairly well.

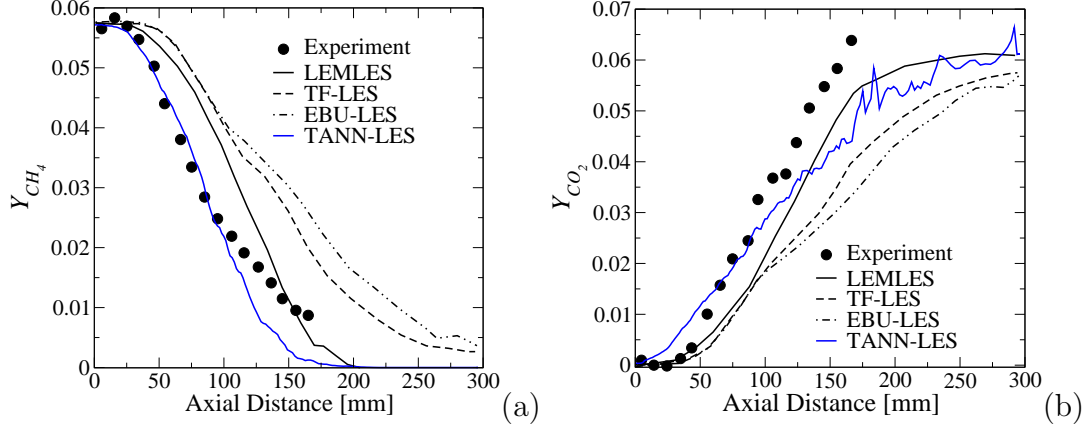


Figure 83: Comparison of the time-averaged (a) CH_4 and (b) CO_2 mole fraction along the centerline. Experiment, LEMLES, TF-LES and EBU-LES, from (88).

The results indicate that the axial variation of the temperature is captured well by the TANN-LES approach compared to the LANN-LEMLES. However, the predictions for the axial velocity is worst than the LANN-LEMLES results, which is interesting. The eddy sizes for turbulent stirring in the TANN training is selected within a range of η (Kolmogorov’s length scale) to the L (integral length scale. In the actual LEMLES approach, however, the eddy sizes are restricted within a range of η to Δx_{LES} (LES grid spacing). Hence, the current TANN-LES provides small scale turbulent stirring with eddy sizes effectively larger than those that should have seen in the actual LEMLES. This leads to a more wrinkled flame front, which in turn increases the turbulence level within the combustor. As a result, although the heat release is calculated correctly (as evidenced by the temperature plot), the velocity field is not.

Similar to the axial variation of the time averaged temperature, the time averaged CH_4 and CO mole fraction plots given in Figs. 83a-b show that the current TANN-LES approach agrees well with the experimental data especially close to the injector (axial distance less than 100 mm.). The time averaged CH_4 mole fraction vanishes completely at an axial distance of 175 mm, whereas the experimental data shows that the fuel exists over a much longer region. Nevertheless, the experimental variation

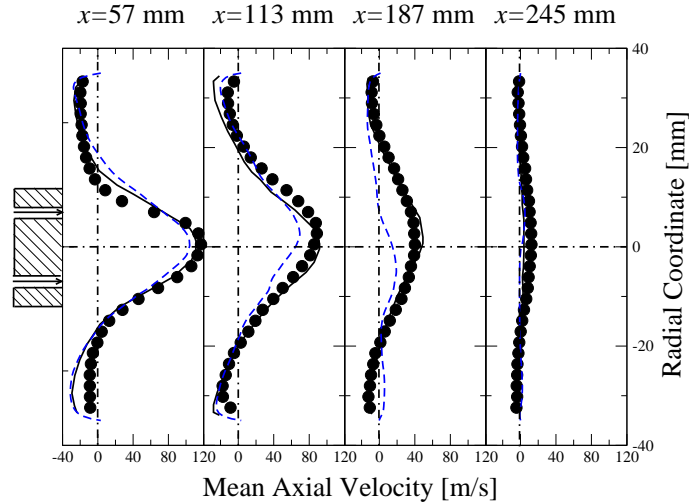


Figure 84: Comparison of the time-averaged axial velocity radial profiles at four sections. (●) Experiments, (—) LEMLES with DTSE and (---) TANN-LEMLES. Experiments and LEMLES from (88).

of the fuel mole fraction after an axial distance of 175 mm is not known. The CO_2 mole fraction variation along the axial distance is not captured as good as the CH_4 , as seen in Fig. 84b.

Finally, the radial profiles of the time averaged axial velocity obtained by experiments, calculated by LEMLES and TANN-LES at four sections are given in Figs. 84. The results given in Fig. 82a for the axial variation of the axial velocity indicated that the TANN-LES results under predicts the experimental data. The same feature can be seen in the current figure as well. At the first section ($x = 57$ mm), the TANN-LES provides almost the same data with the LEMLES predictions. At the second section located at $x = 113$ mm, although the general trends are correct, the maximum value at a radial distance equal to 0 mm is under predicted by almost 30 m/s. The situation is worst at $x = 187$ mm, where the TANN-LES indicates that the flow is almost stagnating.

7.4 *Time and Memory Savings*

The methane reaction mechanisms are known to be much stiffer than the syngas mechanisms, since they typically involve more radical species. Hence, as it was shown previously in Section 5.3.4, the speed-up obtained for the current mechanism is much higher than it is obtained for the syngas based computations demonstrated throughout the current thesis work. The comparison of the speed-up obtained for the TANN-LES, LANN-LES, DSTE-LEMLES and DI-LEMLES are given in Table 23. In the DSTE-LEMLES method, the reaction rate is time integrated with 10 steps within a given LEM diffusion time step. Hence, compared to the DI-LEMLES methodology, DSTE-LEMLES provides an almost 8 times speed-up. The LANN-LEMLES, on the other hand, is 49 times faster than the DI-LEMLES, which is even better than the DSTE-LEMLES. The speed-up obtained by the DSTE-LEMLES can be improved by using less number of steps for chemistry sub-integrations, however, as it was shown in Fig. 74-75, the reaction rates are already being over-predicted for the number of steps that are used here. All LEMLES based methodologies solve the species equation on the LEM level, which are essentially 1D lines embedded within each LES grid. The TANN-LES, on the other hand, solves the species equation on the LES level. Hence, the speed-up obtained for this methodology is much more than it can be obtained by using LEMLES based methodologies. For this particular case TANN-LEMLES provides 135 times speed-up compared to the DI-LEMLES. It is almost 2.5 times faster than the LANN-LEMLES, which is still considerable.

The ANN based methodologies require a training table. However, unlike the conventional look-up table approaches there is no need to link the flow solver with the table, but the ANN coefficients would be enough. The table used for LANN training in this study is 470 MB, whereas ANN required only 0.27 MB of memory. For TANN training the table size is much smaller, since it essentially includes the filtered states from the LANN table. The ANN size requirement during the actual

Table 22: Speed-up obtained for 12 steps methane skeletal mechanism.

	Species Equation	Time/(step×cell)	Speed-Up
TANN-LES	LES level	7.78×10^{-5}	134.9
LANN-LEMLES	LEM level (LES/12)	2.14×10^{-4}	49.2
DSTE-LEMLES	LEM level (LES/12)	8.79×10^{-3}	7.8
DI-LEMLES	LEM level (LES/12)	1.05×10^{-2}	1.0

Table 23: Memory savings obtained for 12 steps methane skeletal mechanism.

	Training Table Size	Memory Requirement During LES
TANN-LES	182 MB	0.30 MB
LANN-LEMLES	470 MB	0.27 MB
DSTE-LEMLES	—	—
DI-LEMLES	—	—

LES is still negligible, which is only 0.30 MB.

CHAPTER VIII

CONCLUSIONS AND FUTURE WORK

8.1 Conclusions

In this study, two new models to calculate the instantaneous and filtered form of the chemical reaction rates are developed and studied in detail. The models are based on the ANN approach, which is a very powerful interpolation scheme that can be used to map input-output pairs. ANN has the capability to identify the underlying relations (if exists) between the inputs and outputs and can represent these relations through simple algebraic equations. Hence, instead of solving the governing equations of the physical process of interest, it is possible to use ANNs to represent the same process in a time and memory efficient manner. This ANN based modeling approach is validated extensively within the thesis work to decrease the computational time required to calculate the chemical source terms in the LES of turbulent reactive flow computations.

The most important tasks in the ANN modeling are (i) developing a database which is representative of the actual process that is going to be simulated, (ii) and training the ANN on this database. Although tabulation methodologies exist in the literature, such as ILDM, ISAT, flamelet, etc., they are found not to be suitable for representing the interaction between turbulence and flame without any reduction in the number of parameters defining the system of governing equations. Hence, as a first step, new tabulation strategies are sought and tested along with the ANN approach for canonical premixed flame turbulence interaction studies.

Basically three distinct tabulation strategies for the first task are proposed in the thesis work. The first one is based on constructing the thermo-chemical database

by steady, laminar premixed flame calculations. The ANN trained on this table worked fairly well on laminar simulations, but not on turbulent flames. The second method is based on generating the database by simulating the interaction between a laminar flame front and a single vortex (FVI). Different cases are run by varying the strength of the initial vortex and it is observed that as the vortex interacts with the flame, it is broken into smaller structures and leads to different level of scalar mixing. Hence, in the final ANN training table, each different case accessed different regions on the compositional state-space. The last method is based on simulating the interaction of an initially laminar flame front with a homogeneous turbulent flow field (FTI). The computations are carried out by using a stand-alone LEM solver, which is developed as a tool within the current thesis work. In the LEM framework, the governing equations for the scalar field are solved on one-dimensional lines and turbulent stirrings are modeled by using a stochastic model.

As for the second task, an ANN training code is developed which is used for manipulating the weight coefficients between the PEs in a given ANN architecture, so as to provide the correct output for the given inputs. A modified version of the GDR is developed and used as a learning algorithm in order to avoid being trapped in one of the local minima of the error surface topology during the training phase. The code and the proposed learning algorithm are validated by using simple test functions.

The LES of premixed flame- turbulence-vortex interactions using ANN trained on tabulation achieved by FVI and FTI approaches provided fairly good predictions compared to results obtained by employing a stiff ODE solver. This proves that although the chemical reaction rates are calculated using the chemical kinetics formulations, the perturbation of the flow on the thermo-chemistry is also important and plays an important role on deciding which part of the thermo-chemical state space is accessed during the LES. Although the databases constructed based on FVI

and FTI are found to be working fairly well, the latter is selected over the former within the current thesis work due to its robustness and ease to use. Hence, all the validation studies used the database generated by stand-alone LEM computations for ANN training.

The thermo-chemical database construction relevant to the LES of practical flames is one of the major problems in the modeling of turbulent reactive flow applications. Often the databases are constructed based on prototype flames such as laminar flames. In the current thesis work the look-up tables are created systematically by more complex techniques, which allowed us to identify the effect of the turbulence on the generated databases. Overall, the results indicated that species have distinct sensitivities to the turbulent stirring. Against the action of a turbulent eddy, a highly diffusive species such as H_2 can recover its initial profile very quickly, whereas heavier species remain wrinkled for the most of the time. Hence, the compositional state-space exhibits a multi-dimensional variation which cannot be captured by the laminar flames.

The proposed thermo-chemical database generation methodology and the ANN modeling are validated further in two distinct test cases. The first case is a temporally evolving, planar, non-premixed syngas/air flame, which has been recently studied by using DNS (26). The species conditional statistics, syngas flame structure and the scalar dissipation rate statistics are investigated extensively to test both the LANN and TANN approaches. The results indicated that both the LANN and TANN methodologies can detect the extinction reignition processes fairly well. The DNS results showed that the fuel components CO and H_2 has distinct combustion characteristics. The highly diffusive and reactive H_2 species is consumed much earlier than the CO . The H_2 combustion provides the radical species needed for CO oxidation. As a result, considerable amount of CO can be detected at the regions where there is almost no H_2 . This also led to the fact that the radical species are distributed

differently within the shear layers. The exact locations of the species depend mostly on their diffusion characteristics and reactions that they are involved with. All of these effects were captured successfully by both of the proposed ANN methodologies. The LANN is particularly efficient compared to the TANN in predicting the H species and temperature conditional statistics. This is essentially an expected outcome of the computations, since, unlike the LANN, the TANN is solving the species equation on the LES level.

The second test case is the LES of SPRF combustor (10; 23; 87). Here, similar to the previous test case, both the LANN and TANN closure is used, and the results are compared with the experimental, as well as, the computational data that exists in the literature (87) for this particular combustor. The axial variation of the time averaged velocity and temperature obtained by the LANN-LEMLES approach showed that the current results are very similar to the LEMLES. The TANN approach provided good results for the scalar field. Accompanied by the fact that the overall temperature field is underpredicted, the flow field within the combustor is found to be slower than that of identified by the experimental study. Both of these observations point out a lower heat release rate calculated by the TANN-LES, which gives less temperature, and hence, less acceleration.

The test cases are selected in order to provide a detailed evaluation of the ANN based modeling as much as possible. It is well known that the flame-turbulence interaction models that exist in the literature are working fairly well for steady flames. The goal here is to simulate flames that exhibit complex flame dynamics, where the chemical kinetics is not de-coupled from the fluid mechanics, and chemical rates become very important. Detailed chemical kinetics mechanisms are needed for such simulations that increases the computational burden. Hence, the test cases selected here to evaluate the ANN capabilities cover a wide range of conditions. Results obtained based on the LEMLES of a premixed syngas flame that assesses the ANN

accuracy for different level of premixing and turbulence is presented in Section 6.3. Chapter 6 provided results for a nonpremixed syngas flame which exhibits extinction characteristics. Eventually the ANN is tested on a practical combustor simulation in Chapter 7 for a premixed methane case where there is product gas re-circulation. Each test case used different reaction mechanism ranging from 11 to 16 species with a different level of stiffness. As shown in the results, the proposed ANN training and application procedure demonstrated here provides consistently acceptable predictions to all of these different test cases. Hence, it can be concluded that the proposed ANN training methodology is not specific for a particular combustion regime or a reduced mechanism.

The case setup for ANN training table generation and optimization of the ANN architecture needs to be defined by the user in this newly proposed approach. The ANN training table generation through stand-alone LEM code requires selection of the integral length scale and the range of turbulent Reynolds number. For higher values of the Re_t it is shown that the turbulence effects become the dominant feature and the flame exhibits a high deviation from the equilibrium solution. Thus, flames exhibiting high level of local extinction needs to be trained on a data generated specifically for high values of Re_t . A reference value for Re_t can be calculated based on the information on u' , l and T . The definition of the degrees of freedom in the ANN architecture so far is user dependent and found upon experimenting different values. The ANN community reports that any continuous function can be represented by a single hidden layer ANN architecture (16). For the problems considered in this study, however, the function of interest is N s dimensional and highly non-linear. Thus, a three hidden layer ANN is used for most of the calculations. Still, as indicated in Section 5.3.3.1, the optimum ANN needs to be selected based on the ANN training error and the speed-up that can be obtained. As mentioned repeatedly in the current dissertation, an optimum way of defining the ANNs has recently being proposed and

for a future work this can be used to define the ANN architecture for the given chemical kinetics mechanism and the operating conditions.

The most important merit of using LANN and TANN is the time and memory savings. Several different reaction mechanisms are used throughout the thesis work and different speed-ups are found. The speed-up obtained by using ANN is mainly based on the stiffness of the mechanism which is considered. For the 21 reactions syngas mechanism the maximum speed-up that can be obtained is almost 6X. For the skeletal syngas mechanism, on the other hand, a speed-up of 11X was obtained. The LANN used to replace the one-step methane mechanism showed that there is almost no gain. However, the LANN based on 12 reactions skeletal methane mechanism provided almost a 50X speed-up. The speed-up obtained by TANN is much larger than LANN, since with the TANN approach, unlike the LANN-LEMLES, the species equations are solved on the LES level. For the SPRF case the TANN provided 134X speed-up compared to LEMLES using a stiff ODE solver.

8.2 Recommendations for Future Work

The current thesis study provided discussion for the use of ANN approach in the LES modeling of turbulent reactive flows. Most of the results provided in this work, especially for the LANN approach, proved that the model is working fairly accurate with good speed-up and memory savings compared to the DI. However, it should be noted that the current way of incorporating the ANN into LES applications is based on the author's understanding of the physical phenomenon investigated and the modeling approaches used in the literature. Hence, the modeling can be improved and/or expanded into different directions. Nevertheless, it is expected that this thesis work will stay as a basic reference that can be used to understand the ANN in LES applications. The author believes that the following points should (or may) be studied further to improve the modeling approaches used in the thesis work:

ANN Training:

The current ANN training approach for both the LANN and TANN is based on off-line training. A training table is generated based on the techniques introduced in the thesis work (i.e., FVI, stand-alone LEM, etc.) and once the ANN is trained on this database, it is used as is in the LES. An alternative approach into this method would be to use a combined off- and on-line training approach. The ANN, in this approach, would be trained first on a certain database, as it is introduced in the thesis work. Then, during the actual flow simulation, once the states that were not included in the original training table, or the states that contribute large training error, are encountered, then DI can be used to calculate the reaction rates and the ANN can be re-trained on this new dataset. This combined on- and off-line training necessitates the identification of (i) the new states and (ii) states with large error. For the first one, a new parameter which determines the ellipsoid of accuracy of a given state, similar to the ISAT approach, can be used. In that case the number of ANN inputs needs to be increased. The latter, on the other hand, requires a second ANN architecture. This second ANN is trained on the training error of the original ANN. Hence, the training error of the first ANN can be continuously controlled with this second (and preferably much smaller) ANN during the actual computation. This approach has actually been tested within the context of this thesis work to some extent, and it has been observed that once the ANNs are trained on new states, they tend to forget the relations that they were trained in the first place. Once new data is learned, unless they are linked to the previously learned data, they will be eventually forgotten. This feature, needs to be studied further to come up with a well established methodology.

The ANNs are capable of defining the relations between different processes through their non-linear processing elements. This feature of the ANNs can be used for chemical mechanism reduction. Once trained on a database, ANNs can provide the information of which species are more important than the others in certain pressure and

temperature conditions. Hence, by defining some key species, the ANN trained on a full mechanism can be used on a much smaller number of inputs, which can provide substantial amount of speed-up.

Stand-alone LEM:

The current way of thermo-chemical database generation depends on the stand-alone LEM computations: The diffusion and reaction equations are solved exactly and turbulent stirrings are modeled through a numerical re-arrangement procedure. For future studies few concepts for this solver can be changed and/or improved as well. To start with, the current way of simulating the turbulent stirrings depend on the homogeneity assumption. It is well known that the turbulence is hardly homogeneous for practical turbulent flames and turbulent structures are mostly concentrated on the flame front. Also, the turbulent stirring in the current LEM concept is simulated as an instantaneous re-arrangement process. The fundamental studies in flame-turbulence interaction reveal that the flame front wrinkling due to the turbulent structures occur over a certain time and most of the time scales on the order of Kolmogorov's scale are very weak for changing the structure of the flame (61). These effects can be considered for investigation in the future studies.

The stand-alone LEM computations start from an initial distribution of the scalar field, which is obtained from laminar 1-D flame solution. The stand-alone LEM code can be extended to generate its own initial data based on the relevant conditions (i.e., premixing, scalar dissipation rate, temperature, composition, etc.), which would make this code a package on its own.

TANN:

The TANN approach is introduced in this thesis work and the capabilities of this method is assessed for the temporally evolving syngas flames and the SPRF combustor as shown in Chapters 4 and 5, respectively. It should be noted that this approach still needs to be studied further, and the current thesis only establishes a basis (a first

step) for this effort. As a matter of fact, the LANN approach is specific to the DNS, CMC-LES, PDF-LES and LEM-LES approaches. The TANN approach, on the other hand, is a LES subgrid closure by its own, and has more potential in the numerical modeling of turbulent flames compared to the LANN.

The selection of the variables used to parameterize the filtered reaction rates are not validated within this thesis work. Subgrid Reynolds number and the resolved level species gradients in addition to the filtered thermodynamic state vector are used for parameterizing the filtered reaction rate. These parameters may not be enough and appropriate for representing the filtered reaction rate. This needs to be studied further, and perhaps needs to be validated on several different basic flames.

APPENDIX A

SHORT MANUAL FOR 1-D STAND-ALONE LINEAR EDDY MIXING MODEL SOLVER

A.1 Introduction

The stand-alone LEM code solves turbulent stirring, molecular diffusion, and reaction equation for the scalar field (species and temperature) evolution on a one dimensional line. The turbulent stirring is modeled stochastically by *triplet-maps*, where as molecular diffusion and reaction is solved deterministically. Turbulent Reynolds number (Re_t) and integral length scale (l) are selected as the parameters defining triplet mappings. Current version of the stand-alone LEM code is capable of running multiple simulations for a range of Re_t . However l is always constant. This can be changed by modifying the INIT_GRID subroutine in the 1dlem.F file.

For more information on LEM model please refer to previous publications on the literature (78; 13; 75).

The case setup and the input parameters are modified in the Makefile and the input.data. The executable is generated by typing "make". Once the computation is finished, type "make collect" and "c.exe" to collect the LEM accessed states into a single file called ANN_TABLE.dat.

A.2 Directory Structure and the Initialization

The main solver is in 1dlem.F file. Modify the path.dat file to indicate where the code is going to be run (work directory). Copy *.dat and *.data files into the work directory with the executable to run the code. Under the work directory create a post folder. Under post folder, create filt and post folders. post/post will contain

the restart files on the LEM level, where as post/ave will have the restart files on the LES (filtered) level.

Check and/or modify the following files before starting a computation: 1) input.dat, 2) LEMin.dat, 3) diff.dat, 4) therm.dat, 5) curv_fit_coeff.F, 6) chemrate16.F, 7) Makefile

1) input.dat:

Most of the simulation parameters are defined in input.data. The description of the variables are given in Table 24

The species molecular formula and weights in the input file need to be written in the same order that they are presented in the reduced mechanism and the restart file (LEMin.dat).

2) LEMin.dat or chemkin.dat:

The initial profiles of the scalar field is given in LEMin.dat file. The order is: T , Y_k . The profile given in LEMin.dat represents the LES (filtered) level. This is analogous to initializing an LEM-LES with the LES level scalar profiles. The LEM, however, increases the number of grid points based on the turbulence parameters (Re_t , L) and initializes itself based on the given LES level profiles. Hence, the number of grid points given in LEMin.dat file should be less than the expected number of grid points for the LEM computation. The number of states in the LEMin.dat file should be equal to the LES_GRID.

The LEM can be initialized by using the chemkin.dat file instead of LEMin.dat as well. chemkin.dat contains the output obtained directly from a CHEMKIN solver (i.e., PREMIX or OPPDIF). The order of the variables in the chemkin.dat file should be: i , $x(i)$, $\rho(i)$, $T(i)$, $V(i)$, $Y_k(i)$, with i denoting the index number. The output from chemkin.dat is read if CHEMFILE.INP is included as a compile option in the Makefile. In this case, at the first iteration, the stand-alone LEM solver reads the data in chemkin.data file, interpolates it onto a new grid, which has LES_GRID number of

grid points and writes it into the LEMin.dat file. In this manner, LEMin.dat is created automatically by the solver.

3) diff.dat:

Polynomial coefficients to calculate the binary diffusion coefficients. This is in consistency with the Transport package of CHEMKIN. This file includes most of the species, but check it before starting a simulation to see if species related with that particular simulation is included in this file or not. This file is used whenever TRANSPORT option is selected in the Makefile. In case species information cannot be found in diff.dat, this can be generated easily by using the TRANSPORT package of CHEMKIN.

4) therm.dat:

Polynomial coefficients for the thermodynamic database (c_p and H). This is in the CHEMKIN format

5) curv_fit_coeff.F:

TRANSPORT_CURVE_FIT subroutine includes the polynomial coefficients to calculate species viscosity and conductivity. Check it before starting a simulation to see if species related with that particular simulation is included in this file or not.

6) chemrate16.F:

This is the reduced mechanism which is used to calculate the chemical source terms. The current version uses 16 species, 12 steps reduced skeletal mechanism for CH_4 /Air combustion. See <http://public.ca.sandia.gov/TNF/chemistry.html> for more information on the reduced mechanism. To perform an LEM simulation with another mechanism, simply replace the chemrate files, and check SOURCE subroutine in the 1dlem.F file. The inputs for this file are the pressure (dynes/cm²), temperature, mass fractions. The output is the reaction rates of the species (moles/(cm³sec)).

7) Makefile: Makefile is used to compile the *.F files and to create the executable. Some of the solver options are defined here. Their descriptions are provided in Table

For a full LEM computation (with turbulent stirring, diffusion, reaction) on a reasonable computational time add the following line to your Makefile:

```
FFLAGS = -DSTIRRING -DDIFFUSION -DTRANSPORT -DMIXTURE_AVE -  
DNEWDIF -DDIRECT_INT -DCHEMKIN_IN -DMAN
```

Finally, the descriptions for the Fortran files are given in Table 26. A sample input file is also given in Table 27

Table 24: Explanations for the variables defined in input.data

SIMTIME	:	Total simulation time in seconds.
DELTAT	:	A reference time step size, which is larger than the Δt_{diff} and Δt_{stir} .
PRESSURE	:	Pressure in Pa.
NSPECI	:	Number of species.
NREST	:	Number of restart files written for the given Re_t and realization.
NSTR	:	Number of stirring per one deltat. Used only if the code is compiled with the -DART_STIR option.
L	:	Domain length in meters.
LES_GRID	:	Total number of grid points used for initialization.
MOLE2MASS	:	Type 1 if the initial data (i.e., chemkin.dat) is in mole fractions.
EDDYSIZE	:	Integral length scale in meters.
REYLS	:	Starting value for turbulent Reynolds number (Re_t).
REYLE	:	End value for Re_t .
NREYL	:	Number of Re_t that the code is going to be run for.
NREAL	:	Number of realizations.
TREF	:	Used only for post-processing. States corresponding to a temperature value less than TREF are not written into the table.
NEULER	:	Number of Euler steps per given diffusion time step used for chemistry integration. Used only if -DINDIRECT_INT option is selected in the makefile.
LOC_ST	:	If the code is expected to be run for a subset range of turbulent Reynolds numbers, this can be set through LOC_ST and LOC_TOT. Let's say among (1-20) Re_t , only (3-7) are wanted. In this case set NREYL to 20, LOC_ST to 3 and LOC_TOT to 4.
SPEC	:	Species molecular formula.
WT	:	Species molecular weight.

Table 25: The compilation options that can be defined in the Makefile.

NREAC	:	No reaction rates calculation.
NDIF	:	No diffusion calculation.
ART_STIR	:	Once this option is selected, number of stirrings per LEM iteration are not determined by the original LEM formulation, but by the NSTR given in the input.dat file.
TRANSPORT	:	To access advanced transport options, should be always followed by SCHMDT, MIXTURE_AVE, or, MULTI_COMP.
SCHMDT	:	The mixture averaged species diffusion coefficients are calculated based on constant Lewis and Schmidt number assumptions for all species.
MIXTURE_AVE	:	The mixture averaged species diffusion coefficients are calculated by using the Binary diffusion coefficients.
MULTI_COMP	:	Multi component diffusion coefficients are calculated and used for the diffusion velocity.
VEL_COR	:	Used only with MIXTURE_AVE. It can be used to ensure that the summation of the species diffusion velocities are equal to zero.
OLDDIF	:	Works only with SCHMDT or MIXTURE_AVE. Assumes the diffusion velocity is in the form of $(1/Y_k)(dY_k/ds)$. Valid for binary mixtures.
NEWDIF	:	Works only with SCHMDT or MIXTURE_AVE. Assumes the diffusion velocity is in the form of $(W_k/(WY_k))(dX_k/ds)$. Valid for multi-species mixtures.
DIRECT_INT	:	Works only with REACTION. Uses a stiff ODE solver to calculate the chemical source terms.
ANN	:	Works only with REACTION. Uses ANN to calculate the chemical source terms. ANN coefficients are needed to be given in the ANN/ folder.
INDIRECT_INT	:	Instead of using a stiff ODE solver to calculate the reaction rates, the code uses a step-wise integration with a given number of sub-iterations. The number of integration steps are defined by NEULER.
PREMIXED	:	Used only for Premixed configurations. The LEM observation window is shifted during the computations based on the mass fraction of a reference species defined by NREF in the input file.
SGS	:	The filtered (averaged) Y_k , T , Re_t , dY_k/ds and reaction rates are calculated and written into the post/filt/filt_XX_YY_ZZ.dat files for TANN approach.
RSTSGS	:	The LEM level Y_k , T are written into the post/post/post_XX_YY_ZZ.dat files for LANN approach.
MAN	:	The initialization file (chemkin.dat) is provided.
CHEMKIN_IN	:	Read the CHEMKIN output directly and prepare LEMin.dat file according to the LES domain size and number of grid points.

Table 26: Explanations for the Fortran files

ldlem.F	:	Includes main routines to read the input, initial profiles, LEM field initialization, allocating-deallocating arrays and calling routines to calculate the properties.
all_data.F	:	Most of the declarations are made here.
lem.F	:	Main routine for LEM. Evaluates the time scales and calls the turbulent stirring and diffusion_reaction solver.
stir.F	:	For turbulent stirring.
diff_reac.F	:	Solving the diffusion-reaction equations for the species and energy conservation.
chemrate.F	:	Calculating the species reaction rates.
dvode.F	:	Performing chemical integration (stiff ODE solver for chemistry)
ann.F	:	Performing chemical integration using ANN.
rest.F	:	Based on the options selected in the Makefile, writes the restart files for the LEM and/or LES level.
init.F	:	Used basically to generate the initial data. INIT_DATA subroutine reads the chemkin output and turns it into a format compatible with the current solver. PREP_REST subroutine is used for user defined initial profiles. In its current form it is hardcoded for a non-premixed system.

Table 27: A sample input file used for stand-alone LEM computations for the Case B in Section 5.3.

SIMTIME	DELTAT	PRESSURE	NSPECI	NREST	NSTR
4E-4	1E-7	101325D0	16	500	0
L (M)	LES_GRID	MOLE2MASS			
0.035D0	82	1			
EDDYSIZE	REYLS	REYLE	NREYL	NREAL	TREF
0.001	200	400	20	2	510
LOC_ST	LOC_TOT	NEULER			
1	20	2			
SPEC	WT	NO			
H2	2.0159	1			
H	1.0080	2			
O2	31.9988	3			
OH	17.0074	4			
H2O	18.0153	5			
HO2	33.0068	6			
H2O2	34.0148	7			
CH3	15.0351	8			
CH4	16.0431	9			
CO	28.0106	10			
CO2	44.0100	11			
CH2O	30.0265	12			
C2H2	26.0384	13			
C2H4	28.0543	14			
C2H6	30.0702	15			
N2	28.0134	16			

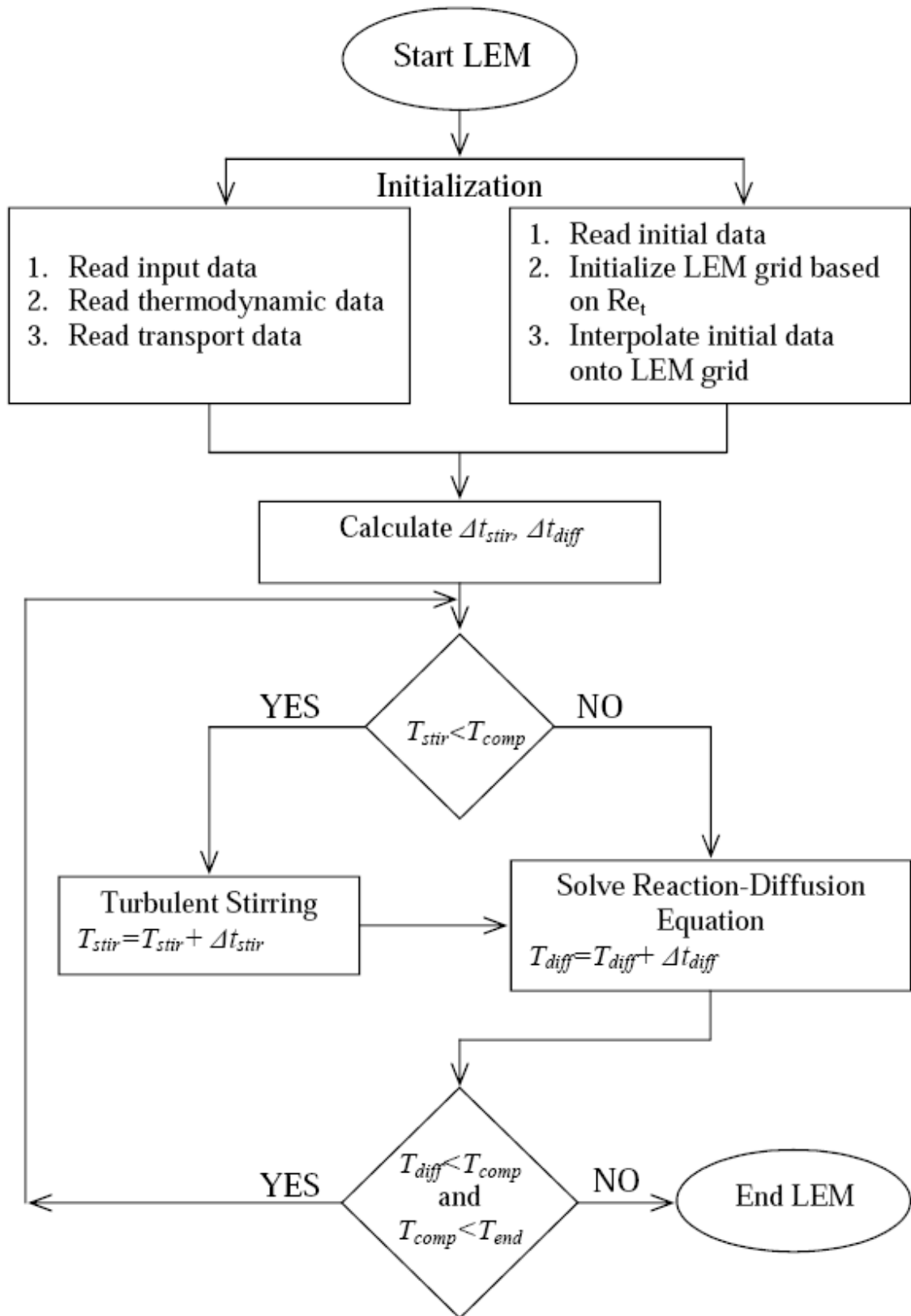


Figure 85: Flow chart for the stand-alone LEM code.

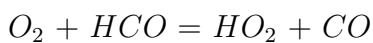
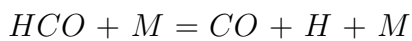
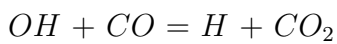
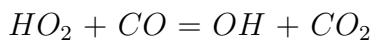
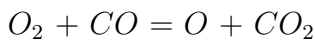
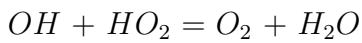
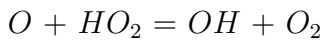
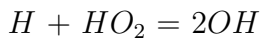
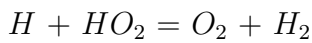
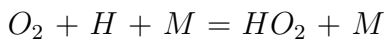
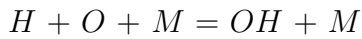
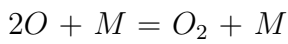
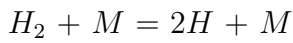
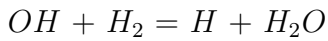
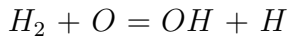
APPENDIX B

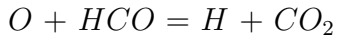
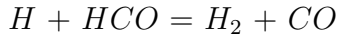
REDUCED MECHANISMS USED IN THE STUDY

B.1 21 Steps, 11 Species Syngas Mechanism

This mechanism is used in Section 5.3.3.4 and Chapter 6. See (26) for more information on the mechanism.

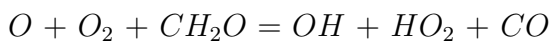
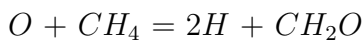
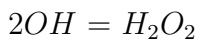
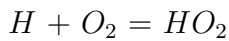
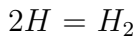
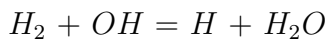
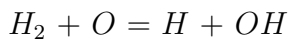
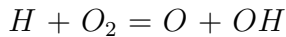
Species: H_2 , O_2 , O , OH , H_2O , H , HO_2 , CO , CO_2 , HCO , N_2 $O_2 + H = OH + O$





B.2 10 Steps, 14 Species Skeletal Syngas Mechanism

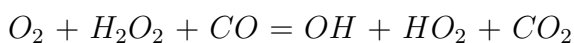
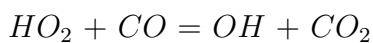
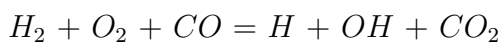
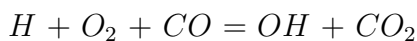
This mechanism is used in Sections 5.1.2.2, 5.2 and 5.3.3.2. Species: H_2 , H , O , OH , HO_2 , H_2O , CO , O_2 , H_2O_2 , CO_2 , CH_4 , CH_2O , NO , N_2

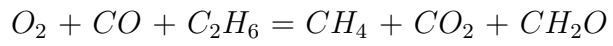
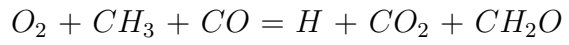
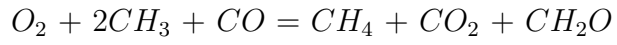
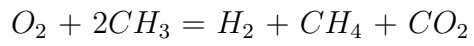
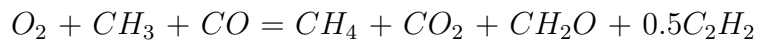
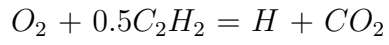


B.3 12 Steps, 16 Species Skeletal Methane Mechanism

This mechanism is used in Section 5.3.3.3 and Chapter 7. See (83) for more information on the mechanism.

Species: H_2 , H , O_2 , OH , H_2O , HO_2 , H_2O_2 , CH_3 , CH_4 , CO , CO_2 , CH_2O , C_2H_2 , C_2H_4 , C_2H_6 , N_2





Bibliography

- [1] BARLOW, R. E., *Proceedings of the TNF Workshops*. Sandia National Laboratories, Livermore, CA, 2005. www.ca.sandia.gov/TNF.
- [2] BAUM, M., POINSOT, T., HAWORTH, D. C., and DARABIHA, N., “H₂/O₂/N₂ flames with complex chemistry in two-dimensional turbulent flows,” *J. Fluid Mech.*, vol. 281, pp. 1 – 32, 1994.
- [3] BELL, J. B., CHENG, R. K., DAY, M. S., and SHEPHERD, I. G., “Numerical simulation of Lewis number effects on lean premixed turbulent flames,” *Proc. Combust. Inst.*, vol. 31, pp. 1309–1317, 2007.
- [4] BELL, J. B., DAY, M. S., and GRGAR, J. F., “Numerical simulation of premixed turbulent methane combustion,” *Proc. Combust. Inst.*, vol. 29, pp. 1987–1993, 2002.
- [5] BELL, J. B., DAY, M. S., GRGAR, J. F., LIJEWSKI, M. J., DRISCOLL, J. F., and FILATYEV, S. A., “Numerical simulation of a laboratory-scale turbulent slot flame,” *Proc. Combust. Inst.*, vol. 31, pp. 1299–1307, 2007.
- [6] BILGER, R. W., STARNER, S. H., and KEE, R. J., “On reduced mechanisms for methane-air combustion in nonpremixed flames,” *Combust. Flame*, vol. 80, pp. 135–149, 1990.
- [7] BLASCO, J. A., FUEYO, N., DOPAZO, C., and BALLESTER, J., “Modelling the temporal evolution of a reduced combustion chemical system with an artificial neural networks,” *Combust. Flame*, vol. 123, pp. 38 – 52, 1998.
- [8] BLASCO, J. A., FUEYO, N., LARROYA, J. C., DOPAZO, C., and CHEN, J. Y., “A single-step time-integrator of a methane-air chemical system using artificial neural networks,” *Comput. Chem. Eng.*, vol. 23, pp. 1127 – 1133, 1999.
- [9] BLASENBREY, T. and MAAS, U., “ILDMS of higher hydrocarbons and the hierarchy of chemical kinetics,” *Proc. Combust. Inst.*, vol. 28, pp. 1623–1630, 2000.
- [10] BOBBA, M. K., *Flame Stabilization and Mixing Characteristics in a Stagnation Point Reverse Flow Combustor*. PhD thesis, Georgia Institute of Technology, Atlanta, GA, October 2007.
- [11] BRADAR, R. D. and JONES, R. M., “GE IGCC technology and experience with advanced gas turbines,” ger-4207, GE Power Systems, Schenectady, NY, October 2000.
- [12] CHAKRAVARTHY, V. and MENON, S., “Large-eddy simulations of turbulent premixed flames in the flamelet regime,” *Combust. Sci and Tech*, vol. 162, pp. 1–48, 2000.

- [13] CHAKRAVARTHY, V. and MENON, S., “Linear-eddy simulations of Reynolds and Schmidt number dependencies in turbulent scalar mixing,” *Physics of Fluids*, vol. 13, pp. 488–499, 2001.
- [14] CHEN, J. Y., BLASCO, J. A., FUEYO, N., and DOPAZO, C., “An economical strategy for storage of chemical kinetics: fitting *insitu* adaptive tabulation with artificial neural networks,” *Proc. Combust. Inst.*, vol. 28, pp. 115–121, 2000.
- [15] CHOI, Y. and CHEN, J.-Y., “Fast prediction of start-of-combustion in HCCI with combined artificial neural networks and ignition delay model,” *Proc. Combust. Inst.*, vol. 30, pp. 2711–2718, 2005.
- [16] CHRISTODOULOU, C. and GEORGIPOULOS, M., *Applications of Neural Networks in Electromagnetics*. Artech House, 2000.
- [17] CHUANYL, J., SNAPP, R. R., and PSALTIS, D., “Generalizing smoothness constraints from discrete samples,” *Neural Computation*, vol. 2, pp. 188–197, 1990.
- [18] ECHEKKI, T. and CHEN, J. H., “Unsteady strain rate and curvature effects in turbulent premixed methane-air flames,” *Combust. Flame*, vol. 106, no. 1, pp. 184–202, 1996.
- [19] EGGENSPIELER, G., *Numerical Simulation of Pollutant Emission and Flame Extinction in Lean Premixed Systems*. PhD thesis, Georgia Institute of Technology, Atlanta, USA, July 2005.
- [20] EGGENSPIELER, G. and MENON, S., “Combustion and emission modeling near lean blow-out in gas turbine engines,” *Prog. Comp. Fluid Dyn.*, vol. 5, no. 6, pp. 281–297, 2005.
- [21] FUREBY, C., “Large-eddy simulation of turbulent anisochoric flows,” *AIAA Journal*, vol. 33, no. 7, pp. 1263–1272, 1995.
- [22] GOLDIN, G. M. and MENON, S., “Scalar pdf construction model for turbulent non-premixed combustion,” *Combust. Sci. Tech.*, vol. 125, pp. 47 – 72, 1997.
- [23] GOPALAKRISHNAN, P., *Effects of the Reacting Flowfield on Combustion Processes in a Stagnation Point Reverse Flow Combustor*. PhD thesis, Georgia Institute of Technology, Atlanta, GA, January 2008.
- [24] GOPALAKRISHNAN, P., BOBBA, M. K., and SEITZMAN, J. M., “Controlling mechanisms for low NOx emissions in a non-premixed stagnation point reverse flow combustor,” *Proc. Combust. Inst.*, vol. 31, pp. 3401 – 3408, 2007.
- [25] GRGAR, J. F., BELL, J. B., and DAY, M. S., “The soot effect in naturally propagating, premixed, lean, hydrogen-air flames,” *Proc. Combust. Inst.*, vol. 32, pp. 1173–1180, 2009.

- [26] HAWKES, E. R., SANKARAN, R., SUTHERLAND, J. C., and CHEN, J. H., “Scalar mixing in direct numerical simulations of temporally evolving plane jet flames with skeletal CO/H₂ kinetics,” *Proceedings of the Combustion Institute*, vol. 31, pp. 1633–1640, 2007.
- [27] HECHT-NIELSEN, R., *Neurocomputing*. Addison-Wesley, 1990.
- [28] IHME, M., MARSDEN, A. L., and PITSCH, H., “Generation of optimal artificial neural networks using a pattern search algorithm: Application to approximation of chemical systems,” *Neural Computation*, vol. 20, pp. 573–601, 2008.
- [29] IHME, M., SCHMITT, C., and PITSCH, H., “Optimal artificial neural networks and tabulation methods for chemistry representation in LES of a bluff-body swirl-stabilized flame,” *Proc. Combust. Inst.*, vol. 32, pp. 1527–1535, 2008.
- [30] IM, H. G. and CHEN, J. H., “Preferential diffusion effects on the burning rate of interacting turbulent premixed hydrogen-air flames,” *Combust. Flame*, vol. 131, pp. 246–258, 2002.
- [31] JONES, W. P. and LINDSTEDT, P. R., “Global reaction schemes for hydrocarbon combustion,” *Combust. Flame*, pp. 223 – 233, 1988.
- [32] KAPOOR, R., LENTATI, A., and MENON, S., “Simulations of methane-air flames using ISAT and ANN,” *AIAA-01-3847*, 2001.
- [33] KEE, R. J., RUPLEY, F. M., MILLER, J. A., COLTRIN, M. E., F., G. J., MEEKS, E., MOFFAT, H. K., LUTZ, A. E., DIXON-LEWIS, G., SMOOKE, M. D., WARNATZ, J., EVANS, G. H., LARSON, R. S., MITCHELL, R. E., PETZOLD, L. R., REYNOLDS, W. C., CARACOTSIS, M., STEWART, W. E., GLARBORG, P., WANG, C., ADIGUN, O., HOUF, W. G., CHOU, C. P., and MILLER, S. F., “The transport pre-processor and subroutine library,” *Chemkin collection, Release 3.7.1*, 2003.
- [34] KEMPF, A., FLEMMING, F., and JANICKA, J., “Simulation of soot formation in turbulent premixed flame,” *Proc. Combust. Inst.*, vol. 30, pp. 557 – 565, 2005.
- [35] KERSTEIN, A. R., “Linear-eddy model of turbulent scalar transport and mixing,” *Combust. Sci. Tech.*, vol. 60, pp. 391–421, 1988.
- [36] KERSTEIN, A. R., “Linear-eddy model of turbulent transport II,” *Combust. Flame*, vol. 75, pp. 397–413, 1989.
- [37] KIM, W.-W. and MENON, S., “A new dynamic one-equation subgrid-scale model for large-eddy simulations,” *AIAA-95-0356*, 1995.
- [38] KIM, W.-W. and MENON, S., “A new incompressible solver for large-eddy simulations,” *International Journal of Numerical Fluid Mech.*, vol. 31, pp. 983–1017, 1999.

- [39] KONIG, K. and MAAS, U., “On-demand generation of reduced mechanisms based on hierarchically extended intrinsic low-dimensional manifolds in generalized coordinates,” *Proc. Combust. Inst.*, vol. 32, pp. 553–560, 2009.
- [40] LANDAU, L. J., *Concepts for Neural Networks : a Survey*. Springer, 1998.
- [41] LIGNELL, D. O., CHEN, J. H., SMITH, P. J., LU, T., and LAW, C. K., “The effect of flame structure on soot formation and transport in turbulent non-premixed flames using direct numerical simulation,” *Combust. Flame*, vol. 151, pp. 2–28, 2005.
- [42] LILLY, D. K., “A proposed modification of the Germano subgrid-scale closure method,” *Physics of Fluids A*, vol. 4, no. 3, pp. 633–635, 1992.
- [43] LIU, S., MENEVEAU, C., and KATZ, J., “On the properties of similarity subgrid-scale models as deduced from measurements in a turbulent jet,” *Journal of Fluid Mechanics*, vol. 275, pp. 83–119, 1994.
- [44] MAAS, U. and POPE, S. B., “Laminar flame calculations using simplified chemical kinetics based on intrinsic low-dimensional manifolds,” *Proc. Combust. Inst.*, vol. 25, pp. 1349–1356, 1992.
- [45] MAAS, U. and POPE, S. B., “Simplifying chemical kinetics: Intrinsic low-dimensional manifolds in the composition space,” *Combust. Flame*, vol. 88, pp. 239–264, 1992.
- [46] MAGNUSSEN, B. F. and HJERTAGER, B. H., “On mathematical modeling of turbulent combustion with special emphasis on soot formation and combustion,” *Proc. Combust. Inst.*, vol. 16, pp. 719–729, 1977.
- [47] MEHROTRA, K., MOHAN, C. K., and RANKA, S., *Elements of Artificial Neural Networks*. MIT Press, 1997.
- [48] MENON, S. and KIM, W.-W., “High reynolds number flow simulations using the localized dynamic subgrid-scale model,” *AIAA-96-0425*, 1996.
- [49] MENON, S. and PATEL, N., “Subgrid modeling for LES of spray combustion in large-scale combustors,” *AIAA Journal*, vol. 44, no. 4, pp. 709–723, 2006.
- [50] MOSBACHER, M., HAYNES, J., JANSSEN, J., BRUMBERG, J., LIEUWEN, T., MENON, S., SEITZMAN, S., and ANAND, A., “Fuel-flexible combustion system for co-production plant applications,” de-fc26-03nt41776, GE Global Research, Schenectady, NY, October 2006.
- [51] NATARAJAN, J., NANDULA, S., LIEUWEN, T., and SEITZMAN, J., “Laminar flame speeds of synthetic gas fuel mixtures,” *ASME Paper*, 2005.
- [52] NELSON, C. C., *Simulations of spatially evolving compressible turbulence using a local dynamic subgrid model*. PhD thesis, Georgia Institute of Technology, 1997.

- [53] NEURALWARE, *Neural Computing. A Technology Handbook for NeuralWorks Professional II / PLUS*. NeuralWare, 2001.
- [54] PANTANO, C., “Direct simulation of non-premixed flame extinction in a methane-air jet with reduced chemistry,” *J. Fluid Mech.*, vol. 514, pp. 231–270, 2004.
- [55] PATEL, N., KIRTAS, M., SANKARAN, V., and MENON, S., “Simulation of spray combustion in a lean direct injection combustor,” *Proc. Combust. Inst.*, vol. 31, pp. 2327–2334, 2007.
- [56] PETERS, N., *Numerical Simulation of Combustion Phenomena*. Springer-Verlag, 1985.
- [57] PETERS, N., *Turbulent Combustion*. Cambridge Monographs on Mechanics, 2000.
- [58] PITSCH, H., “Unsteady flamelet modeling of differential diffusion in turbulent jet flames,” *Combust. Flame*, vol. 123, pp. 358–374, 2000.
- [59] PITSCH, H., “Large eddy simulation of turbulent flames,” *Ann. Rev. Fluid Mech.*, vol. 38, pp. 233–266, 2006.
- [60] POINSOT, T., VEYNANTE, D., and CANDEL, S., “Diagrams of premixed turbulent combustion based on direct simulation,” *Proc. Combust. Inst.*, vol. 23, pp. 613–619, 1990.
- [61] POINSOT, T., VEYNANTE, D., and CANDEL, S., “Quenching processes and premixed turbulent combustion diagrams,” *Journal of Fluid Mechanics*, vol. 228, pp. 561–606, 1991.
- [62] POINSOT, T. and LELE, S., “Boundary conditions for direct simulations of compressible viscous flow,” *Journal of Computational Phys.*, vol. 101, pp. 104–129, 1992.
- [63] POINSOT, T. and VEYNANTE, D., *Theoretical and Numerical Combustion*. Edwards, Inc., second ed., 2005.
- [64] POPE, S. B., “Pdf methods for turbulent reactive flows,” *Prog. Energy Combust. Sci.*, pp. 119–192, 1985.
- [65] POPE, S. B., “Computationally efficient implementation of combustion chemistry using *in situ* adaptive tabulation,” *Combust. Theory Modelling*, vol. 1, pp. 41–63, 1997.
- [66] POPE, S. B., *Turbulent Flow*. Cambridge Book Company, first ed., 2000.
- [67] ROJAS, R., *Neural Networks - A Systematic Introduction*. Springer-Verlag, Berlin, New-York, 1996.

- [68] SANKARAN, V. and MENON, S., “Subgrid combustion modeling of 3-d premixed flames in the thin-reaction-zone regime,” *Proc. Combust. Inst.*, vol. 30, no. 1, pp. 575–582, 2005.
- [69] SANKARAN, V., PORUMBEL, I., and MENON, S., “Large-eddy simulation of a single-cup gas turbine combustor,” *AIAA-2003-5083*, 2003.
- [70] SCHUMANN, U., “Realizability of Reynolds-stress turbulence models,” *Physics of Fluids*, vol. 20, no. 5, pp. 721–725, 1977.
- [71] SEN, B. A., “Development of a simplified scheme for intrinsic low-dimensional manifolds by exploiting the hierarchical structures of hydrocarbon fuels,” Master’s thesis, Istanbul Technical University - Mechanical Engineering Department, Istanbul, Turkey, 2003.
- [72] SEN, B. A. and MENON, S., “Large-eddy simulations of turbulent flames in syn-gas fuel-air mixtures,” *AIAA-2007-1435*, 2007.
- [73] SEN, B. A. and MENON, S., “Representation of chemical kinetics by artificial neural networks for large eddy simulations,” *AIAA-2007-5635*, 2007.
- [74] SEN, B. A. and MENON, S., “Artificial neural networks based chemistry-mixing subgrid model for LES,” *AIAA-2009-0241*, 2009.
- [75] SEN, B. A. and MENON, S., “Linear eddy mixing and artificial neural networks for LES sub-grid chemistry closure,” *Combust. Flame*, *accepted for publication*, 2009.
- [76] SEN, B. A. and MENON, S., “Turbulent premixed flame modeling using artificial neural network based chemical kinetics,” *Proc. Combust. Inst.*, vol. 32, pp. 1605–1611, 2009.
- [77] SEN, B. A., OZDEMIR, I. B., and WARNATZ, J., “Implementation of the hierarchical structures of the combustion processes into intrinsic low-dimensional manifolds technique,” *4th International Symposium on Turbulence, Heat and Mass Transfer*, 2003.
- [78] SMITH, T. and MENON, S., “One-dimensional simulations of freely propagating turbulent premixed flames,” *Combust. Sci. and Tech.*, vol. 128, pp. 99–130, 1996.
- [79] SPALDING, D. B., “Concentration fluctuations in a round turbulent free jet,” *Chem. Eng. Sci.*, vol. 26, p. 95, 1971.
- [80] SPALDING, D. B., “Development of the eddy-break-up model of turbulent combustion,” *16th Symp. (Int.) on Combustion*, vol. 16, pp. 1657–1663, 1976.
- [81] SRIPAKAGORN, P., MITARAI, S., KOSALY, G., and PITSCH, H., “Extinction and reignition in a diffusion flame: A direct numerical simulation study,” *J. Fluid Mech.*, vol. 518, pp. 231–259, 2004.

- [82] SU, L. and CLEMENS, N., “The structure of fine-scale scalar mixing in gas-phase planar turbulent jets,” *Journal of Fluid Mechanics*, vol. 488, pp. 1–29, 2003.
- [83] SUNG, C., LAW, C., and CHEN, J., “An augmented reduced mechanism for methane oxidation with comprehensive global parametric validation,” *Proc. Combust. Inst.*, vol. 27, pp. 295–304, 1998.
- [84] TENNEKES, H. and LUMLEY, J. L., *A First Course in Turbulence*. MIT Press, 1992.
- [85] TROUVÉ, A. and POINSOT, T., “The evolution equation for the flame surface density in turbulent premixed combustion,” *Journal of Fluid Mech.*, vol. 278, pp. 1–31, 1994.
- [86] TURNS, S. R., *An Introduction to Combustion*. McGraw-Hill, 2000.
- [87] UNDAPELLI, S., *Large Eddy Simulation of Premixed and Non-premixed Combustion in a Stagnation Point Reverse Flow Combustor*. PhD thesis, Georgia Institute of Technology, Atlanta, GA, May 2008.
- [88] UNDAPELLI, S. and MENON, S., “LES of premixed and non-premixed combustion in a stagnation point reverse flow combustor,” *Proc. Combust. Inst.*, vol. 32, pp. 1537–1544, 2009.
- [89] VAGELOPOULOS, C. M. and EGOLFOPOULOS, F. N., “Laminar flame speeds and extinction strain rates of mixtures of carbon monoxide with hydrogen, methane and air,” *Proc. Combust. Inst.*, vol. 25, pp. 1317–1323, 1994.
- [90] VEYNANTE, D. and VERVISCH, L., “Turbulent combustion modeling,” *Prog. in Energy and Combust. Sci.*, vol. 28, pp. 193–266, 2002.
- [91] VINCENTI, W. G. and KRUGER, C. H., *Introduction to Physical Gas Dynamic*. Krieger Company Malabar, Florida, 1965.
- [92] VREMAN, B., GEURTS, B., and KUERTEN, H., “Realizability conditions for the turbulent stress tensor in large-eddy simulation,” *Journal of Fluid Mechanics*, vol. 278, pp. 351–362, 1994.
- [93] WARNATZ, J., MAAS, U., and DIBBLE, R. W., *Combustion: Physical and Chemical Fundamentals, Modeling and Simulation, Experiments, Pollutant Formation*. Springer, 2006.
- [94] WILCOX, D. C., *Turbulence Modeling for CFD*. La Canada, CA:DCW Industries, Inc., c1994, 11994.
- [95] XU, J. and POPE, H., “Pdf calculations of turbulent nonpremixed flames with local extinction,” *Combust. Flame*, vol. 123, pp. 281–307, 2000.

VITA

Baris Ali Sen was born on January 11-*th*, 1979 in Kassel, Germany. He had his high school education at the Ordu Anatolian High School. He attended Istanbul Technical University (ITU), Mechanical Engineering Department in 1996, where he received BS and MS degrees in 2001 and 2003, respectively. During his undergraduate and graduate studies in the ITU he worked at the Fluids Mechanics Laboratories. For his Masters study he spent three months as a visiting research assistant at the Interdisciplinary Center for Scientific Computing of Heidelberg University. After spending one year for Ph.D. at the ITU, he joined the Computational Combustion Lab at School of Aerospace Engineering, Georgia Institute of Technology in 2004. Since then he has been working in the field of computational modeling of reactive flows under the supervision of Dr. Suresh Menon. He expects to receive his Ph.D. in December 2009 and to live happily ever after.